SYNTHESIS, CHARACTERIZATION AND PROPERTIES OF MOLYBDATE BASED GLASS FREE MICROWAVE CERAMICS FOR LTCC AND ULTCC APPLICATIONS

Thesis submitted to the
UNIVERSITY OF CALICUT, KERALA
for the partial fulfillment of the requirements
for the award of the degree of
DOCTOR OF PHILOSOPHY IN PHYSICS
Under the Faculty of Science
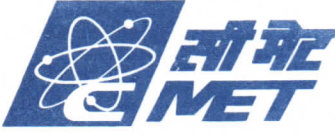
by

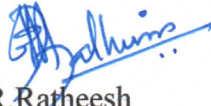**Dhanya Johnson**

Under the Guidance of

Dr. R. Ratheesh

CENTRE FOR MATERIALS FOR ELECTRONICS TECHNOLOGY (C-MET)

SCIENTIFIC SOCIETY, MINISTRY OF ELECTRONICS AND INFORMATION TECHNOLOGY,

GOVERNMENT OF INDIA, SHORNUR ROAD, P.O MULAKUNNATHUKAVU, ATHANI,

THRISSUR- 680581, KERALA, INDIA

APRIL 2019

TO WHOM SO EVER IT MAY CONCERN

This is to certify that the error bars are incorporated in the figures of the thesis titled "SYNTHESIS, CHARACTERIZATION AND PROPERTIES OF MOLYBDATE BASED GLASS FREE MICROWAVE CERAMICS FOR LTCC AND ULTCC APPLICATIONS" as suggested by the adjudicator.

10.01.2020
Hyderabad

Dr.R.Ratheesh
Research Supervisor

Certificate

This is to certify that the thesis titled **SYNTHESIS, CHARACTERIZATION AND PROPERTIES OF MOLYBDATE BASED GLASS FREE MICROWAVE CERAMICS FOR LTCC AND ULTCC APPLICATIONS** submitted to University of Calicut in partial fulfillment of the requirements for the award of the degree of **Doctor of Philosophy in Physics** is a record of the authentic work carried out by Smt. Dhanya Johnson, at Microwave Materials Division, Centre for Materials for Electronics Technology, Thrissur, under my guidance. The work presented in this thesis has not been included in any other thesis submitted previously for the award of any degree.

Thrissur

Dr. R. Ratheesh
(Supervising Guide)

SYNTHESIS, CHARACTERIZATION AND PROPERTIES OF MOLYBDATE BASED GLASS FREE MICROWAVE CERAMICS FOR LTCC AND ULTCC APPLICATIONS

PhD Thesis

Submitted by

Dhanya Johnson
Kakkassery House
Chaithanya
Puthenvettuvazhi
Chembukkavu
Thrissur-680020
Kerala, India
e-mail: dhanyaedwin@gmail.com

Research Supervisor

Dr. R. Ratheesh
Scientist F
Centre for Materials for Electronics Technology (C-MET)
e-mail: ratheesh@cmet.gov.in

April 2019

DECLARATION

I hereby declare that the thesis entitled **"SYNTHESIS, CHARACTERIZATION AND PROPERTIES OF MOLYBDATE BASED GLASS FREE MICROWAVE CERAMICS FOR LTCC AND ULTCC APPLICATIONS"** submitted to University of Calicut, is based on the original work carried out by me under the guidance and supervision of Dr. R. Ratheesh, Scientist F, Centre for Materials for Electronics Technology. No part of this work has been presented for the award of any other degree from any other institution.

Place: Thrissur

Date: 1-4-19

Dhanya Johnson

Dedicated to my loving parents

Acknowledgements

'Give thanks to the Lord, for he is good'

First and foremost I thank God almighty for giving me an enriching research period and institute for initiating my research activities. I remember with gratitude all the ups and downs through my research years which have helped me to remould myself as a better person and a better researcher. I take this opportunity to express my gratitude to all those who have been instrumental in the successful completion of this thesis.

I would like to extend my gratitude to my research supervisor Dr. R. Ratheesh, Scientist, Centre for Materials for Electronics Technology (C-MET), for his inspiring guidance, constant encouragements and valuable suggestions throughout my research work. Thank you for helping me to take the right decisions at the right time and for all selfless efforts you put in to equip me to complete this thesis in the best way possible. Thank you for all the fruitful discussions and inculcating in me a good research culture through the years of my research work.

I wish to express my sincere thanks to Dr. N. Raghu, Director, C-MET, Thrissur, for providing me the experimental facilities to carry out my research work in C-MET, and also for all the valuable suggestions and encouragements in bringing out the thesis.

I place on record, my sincere gratitude to Dr. N. R. Munirathnam, Director General, C-MET, and Dr. D. P. Amalnerker, former Executive Director of C-MET, for providing me the opportunity to pursue my research work at C-MET. I also gratefully acknowledge my indebtedness to Dr. K. R. Dayas, former Director, C-MET, Thrissur for granting me an opportunity to pursue research at C-MET and for his continuous support and guidance.

I thank profoundly the valuable guidance of Dr. S. N. Potty, scientist, C-MET, Thrissur. I also acknowledge the continuous support and timely assistance rendered by sir which helped me in the successful completion of this thesis.

I place on record my sincere thanks to Principal and Management of Vimala College (autonomous), Thrissur for granting me the permission to pursue Ph.D. I thank Dr. Sr. Ritty J Nedumpara, former Head of Dept. & Vice Principal, Dr. Malini K. A, Head of Dept. and all my seniors and colleagues at Post Graduate and Research Department of Physics, Vimala College for their continuous support and cooperation through out my research period.

I extend my sincere thanks to Dr. V. Kumar, Dr. N. C. Pramanik, Dr. A. Seema, Dr. Radhika T, Dr. K.V. Baiju, Dr. Stanly Jacob and all the members at C-MET for their suggestions

Preface

The thesis investigates the structure and microwave dielectric properties of a wide range of molybdate ceramics and studied their suitability for LTCC and ULTCC applications. Multilayer co-firing technology requires microwave ceramics having low dielectric loss, stable dielectric constant together with temperature independent dielectric properties. LTCC (Low Temperature Co-fired Ceramics) materials are those ceramics which can be co-fired with silver metal electrode and are having sintering temperatures below 961°C, which is the melting point of silver. Whereas ULTCC (Ultra Low Temperature Co-fired Ceramics) materials are ceramics having sintering temperatures below 660°C, the melting point of aluminium. Multilayer stacking technique consists of tape casting the ceramic powder, followed by screen printing of the required microwave circuits, stacking the different layers and co-firing them into a single monolithic package. Phase pure ceramics with low sintering temperature are the much sought after materials for LTCC and ULTCC substrate fabrication.

The compounds selected for the study are binary molybdates in the alkaline earth molybdate - rare earth molybdate $AMoO_4$-$R_2(MoO_4)_3$, sodium molybdate - alkaline earth molybdate Na_2MoO_4-$AMoO_4$ and sodium molybdate - rare earth molybdate Na_2MoO_4-$R_2(MoO_4)_3$ systems, which are having crystal structures related to the scheelite structure. The scheelite structured compounds are selected for the study based on the phase purity of these compositional type, their low loss tangent and compatibility with Ag and Al metal electrodes, which are ideally suited for LTCC and ULTCC applications.

Chapter 1 presents an introduction about the microwave materials and their applications. The dielectric properties of materials, factors affecting dielectric constant, quality factor and temperature coefficient of resonant frequency and the theory of dielectric resonators are discussed. The significance of multilayer co-firing technology and the critical material requirements in this regard are also dealt in detail. A comprehensive review of the molybdate based LTCC/ULTCC systems are also highlighted. **Chapter 2** gives an outline of the synthesis and characterization techniques adopted in the thesis.

The crystal structure, microwave dielectric properties and chemical compatibility of the $Na_5R(MoO_4)_4$ (R = La, Pr, Nd, Sm, Y and Yb) ceramics are presented in **Chapter 3**. These compositions are reported to have modulated scheelite-like structure. The phase purity of the compositions are confirmed through

powder X-ray diffraction studies. Raman studies show that these compositions consist of MoO_4 tetrahedra in the crystal structure. All the compositions have ultra low sintering temperatures. $Na_5Yb(MoO_4)_4$ has a dielectric constant of 6.9, $Q_u \times f$ of 43,400 GHz and τ_f of -68 ppm/°C at microwave frequency. XRD and EDS studies show that $Na_5Yb(MoO_4)_4$ has excellent chemical compatibility with Al electrode. Present study shows that $Na_5Yb(MoO_4)_4$ is an ideal candidate material for ULTCC applications owing to its ultra low sintering temperature, excellent microwave dielectric properties and good chemical compatibility with Al electrode.

The **chapter 4** presents the structure-property relationship and compatibility studies of $NaR_5(MoO_4)_8$ (R = La, Pr, Nd, Sm) ceramics with incommensurately modulated scheelite structure. XRD, Raman and SEM studies show that the compositions are phase pure in nature. The dielectric constant of these compositions ranges from 10.6 to 11.5, $Q_u \times f$ from 56,200 to 78,600 GHz and τ_f from -42 to -72 ppm/°C. The XRD patterns of the co-fired samples show characteristic peaks of the ceramics, together with weak Ag peaks. The EDS analysis of the samples confirm the diffusion of silver into the ceramic during co-firing, which limits their application in LTCC devices.

Detailed studies on the structure, microwave dielectric properties and chemical compatibility studies of $Na_2A_5(MoO_4)_6$ (A = Zn, Mg, Ca, Ba, Sr) compositions are presented in **Chapter 5**. TG/DTA studies confirm the phase formation of $Na_2Zn_5(MoO_4)_6$ and $Na_2Mg_5(MoO_4)_6$ compositions in the ULTCC temperature range. The XRD analysis shows that the $Na_2Zn_5(MoO_4)_6$ and $Na_2Mg_5(MoO_4)_6$ compositions are phase pure whereas Ba, Sr and Ca analogues exist as multiphase compositions consisting of Na_2MoO_4 and corresponding alkaline earth molybdate. $Na_2Zn_5(MoO_4)_6$ possesses a dielectric constant of 8.1, $Q_u \times f$ of 35,800 GHz and τ_f of -95 ppm/°C along with excellent compatibility with Al electrode, which has been confirmed by XRD and EDS analyses of the co-fired sample.

The **chapter 6** presents the structure and microwave dielectric properties of $AR_4(MoO_4)_7$ (A = Ba, Sr, Ca; R = La, Pr, Nd, Sm) ceramics. Among these, $BaR_4(MoO_4)_7$ (R = Pr, Nd, Sm) exist as multiphase comprising of $BaR_2(MoO_4)_4$ and $R_2(MoO_4)_3$ phases. The dielectric constant of the phase pure compositions range from 9 to 11.8, quality factor $Q_u \times f$ from 30,200 to 91,000 GHz and τ_f from -39 to -90 ppm/°C. The highest $Q_u \times f$ is obtained for $CaPr_4(MoO_4)_7$ ceramic. The co-firability of these compositions with silver has been investigated by XRD and EDS analyses.

The effect of titanium substitution on the structure and microwave dielectric properties of $Pr_2Zr_3(MoO_4)_9$ is investigated in **Chapter 7**. The motivation of this work

is to bring down the temperature coefficient of resonant frequency of $Pr_2Zr_3(MoO_4)_9$ to utilize it for outdoor wireless applications. In the present work, Zr^{4+} ions are systematically substituted with Ti^{4+} ions in $Pr_2Zr_3(MoO_4)_9$ and investigated their structural, microstructural and microwave dielectric properties in detail. XRD and Laser Raman studies show that titanium substituted $Pr_2Zr_{(3-x)}Ti_x(MoO_4)_9$ ceramics are phase pure only up to x=1. It is found that for $Pr_2Zr_{(3-x)}Ti_x(MoO_4)_9$ (x=0-3) ceramics, the sintering temperature decreases and dielectric constant increases with increasing titanium content. $Pr_2Zr_3(MoO_4)_9$ possesses a dielectric constant of 9.6, Q_u x f of 42,900 GHz and τ_f of -30 ppm/°C whereas the completely titanium replaced ceramic exhibits a dielectric constant of 12.7, quality factor of 27,400 GHz and τ_f of 0 ppm/°C. XRD and EDS studies show that $Pr_2Zr_{(3-x)}Ti_x(MoO_4)_9$ (x=0-3) ceramics are not compatible with Ag/Al electrodes and hence unsuited LTCC/ULTCC applications.

HDPE/$Pr_2Zr_3(MoO_4)_9$ composite preparation by intimate mixing followed by compression moulding technique are presented in **Chapter 8**. A detailed study on the characterization of the composites, simulation studies using High Frequency Structure Simulator (HFSS), microstrip patch antenna fabrication and testing are also included in Chapter 8. The optimum (48 vol%) filler loaded composite sample has a dielectric constant of 4.84, loss tangent of 0.003, coefficient of thermal expansion of 57 ppm/°C (coefficient of thermal expansion) and ultimate tensile strength of 7.8 MPa. The dielectric, thermal and mechanical properties of HDPE/$Pr_2Zr_3(MoO_4)_9$ composites are studied as a function of filler fraction. ANSYS High Frequency Structure Simulator (HFSS) is used to design microstrip patch antenna that operates at Industrial, Scientific and Medical Radio (ISM) band (5.8 GHz). Microstrip patch antenna is fabricated using photolithographic technique on copper cladded planar HDPE/$Pr_2Zr_3(MoO_4)_9$ composite. The antenna parameters are measured using a vector network analyzer and are in good agreement with simulated data.

The conclusions drawn from the previous chapters are summarized in **Chapter 9**. The LTCC and ULTCC materials developed in the present thesis work are compiled in this chapter highlighting the microwave dielectric properties and their compatibility with metal electrodes. The thesis presents a systematic study of molybdate ceramics with superior microwave dielectric properties together with good chemical compatibility with Ag/Al electrodes are ideal materials for LTCC/ULTCC circuit fabrication. The design and fabrication of substrate integrated waveguide (SIW) circuits using new LTCC/ULTCC compositions identified in the present work are proposed as the future work.

LIST OF PAPERS PUBLISHED IN INTERNATIONAL JOURNALS

[1] **J. Dhanya,** E. K. Suresh, R. Naveenraj, R. Ratheesh, Structure and microwave dielectric properties of low temperature sinterable $NaR_5(MoO_4)_8$ (R= La, Pr, Nd, Sm) ceramics, J. Electron. Mater., (2019). (in press)
doi: 10.1007/s11664-019-07165-y

[2] **J. Dhanya,** P. V. Sarika, R. Naveenraj, E. K. Suresh, R. Ratheesh, Structure and microwave dielectric properties of $ALn_4(MoO_4)_7$ (A= Ba, Sr, Ca, Ln= La, Pr, Nd and Sm) ceramics, Int. J. Appl. Ceram. Technol., (2019). (in press)
doi: 10.1111/ijac.13178

[3] **J. Dhanya,** E. K. Suresh, R. Naveenraj, R. Ratheesh, Synthesis and characterization of $Na_5M(MoO_4)_4$ (M= Y, Yb) microwave ceramics for ULTCC applications, Ceram. Int., 44 [6] (2018) 6699-6704.

[4] **J. Dhanya,** A. V. Basiluddeen, R. Ratheesh, Synthesis of ultra low temperature sinterable $Na_2Zn_5(MoO_4)_6$ ceramics and the effect of microstructure on microwave dielectric properties, Scr. Mater., 132 (2017) 1-4.

[5] **J. Dhanya,** A. N. Unnimaya, R. Ratheesh, Dielectric resonators with complex crystal structures in the $La_2O_3–Al_2O_3–TiO_2$ system for microwave applications, J. Mater. Sci.: Mater. Electron., 25 [10] (2014) 4617-4622.

[6] R. Naveenraj, E. K. Suresh, **J. Dhanya,** R. Ratheesh, Preparation and microwave dielectric properties of $Ba_3A(V_2O_7)_2$ (A= Mg, Zn) ceramics for ULTCC applications, Eur. J. Inorg. Chem., (2019). (in press)
doi: 10.1002/ejic.201801369

[7] A. N. Unnimaya, E. K. Suresh, **J. Dhanya,** R. Ratheesh, Structure and microwave dielectric properties of $5BaO–2V_2O_5$ binary ceramic system, J. Mater. Sci.: Mater. Electron., 25 [2] (2014) 1127-1131.

List of conference proceedings

[1] **J. Dhanya,** K. Anju, R. Ratheesh, "NaMg$_3$In(MoO$_4$)$_5$ ceramic for ultra low temperature co-firable (ULTCC) applications", International Conference on "Expanding Horizons of Technological Applications of Ceramics and Glasses" (EH-TACAG'17), Pune, 14-16 December, 2017. (Bagged first prize under Electroceramics poster presentation)

[2] **J. Dhanya,** E. K. Suresh, R. Naveenraj, R. Ratheesh, "Microwave dielectric characterization of ultra-low temperature firing Na$_5$Nd(MoO$_4$)$_4$ ceramic", International conference on Science Technology and Applications of Rare Earths, (ICSTAR), Tirupathi, 23-25 September, 2018.

CONTENTS

LIST OF TABLES   **Page No.**

ABBREVIATIONS

CTE	Coefficient of Thermal expansion
DPSS	Diode-pumped solid-state
DTA	Differential thermal analysis
DTG	Differential thermogravimetry
EDS	Energy dispersive X-ray spectroscopy
HDPE	High-density polyethylene
HFSS	High frequency structure simulator
HTCC	High Temperature Co-fired Ceramics
ICDD	International Centre for Diffraction Data
ISM	Industrial, scientific and medical
LTCC	Low Temperature Co-fired Ceramics
PCB	Printed circuit board
PVA	Polyvinyl alcohol
SEM	Scanning electron microscope
SIW	Substrate integrated waveguide
TE	Transverse Electric
TGA	Thermogravimetry analysis
TMA	Thermomechanical analyzer
ULTCC	Ultra Low Temperature Co-fired Ceramics
UTM	Universal testing machine
XRD	X-ray diffraction

Chapter 1

Introduction

1.1 An overview of microwave materials and applications

1.2 Dielectric properties of materials

1.3 Dielectric resonators

1.4 Multilayer co-firing technology

1.5 Review of literature - LTCC and ULTCC molybdate ceramics

1.6 Significance of scheelite structure

1.7 Objectives of the present study

1.1 An overview of microwave materials and applications

Microwave materials and technologies have made a huge impact on all realms of human activity with a host of commercial, scientific and consumer applications. The microwave frequencies range from 300 MHz to 300 GHz and the electromagnetic spectrum is shown in Figure 1.1.
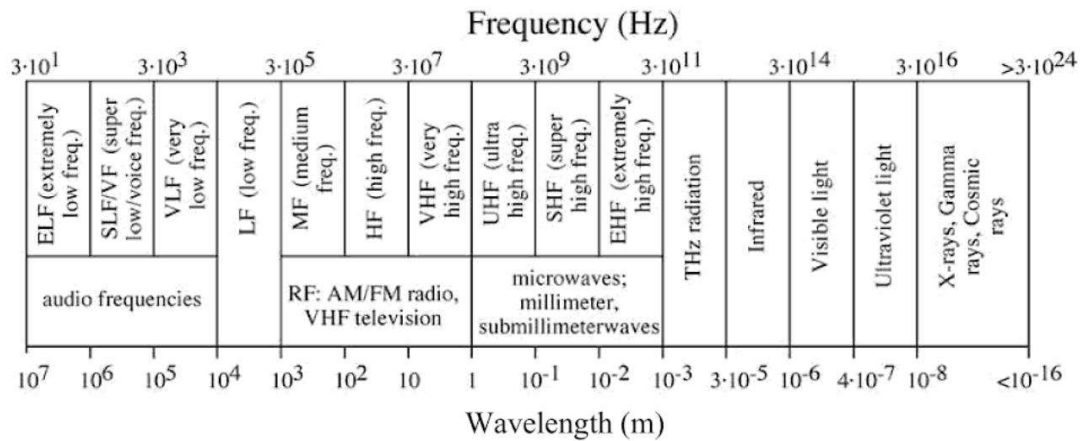
Figure 1.1 Electromagnetic spectrum [Ref. 1]

The major application of microwaves are wireless communication devices. The history of wireless technology tracks back to 1901, which marked the first wireless transmission of signal across the Atlantic Ocean by Guglielmo Marconi [2,3]. The invention of transistors gave impetus to the rapid growth of wireless communication. Wireless communication using radio frequency RF and microwaves were primarily used for military radar systems. The early commercial use of microwaves were long distance terrestrial communications for telephony and satellite transmission of video and voice [4,5]. The earth's atmosphere acts as a transparent window to microwave frequency carriers with limited absorption losses. In addition to this, high frequency microwave signals provide wide absolute bandwidth with narrow fractional bandwidth accommodating many voice and data channels than low frequency carriers [1].

The standard radar frequency letter-band nomenclature according to the IEEE standard 521-2002 last updated in 1984 is given in Table 1.1 [6].

2

Table 1.1 Standard radar frequency letter-band nomenclature
IEEE standard 521-2002 [Ref. 6]

Band Designator	Frequency (GHz)	Wavelength in free space (cm)
HF	0.003 to 0.030	10000 to 1000
VHF	0.030 to 0.300	1000 to 100
UHF	0.300 to 1	100 to 30.0
L band	1 to 2	30.0 to 15.0
S band	2 to 4	15 to 7.5
C band	4 to 8	7.5 to 3.8
X band	8 to 12	3.8 to 2.5
Ku band	12 to 18	2.5 to 1.7
K band	18 to 27	1.7 to 1.1
Ka band	27 to 40	1.1 to 0.75
V band	40 to 75	0.75 to 0.40
W band	75 to 110	0.40 to 0.27
mm	110 to 300	0.27 to 0.10

The L band refers to "long wave", S band refers to "short" wave, C band refers to "compromise" between S and X band, Ku refers to "kurz-under", K refers to German word "kurz" meaning short, referring to short wavelength, Ka refers to "kurz-above", V refers to "very" high frequency band and W follows V in the alphabet [6].

The wireless communication systems using microwaves include terrestrial television, satellite communications and broadcasting, cellular mobile communications, wireless indoor networks, Radio frequency identification (RFID), near-field communications (NFC) and inductively coupled telemetry (ICT), wireless sensor networks, wearables and body area networks and machine-to-machine and

robotic communication. Apart from communication, the non-radiative heating property of microwaves are used for cooking purposes and microwave-induced localised hyperthermia in cancer treatments [5].

The wireless communication devices and technologies have undergone giant strides, encompassing wide spectrum of electromagnetic waves and is fast heading towards utilization of millimetre and terahertz frequencies. The ever increasing connectivity requirements are pushing the limits of usable range of electromagnetic frequencies. Millimetre wave based systems are employed for 5G data transfer rates of 20 Gbps. This high speed wireless communication regime enables interconnected machine level communication, smart homes, driverless cars, artificial intelligence and virtual reality. The boom in the data transfer rates and device to device connectivity is termed as Internet of Things (IoT), which has already made its presence felt in the lives of common man. Terahertz (10^{12} Hz) radiations are non-ionizing radiations with frequencies in the range 0.3–3 THz. These radiations are sensitive to water and hence find immense applications in biomedical THz imaging in addition to THz sensors, screening non-metallic weapons or explosives and THz antennas for communication [7-12]. In the current scenario, microwave technology remains as the key technology for mass production of ever increasing demand for modern gadgets for communication, at the minimum cost and acceptable performance. The large scale production, cost reduction, enhanced data speeds and miniaturization of microwave integrated circuits are attributed to the use of low loss dielectric ceramics, instead of bulky metallic circuit components [1-5].

The microwave materials find applications in the form of dielectric resonators which are cylindrical pucks that show resonance at microwave and millimetre wave frequencies. The dielectric resonators are widely used in the fabrication of filters, dielectric resonator antenna (DRA) and oscillators. The ceramics are filled in suitable polymer matrix to form polymer/ceramic composites with improved dielectric, thermal and mechanical properties for microwave substrate fabrication. Microwave materials are also widely used as tunable dielectrics, dielectric inks and also in electromagnetic shielding. Multilayer circuit fabrication technologies broadly classified into high temperature co-fired ceramics (HTCC), low temperature co-fired ceramics (LTCC) and ultra low temperature co-fired ceramics (ULTCC) utilizing microwave ceramics as the basic building block in microelectronics packaging industry and resulted in large scale

miniaturization of the devices. LTCC materials have low sintering temperature (<960°C) and are compatible with silver electrodes with high electrical conductivity, whereas ULTCC materials with ultra low sintering temperature (<660°C) and compatibility with aluminium electrodes offer an attractive and cost effective technique for integrated packaging [13].

Identification of microwave ceramics with required material properties for the above mentioned functionalities have always been a challenging task for the material scientists. A major share of the reported LTCC and ULTCC ceramics belong to molybdate compositions. Hence the objectives of the present work encompasses a detailed study of LTCC and ULTCC molybdate ceramics, their preparation by solid-state ceramic route, structural and microstructural characterization, detailed investigation on the dielectric properties, correlation of structure with dielectric properties and their co-firability with Ag/Al electrodes. The microwave materials are made into cylindrical dielectric resonators and the dielectric properties in the microwave frequency region are studied in detail. The dielectric and thermal behaviour including the shrinkage behaviour of the ceramics relevant to the ULTCC and LTCC applications are investigated. The suitable ceramic filler is incorporated in the HDPE matrix and the dielectric, thermal and mechanical properties of the polymer/ceramic composites are investigated. The optimum filler loaded composite is used as substrate for microstrip patch antenna fabrication. The dielectric properties of materials and the factors which affect the microwave dielectric properties of LTCC and ULTCC materials are discussed in the following sections.

1.2 Dielectric properties of materials

The dielectric properties of the ceramics namely, dielectric constant ε_r, dielectric loss tan δ, temperature coefficient of resonant frequency τ_f and the factors influencing these properties are detailed below.

1.2.1 Dielectric constant

The atoms in a dielectric medium act as tiny electric dipoles in the presence of external electric field.

The electric dipole moment $\boldsymbol{p} = \alpha\boldsymbol{E}$ (1.1)

with α the atomic polarizability. The polarization $\boldsymbol{P}$ is defined as the dipole moment per unit volume.

For N dipoles per unit volume, $\boldsymbol{P} = N\boldsymbol{p} = N\alpha\boldsymbol{E}$ (1.2)

The polarization $\boldsymbol{P} = \varepsilon_o\chi_e\boldsymbol{E}$ (1.3)

where χ_e is the electric susceptibility. The capacitance of a parallel plate capacitor is given by $C = \frac{\varepsilon_o A}{d}$ (1.4)

where, A the area of the plates and d the distance between them. The insertion of a dielectric medium between the plates increases the capacitance to $C' = \frac{\varepsilon_o \varepsilon_r A}{d}$ (1.5)

The dielectric constant ε_r is given by the ratio of the capacitance of a parallel plate capacitor with dielectric as the medium to the capacitance with air as the medium [14-23].

The electric displacement vector

$D = \varepsilon_o E + P = \varepsilon_o(1 + \chi_e)E = \varepsilon E = \varepsilon_o\varepsilon_r E$, therefore $\varepsilon_r = (1 + \chi_e)$ (1.6)

The frequency dependence of complex dielectric constant is given by the relation

$$\varepsilon^*(\omega) = \varepsilon'(\omega) - i\,\varepsilon''(\omega) = \varepsilon_\infty + \frac{\varepsilon_s - \varepsilon_\infty}{1+(i\omega\tau)^\alpha} \qquad (1.7)$$

where ε_s the static dielectric constant, ε_∞ the dielectric constant in the high frequency limit, τ the most probable relaxation time and α a constant with values between 0 and 1, with $\alpha = 1$ for ideal Debye relaxation.

The real part of the complex dielectric constant is $\varepsilon'(\omega) = \varepsilon_\infty + \frac{\varepsilon_s - \varepsilon_\infty}{1+\omega^2\tau^2}$ (1.8)

and the imaginary part is $\varepsilon''(\omega) = \frac{(\varepsilon_s - \varepsilon_\infty)\omega\tau}{1+\omega^2\tau^2}$ (1.9)

The loss tangent $\tan\delta$ is defined as $\frac{\varepsilon''}{\varepsilon'} = \frac{(\varepsilon_s - \varepsilon_\infty)\omega\tau}{\varepsilon_s + \varepsilon_\infty(\omega^2\tau^2)}$ (1.10)

The dielectric constant for cubic systems can be calculated using Clausius Mossotti equation,

$$\frac{\varepsilon_r - 1}{\varepsilon_r + 1} = \frac{4\pi\alpha_D}{3V_m} \quad \text{and} \quad \varepsilon_r = \frac{3V_m + 8\pi\alpha_D}{3V_m - 4\pi\alpha_D} \qquad (1.11)$$

where, V_m is the molar volume, α_D the sum of dielectric polarizabilities of individual ions [16-34].

In a dielectric medium, the applied electric field causes four types of polarization mechanisms namely electronic, ionic, orientation and space-charge polarizations [18]. A schematic of the polarization mechanisms is shown in Figure 1.2. Total polarizability of the dielectric is given by

$$\alpha = \alpha_e + \alpha_i + \alpha_o + \alpha_s \qquad (1.12)$$

Electronic polarization involves the relative displacement of negative electron cloud and the positive nuclei as a result of the external electric field, thereby establishing an induced dipole moment. Whereas, in ionic polarization positive and negative ions are displaced in relation to one another. Orientation polarization involves the lining up of the permanent electric dipoles in the direction of field. Space charge polarization is attributed to the mobile charges impeded at the interfaces, which is manifested as an increase in capacitance in the exterior circuit [16-18].
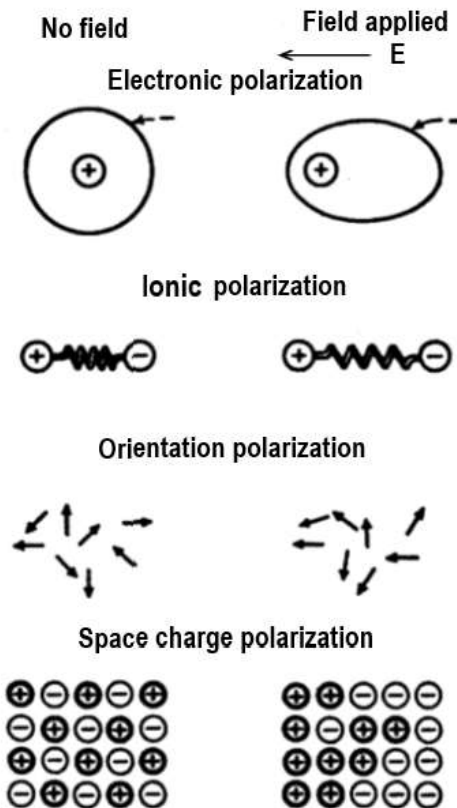
Figure 1.2 Polarization mechanisms in dielectric medium [Ref. 18]

The frequency dependence of dielectric polarizability is shown in Figure 1.3. As elastic strain follows the elastic stress with a lag, the polarization in a dielectric follows the application of electric field after a delay time known as relaxation time τ. The relaxation time for charge transport is a measure of the inertia to charge movement. The

relaxation time is maximum for space charge polarization, lesser for orientation polarization, followed by ionic polarization and the least for electronic polarization. Ionic polarization gives significant contribution to dielectric constant upto infrared region of frequency. Among microwave ceramics, the prominent contribution to dielectric polarizability is attributed by ionic and electronic polarizations.

Dielectric constant ε_r plays a decisive role in determining the physical dimension of devices as well as the propagation delay time t_d in circuits. The wavelength in the dielectric medium λ_d is reduced by a factor of $\sqrt{\varepsilon_r}$ compared to that of free space wavelength λ_o. The dimension of the dielectric resonator must be an integral multiple of half wavelength in the dielectric for resonance in the simplest fundamental mode and hence high ε_r materials, lower the physical dimensions of the circuits. However the propagation delay time is directly proportional to $\sqrt{\varepsilon_r}$ and low dielectric constant materials offer faster signal propagation in microwave medium [13].
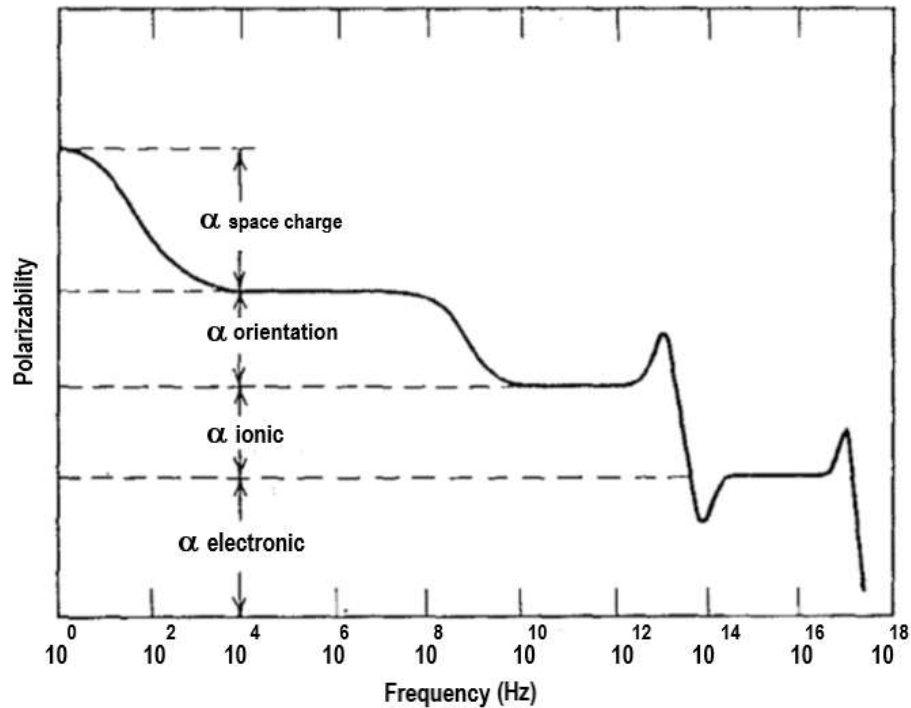
Figure 1.3 Frequency dependence of dielectric polarizability [Ref. 17]

1.2.2 Quality factor

The quality factor Q determines the frequency selectivity of the resonator and is a measure of power loss of a microwave system.

$$Q = 2\pi \frac{\text{maximum energy stored per cycle}}{\text{average energy dissipated per cycle}} \qquad (1.13)$$

8

Q is the inverse of loss tangent tan δ [16]. The actual physical mechanism causing dielectric loss is attributed to the delay between change in applied electric field direction and the associated flipping of electric dipoles in the dielectric. The dielectric loss of the materials is the sum of extrinsic and intrinsic losses. The dielectric loss of single crystals show dependence on the associated crystal symmetry and the interaction of phonon system with the AC electric field. The major extrinsic factors like impurities, microstructural defects, grain boundaries, porosity, vacancies etc. also contribute to the dielectric loss of the materials [13].

The frequency response of a microwave resonator is as shown in Figure 1.4. Q_L is the loaded quality factor measured at resonant frequency f and half power (-3 dB) bandwidth Δf of TE$_{01\delta}$ mode resonance of a cylindrical dielectric resonator made out of microwave ceramic material.

$$Q_L = \frac{f}{\Delta f} \tag{1.14}$$

The resonator bandwidth is inversely proportional to the quality factor. Quality factor is a measure of the power loss of a microwave system through dielectric loss $\frac{1}{Q_d}$, loss due to conductivity of metallic plates $\frac{1}{Q_c}$, loss due to radiation $\frac{1}{Q_r}$ and external losses $\frac{1}{Q_{ext}}$ due to coupling between the resonator and the microwave conducting probe.
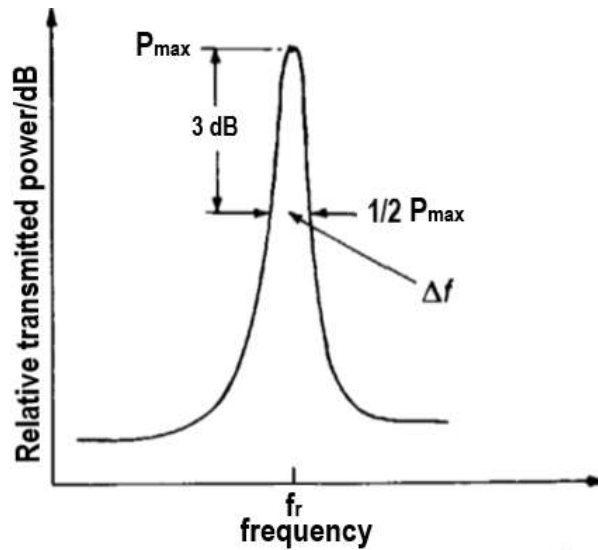
Figure 1.4 Frequency response of a microwave resonator [Ref. 23]

$$\frac{1}{Q_L} = \frac{1}{Q_d} + \frac{1}{Q_c} + \frac{1}{Q_r} + \frac{1}{Q_{ext}} \tag{1.15}$$

9

$$\frac{1}{Q_u} = \frac{1}{Q_d} + \frac{1}{Q_c} + \frac{1}{Q_r} = \frac{1/Q_L}{1+\beta c_1 + \beta c_2} \qquad (1.16)$$

where, βc_1 and βc_2 are the coupling coefficients for a resonator with two coupling ports [13,16]. The Q_u varies with the frequency of measurement and hence the product of quality factor and frequency Q_u x f in GHz is taken.

1.2.3 Temperature coefficient of resonant frequency

The temperature coefficient of resonant frequency is an important parameter which shows the variation of resonant frequency with temperature and is given by the equation

$$\tau_f = \frac{(f_{final} - f_{initial})}{f_{initial} \times (T_{final} - T_{initial})} \qquad (1.17)$$

The τ_f is related to temperature coefficient of dielectric constant τ_{ε_r} and coefficient of linear thermal expansion α_L of the dielectrics as

$$\tau_f = -\alpha_L - \frac{\tau_{\varepsilon_r}}{2} \qquad (1.18)$$

For electronic ceramics α_L is around +10 ppm/°C and τ_f is largely influenced by τ_{ε_r}. The influence of temperature on the dielectric constant is determined by three factors given in equation 1.19.

$$\frac{1}{(\varepsilon_r - 1)(\varepsilon_r + 2)} \left(\frac{\delta\varepsilon}{\delta T} \right)_p$$

$$= -\frac{1}{3V_m} \left(\frac{\delta V_m}{\delta T} \right)_p + \frac{V_m}{\alpha_D} \left(\frac{\delta\alpha_D}{\delta V_m} \right)_T \frac{1}{3V_m} \left(\frac{\delta V_m}{\delta T} \right)_p + \frac{1}{3\alpha_D} \left(\frac{\delta\alpha_D}{\delta T} \right)_{V_m}$$

$$= A + B + C \qquad (1.19)$$

The term A represents the decrease in the number of polarizable ions per unit volume as a result of thermal expansion. The volume increases with temperature in most cases and hence the term B shows the increase in polarization with increase in the volume in which ions are able to move as temperature increases. The term C represents the direct dependence of polarizability on temperature with volume remaining constant. The low ε_r materials are reported to show an increase in dielectric constant and high ε_r materials show a decrease of dielectric constant with increase of temperature [16, 25,26,28,35-38].

1.3 Dielectric resonators

The resonators and filters suitable for different frequencies in the RF and microwave frequency range are shown in Figure 1.5 [2]. Bulk-wave, helical and SAW resonators are used for frequencies below 1 GHz, whereas coaxial, dielectric, waveguide, and stripline resonators are used for high frequency range. Coaxial resonators are operated up to 10 GHz and bulky waveguide resonators are used up to 100 GHz.

Dielectric resonators are ceramic compacts which can confine electromagnetic energy through total internal reflection by virtue of their high dielectric constant. These resonators operate below 50 GHz and exhibit low-loss characteristics, small size and acceptable temperature stability. Stripline resonators can be easily fabricated by photolithography technique and can integrate with active circuit elements operating in RF and microwave circuits. They offer wide range of operating frequency by using different substrate materials, however high insertion loss is a major drawback [2].

In this section, we discuss the dielectric resonators and the dielectric characterization of these materials in the microwave frequency range. Dielectric resonator is a cylindrical puck of low-loss ceramic material which functions as a resonator in microwave and millimetre wave frequencies. Dielectric resonators are commonly used in solid cylinder geometry, but tubular, spherical and parallelepiped shapes are also used. Standing electromagnetic waves corresponding to the resonant frequency can be sustained within its volume, by total internal reflection at the dielectric-air interface. The resonant frequency is determined by the dimension, dielectric constant and the surrounding medium of the resonator.
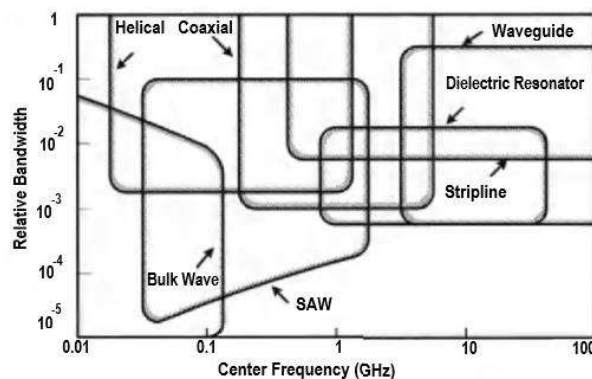
Figure 1.5 Frequency range of typical resonators and filters [Ref. 2]

In 1897, Lord Rayleigh has reported the interaction of electric waves through dielectric cylinders [39,40]. In 1939, Richtmyer coined the word 'dielectric resonator' to denote non-metallic dielectric materials that can act as microwave resonators [41]. The first dielectric resonator reported was high dielectric material-single crystal TiO_2 (rutile) by Okaya and Barash in 1960 [42]. However, the temperature stability of rutile dielectric resonator was poor. $(Zr\text{-}Sn)TiO_4$, $Ba_2Ti_9O_{20}$, $Ba(Sn,Mg,Ta)O_3$, $(Ba,Sr,Ca)(Zr,Ti)O_3$, $MgTiO_3\text{-}CaTiO_3$, $Ba(Zr,Zn,Ta)O_3$ are some of the initially reported temperature stable and low loss dielectric resonators from Murata Manufacturing Company, Japan in 1970's [43-46].

Low loss temperature stable dielectric resonators offer a low cost substitute for conventional metallic microwave resonant cavities with miniaturized size. In the present study, the dielectric constant of ceramic resonators is measured in microwave frequency using Hakki and Colemann (Courtney) method and resonant cavity method (Krupka cavity) [19, 47-49]. Among the Transverse electric TE, Transverse magnetic TM and Hybrid electromagnetic HEM resonant modes excited in a dielectric resonator, the lowest order circular symmetric mode, $TE_{01\delta}$ resonant mode, is traditionally used for accurate microwave measurements. The TE and TM modes do not contain electric and magnetic fields in the axial (z) direction. The $TE_{01\delta}$ mode propagates inside the sample and is evanescent outside the dielectric resonator sample. The $TE_{01\delta}$ resonant mode of a cylindrical dielectric resonator also called magnetic dipole mode constitute magnetic field lines as shown in Figure 1.6.
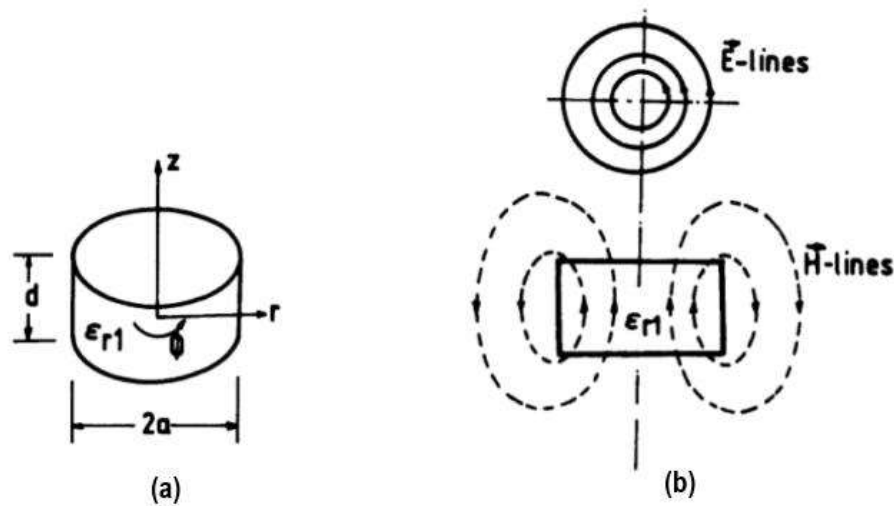
Figure 1.6 Isolated disc dielectric resonator and field lines for the dominant $TE_{01\delta}$ mode [Ref. 19]

The electric field lines form concentric circles around z axis and the magnetic field lines lie in the meridian plane. For a dielectric resonator of ε_r around 40, more than 95% of the stored electric energy of $TE_{01\delta}$ mode and a major part of the stored magnetic energy are confined within the cylinder and the remaining energy is distributed in the air around the resonator, decaying rapidly with distance away from the resonator surface.

The microwaves entering in a dielectric medium is slowed down by a factor $\sqrt{\varepsilon_r}$. The wavelength of microwaves inside the dielectric λ_d is $\lambda_0/\sqrt{\varepsilon_r}$, λ_0 being the free space wavelength. At resonant frequency f_o, λ_d is approximately equal to the diameter of the resonator, with

$$f_o = \frac{c}{D\sqrt{\varepsilon_r}} \tag{1.20}$$

The exact resonant frequency of $TE_{01\delta}$ resonant mode computed by numerical procedures, for an isolated dielectric resonator is

$$f_{GHz} = \frac{34}{\sqrt{\varepsilon_r}\, a} \left(\frac{a}{L} + 3.45\right) \tag{1.21}$$

'a' the radius and 'L' the length of the resonator in mm, ε_r the dielectric constant, which is correct within the range $0.5 < \frac{a}{L} < 2$ and $30 < \varepsilon_r < 50$ for proper mode separation and accuracy of measurement [40, 50-55].

The dielectric constant ε_r calculated from the resonant frequency (f) of the $TE_{01\delta}$ measured using Hakki and Colemann (Courtney) method is given by

$$\varepsilon_r = 1 + \left[\frac{c}{\pi D f}\right]^2 (\alpha_1^2 + \beta_1^2) \tag{1.22}$$

Where D is the diameter of the dielectric resonator and (α_1, β_1) are the mode chart parameters.

The resonant frequency corresponding to the $TE_{01\delta}$ mode of the resonator is measured as a function of temperature and the temperature coefficient of resonant frequency τ_f is calculated using the formula $\tau_f = \frac{f_{100} - f_{30}}{f_{30}\,(100-30)}$, where f_{30} and f_{100} are respectively the resonant frequencies at 30°C and 100°C.

The quality factor measurement is not done using Hakki and Coleman (Courtney) method as conductor and radiation losses affect the measurement. The quality factor is measured using resonant cavity method using Krupka cavity, which

again employs $TE_{01\delta}$ mode and the unloaded quality factor $Q_u = \dfrac{Q}{1-10^{-\frac{IL}{20}}}$, where Q is

the quality factor obtained form the measurement and I_L is the insertion loss in dB. Usually the product of unloaded quality factor with the corresponding resonant frequency is reported as $Q_u \times f$ in GHz [40,50-55]. The other experimental details of the measurements are discussed in detail in chapter 2.

1.4 Multilayer co-firing technology

Multilayer co-firing technology is a cost effective and competitive technology for electronic packaging enabling large scale vertical integration of circuit components into a single monolithic module. Multilayer co-firing technology is broadly classified into HTCC, LTCC and ULTCC depending on the processing temperature. HTCC refers to high temperature co-fired ceramics, LTCC low temperature co-fired ceramics and ULTCC ultra low temperature co-fired ceramics. The ceramics are fired along with the internal conductors at sintering temperatures below the melting point of the conductor. Alumina ceramics are the commonly used HTCC material with high firing temperature of 1600-1800°C. Conductors with high meting point, Molybdenum Mo (electrical resistance 5.8 μΩcm, melting point 2610°C), W (5.5 μΩcm, 3410°C) and Mo-Mn (1246- 1500°C) are commonly used for HTCC, however these conductors are having lower conductivity and higher loss compared to Ag and Au electrodes [56-58]. The high temperature of processing and high cost of fabrication involved in HTCC technology can be overcomed by LTCC technology, which utilizes ceramic materials that sinter at relatively low temperatures (<960°C), the melting point of Ag and further improved by ULTCC technology utilizing ceramics that get sintered at ultra low sintering temperatures below 660°C, which is the melting point of Al [56-58]. In addition to low sintering temperatures, the co-firability of these ceramics with the respective metal electrodes at the appropriate sintering temperatures is also essential. Low processing energy and use of cheaper electrodes make the LTCC and ULTCC technologies cost effective compared to HTCC.

1.4.1 LTCC multilayer substrate fabrication

LTCC multilayer stacks are generally prepared using tape casting technique. A schematic of the LTCC process is shown in Figure 1.7.
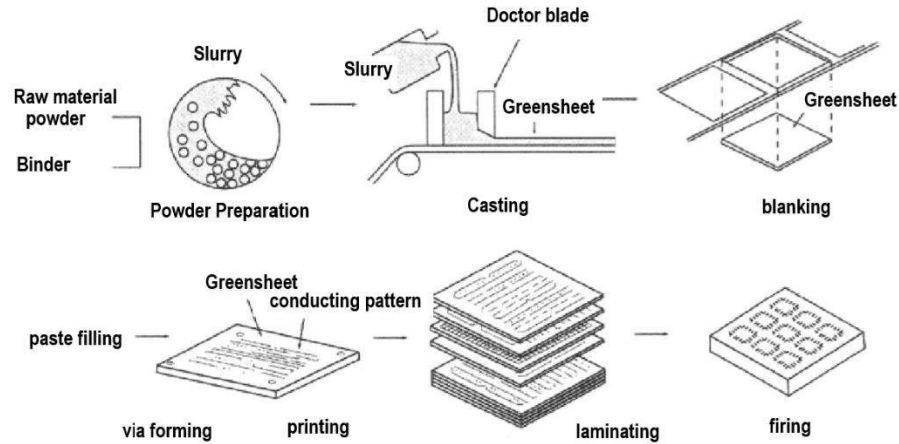
Figure 1.7 Typical multilayer ceramic substrate manufacturing process [Ref. 58]

A slurry of the ceramic powder along with glass frits, binder, plasticizer, solvent and dispersant is prepared and tape casted onto a carrier film. The organics are removed from the tape before densification of inorganic components. The properties of ceramic particles are crucial in determining the properties of the final sintered product [59].

The LTCC process includes preparation of green tapes by tape casting, followed by blanking of the tapes, punching, via filling, conductor printing, inspection, lamination under temperature and pressure, burn out, firing and dicing [60 - 64].

1.4.2 Design of LTCC modules

A cross section of a typical LTCC module is shown in Figure 1.8. The required circuit patterns are screen printed on green ceramic tapes using suitable conductive pastes. These layers are stacked together, laminated under pressure and co-fired. The substrate has embedded passive components including buried resistors made of resistive pastes. The electrical contact between circuits placed on different LTCC layers are achieved by vias [61]. Ground meshes or ground planes, inner microstrip lines, coplanar waveguides and passive lumped components like inductors and capacitors are fabricated within the LTCC layers using Ag/Au/Cu conductors. Cavities and windows allow to construct openings inside the circuit to realize resonators [64]. The IC and other components are mounted on the surface of the substrates by wire bonding or die bonding [60-63]. The thermal management of LTCC package is improved by thermal vias through LTCC substrates [65].
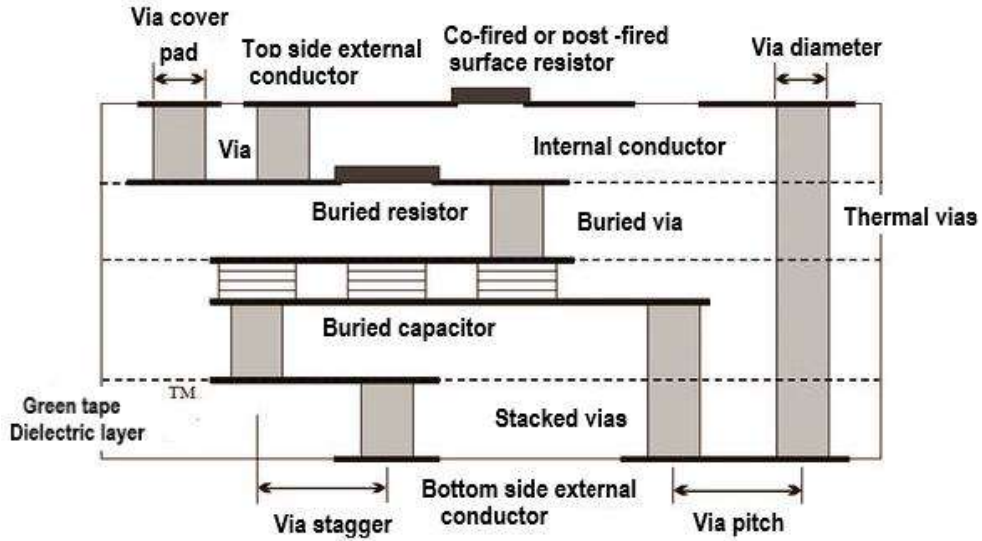
Figure 1. 8 Cross-section of a typical LTCC module [Ref. 66]

The substrate characteristics like surface energy, porosity, roughness and compatibility with ink are some of the key parameters to be considered. LTCC commercial tapes DP951 DuPont USA has a typical surface energy 30 mJ/m^2, roughness 235 nm and surface pore size 0.5 to 1 μm for green tapes. LTCC conductors must have good shrinkage and thermal expansion matching with the dielectric tape as well as excellent chemical compatibility with co-fired ceramic. The conductive lines in the co-fired LTCC substrates can be examined by energy dispersive X-ray spectroscopy and optical microscopy. Backscattered SEM image of Al co-fired $BaTe_4O_9$ is shown in Figure 1.9. Conductive pastes based on Ag, Au or their alloys with Pt, Pd with good printability are used in multilayer LTCC systems [60, 67]. The properties of particle wetting, film formation and adhesion to substrate are also significant. Noble metals with high conductivity and chemical inertness dispersed as micro and nano particles in suitable solvents are used as inks for circuit printing. Au has an electrical resistivity of 2.3 μΩcm and melting point of 1063°C, whereas Ag has a lower resistivity of 1.6 μΩcm and lower melting point of 960°C. The electrical resistivity and the melting point of Pd and Pt are 10.3 μΩcm, 1552°C and 10.6 μΩcm, 1769°C respectively. Ag-Pd and Ag-Pt conductors have melting points of 960 °C to 1555°C and 960°C to 1186°C respectively. Non noble metals like Cu (electrical resistance 1.7 μΩcm, melting point 1083°C), Ni (6.9 μΩcm, 1455°C) and non metallic conductive particles such as carbon black, carbon nanotubes, graphite also used as conductive materials. The oxidation of metals can be avoided by sintering in N_2, H_2 or forming gas atmosphere [60, 67]. Al is used as the

electrode material with an electrical resistivity of 2.7 µΩcm and melting point of 660°C for ULTCC applications.
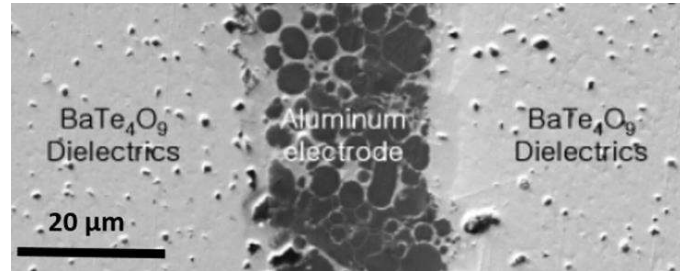
Figure 1.9 Backscattered SEM image of Al co-fired $BaTe_4O_9$ [Ref. 68]

Environment friendly water based silver ink formulations have been reported. Compared to lithography and direct laser write techniques, screen printing offers a fast, reliable and cost effective method, with a line width of 0.8 to 20 µm for the conductor lines [67]. The ink formulations consist of the conductive material, inorganic binder and vehicle consisting of organic solvent, binders and additives. The solvent evaporates and the binder phase keeps the particles together. As silver content increases the viscosity of ink increases and hinders the spreading of ink which decreases the line width of the conducting lines. Silver migration is attributed as one of the reasons for short circuit [60, 67]. The rheology, colloidal properties, particle size distribution and surface tension of ink as well as the printing parameters like speed, force applied to squeegee, off-contact distance etc. determines the line width of conducting lines. As the line width of the conducting lines decreases the density of components integrated in the substrate increases.

1.4.3 Advantages of LTCC over conventional PCBs

LTCC technology enables large scale vertical integration of passive components into an arbitrary number of dielectric layers which minimizes the module size. LTCC materials have low dielectric loss, low dielectric constant and enable faster propagation of high frequency signals. [69,70]. LTCC substrates offer better thermal management capability due to good thermal conductivity and mechanical properties compared to conventional PCBs. Heat dissipation is achieved by thermal vias and enables the integration of high power devices [63]. CTE mismatch of the different components in a LTCC package can cause strain due to firing shrinkage mismatch [65]. Ferro A6-M, DuPont 943-A5 are some of the commercially available LTCC substrates. FR-4 is an example of widely used conventional PCB made out of glass-reinforced epoxy laminate

material [65]. The use of FR-4 is limited to few GHz of lower ISM band frequencies due to relatively high loss tangent and are not suitable for high frequencies. FR-4 exhibits a dielectric constant of 4.4 and loss tangent of 0.02 at 1 MHz together with a CTE of 18 ppm/K and thermal conductivity 0.2 W/mK [65]. Compared to FR-4, commercial LTCC tapes offer a wide range of small dielectric constant with significantly low loss tangent at 1 MHz and very high thermal conductivity of 2-3 W/mK which is 10 times of PCBs 0.2 W/mK. LTCC substrates have better dielectric and thermal properties than most of the other packaging materials based on polymer compsite substrates [71]. LTCC substrates show better chemical and humidity resistance in comparison to PCBs [61,62]. LTCC tapes are soft, flexible, can be easily handled and mechanically shaped. The component size and weight can be reduced with better reliability and integration. LTCC substrates offer high speed signal transmission at high frequencies. LTCC substrates have thinner line width and spacing and hence the integration achieved is higher than PCBs [63]. The CTE of LTCC substrates must match with the CTE values of Si or GaAs wafers onto which the substrates are bonded. The components should be chemically inert on co-firing and stresses can cause warping or crack on LTCC tapes [61].

1.4.4 Applications of LTCC technology

LTCC substrates are widely used for multilayer SiP System in Package applications [69] and a host of microwave and millimetre wave applications [60]. 3D Multichip modules can be fabricated making use of the large scale vertical integration of LTCC substrates [60]. LTCC products can be broadly classified into modules, packages or substrates and surface mount devices (SMD). LTCC technique finds application in the fabrication of substrate integrated waveguides (SIW) [71,72], THz filters [71], monolithic SiP front end modules, radar modules with integrated stacked patch antenna [69], antenna arrays for space applications [64], filters, balun, couplers and duplexers. LTCC packaging offers hermetic and clean sealing of the sensitive RF MEMS Micro-Electro-Mechanical Systems devices [65]. Mechanical structures like cantilevers, bridges, springs, beams and membranes can be integrated into LTCC substrates. Microvaristors, microresistors and filters can be embedded in the LTCC module [73-75]. LTCC based low cost sensors, actuators and microsystems can be fabricated with better reliability. LTCC based sensors can work in harsh environment, high temperature and humidity. LTCC based strain gauge, pressure sensor,

piezoresistive force sensor, fluid flow sensors, moisture sensor, temperature sensor, gas sensor, microvalve, micropump, thermistors and thermocouples are also reported [75-77].

1.4.5 LTCC and ULTCC material systems

LTCC materials can be classified as glass/ceramic composites, crystallized glass, crystallized glass/ceramic composite and liquid phase sintered ceramics [58]. Silicates and aluminates are the extensively used ceramics in the electronic device fabrication, but the high processing temperature limits their application as phase pure LTCC and ULTCC materials. Various attempts are being made to lower the sintering temperature of the ceramics by addition of low temperature softening glass phases. CaO-B_2O_3-SiO_2, La-B-Ti-O glass, B-Bi-Zn-O BBSZ systems are some of the glass based systems reported for LTCC applications [78-79]. The glass frits melt at lower temperature and exhibit wetting behaviour. During liquid phase sintering the liquid phase present helps in rearranging the ceramic particles due to capillary pressure and leads to maximum packaging at lower sintering temperatures compared to solid-state sintering. The glass addition to lower sintering temperature can deteriorate the dielectric properties of LTCC tapes, and hence glass free phase pure LTCC materials are of much significance. Glass ceramic composites are prone to secondary phase formation, defects, grain boundaries, porosity etc. which enhance extrinsic losses and thereby decreases the quality factor.

The glass networks also absorb higher microwave power and increases the dielectric loss. Apart from glass addition, low melting point phases like Ag_2O, CuO, B_2O_3 and LiF addition have been reported for lowering the sintering temperatures. Glass free materials with inherent low sintering temperatures are of much demand and most of the reported phase pure LTCC and ULTCC materials comprise of low melting point oxides TeO_2 (m.p. 732°C), V_2O_5 (m.p. 690°C) and MoO_3 (m.p. 795°C). The ionic polarizability of Te, V and Mo are 5.23 $Å^3$, 2.92 $Å^3$ and 3.28 $Å^3$ respectively [56-58,80]. Some of the tellurates based LTCC and ULTCC compositions reported are $BaTe_4O_9$, $SnTe_3O_8$, $ZrTe_3O_8$, $Zn_2Te_3O_8$, $BaTiTe_3O_9$ and $TiTe_3O_8$ [68, 81-84]. Toxic nature, high cost and reactivity with Ag electrodes limit their wider applications. Some of the vanadium based LTCC and ULTCC compositions reported are $A_{16}V_{18}O_{61}$ (A = Ba, Sr, Ca), $Ba_3V_4O_{13}$, BaV_2O_6, $Mg_4V_2O_9$, $BaMV_2O_7$ (M=Mg, Zn), $NaMg_4V_3O_{12}$, $Ba_3MV_4O_{15}$ (M = Ti, Zr) [85-91]. Vanadium and molybdenum based systems are reported to show

good compatibility with Ag and Al. The volatility of molybdenum based systems at high temperature and the reactivity with Ag are also reported, however a major share of the reported ULTCC systems comprise of molybdate based systems and they offer better machinability than vanadates. In the present study, we focus on the development and structure-property characterization of phase pure molybdate ceramics for LTCC and ULTCC applications. A comprehensive review of molybdate based ULTCC and LTCC phase pure ceramics is given in the following section.

1.5 Review of literature - LTCC and ULTCC molybdate ceramics

Phase pure glass free molybdate based ceramics reported as ultra low temperature and low temperature firing materials, along with their sintering temperature, microwave dielectric properties, crystal structure and co-firability with metal electrodes Ag/Al are mentioned below.

Zhou et al. has reported the microwave dielectric properties of ultra low temperature firing NaAgMoO$_4$ ceramic with spinel like cubic crystal structure, Fd-3m space group which exhibits ε_r = 7.9, $Q_u \times f$ = 33,000 GHz, τ_f = -120 ppm/^{o}C at 400°C and compatible with both Ag and Al [92]. Zhang et al. has reported the microwave dielectric properties of phase pure compositions in the Na$_2$O-MoO$_3$ and Ag$_2$O–MoO$_3$ binary systems. Na$_2$MoO$_4$ ceramic with spinel like cubic structure is reported to have ε_r = 4.1, $Q_u \times f$ = 35,000 GHz and τ_f = -76 ppm/^{o}C at optimum sintering temperature of 660°C and is compatible with both Ag and Al [93]. Na$_2$Mo$_2$O$_7$ ceramic with orthorhombic structure is reported to have ε_r = 12.9, $Q_u \times f$ = 62,400 GHz and τ_f = -72 ppm/^{o}C at optimum sintering temperature of 575°C and is compatible with Al [93], whereas Na$_6$Mo$_{11}$O$_{36}$ ceramic with Anorthic P$\bar{1}$ structure with ε_r = 9.9, $Q_u \times f$ = 57,000 GHz and τ_f = -61ppm/^{o}C at optimum sintering temperature of 510°C is not compatible with Al [93]. Among the phases in Ag$_2$O–MoO$_3$ binary systems, Ag$_2$MoO$_4$ ceramic is reported to have ε_r = 8.1, $Q_u \times f$ = 17,000 GHz, τ_f = -133 ppm/^{o}C at optimum sintering temperature of 450°C [94]. Ag$_2$Mo$_2$O$_7$ ceramic with triclinic crystal structure, space group P$\bar{1}$ is reported to have ε_r of 13.3, $Q_u \times f$ of 25,300 GHz and τ_f of -142 ppm/^{o}C at optimum sintering temperature of 460°C and is compatible with both Ag and Al [94]. Ag$_6$Mo$_{10}$O$_{33}$ is reported to have ε_r of 14, $Q_u \times f$ of 8500 GHz and τ_f of -50 ppm/^{o}C at optimum sintering temperature of 500°C [94].

Xi et al. has reported the microwave dielectric properties of ultra low temperature firing $PbMoO_4$ ceramic with pure scheelite tetragonal crystal structure with space group $I4_1/a$ and $\varepsilon_r = 26.7$, $Q_u \times f = 42,800$ GHz, $\tau_f = +6.2$ ppm/^{o}C at 650°C showing compatibility with both Ag and Al [95]. Zhou et al. has reported the microwave dielectric properties of $(ABi)_{1/2}MoO_4$ (A= Li, Na, K, Rb, Ag) compositions among which ULTCC compositions $Na_{0.5}Bi_{0.5}MoO_4$, $Ag_{0.5}Bi_{0.5}MoO_4$ and $Li_{0.5}Bi_{0.5}MoO_4$ have pure scheelite tetragonal $I4_1/a$ structure and $K_{0.5}Bi_{0.5}MoO_4$ and $Rb_{0.5}Bi_{0.5}MoO_4$ compositions have monoclinic scheelite related structure [96]. $Ag_{0.5}Bi_{0.5}MoO_4$ ceramic is reported to have ε_r of 30.4, $Q_u \times f$ of 12,600 GHz and τ_f of +57 ppm/^{o}C at optimum sintering temperature of 690°C, but is reported to react with Ag [96]. $Li_{0.5}Bi_{0.5}MoO_4$ ceramic is reported to have ε_r of 41.7, $Q_u \times f$ of 3200 GHz and τ_f of +240 ppm/^{o}C at optimum sintering temperature of 560°C and weakly reacts with Al [96]. $Na_{0.5}Bi_{0.5}MoO_4$ ceramic is reported to have ε_r of 34.4, $Q_u \times f$ of 12,300 GHz and τ_f of +43 ppm/^{o}C at optimum sintering temperature of 590°C and reacts with Ag [96]. $K_{0.5}Bi_{0.5}MoO_4$ ceramic is reported to have ε_r of 37, $Q_u \times f$ of 4000 GHz and τ_f of +117 ppm/^{o}C at optimum sintering temperature of 630°C and is compatible with Al, but reacts with Ag [96]. $Rb_{0.5}Bi_{0.5}MoO_4$ ceramic is reported to have ε_r of 21.4, $Q_u \times f$ of 6200 GHz and τ_f of -30 ppm/^{o}C at optimum sintering temperature of 550°C and reacts with Al and Ag [96].

Zhou et al. have reported the microwave dielectric properties of phases in Li_2O–Bi_2O_3–MoO_3 system, among which Li_2MoO_4 ceramic has $\varepsilon_r = 5.5$, $Q_u \times f = 46,000$ GHz and $\tau_f = -160$ ppm/^{o}C at optimum sintering temperature of 540°C and is compatible with both Al and Ag [97]. Pang et al. have reported the microwave dielectric properties of $(Li_{0.5}Ln_{0.5})MoO_4$ (Ln= Nd, Er, Gd, Y, Yb, Sm, and Ce) ceramics [98], among which $Li_{0.5}Sm_{0.5}MoO_4$ is reported to have $\varepsilon_r = 20.5$, $Q_u \times f = 4570$ GHz and $\tau_f = +231$ ppm/^{o}C at optimum sintering temperature of 640°C and is compatible with Al [98], $Li_{0.5}Nd_{0.5}MoO_4$ is reported to have $\varepsilon_r = 23.7$, $Q_u \times f = 3000$ GHz and $\tau_f = +235$ ppm/^{o}C at optimum sintering temperature of 660°C and is compatible with Al [98], $Li_{0.5}Ce_{0.5}MoO_4$ is reported to have $\varepsilon_r = 21.5$, $Q_u \times f = 1990$ GHz and $\tau_f = +228$ ppm/^{o}C at optimum sintering temperature of 580°C and is compatible with Al [98]. Jobin et al. have reported the microwave dielectric properties of α-MoO_3 with orthorhombic crystal structure, $\varepsilon_r = 6.6$, $Q_u \times f = 41,000$ GHz and $\tau_f = -25$ ppm/^{o}C at optimum sintering temperature of 650°C [99].

Zhou et al. have reported the microwave dielectric properties of $Li_2Zn_2Mo_3O_{12}$, $Li_3AlMo_3O_{12}$ and $Li_3InMo_3O_{12}$ ceramics with orthorhombic crystal structure compatible with both Ag and Al [100]. Wen et al. have reported the microwave dielectric properties of orthorhombic $Cu_3Mo_2O_9$ ceramics with $\varepsilon_r = 7.2$, $Q_u \times f = 19,300$ GHz, $\tau_f = -7.8$ ppm/°C at optimum sintering temperature of 660°C and compatible with Al [101]. Zhai et al. have reported the microwave dielectric properties of $LiKSm_2(MoO_4)_4$ ceramics with scheelite related monoclinic structure with $\varepsilon_r = 11.5$, $Q_u \times f = 39,000$ GHz, $\tau_f = -15.9$ ppm/°C at optimum sintering temperature of 620°C and compatible with Al [102].

Zhou et al. have reported the microwave dielectric properties of the bismuth molybdate compositions $Bi_2Mo_3O_{12}$ [103], $Bi_2Mo_2O_9$ [104] and Bi_2MoO_6 [104] with monoclinic crystal structure. $Bi_2Mo_3O_{12}$ is reported to have $\varepsilon_r = 19$, $Q_u \times f = 21,800$ GHz and $\tau_f = -215$ ppm/°C at optimum sintering temperature of 610°C and is compatible with Al, but reacts with Ag [103]. $Bi_2Mo_2O_9$ is reported to have $\varepsilon_r = 38$, $Q_u \times f = 12,500$ GHz and $\tau_f = +31$ ppm/°C at optimum sintering temperature of 620°C and is compatible with Al [104]. Bi_2MoO_6 is reported to have $\varepsilon_r = 31$, $Q_u \times f = 16,700$ GHz and $\tau_f = -114$ ppm/°C at optimum sintering temperature of 750°C [104].

Zhang et al. have reported the microwave dielectric properties and compatibility of phases in K_2O-MoO_3 binary system [105]. $K_2Mo_3O_{10}$ is reported to have $\varepsilon_r = 5.6$, $Q_u \times f = 35,830$ GHz and $\tau_f = -92$ ppm/°C at optimum sintering temperature of 520°C and is compatible with Ag [105]. $K_2Mo_4O_{13}$ is reported to have $\varepsilon_r = 6.8$, $Q_u \times f = 39,290$ GHz and $\tau_f = -67$ ppm/°C at optimum sintering temperature of 540°C and is compatible with Al [105]. $K_2Mo_2O_7$ is reported to have $\varepsilon_r = 7.5$, $Q_u \times f = 22,000$ GHz and $\tau_f = -63$ ppm/°C at optimum sintering temperature of 460°C and is compatible with Ag and Al [105]. Xie et al. have reported the microwave dielectric properties of Pb_2MoO_5 as $\varepsilon_r = 19.1$, $Q_u \times f = 21,800$ GHz and $\tau_f = -60$ ppm/°C at optimum sintering temperature of 610°C [106]. Wang et al. have reported the microwave dielectric properties of Te_2MoO_7 as $\varepsilon_r = 13.6$, $Q_u \times f = 46,900$ GHz and $\tau_f = -36$ ppm/°C at optimum sintering temperature of 520°C [107]. Joseph et al. have reported the microwave dielectric properties of $CuMoO_4$ with $\varepsilon_r = 7.9$, $Q_u \times f = 53,000$ GHz and $\tau_f = -36$ ppm/°C at optimum sintering temperature of 650°C and is compatible with Al [108].

Choi et al. have reported the microwave dielectric properties of scheelite (A= Ca, Sr, Ba) and wolframite (A= Mg, Zn, Mn) $AMoO_4$ compositions [109]. $BaMoO_4$

ceramic with scheelite crystal structure is reported to have ε_r = 9.3, $Q_u \times f$ = 37,200 GHz and τ_f = -79 ppm/°C at optimum sintering temperature of 900°C [109]. MgMoO$_4$ ceramic with monoclinic wolframite crystal structure is reported to have ε_r = 7.07, $Q_u \times f$ = 79,100 GHz and τ_f = -46 ppm/°C at optimum sintering temperature of 900°C [109]. MnMoO$_4$ ceramic with monoclinic wolframite crystal structure is reported to have ε_r = 8.55, $Q_u \times f$ = 54,100 GHz and τ_f = -73 ppm/°C at optimum sintering temperature of 900°C [109]. ZnMoO$_4$ ceramic has triclinic crystal structure with ε_r = 8.67, $Q_u \times f$ = 49,900 GHz and τ_f = -87 ppm/°C at optimum sintering temperature of 800°C [109].

Surjith et al. have reported the microwave dielectric properties of monoclinic BaCe$_2$(MoO$_4$)$_4$ with ε_r = 12.3, $Q_u \times f$ = 24,732 GHz and τ_f = -37 ppm/°C at optimum sintering temperature of 835°C [110], whereas tetragonal SrCe$_2$(MoO$_4$)$_4$ and CaCe$_2$(MoO$_4$)$_4$ ceramics are also reported to have excellent microwave dielectric properties [110]. Xi et al. have investigated the microwave dielectric properties of (Na$_{0.5}$Ln$_{0.5}$)MoO$_4$ (Ln= La, Nd and Ce) ceramics with pure scheelite crystal structure [111,112]. (Na$_{0.5}$La$_{0.5}$)MoO$_4$ ceramic is reported to have ε_r = 11, $Q_u \times f$ = 25,050 GHz and τ_f = -59 ppm/°C at optimum sintering temperature of 740°C and compatible with Ag [111]. (Na$_{0.5}$Nd$_{0.5}$)MoO$_4$ ceramic is reported to have ε_r = 10.5, $Q_u \times f$ = 19,605 GHz and τ_f = -49 ppm/°C at optimum sintering temperature of 760°C and compatible with Ag [112]. (Na$_{0.5}$Ce$_{0.5}$)MoO$_4$ ceramic is reported to have ε_r = 11.2, $Q_u \times f$ = 19,365 GHz and τ_f = -44 ppm/°C at optimum sintering temperature of 780°C and compatible with Ag [112].

Surjith et al. have reported the microwave dielectric properties of two Ag compatible ceramics Sm$_2$Mo$_4$O$_{15}$ and Nd$_2$Mo$_4$O$_{15}$ with triclinic structure and space group P$\overline{1}$ and excellent microwave dielectric properties [113]. Bi(Ga$_{1/3}$Mo$_{2/3}$)O$_4$ [114], Bi(Sc$_{1/3}$Mo$_{2/3}$)O$_4$, Bi(Fe$_{1/3}$Mo$_{2/3}$)O$_4$ and Bi(In$_{1/3}$Mo$_{2/3}$)O$_4$ [115] ceramics with monoclinic scheelite structure are reported to exhibit good microwave dielectric properties.

Pang et al. have reported the microwave dielectric properties of Nd$_2$Mo$_3$O$_{12}$ and La$_2$Mo$_3$O$_{12}$ ceramics with monoclinic scheelite structure [116]. Zhou et al. have reported the microwave dielectric properties of (K$_{0.5}$Nd$_{0.5}$)MoO$_4$ with ε_r = 9.8, $Q_u \times f$ = 69,000 GHz and τ_f = -62 ppm/°C at optimum sintering temperature of 760°C and (K$_{0.5}$Sm$_{0.5}$)MoO$_4$ with ε_r = 9.7, $Q_u \times f$ = 20,000 GHz and τ_f = -65 ppm/°C at optimum

sintering temperature of 800°C with monoclinic scheelite crystal structure and space group I2/b (αβ0)00 [117].

Li et al. have reported the microwave dielectric properties of $Zn_3Mo_2O_9$ as ε_r = 8.7, $Q_u \times f$ = 23,400 GHz and τ_f = -79 ppm/°C at optimum sintering temperature range 940-1000°C [118]. $BaLa_2(MoO_4)_4$ [119], $BaY_2(MoO_4)_4$ [120], $BaNd_2(MoO_4)_4$ and $BaSm_2(MoO_4)_4$ [121] ceramics with monoclinic crystal structure were reported to have good microwave dielectric properties. $BaLa_2(MoO_4)_4$ ceramic is reported to have ε_r = 10.3, $Q_u \times f$ = 29,800 GHz and τ_f = -76 ppm/°C at optimum sintering temperature of 860°C [119]. $BaY_2(MoO_4)_4$ ceramic has ε_r of 11.5, $Q_u \times f$ of 45,000 GHz and τ_f of -35 ppm/°C at optimum sintering temperature of 925°C [120]. $BaNd_2(MoO_4)_4$ ceramic has ε_r of 11.7, $Q_u \times f$ of 45,000 GHz and τ_f of - 41 ppm/°C at optimum sintering temperature of 960°C [121]. $BaSm_2(MoO_4)_4$ ceramic has ε_r of 11.8, $Q_u \times f$ of 20,000 GHz and τ_f of - 34 ppm/°C at optimum sintering temperature of 960°C [121].

Pang et al. have reported the microwave dielectric properties of monoclinic $(K_{0.5}La_{0.5})MoO_4$ with ε_r = 10.3, $Q_u \times f$ = 59,000 GHz and τ_f = -81 ppm/°C at optimum sintering temperature of 680°C [122]. Liu et al. have reported the microwave dielectric properties of $Sm_2Zr_3(MoO_4)_9$ with ε_r = 11, $Q_u \times f$ = 74,012 GHz and τ_f = -45.3 ppm/°C at optimum sintering temperature of 875°C and $Nd_2Zr_3(MoO_4)_9$ with ε_r = 10.8, $Q_u \times f$ = 58,942 GHz and τ_f = -40.9 ppm/°C at optimum sintering temperature of 850°C both having hexagonal crystal structure with R$\overline{3}$c space group[123].

A close look at the reported molybdate-based LTCC and ULTCC compositions clearly shows that scheelite structure based materials are widely reported as co-firable ceramics. The reported LTCC and ULTCC molybdate ceramics show that crystal structure has a significant influence on the degree of co-firability along with several other thermodynamic factors. It is also observed that most of the LTCC and ULTCC molybdate systems contain $(MoO_4)^{2-}$ tetrahedra in the crystal structure. Many reports on phase pure molybdates with low and ultra low temperature sinterability are reported and co-firability with Al or Ag electrodes are proposed. There are more number of Al compatible molybdate ceramics than that are compatible with Ag. The formation of $Al_2(MoO_4)_3$, Ag_2MoO_4 etc. are reported as the common secondary phases formed during co-firing of molybdate ceramics with Al or Ag. The high volatility of MoO_3 can be one of the factors affecting the co-firability. However, the superior dielectric properties, low dielectric loss, better machinability and temperature stability of

molybdate ceramics, makes them the ideal choice for LTCC and ULTCC substrates as well as for other microwave circuit applications.

1.6 Significance of scheelite structure

Scheelite is a natural mineral $CaWO_4$ which belongs to tetragonal crystal system with $I4_1/a$ space group having four molecules per unit cell. The mineral powellite $CaMoO_4$ also crystallizes in the scheelite structure. In general, the scheelite compounds of general formula $A^{2+}B^{6+}O_4$ consists of cubic close-packed array of ordered A^{2+} and BO_4^{2-} units. The ABO_4 type compounds with radius of A site cation ≥ 0.99 Å crystallize in scheelite structure (A = Ca, Sr, Ba) and that with radius ≤ 0.99 Å (A = Mg, Mn, Zn) crystallize in wolframite structure. The scheelite structure can accommodate a wide range of oxidation states +1, +2, +3 and +4 for A site cations along with oxidation states +7, +6, +5 and +4 for B site cations respectively. The scheelite structure consists of two constituent cation polyhedra, eight-coordinated calcium site and the tetrahedral molybdenum site. The coordination polyhedra in scheelite structure is shown in Figure 1.10 [124].
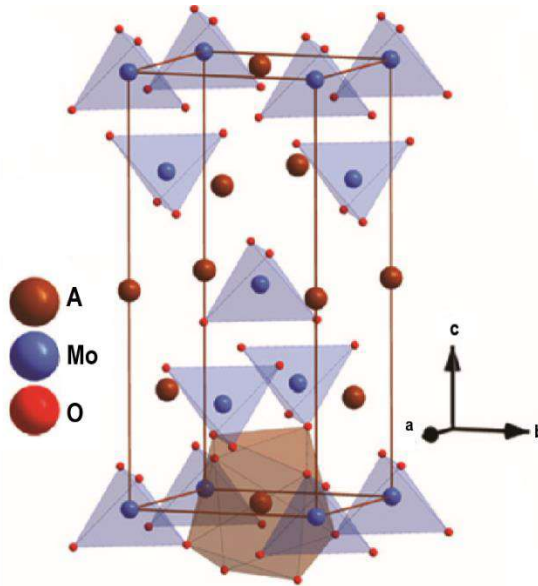
Figure 1.10 Coordination polyhedra in scheelite structure [Ref. 124]

There are three symmetrically distinct atoms in the tetragonal scheelite structure. Each calcium site shares edges with four adjacent calcium sites and shares corners with eight adjacent $(MoO_4)^{2-}$ tetrahedra [125]. Each tetrahedron is linked to eight calcium sites (two to each oxygen). A-site ions are positioned at the corner of the primitive unit cell and the B-site ions at the face-centre respectively, while the oxygen

ion is located at the corner of a tetrahedron that also include two A-site ions and one B-site ion, with coordination number 3 for oxygen atoms. The arrangement of ions in scheelite unit cell is shown in Figure 1.11. The ionic positions in the unit cell are A-site cation $((0, 0, 1/2), (1/2, 0, 1/4), (1/2, 1/2, 0), (0, 1/2, 3/4))$, B-site cation $((0, 0, 0), (0, 1/2, 1/4), (1/2, 1/2, 1/2), (1/2, 0, 3/4))$, Oxygen ion $((x, y, z), (-x, -y, z), (x, 1/2 + y, 1/4 - z), (-x, 1/2 - y, 1/4 - z), (-y, x, -z), (y, -x, -z), (-y, 1/2 + x, 1/4 + z), (y, 1/2 - x, 1/4 + z), (x = 0.241, y = 0.151, z = 0.081))$ [124-129].
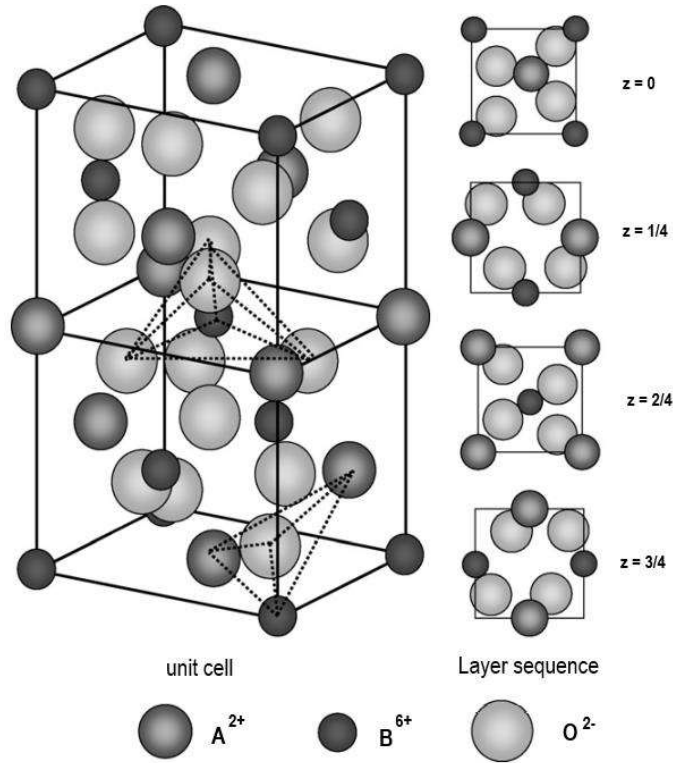
Figure 1.11 Arrangement of ions in scheelite unit cell [Ref. 125]

CaMoO$_4$ is reported to be sintered at 1100°C and exhibits microwave dielectric properties of $\varepsilon_r = 10.79$, $Q_u \times f = 89{,}700$ GHz and $\tau_f = -57$ ppm/°C. The applicability of CaMoO$_4$ for LTCC applications with Ag electrodes is limited because of the high sintering temperature. Many attempts have been made to lower the sintering temperature of CaMoO$_4$ by A site substitution as well as by the addition of sintering aids. Scheelite structure based phase pure compositions with lower sintering temperatures are promising materials for LTCC and ULTCC applications [124-129].

1.7 Objectives of the present study

In the present study, efforts have been done to develop single phase scheelite based phase pure molybdate ceramics with excellent microwave dielectric properties and compatibility with either Al or Ag metal electrodes for LTCC and ULTCC applications. Binary molybdates in the phase diagram comprising of alkali metal molybdates, alkaline earth metal molybdates and rare earth molybdates are investigated in detail. Among the alkali metal molybdates, sodium molybdate based systems are chosen for the present study since lithium based systems have high ionic conductivity and potassium based systems have hygroscopic nature which restrict their use in multilayer packaging systems. The compositions in the phase diagrams of Na_2MoO_4-$AMoO_4$ (A = Zn, Mg, Ba, Sr, Ca), Na_2MoO_4-$R_2(MoO_4)_3$ (R = La, Pr, Nd, Sm, Y and Yb) and $AMoO_4$-$R_2(MoO_4)_3$ (A = Ba, Sr, Ca; R = La, Pr, Nd and Sm) are studied. Na_2MoO_4-$AMoO_4$ (A = Zn, Mg) systems have two triclinic compositions $Na_2Zn_5(MoO_4)_6$ and $Na_2Mg_5(MoO_4)_6$ having single phase nature. These ceramics are prepared by the solid-state ceramic route, structural and microwave dielectric characterization have been done and their compatibility with Al electrodes are studied. The structure and microstructure are correlated with the microwave dielectric properties. Na_2MoO_4-$R_2(MoO_4)_3$ system include $Na_5R(MoO_4)_4$ (Ln = La-Sm,Y,Yb) compositions belonging to tetragonal crystal system with commensurately modulated scheelite structure and $NaR_5(MoO_4)_8$ (R = La-Sm) compositions belonging to monoclinic crystal system possessing incommensurately modulated scheelite structure. $AR_4(MoO_4)_7$ (A = Ba, Sr, Ca; R = La, Pr, Nd and Sm) in the $A_2(MoO_4)_3$-$R_2(MoO_4)_3$ system, which is reported to have monoclinic scheelite based structure are also investigated in detail. The microwave dielectric properties and the co-firability of these systems with Ag/Al are extensively investigated in the present work. An effort has also been made to prepare phase pure composition $Pr_2Zr_3(MoO_4)_9$ in the $Pr_2(MoO_4)_3$-$Zr(MoO_4)_2$ phase diagram with mixed frame work and open cage structure. The effect of Ti^{4+} substitution on the crystal structure and co-firability of these ceramics are also investigated. The $Pr_2Zr_3(MoO_4)_9$ ceramics are used as particulate filler and incorporated in the HDPE polymer matrix to fabricate planar and dimensionally stable substrates for microstrip patch antenna fabrication.The molybdate ceramics which are having phase purity, good dielectric properties and chemical compatibility are ideal candidate materials for multilayer circuit fabrication.

References

[1] M. Golio, *The RF and microwave handbook*, CRC press (2000).

[2] M. Makimoto, S. Yamashita, *Microwave resonators and filters for wireless communication: theory, design and application* (Vol. 4), Springer Science & Business Media (2001).

[3] S. Hong, *Wireless: From Marconi's black-box to the audion*, MIT Press (2001).

[4] T. A. Vanderah, Talking ceramics, Science, 298 [5596] (2002) 1182-1184.

[5] I. Robertson, N. Somjit, M. Chongcheawchamnan, *Microwave and millimetre-wave design for wireless communications*, John Wiley & Sons (2016).

[6] https://www.microwaves101.com/encyclopedias/frequency-letter-bands

[7] K. Kaur, S. Kumar, A. Baliyan, 5G: a new era of wireless communication, Int. J. Inf. Tecnol., (2018) 1-6.

[8] P. H. Siegel, Terahertz technology, IEEE Trans. Microw. Theory Tech., 50 [3] (2002) 910-928.

[9] E. Pickwell, V. P. Wallace, Biomedical applications of terahertz technology, J. Phys. D: Appl. Phys., 39 [17] (2006) R301-R310.

[10] N. Naeem, S. Parveen, A. Ismail, Terahertz Communications for 5G and Beyond, In *Antenna Fundamentals for Legacy Mobile Applications and Beyond,* Springer, Cham (2018) 305-322.

[11] S. Li, L. Da Xu, S. Zhao, 5G internet of things: A survey, J. Ind. Informat. Integr., 10 (2018) 1-9.

[12] A. Tiwary, M. Mahato, A. Chidar, M. K. Chandrol, M. Shrivastava, M. Tripathi, Internet of Things (IoT): Research, Architectures and Applications, International Journal on Future Revolution in Computer Science & Communication Engineering, 4 [3] (2018) 23-27.

[13] M. T. Sebastian, H. Jantunen, High Temperature Cofired Ceramic (HTCC), Low Temperature Cofired Ceramic (LTCC), and Ultralow Temperature Cofired Ceramic (ULTCC) Materials, *Microwave Materials and Applications,* 2V Set, (2017) 355-425.

[14] D. J. Griffiths, *Introduction to electrodynamics,* Pearson Education (2014).

[15] L. F. Chen, C. K. Ong, C. P. Neo, V. V. Varadan, V. K. Varadan, *Microwave electronics: measurement and materials characterization*, John Wiley & Sons (2004).

[16] M. T. Sebastian, *Dielectric materials for wireless communication*, Elsevier (2008).

[17] W. D. Kingery, H. K. Bowen, D. R. Uhlmann, *Introduction to ceramics*, Wiley and Sons (1976).

[18] A. R. Von Hippel, *Dielectrics and waves*, New York, NY: Wiley (1954).

[19] V. R. K. Murthy, S. Sundaram, B. Viswanathan, eds., *Microwave materials*, New York: Springer (1994).

[20] M. T. Sebastian, R. Ubic, H. Jantunen, Low-loss dielectric ceramic materials and their properties, Inter. Mater. Rev., 60 [7] (2015) 392-412.

[21] W. Wersing, Microwave ceramics for resonators and filters, Curr. Opin. Solid State Mater. Sci., 1 [5] (1996) 715-731.

[22] V. N. Kestelman, L. S. Pinchuk, V. A. Goldade, *Electrets in engineering: fundamentals and applications,* Springer Science & Business Media (2013).

[23] A. J. Moulson, J. M. Herbert, *Electroceramics: materials, properties, applications*, John Wiley & Sons (2003).

[24] A. K. Jonscher, The 'universal' dielectric response, Nature, 267 [5613] (1977) 673.

[25] R. Freer, F. Azough, Microstructural engineering of microwave dielectric ceramics, J. Eur. Ceram. Soc., 28 [7] (2008) 1433-1441.

[26] J. Shanker, S. Dixit, Dielectric constants and their pressure and temperature derivatives for ionic crystals, Phys. Stat. Sol. A, 123 [1] (1991) 17-50.

[27] R. H. Cole, Dielectric Polarization and Loss, Annu. Rev. Phys. Chem., 11 [1] (1960) 149-168.

[28] E. L. Colla, I. M. Reaney, N. Setter, Effect of structural changes in complex perovskites on the temperature coefficient of the relative permittivity, J. Appl. Phys., 74 [5] (1993) 3414-3425.

[29] F. E. Harris, B. J. Alder, Statistical mechanical derivation of onsager's equation for dielectric polarization, J. Chem. Phys., 22 [11] (1954) 1806-1808.

[30] O. F. Mossotti, Discussione analitica sull'influenza che l'azione di un mezzo dielettrico ha sulla distribuzione dell'elettricità alla superficie di più corpi elettrici disseminati in esso, Mem. Math. Fisca Moderna, vol. XXIV, (1850) 49–74.

[31] R. Clausius, *Die mechanische behandlung der electricität* (Vol. 2). Vieweg+ Teubner Verlag (1879).

[32] J. Liu, C. G. Duan, W. N. Mei, R. W. Smith, J. R. Hardy, Dielectric properties and Maxwell-Wagner relaxation of compounds $ACu_3Ti_4O_{12}$ (A= Ca, $Bi_{2/3}$, $Y_{2/3}$, $La_{2/3}$), J. Appl. Phys., 98 [9] (2005) 093703.

[33] S. H. Wemple, M. DiDomenico Jr, Behavior of the electronic dielectric constant in covalent and ionic materials, Phys. Rev. B, 3 [4] (1971) 1338.

[34] K. S. Cole, R. H. Cole, Dispersion and absorption in dielectrics I. Alternating current characteristics, J. Chem. Phys., 9 [4] (1941) 341-351.

[35] E. L. Colla, I. M. Reaney, N. Setter, A microscopic model for the temperature coefficient of the resonant frequency (τ_f) in complex perovskites used for microwave filter, Ferroelectrics, 154 [1] (1994) 35-40.

[36] P. J. Harrop, Temperature coefficients of capacitance of solids, J. Mater. Sci., 4 [4] (1969) 370-374.

[37] A. J. Bosman, E. E. Havinga, Temperature dependence of dielectric constants of cubic ionic compounds, Phys. Rev., 129 [4] (1963) 1593-1600.

[38] I. M. Reaney, P. Wise, R. Ubic, J. Breeze, N. M. Alford, D. Iddles, D. Cannell, T. Price, On the temperature coefficient of resonant frequency in microwave dielectrics, Philos. Mag., 81 [2] (2001) 501-510.

[39] L. Rayleigh, XVIII On the passage of electric waves through tubes, or the vibrations of dielectric cylinders, The London, Edinburgh, and Dublin Philosophical Magazine and Journal of Science, 43 [261] (1897) 125-132.

[40] D. Kajfez, P. Guillon, *Dielectric resonators*, Norwood, MA, Artech House, Inc., (1986).

[41] R. D. Richtmyer, Dielectric resonators, J. Appl. Phys., 10 [6] (1939) 391-398.

[42] A. Okaya, L. F. Barash, The dielectric microwave resonator, Proc. IRE, 50 [10] (1962) 2081-2092.

[43] K. Wakino, K. Minai, H. Tamura, Microwave Characteristics of (Zr, Sn) TiO_4 and BaO-PbO-Nd_2O_3-TiO_2 Dielectric Resonators, J. Am. Ceram. Soc., 67 [4] (1984) 278-281.

[44] K. Wakino, Recent development of dielectric resonator materials and filters in Japan, Ferroelectrics, 91 [1] (1989) 69-86.

[45] J. K. Plourde, D. F. Linn, H. M. O'Bryan Jr, J. Thomson Jr, $Ba_2Ti_9O_{20}$ as a microwave dielectric resonator, J. Am. Ceram. Soc., 58 [9-10] (1975) 418-420.

[46] K. Zhang, D. Li, K. Chang, K. Zhang, D. Li, *Electromagnetic theory for microwaves and optoelectronics,* Berlin: Springer (1998).

[47] D. Kajfez, A. W. Glisson, J. James, Computed modal field distributions for isolated dielectric resonators, IEEE Trans. Microw. Theory Tech., 32 [12] (1984) 1609-1616.

[48] B. W. Hakki, P. D. Coleman, A dielectric resonator method of measuring inductive capacities in the millimeter range, IRE Trans. Microwave Theory Techn., 8 [4] (1960) 402-410.

[49] J. Krupka, K. Derzakowski, B. Riddle, J. B. Jarvis, A dielectric resonator for measurements of complex permittivity of low loss dielectric materials as a function of temperature, Meas. Sci. Technol., 9 [10] (1998) 1751-1756.

[50] P. Guillon, Y. Garault, Accurate resonant frequencies of dielectric resonators, IEEE Trans. Microw. Theory Tech., 25 [11] (1977) 916-922.

[51] M. W. Pospieszalski, Cylindrical dielectric resonators and their applications in TEM line microwave circuits, IEEE Trans. Microw. Theory Tech., 27 [3] (1979) 233-238.

[52] H. Y. Yee, Natural resonant frequencies of microwave dielectric resonators, IEEE Trans. Microw. Theory Tech., 13 [2] (1965) 256-256.

[53] D. Kajfez, A. W. Glisson, J. James, Evaluation of modes in dielectric resonators using a surface integral equation formulation, IEEE MTT-S International Microwave Symposium Digest, Boston USA (1983) 409-411.

[54] M. E. Tobar, A. G. Mann, Resonant frequencies of higher order modes in cylindrical anisotropic dielectric resonators, IEEE Trans. Microw. Theory Tech., 39 [12] (1991) 2077-2082.

[55] T. Itoh, R. S. Rudokas, New method for computing the resonant frequencies of dielectric resonators, IEEE Trans. Microw. Theory Tech., 25 [1] (1977) 52-54.

[56] M. T. Sebastian, H. Jantunen, Low loss dielectric materials for LTCC applications: a review, Inter. Mater. Rev., 53 [2] (2008) 57-90.

[57] M. T. Sebastian, H. Wang, H. Jantunen, Low temperature co-fired ceramics with ultra-low sintering temperature: a review, Curr. Opin. Solid State. Mater Sci., 20 [3] (2016) 151-170.

[58] Y. Imanaka, *Multilayered low temperature cofired ceramics (LTCC) technology*, Springer Science & Business Media (2005).

[59] D. Jurków, J. Stiernstedt, Investigation of High Temperature Co-fired Ceramics sintering conditions using Taguchi Design of the experiment, Ceram. Int., 40 [7] (2014) 10447-10455.

[60] I. Wolff, Design and technology of microwave and millimeterwave LTCC circuits and systems, International Symposium on Signals, Systems and Electronics ISSSE'07, Montreal, QC, Canada (2007) 505-512.

[61] D. Jurków, T. Maeder, A. Dąbrowski, M. Santo Zarnik, D. Belavič, H. Bartsch, J. Müller, Overview on low temperature co-fired ceramic sensors, Sens Actuators A: Phys., 233 (2015) 125-146.

[62] J. I. Steinberg, S. J. Horowitz, R. J. Bacher, Low Temperature Co-fired Tape Dielectric Materials System for Multilayer Interconnections, Microelectro. Int., 3 [1] (1986) 36-39.

[63] Z. Wang, J. Yang, Layout and process characteristics of LTCC substrate for microwave module, IEEE International Symposium on Radio-Frequency Integration Technology RFIT, Singapore (2009) 361-366.

[64] I. Wolff, From antennas to microwave systems-LTCC as an integration technology for space applications, 3rd European Conference on Antennas and Propagation, EuCAP, Berlin (2009) 3-8.

[65] J. Lenkkeri, E. Juntunen, M. Lahti, S. Bouwstra, Thermo-mechanical simulations of LTCC packages for RF MEMS applications, 11th International Conference on Thermal, Mechanical & Multi-Physics Simulation, and Experiments in Microelectronics and Microsystems (EuroSimE), Bordeaux (2010) 1-6.

[66] https://epp-europe.industrie.de/technology/products/greentape-for-low-temperature-co-fired-ceramic/

[67] R. Faddoul, N. Reverdy-Bruas, A. Blayo, Formulation and screen printing of water based conductive flake silver pastes onto green ceramic tapes for electronic applications, Mater. Sci. Eng. B, 177 [13] (2012) 1053-1066.

[68] D. K. Kwon, M. T. Lanagan, T. R. Shrout, Microwave dielectric properties and low-temperature cofiring of $BaTe_4O_9$ with aluminum metal electrode, J. Am. Ceram. Soc., 88 [12] (2005) 3419-3422.

[69] Z. Xiangjun, F. Dagang, Miniaturization of C band LTCC channel receiver front-end SiP module, International Conference on Microwave and Millimeter Wave Technology (ICMMT), Nanjing China (2008) 1412-1414.

[70] L. Z. Zhu, X. B. Wei, P. Wang, S. Ma, Z. Y. Zeng, B. C. Yang, Compact LTCC module for WLAN RF front-end, International Conference on Computational Problem-Solving (ICCP), Chengdu China (2011) 387-389.

[71] X. Zhang, M. Miao, Z. Li, Y. Zhang, Y. Lv, Y. Yao, THz filters embedded in LTCC multi-layer substrate, 13th International Conference on Electronic Packaging Technology and High Density Packaging (ICEPT-HDP), Guilin China (2012) 1003-1005.

[72] S. B. Yeap, X. Qing, M. Sun, Z. N. Chen, 140-GHz 2× 2 SIW horn array on LTCC, IEEE Asia-Pacific Conference on Antennas and Propagation (APCAP), Singapore (2012) 279-280.

[73] D. Nowak, E. Miś, A. Dziedzic, J. Kita, Fabrication and electrical properties of laser-shaped thick-film and LTCC microresistors, Microelectron. Reliab., 49 [6] (2009) 600-606.

[74] E. Miś, A. Dziedzic, W. Mielcarek, Microvaristors in thick-film and LTCC circuits, Microelectron. Reliab., 49 [6] (2009) 607-613.

[75] C. Lenz, S. Ziesche, U. Partsch, H. Neubert, Technological Investigation of LTCC-Based Micro-electro-mechanical Systems (MEMS) to improve reliability and accuracy, IEEE European Microelectronics Packaging Conference (EMPC), Grenoble France (2013) 1-6.

[76] L. J. Golonka, New application of LTCC technology, IEEE 28th International Spring Seminar on Electronics Technology: Meeting the Challenges of Electronics Technology Progress, Wiener Neustadt, Austria (2005) 162-166.

[77] D. Jurków, T. Maeder, A. Dąbrowski, M. Santo Zarnik, D. Belavič, H. Bartsch, J. Müller, Overview on low temperature co-fired ceramic sensors, Sens. Actuator A-Phys., 233 (2015) 125-146.

[78] O. Dernovsek, M. Eberstein, W. A. Schiller, A. Naeini, G. Preu, W. Wersing, LTCC glass-ceramic composites for microwave application, J. Eur. Ceram. Soc., 21 [10-11] (2001) 1693-1697.

[79] C. R. Chang, J. H. Jean, Crystallization Kinetics and Mechanism of Low-Dielectric, Low-Temperature, Cofirable CaO-B_2O_3-SiO_2 Glass-Ceramics, J. Am. Ceram. Soc., 82 [7] (1999) 1725-1732.

[80] R. D. Shannon, Dielectric polarizabilities of ions in oxides and fluorides, J. Appl. Phys., 73 [1] (1993) 348-366.

[81] G. Subodh, M. T. Sebastian, Microwave dielectric properties of ATe_3O_8 (A= Sn, Zr) ceramics, Jpn. J. Appl. Phys., 47 [10R] (2008) 7943-7946.

[82] G. Subodh, M. T. Sebastian, Glass-free $Zn_2Te_3O_8$ microwave ceramic for LTCC applications, J. Am. Ceram. Soc., 90 [7] (2007) 2266-2268.

[83] D. K. Kwon, M. T. Lanagan, T. R. Shrout, Synthesis of $BaTiTe_3O_9$ ceramics for LTCC application and its dielectric properties, J. Ceram. Soc. Jpn., 113 [1315] (2005) 216-219.

[84] S. F. Wang, Y. F. Hsu, Y. R. Wang, C. C. Sung, Ultra-Low-Fire $Zn_2Te_3O_8$–$TiTe_3O_8$ Ceramic Composites, J. Am. Ceram. Soc., 94 [3] (2011) 812-816.

[85] E. K. Suresh, K. Prasad, N. S. Arun, R. Ratheesh, Synthesis and microwave dielectric properties of $A_{16}V_{18}O_{61}$ (A=Ba, Sr and Ca) ceramics for LTCC applications, J. Electron. Mater., 45 [6] (2016) 2996-3002.

[86] S. E. Kalathil, U. A. Neelakantan, R. Ratheesh, Microwave Dielectric Properties of Ultralow-Temperature Cofirable $Ba_3V_4O_{13}$ Ceramics, J. Am. Ceram. Soc., 97 [5] (2014) 1530-1533.

[87] U. A. Neelakantan, S. E. Kalathil, R. Ratheesh, Structure and Microwave Dielectric Properties of Ultralow-Temperature Cofirable BaV_2O_6 Ceramics, Eur. J. Inorg. Chem., 2015 [2] (2015) 305-310.

[88] A. N. Unnimaya, E. K. Suresh, R. Ratheesh, Crystal structure and microwave dielectric properties of new alkaline earth vanadate $A_4V_2O_9$ (A= Ba, Sr, Ca, Mg and Zn) ceramics for LTCC applications, Mater. Res. Bull., 88 (2017) 174-181.

[89] L. Fang, Z. Wei, C. Su, F. Xiang, H. Zhang, Novel low-firing microwave dielectric ceramics: $BaMV_2O_7$ (M= Mg, Zn), Ceram. Int., 40 [10] (2014) 16835-16839.

[90] X. Jiang, L. Fang, H. Xiang, H. Guo, J. Li, C. Li, A novel low-firing microwave dielectric ceramic $NaMg_4V_3O_{12}$ and its chemical compatibility with silver electrode, Ceram. Int., 41 [10] (2015) 13878-13882.

[91] E. K. Suresh, A. N. Unnimaya, A. Surjith, R. Ratheesh, New vanadium based $Ba_3MV_4O_{15}$ (M= Ti and Zr) high Q ceramics for LTCC applications, Ceram. Int., 39 [4] (2013) 3635-3639.

[92] Z. Di, P. Li-Xia, Q. Ze-Ming, J. Biao-Bing, Y. Xi, Novel ultra-low temperature co-fired microwave dielectric ceramic at 400 degrees and its chemical compatibility with base metal, Sci. Rep., 4 (2014) 5980.

[93] G. Q. Zhang, H. Wang, J. Guo, L. He, D. D. Wei, Q. B. Yuan, Ultra-low sintering temperature microwave dielectric ceramics based on Na_2O-MoO_3 binary system, J. Am. Ceram. Soc., 98 [2] (2015) 528-533.

[94] G. Q. Zhang, J. Guo, H. Wang, Ultra-low temperature sintering microwave dielectric ceramics based on Ag_2O–MoO_3 binary system, J. Am. Ceram. Soc., 100 [6] (2017) 2604-2611.

[95] H. H. Xi, D. Zhou, B. He, H. D. Xie, Microwave dielectric properties of scheelite structured $PbMoO_4$ ceramic with ultralow sintering temperature, J. Am. Ceram. Soc., 97 [5] (2014) 1375-1378.

[96] D. Zhou, C. A. Randall, L. X. Pang, H. Wang, J. Guo, G. Q. Zhang, Y. Wu, K. T. Guo, L. Shui, X. Yao, Microwave dielectric properties of $(ABi)_{1/2}MoO_4$ (A= Li, Na,

K, Rb, Ag) type ceramics with ultra-low firing temperatures, Mater. Chem. Phys., 129 [3] (2011) 688-692.

[97] D. Zhou, C. A. Randall, H. Wang, L. X. Pang, X. Yao, Microwave dielectric ceramics in $Li_2O–Bi_2O_3–MoO_3$ system with ultra-low sintering temperatures, J. Am. Ceram. Soc., 93 [4] (2010) 1096-1100.

[98] L. X. Pang, D. Zhou, J. Guo, Z. X. Yue, X. Yao, Microwave Dielectric Properties of $(Li_{0.5}Ln_{0.5})MoO_4$ (Ln= Nd, Er, Gd, Y, Yb, Sm, and Ce) Ceramics, J. Am. Ceram. Soc., 98 [1] (2015) 130-135.

[99] J. Varghese, T. Siponkoski, M. Nelo, M. T. Sebastian, H. Jantunen, Microwave dielectric properties of low-temperature sinterable $α-MoO_3$, J. Eur. Ceram. Soc., 38 [4] (2018) 1541-1547.

[100] D. Zhou, C. A. Randall, L. X. Pang, H. Wang, X. G. Wu, J. Guo, G. Q. Zhang, L. Shui, X. Yao, Microwave Dielectric Properties of $Li_2(M^{2+})_2Mo_3O_{12}$ and $Li_3(M^{3+})Mo_3O_{12}$ (M= Zn, Ca, Al, and In) Lyonsite-Related-Type Ceramics with Ultra-Low Sintering Temperatures, J. Am. Ceram. Soc., 94 [3] (2011) 802-805.

[101] W. Wen, C. Li, Y. Sun, Y. Tang, L. Fang, $Cu_3Mo_2O_9$: An Ultralow-Firing Microwave Dielectric Ceramic with Good Temperature Stability and Chemical Compatibility with Aluminum, J. Electron. Mater., 47 [2] (2018) 1003-1008.

[102] X. L. Zhai, X. Zheng, H. H. Xi, W. B. Li, J. Han, D. Zhou, Microwave dielectric properties of $LiKSm_2(MoO_4)_4$ ceramics with ultralow sintering temperatures, J. Am. Ceram. Soc., 98 [9] (2015) 2716-2719.

[103] D. Zhou, H. Wang, L. X. Pang, C. A. Randall, X. Yao, $Bi_2O_3–MoO_3$ binary system: an alternative ultralow sintering temperature microwave dielectric, J. Am. Ceram. Soc., 92 [10] (2009) 2242-2246.

[104] D. Zhou, H. Wang, X. Yao, L. X. Pang, Microwave dielectric properties of low temperature firing $Bi_2Mo_2O_9$ ceramic, J. Am. Ceram. Soc., 91 [10] (2008) 3419-3422.

[105] G. Q. Zhang, J. Guo, L. He, D. Zhou, H. Wang, J. Koruza, M. Kosec, Preparation and Microwave Dielectric Properties of Ultra-low Temperature Sintering Ceramics in $K_2O–MoO_3$ Binary System, J. Am. Ceram. Soc., 97 [1] (2014) 241-245.

[106] H. Xie, H. Xi, F. Li, C. Chen, X. Wang, D. Zhou, Microwave dielectric properties of Pb_2MoO_5 ceramic with ultra-low sintering temperature, J. Eur. Ceram. Soc., 34 [15] (2014) 4089-4093.

[107] S. F. Wang, Y. R. Wang, Y. F. Hsu, H. C. Lu, J. S. Tsai, Ultra-Low-Fire $Te_2(Mo_{1−x}W_x)O_7$ Ceramics: Microstructure and Microwave Dielectric Properties, J. Am. Ceram. Soc., 93 [12] (2010) 4071-4074.

[108] N. Joseph, J. Varghese, T. Siponkoski, M. Teirikangas, M. T. Sebastian, H. Jantunen, Glass-free $CuMoO_4$ ceramic with excellent dielectric and thermal properties for ultralow temperature cofired ceramic applications, ACS Sustain. Chem. Eng., 4 [10] (2016) 5632-5639.

[109] G. K. Choi, J. R. Kim, S. H. Yoon, K. S. Hong, Microwave dielectric properties of scheelite (A= Ca, Sr, Ba) and wolframite (A = Mg, Zn, Mn) $AMoO_4$ compounds, J. Eur. Ceram. Soc., 27 [8-9] (2007) 3063-3067.

[110] A. Surjith, R. Ratheesh, High Q ceramics in the $ACe_2(MoO_4)_4$ (A= Ba, Sr and Ca) system for LTCC applications, J. Alloys Compd., 550, (2013)169-172.

[111] H. Xi, D. Zhou, H. Xie, W. Li, Microwave dielectric properties of low firing scheelite-related $(Na_{0.5}La_{0.5})MoO_4$ ceramic, Mater. Lett., 142, (2015) 221-224.

[112] H. H. Xi, D. Zhou, H. D. Xie, W. B. Li, Microwave dielectric properties of low firing $(Na_{0.5}Ln_{0.5})MoO_4$ (Ln = Nd and Ce) ceramics, Ceram. Inter., 41 [4] (2015) 6103-6107.

[113] A. Surjith, E. K. Suresh, S. Freddy, R. Ratheesh, Microwave dielectric properties of low temperature sinterable $RE_2Mo_4O_{15}$ (RE = Nd, Sm) ceramics for LTCC applications, J. Mater. Sci.: Mater. Electron., 24 [6] (2013) 1818-1822.

[114] L. X. Pang, W. G. Liu, D. Zhou, Z. X. Yue, Novel glass-free low-temperature fired microwave dielectric ceramics: $Bi(Ga_{1/3}Mo_{2/3})O_4$, Ceram. Int., 42 [3] (2016) 4574-4577.

[115] D. Zhou, L. X. Pang, D. W. Wang, H. H. Guo, F. Yang, Z. M. Qi, C. Li, B. B. Jin, I. M. Reaney, Crystal structure, impedance and broadband dielectric spectra of ordered scheelite-structured $Bi(Sc_{1/3}Mo_{2/3})O_4$ ceramic, J. Eur. Ceram. Soc., 38 [4] (2018) 1556-1561.

[116] L. X. Pang, G. B. Sun, D. Zhou, $Ln_2Mo_3O_{12}$ (Ln = La, Nd): A novel group of low loss microwave dielectric ceramics with low sintering temperature, Mater. Lett., 65 [2] (2011) 164-166.

[117] D. Zhou, L. X. Pang, J. Guo, G. Q. Zhang, Y. Wu, H. Wang, X. Yao, Low temperature firing microwave dielectric ceramics $(K_{0.5}Ln_{0.5})MoO_4$ (Ln = Nd and Sm) with low dielectric loss, J. Eur. Ceram. Soc., 31 [15] (2011) 2749-2752.

[118] C. Li, W. Wen, H. Xiang, L. Fang, Y. Sun, Low temperature sintering and microwave dielectric properties of $Zn_3Mo_2O_9$ ceramic, J. Mater. Sci.: Mater. Electron, 29 [3] (2018) 1907-1913.

[119] L. X. Pang, H. Liu, D. Zhou, G. B. Sun, W. G. Qin, W. G. Liu, Microwave dielectric ceramic with intrinsic low firing temperature: $BaLa_2(MoO_4)_4$, Mater. Lett., 72, (2012) 128-130.

[120] W. B. Li, H. H. Xi, D. Zhou, Microwave dielectric properties of $BaY_2(MoO_4)_4$ ceramic with low sintering temperature, J. Mater. Sci.: Mater. Electron, 26 [3] (2015) 1608-1611.

[121] D. Zhou, L. X. Pang, J. Guo, Y. Wu, G. Q. Zhang, W. Dai, H. Wang, X. Yao, New microwave dielectric ceramics $BaLn_2(MoO_4)_4$ (Ln= Nd and Sm) with low loss, J. Am. Ceram. Soc., 94 [9] (2011) 2800-2803.

[122] L. X. Pang, D. Zhou, C. L. Cai, W. G. Liu, Infrared spectroscopy and microwave dielectric properties of ultra-low temperature firing $(K_{0.5}La_{0.5})MoO_4$ ceramics, Mater. Lett., 92 (2013) 36-38.

[123] W. Liu, R. Zuo, Low temperature fired $Ln_2Zr_3(MoO_4)_9$ (Ln=Sm, Nd) microwave dielectric ceramics, Ceram. Int., 43 [18] (2017) 17229-17232.

[124] J. Guo, D. Zhou, L. Wang, H. Wang, T. Shao, Z. M. Qi, X. Yao, Infrared spectra, Raman spectra, microwave dielectric properties and simulation for effective permittivity of temperature stable ceramics $AMoO_4$–TiO_2(A= Ca, Sr), Dalton Trans., 42 [5] (2013) 1483-1491.

[125] E. S. Kim, B. S. Chun, R. Freer, R. J. Cernik, Effects of packing fraction and bond valence on microwave dielectric properties of $A^{2+}B^{6+}O_4$ (A^{2+}: Ca, Pb, Ba; B^{6+}: Mo, W) ceramics, J. Eur. Ceram. Soc., 30 [7] (2010) 1731-1736.

[126] G. K. Choi, J. R. Kim, S. H. Yoon, K. S. Hong, Microwave dielectric properties of scheelite (A= Ca, Sr, Ba) and wolframite (A= Mg, Zn, Mn) $AMoO_4$ compounds, J. Eur. Ceram. Soc., 27 [8-9] (2007) 3063-3067.

[127] A. W. Sleight, Accurate cell dimensions for ABO_4 molybdates and tungstates, Acta Crystallogr. B, 28 [10] (1972) 2899-2902.

[128] R. M. Hazen, L. W. Finger, J. W. Mariathasan, High-pressure crystal chemistry of scheelite-type tungstates and molybdates, J. Phys. Chem. Solids, 46 [2] (1985) 253-263.

[129] F. S. Galasso, *Structure and Properties of Inorganic Solids*, International Series of monographs in solid state Physics (Vol. 7), Elsevier (2016).

Chapter 2

Materials and methods

2.1 Synthesis of microwave ceramics by solid-state ceramic route

2.2 Preparation of polymer ceramic composites

2.3 Powder X-ray diffraction

2.4 Raman spectroscopy

2.5 Scanning Electron Microscopy and Energy Dispersive X-ray Spectroscopy (SEM/EDS)

2.6 Dielectric measurements

2.7 Thermogravimetry and Differential Thermal Analyses (TG/DTA)

2.8 ThermoMechanical Analyzer (TMA)

2.9 Ultimate tensile strength measurement

2.1 Synthesis of microwave ceramics by solid-state ceramic route

In the present study, microwave ceramics were prepared by conventional solid-state ceramic route. High purity oxides and carbonates were taken in stoichiometric proportions and dry mixed in an agate mortar followed by wet mixing in double distilled water medium. The slurry was dried in a hot air oven at 100°C for an hour. The dried powders were then transferred to alumina crucibles and calcined at appropriate temperatures. During calcination the volatile components will be removed and the particles react together to form the phase pure ceramic. The calcined powders were ground well and mixed with 5 wt% polyvinyl alcohol (PVA) solution as binder and dried. These powders were shaped into green pellets by using tungsten carbide (WC) die in a hydraulic hand press taking into account the aspect ratio of the pellets. The ceramic compacts prepared were sintered at appropriate temperatures and duration for proper densification and grain growth. Sintering was done at regular temperature intervals and the density of the sintered samples were measured by dimensional method. The optimum sintering temperature corresponds to that temperature at which the density reaches a maximum value comparable with that of the theoretical density of the ceramic.

Sintering is a processing method to produce high density materials and components from metal or/and ceramic powders by applying thermal energy. Sintering theory is accurately applied in the case of single phase powders sintered by solid state diffusion. The green body prior to sintering is weak and porous. During sintering, the ceramic compact strengthens and shrinks accompanying a dimensional change. In solid-state sintering, the powder compact is densified wholly at the sintering temperature [1-4].

Solid-state sintering mechanism can be interpreted by two-particle model which involves neck formation between contacting particles. During sintering material transport to the neck occur by lattice diffusion, grain boundary diffusion, surface diffusion, gas transport in the form of evaporation/condensation and gas diffusion. When mass transport takes place from a grain boundary to the neck by lattice diffusion, the linear shrinkage or sintering rate for a powder compact is given by Equation 2.1, where γ' is the surface energy, m_d is the atomic volume of a diffusing vacany, D the self-diffusion coefficient, k Boltzmann constant, T absolute temperature, a particle radius and t time for sintering [1,3].

$$\text{Sintering rate} = (20\ \gamma' m_\text{d}D/1.4kT)^{0.4}a^{-1.2}\ t^{0.4} \qquad (2.1)$$

The stages of sintering of polycrystalline solids include an initial stage involving rapid interparticle neck growth, followed by an intermediate stage manifesting a microstructure of equilibrium pore shape with continuous porosity and the final stage with isolated porosity. The driving force for solid-state sintering is the reduction of total interfacial energy by the replacement of solid/vapour interfaces by solid/solid interfaces caused by densification and grain growth. The variables affecting the sinterability and microstructure are material properties and processing conditions. The shape, size distribution and agglomeration of the powders as well as their composition, impurity, homogeneity, and nonstoichiometry are some of the material variables. Process variables include temperature, time, pressure, atmosphere, heating and cooling rate [1-4].

2.2 Preparation of polymer ceramic composites

Phase pure microwave ceramic fillers are dispersed in polymer matrix to form polymer ceramic composites with tailored mechanical, thermal and dielectric properties for microwave substrate applications. These composites are excellent substitutes for woven cloth reinforced polymer PCBs for microelectronic device fabrication and offer excellent signal propagation speed and thermal stability. PTFE, HDPE, LDPE, PS etc. are the commonly used polymers for composite preparation. The polycrystalline microwave ceramic that exhibits phase purity at the calcination stage is mixed with polymer matrix in powder form. The volume percentage of filler loading in the polymer matrix has a decisive role in the dielectric, mechanical and thermal properties of the composite. The composite fabrication is generally done by different techniques such as sigma mixing, melt extrusion, compression moulding etc.

2.3 Powder X-ray diffraction

The structural characterization of the ceramics were done using X-ray diffraction of the powder samples. The crystals have three dimensional periodicity in atomic arrangements with atomic spacing of the order of angstroms. X-rays have small wavelengths ranging from 0.1 Å to 100 Å which are comparable to that of lattice spacings in crystals. Bragg's law relates the wavelength of X-rays to the spacing of the atomic planes. Atoms scatter X-rays and if the scattered waves are in-phase, they interfere to form diffracted beams in specific directions. A typical representation of the

X-ray diffraction from a set of parallel crystallographic planes with miller indices hkl is shown in Figure 2.1 [5-10].

The X-rays are incident at angle of incidence θ and are reflected at the same angle. The additional distance ABC travelled by the X-rays reflected from the second plane equals λ and that of DEF correspond to 2λ and so forth for the constructive interference of the reflected beams form the successive planes. The path difference between the waves scattered by atoms from adjacent hkl lattice planes of spacing d_{hkl} is $2d_{hkl}sinθ$. Bragg's law is given by Equation 2.2, where n is the order of reflection.

$$n\lambda = 2d_{hkl}sin\theta \qquad (2.2)$$
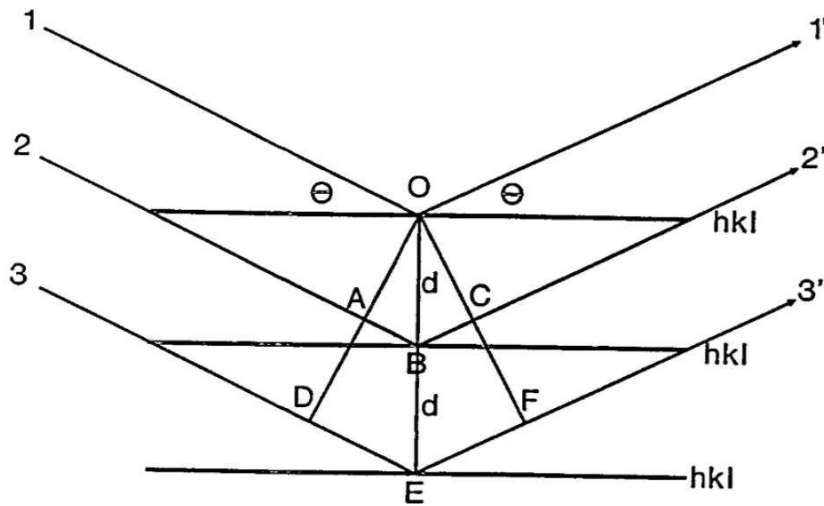
Figure 2.1 Schematic representation of crystallographic planes reflecting X-rays [Ref. 5]

The phase relationship between the waves scattered by the individual atoms of a unit cell is a dominant factor affecting the diffraction intensity. X-rays are made to scatter from a polycrystalline sample and the scattered intensity is recorded. The powdered sample of the polycrystalline ceramic consists of randomly oriented crystallites with all possible interatomic planes and diffraction from each plane will occur at a characteristic diffraction angle [5-10]. Diffraction peaks produced by all the randomly oriented crystallites in the powder are recorded by changing the experimental angle 2θ. The d_{hkl} values along with the Bragg's law can be used to calculate the diffraction angle from a particular set of planes in a crystal. The interplanar spacings d_{hkl} values are geometric functions of the size and shape of the unit cell.
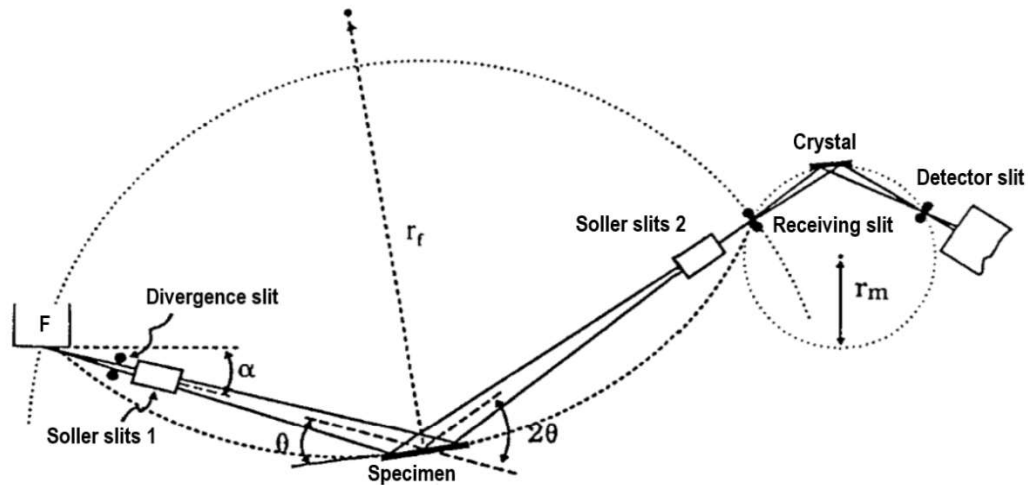
Figure 2.2 Schematic representation of the geometric arrangement of the Bragg-Brentano diffractometer [Ref. 5]

A basic X-ray diffractometer consists of a X-ray source, specimen and a X-ray detector, they all lie on the circumference of a circle, known as focusing circle. X-ray diffractometer is commonly used in Bragg-Brentano geometry also called θ-2θ geometry. A schematic representation of a X-ray diffractometer with Basic Bragg-Brentano geometry is shown in Figure 2.2. In the present work, Bruker Model 5005, Germany, X-ray diffractometer is used for the powder X-ray diffraction studies. The powder sample is ground well and packed in the flat plate sample holder. The instrumentation includes a X-ray generator tube with a typical voltage of 40 kV, target Cu, and a tube current of 30 mA. The diffractometer has a X-ray detector which is a scintillation counter along with divergence slits, scattering slits, receiving slits and a monochromator for Cu. Bragg angle θ is the angle between the plane of the specimen and the X-ray source. The angle between the projection of the X-ray source and the detector is 2θ. Goniometer has 2θ ranging from 10º to 70º with a step size of 0.02º and a scan speed of 15º/min. A collimated beam from the X-ray source is incident onto a sample stationed on the sample holder which may be set at any desired angle to the incident beam. A detector measures the intensity of the diffracted beam, and can be rotated around the sample and set at any desired angular position. X-rays from the line of focus (F) of the X-ray tube passes through a divergence slit, and a parallel plate set collimator Soller slits and are incident on the specimen at an angle θ. The diffracted rays leave the specimen at angle 2θ to the incident beam and θ to the specimen surface

and passes through a second parallel plate collimator through receiving slit to the detector. The diffractometer measures the angle 2θ between the incident and detected beams.

The powder X-ray diffraction pattern of the samples help in confirming the phase purity of the samples by comparison with the standard ICDD (International Centre for Diffraction Data) files. The detailed crystal structure of the compounds can be obtained from a slow scan XRD data by using Rietveld refinement softwares like GSAS General Structure Analysis System, FullProf, TOPAS etc. in cases where the detailed structural data of an isostructural model compound is available.

2.4 Raman spectroscopy

Raman effect is the inelastic scattering of light from solid, liquid or gases. The scattered light contains the original wavelength due to Rayleigh scattering and wavelength components due to Raman scattering. Raman lines consists of Stokes and anti-Stokes lines [11]. A schematic representation of the Rayleigh, Stokes and anti-Stokes transitions are shown in Figure 2.3. According to quantum theory, the quantized vibrational energy of a molecule is given by Equation 2.3, where v is the vibrational quantum number having values 0,1,2 etc. and ν the frequency of vibration.

$$E_v = (v + \tfrac{1}{2})h\nu \qquad\qquad (2.3)$$

Raman spectroscopy probes the vibrational transitions in the compositions under study. Rayleigh scattering arises from the transitions which start and finish at the same vibrational energy level represented by frequency ν_o. Stokes Raman scattering arises from transitions which start at the ground state vibrational level and finish at a higher vibrational level denoted by ν_o-ν_v. The anti-Stokes Raman scattering involves a transition from a higher to a lower vibrational energy level denoted by ν_o+ν_v. Vibrations involving change in atomic polarizability α gives rise to Raman bands. At normal room temperature the population of the higher vibrational levels are low compared to the lower energy levels and hence the Stokes lines are more intense than anti-Stokes lines. Raman effect is a weak effect and only one in 10^7 photons are scattered inelastically. Weak signal strength and interference with fluorescence are two fundamental problems with Raman spectroscopy [11-14].

In the present study, Raman spectrum of the samples are recorded using Thermoscientific DXR Raman microscope. The powder sample is excited by diode-

pumped, solid state DPSS laser of wavelength 532 nm with maximum 10 mW power at sample. Raman spectrum plots the Raman intensity against Raman shift, usually represented in cm^{-1}. The Raman shift is expressed as the difference of wavenumbers of the Stokes Raman lines from the wavenumber corresponding to the wavelength of exciting radiation.

The total intensity of Stokes Raman band of frequency ν, scattered over a solid angle of 4π by randomly oriented N molecules perturbed by electromagnetic radiation from an initial vibronic state m to a final state n is given by Equation 2.4, where I_o is the incident intensity, α_{ij} represents the components of the polarisability tensor associated with the transition from state m to n, μ is the reduced mass of the oscillator and $\frac{\partial \alpha_{ij}}{\partial Q}$ represents the variation of the polarizability tensor with respect to the vibrational coordinate Q [12].
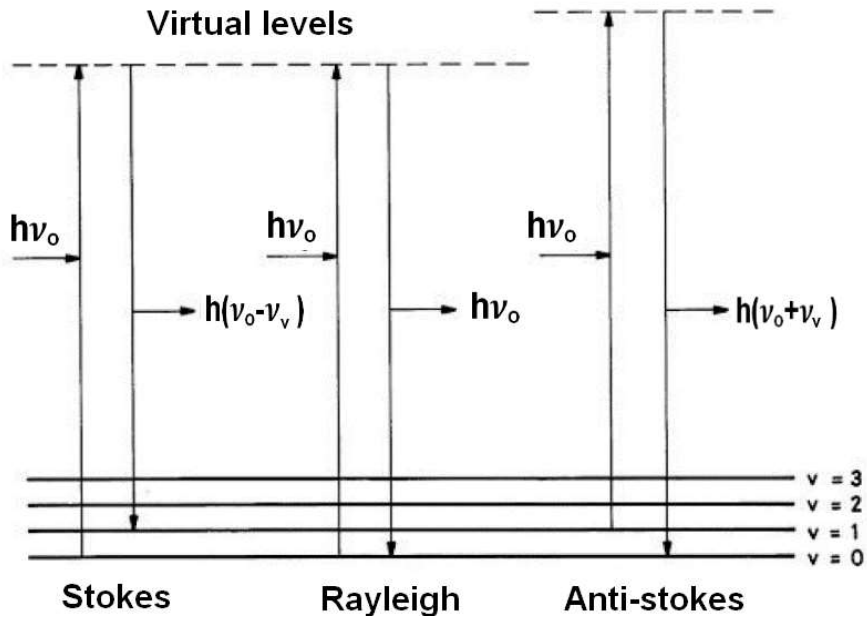
Figure 2.3 Schematic representation of Rayleigh, Stokes and Anti-Stokes Raman scattering [Ref. 12]

$$I_{mn} = \frac{2^4 \pi^3 \, hI_o N (\nu_o - \nu)^4}{3^2 C^4 \, \mu \nu (1 - e^{-\frac{h\nu}{kT}})} \, \Sigma_{ij} \left(\frac{\partial \alpha_{ij}}{\partial Q}\right)^2 \tag{2.4}$$

The Raman bands occur at wavenumbers characteristic of the symmetric and asymmetric stretching and bending modes of the molecular groups present in the unit cell structure of the compounds under study.

2.5 Scanning Electron Microscopy and Energy Dispersive X-ray Spectroscopy (SEM/EDS)

The scanning electron microscope (SEM) is a microscope that scans a focused beam of electrons across a bulk specimen to generate an image. The principle of detection includes the interaction of the high energy primary electron beam with the specimen surface by elastic and inelastic scattering events with the production of secondary electrons SE, backscattered electrons BSE, auger electrons AE, low loss electrons LLE and X-rays which are detected by specific detectors to create images and produce information about the properties of the specimen [15-17]. The interaction of the primary electron beam, the specimen and the energy spectrum of the electrons emitted are shown in Figure 2.4 a and 2.4 b respectively.

The interaction volume is a hemisphere with beam impact point as centre and the range of this volume taking into account the elastic and inelastic scattering processes is given by Kanaya-Okayama range, with A the atomic weight (g/mol), z the atomic number, ρ density in g/cm^3, E_o the incident beam energy in keV. Secondary electrons with low energy (< 50 eV) are liberated from the outer atomic shell of the specimen material by inelastic scattering. The tightly bound inner shell atomic electrons with binding energy of hundreds of thousands of eV are ejected and subsequently result in emission of characteristic X-rays. Backscattered electrons consisting of high energy electrons (>50 eV) are generated by elastic scattering in a much deeper range of the interaction volume and carry depth information [15-17].

$$R_{k-o} \text{ (nm)} = 27.6 \ (A/z^{0.89}\rho)E_o^{1.67} \tag{2.5}$$

In the present study, Carl Zeiss EVO18 SEM with energy dispersive X-ray spectrometer (EDS) attachment, model EDAX is used for the surface morphology studies and X-ray microanalysis of the samples. The sintered ceramic samples were coated with gold-palladium alloy in a Quorum sputter coater unit model SC7620, under conditions of 10 mA current, maintained at 10^{-2} mbar vacuum for 150 s. The SEM consists of plinth, a specimen chamber, electron optical column, monitor and control computer with software smartSEMv05.05. The instrumentation of a typical SEM electron optic column is shown in Figure 2.5.
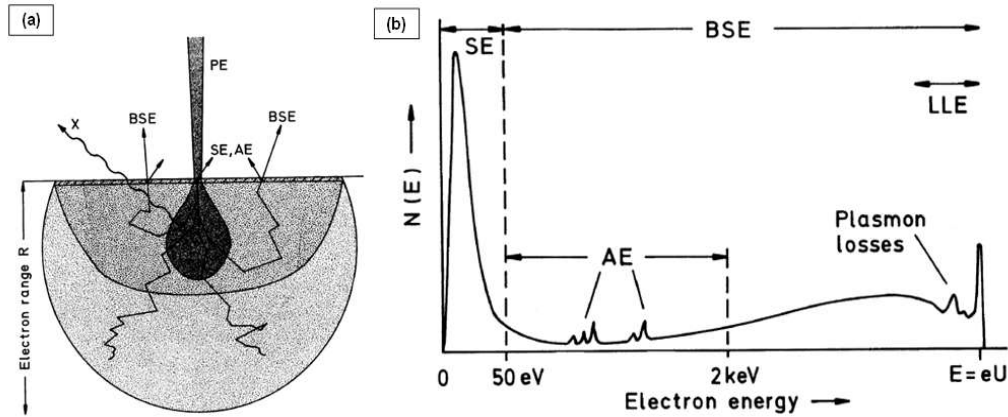
Figure 2.4 a) Interaction between primary electron beam and specimen and b) energy spectrum of electrons emitted [Ref. 17]

W or LaB6 filament is heated by applying suitable filament current and the emitted electrons are accelerated by the acceleration voltage U_{EHT} towards the specimen arranged in the specimen chamber. The electron optic column consists of objective and condenser lenses to properly deflect and focus the electron beam on to the specimen. High vacuum conditions of $<10^{-4}$ Pa are maintained to avoid the unwanted scattering of the beam electrons, SEs and BSEs by atoms and molecules of atmospheric gases [15]. The operating parameters chosen are acceleration voltage in the range 5 kV to 20 kV, with a working distance between 6 mm to 12 mm, which are optimized according to sample requirements. SE2 detector (Everhart-Thornley detector) detects secondary electron signals and backscattered electron detectors detect BSE signals [15].

BSE is an important SEM imaging signal rich in information on the specimen composition, topography, mass thickness and crystallography. The backscattered electron coefficient $\eta = N_{BSE}/N_B$, N_B the number of beam electrons that enter the specimen and N_{BSE} the number of electrons that subsequently emerge as backscattered electrons. The contrast C_{tr} is given by Equation 2.6, where η_1, η_2 are the backscattered coefficients of two materials. η value varies with the atomic number Z and is proportional to θ the specimen tilt or the local surface inclination [15-17]. Figure 2.6 shows the variation of backscattered electron coefficient with atomic number [15].

$$C_{tr} = (\eta_2 - \eta_1)/ \eta_2 \qquad (2.6)$$

The backscatter coefficient increases with increasing atomic number of the elements within the specimen and hence high atomic number regions appear brighter than the lower atomic number regions. Hence, the BSE detector can generate atomic

44

number contrast, or compositional contrast images which are extensively used in this work for determination of Ag/Al compatibility of samples. Thus the backscattered electron signals can be used to construct a meaningful grayscale SEM image and the compositional and topographic contrast of a sample can be studied [15-17].
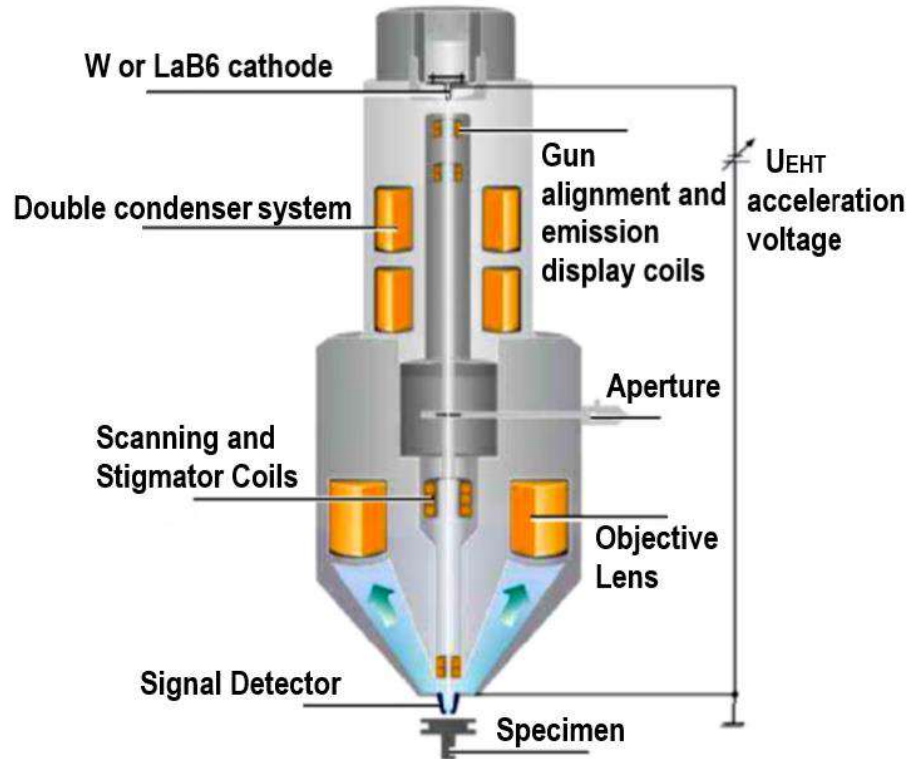
Figure 2.5 Schematic representation of a typical SEM electron optic column [Ref. 15]

The high energy electron beam interaction with specimen produces two types of X-ray photon emissions comprising of characteristic X-rays whose specific energies provide a fingerprint that is specific to each element and continuum X-rays which occur at all photon energies forming a background. Chemical composition identification and quantitative estimation can be done by analyzing the X-ray spectrum with the semiconductor energy dispersive X-ray spectrometer (EDS) that detects photons. The analytical software assigns the characteristic peaks recognised in the spectrum to specific elements. The EDS spectrum at each pixel is collected and after applying the quantitative analysis procedures, images are created for each element where the gray scale (or colour) level is assigned based on the measured concentration creating a compositional elemental mapping [15-17].
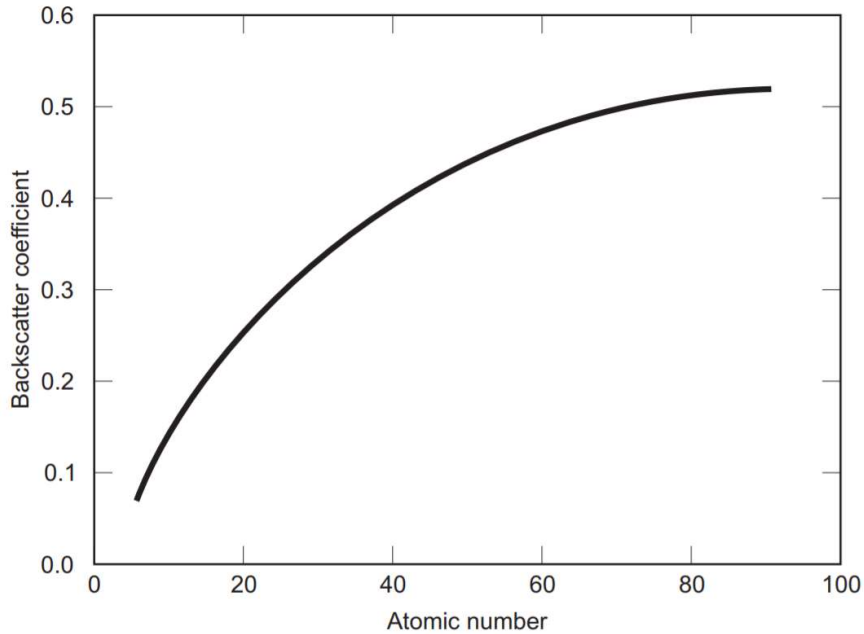
Figure 2.6 Variation of backscattered electron coefficient against atomic number

[Ref. 15]

2.6 Dielectric measurements

2.6.1 Dielectric characterization at low frequencies

The dielectric properties at low frequencies in the range 100 Hz to 13 MHz were measured using parallel plate capacitor method in a precision impedance analyzer, model HP4294A, Agilent, USA which is shown in Figure 2.7.

The dielectric samples were metallized on both sides using room temperature curable silver paste and copper leads are attached on both sides for connecting to the impedance analyzer. Standard capacitors from reputed manufacturers were used as secondary standards in addition to the auto calibration facility available in the impedance analyzer. The relative permittivity ε_r can be evaluated from the capacitance C of a parallel plate capacitor using Equation 2.7, where, d is the thickness and A the area of the sample.

$$\varepsilon_r = \frac{Cd}{A\varepsilon_0} \tag{2.7}$$

Figure 2.7 Precision impedance analyzer

The capacitance and loss tangent in a range of frequencies were noted and the relative permittivity values were calculated from the capacitance values. The temperature variation of ε_r was measured by inserting the sample attached with copper leads inside a hot air oven which can be connected to the impedance analyzer via external connecting leads. The temperature coefficient of dielectric constant was evaluated using the Equation 2.8.

$$\tau_{\varepsilon_r} = \frac{\varepsilon_{r_{100}} - \varepsilon_{r_{30}}}{\varepsilon_{r_{30}}(100-30)} \qquad (2.8)$$

2.6.2 Dielectric characterization at microwave frequencies

The relative permittivity, quality factor and temperature coefficient of resonant frequency were measured in the microwave frequency region using a Vector Network Analyzer, Agilent Technologies, USA model E8362B with measurement range 10 MHz to 20 GHz. In the present work, dielectric constant of the materials in the form of cylindrical dielectric resonators were determined by Hakki and Coleman (modified Courtney) method and quality factor by resonant cavity method.

2.6.2.1 Measurement of dielectric constant by Hakki and Coleman (modified Courtney) method

The microwave resonant frequency of the dielectric resonators were determined by Hakki and Coleman post resonator technique, modified by Courtney [18-23]. The schematic of the arrangement is shown in Figure 2.8.
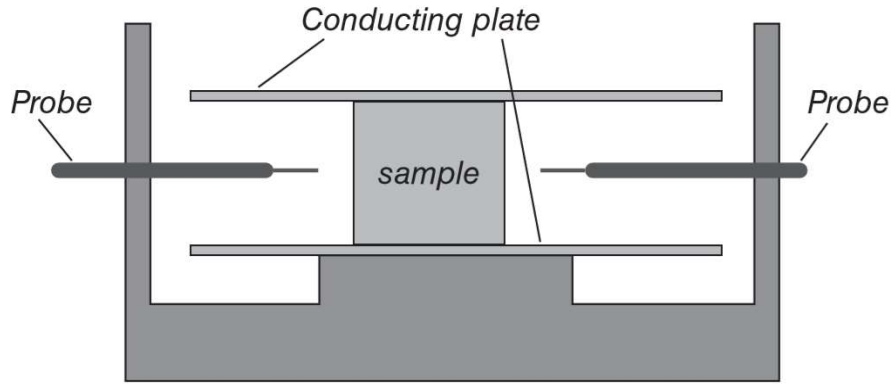
Figure 2.8 Schematic of the Hakki and Coleman (modified Courtney) setup used for measuring the dielectric constant under end shorted condition [Ref. 23]

The ceramics were made into cylindrical pucks of diameter D and length L. The dielectric resonator was inserted between two mathematically infinite conducting plates. The end plates were well-polished copper plates coated with silver or gold. The TE_{011} mode was chosen for study as this mode propagates inside the sample and is evanescent outside the dielectric resonator. TE_{011} mode has only the azimuthal component of the electric field with no electric field along the axial (z) direction. By tilting the top conducting plate, most of the modes except the transverse electric mode TE_{011} move to the right side. The D/L ratio of the dielectric resonator is maintained between 1.5 to 2 to get better mode separation to avoid interference of adjacent modes with that of TE_{011} mode. A typical TE_{011} resonance in a ceramic of $\varepsilon_r = 9.8$, under end shorted condition is shown in Figure 2.9.

For an isotropic dielectric material the characteristic equation for a dielectric resonator for the TE_{0ml} mode is given by Equation 2.9.

$$\alpha \frac{J_0(\alpha)}{J_1(\alpha)} = -\beta \frac{K_0(\beta)}{K_1(\beta)} \tag{2.9}$$

where $J_0(\alpha)$ and $J_1(\alpha)$ are the Bessel functions of first kind of order zero and one respectively and $K_0(\beta)$ and $K_1(\beta)$ are the modified Bessel functions of second kind

of order zero and one respectively. The parameters α and β are given by Equations 2.10 and 2.11 respectively.

$$\alpha = \frac{\pi D}{\lambda_0}\left[\varepsilon_r - \left(\frac{l\lambda_0}{2L}\right)^2\right]^{1/2}$$ (2.10)

$$\beta = \frac{\pi D}{\lambda_0}\left[\left(\frac{l\lambda_0}{2L}\right)^2 - 1\right]^{1/2}$$ (2.11)

where, l is the longitudinal variation of the field along the axis, L is the length and D is the diameter of the dielectric resonator, λ_0 is the free space resonant wavelength.

The real part of the dielectric constant is given by the Equation 2.12.

$$\varepsilon_r = 1 + \left[\frac{c}{\pi D f}\right]^2 \left(\alpha_1^2 + \beta_1^2\right)$$ (2.12)

Where α_1 and β_1 are the parameters obtained from the mode chart provided by Hakki and Coleman given in Figure 2.10. The mode chart shows the variation of α as a function of β with each value of β giving infinite number of α_n that solves the characteristic Equation [18,23].
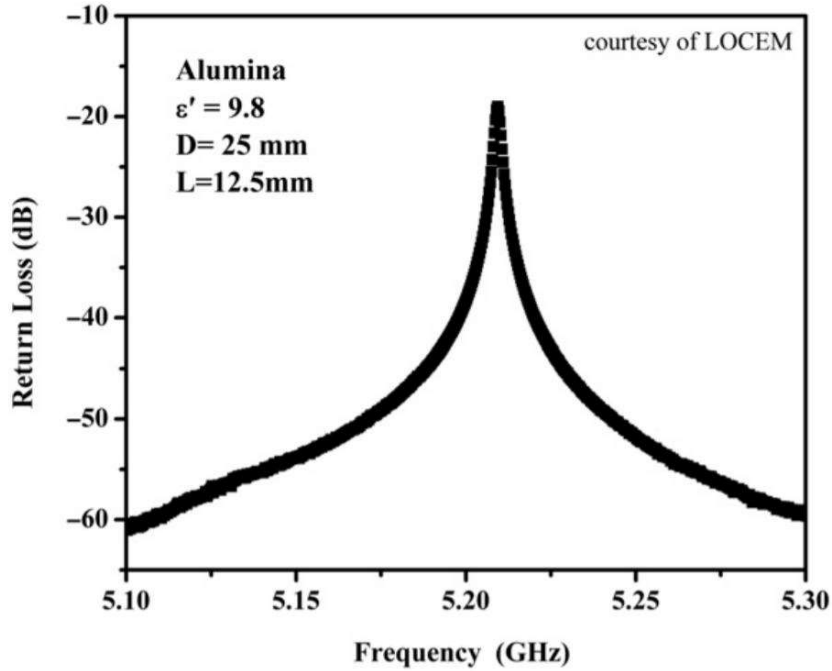
Figure 2.9 Frequency response of the TE$_{011}$ mode of a dielectric resonator with $\varepsilon_r =$ 9.8 under an end shorted condition [Ref. 23]
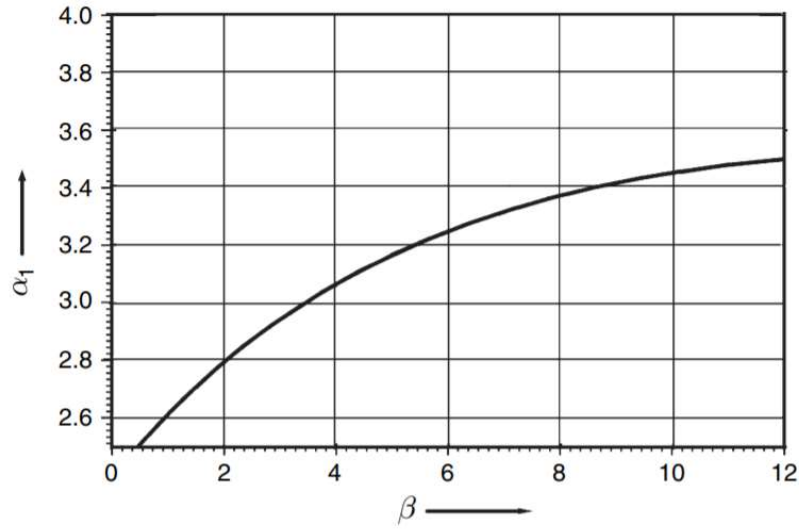
Figure 2.10 Hakki and Coleman Mode chart showing variation of α_1 with β

[Ref. 19,22]

2.6.2.2 Determination of temperature coefficient of resonant frequency

Temperature coefficient of resonant frequency is a very significant property that reflects the temperature stability of the dielectric properties. In order to measure the τ_f of the sample, the dielectric resonator was sandwiched between two hot plates in the Hakki and Coleman measurement configuration. The TE$_{011}$ mode frequency was tracked at regular temperature intervals of 10°C from room temperature to 100°C. The τ_f was calculated using the Equation 2.13, f_{30} and f_{100} are the resonant frequency values at 30°C and 100°C respectively.

$$\tau_f = \frac{f_{100} - f_{30}}{f_{30}\,(100 - 30)} \tag{2.13}$$

2.6.2.3 Measurement of quality factor by resonant cavity method

The quality factor was measured using the resonant cavity method (Krupka cavity), with minimal radiation and conduction losses compared to Hakki and Coleman method. A schematic of the cavity set up for Q-factor measurement is shown in Figure 2.11. The cavity is made up of copper with inner surfaces finely polished and coated with gold or silver. The dielectric resonator is placed inside the cavity on a low loss single crystal quartz or Teflon spacer to isolate the sample from the losses due to the finite resistivity of the metallic cavity. The cavity diameter is almost four times greater than that of the sample diameter to reduce the effect of cavity shielding. The cavity used for measurement is shown in Figure 2.12.

50
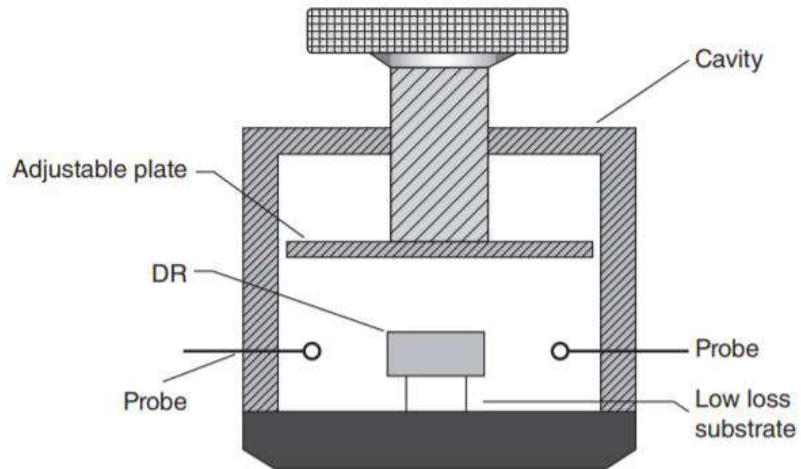
Figure 2.11 Schematic representation of cavity setup for Q-factor measurement

[Ref. 22,23]

Figure 2.12 Cavity setup for the measurement of Q-factor

The closed cavity excited by the applied microwave spectrum fed through loop coupling has infinite number of modes. The TE_{011} mode of the dielectric resonator introduced into the cavity is identified from the other modes present and is taken for measurements. In order to have better mode isolation, the cavity volume can be slightly changed by rotating the top screw and by moving the top plate up or down. The electric field is symmetric with the geometry of the sample and the cavity, and this reduces the sources of loss due to the cavity. A typical microwave response spectrum of $Ba(Mg_{1/3}Ta_{2/3})O_3$ ceramic in transmission configuration is shown in Figure 2.13.

The loaded quality factor Q, bandwidth and insertion loss are obtained from the measurement. The unloaded quality factor (Q_u) of the sample is calculated using the Equation 2.14, where, I_L is the insertion loss of the resonance spectrum. The inverse of the unloaded quality factor is approximately equal to the dielectric loss tangent [21-23].

$$Q_u = \frac{Q}{1-10^{(-I_L/20)}} \qquad (2.14)$$
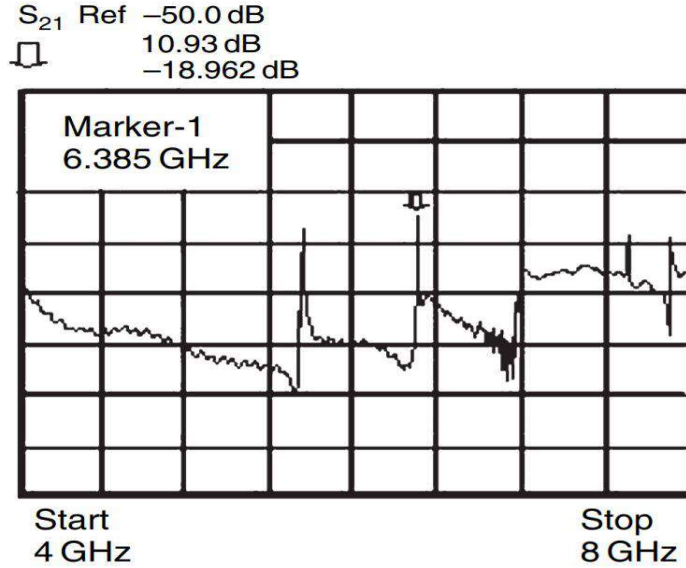
Figure 2.13 Microwave resonance spectrum of Ba(Mg$_{1/3}$Ta$_{2/3}$)O$_3$ ceramic (ε_r=24) in the transmission configuration [Ref. 22]

2.6.2.4 Microwave dielectric characterization of ceramic/polymer composites

The dielectric characterization of composite samples were measured using waveguide cavity perturbation technique using a X-band rectangular waveguide cavity shown in Figure 2.14. The X-band cavity is fabricated out of a standard WR-90 brass waveguide of nearly 13.5 cm length with a thin slot of 4 cm length and 1mm width. Thin samples in the form of strips of 2 mm width and around 0.8 mm thickness were used for the measurement. The conducting plate with an aperture of around 2 mm width on the either sides of the waveguide provides inductive coupling to the cavity. Utilizing the sweep frequency capacity of the analyzer, the standard X-band waveguide cavity has five resonant modes 8.4 GHz, 9.1 GHz, 9.8 GHz, 10.6 GHz and 11.5 GHz. Before the insertion of the sample to the cavity, the resonant frequency of the cavity f_c and the

quality factor Q_c was measured by connecting the cavity to a Vector Network Analyzer corresponding to the mode at 9.8 GHz. The sample was introduced at the position of maximum intensity of the electric field position (E-field antinode) in the rectangular cavity. This position was determined by slowly moving the sample across the slit and finding the position at which the mode that shift to the low frequency side start to retrace back to the higher frequency side [23]. The resonant frequency with sample inserted in the cavity f_s and the corresponding quality factor Q_s were measured.
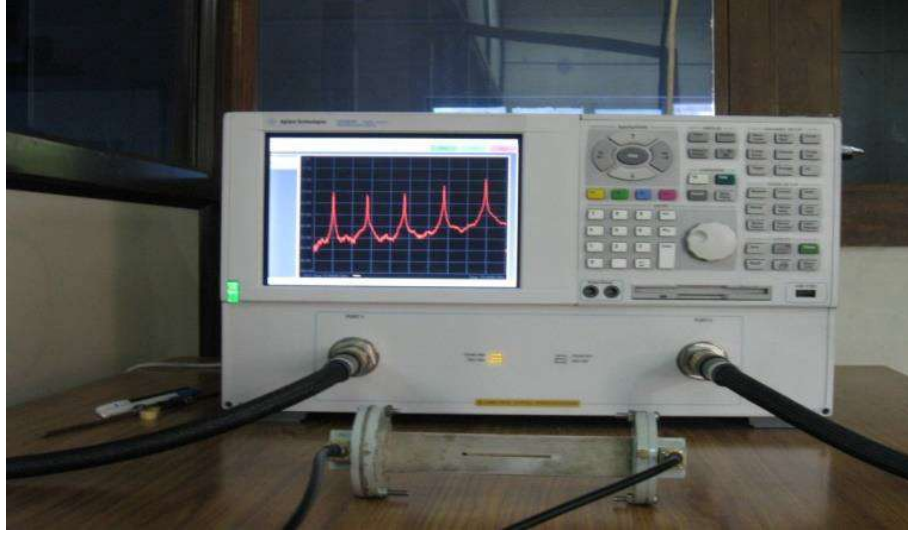
Figure 2.14 X-band waveguide cavity perturbation technique measurement set up

By assuming the dielectric material to be non-magnetic, the real and imaginary parts of the dielectric constant are given by the Equations 2.15 and 2.16.

$$\varepsilon_r' = \left[\frac{f_c - f_s}{2f_s}\right]\frac{V_c}{V_s} + 1 \tag{2.15}$$

$$\varepsilon_r'' = \left[\frac{V_c}{4V_s}\right]\left[\frac{1}{Q_s} - \frac{1}{Q_c}\right] \tag{2.16}$$

Where V_c and V_s are the cavity and sample volumes, Q_c and Q_s are the quality factors of the cavity with and without the sample respectively. Q_u is the theoretical quality factor and called as unloaded quality factor. According to conventional cavity perturbation theory, the presence of the sample in the metal cavity would decrease the quality factor of the cavity due to the dielectric loss of the sample. The loss tangent of the sample is calculated using the Equation 2.17 [22,23].

$$\tan\delta = \frac{1}{Q_d} = \frac{\varepsilon''}{\varepsilon'} \tag{2.17}$$

2.7 Thermogravimetry and Differential Thermal Analyses (TG/DTA)

Thermogravimetric analysis is a technique by which the changes in the physical and chemical properties of materials are measured as a function of increasing temperature with constant heating rate. The thermal behaviour of the powder samples are analysed by detecting the mass change of the material on heating [24-26]. The TG/DTA measurements are carried out by high performance simultaneous TGA & DTA equipment with dual beam technology from setsys evolution par setaram. A schematic representation of the TG/DTA equipment is shown in Figure 2.15 [24]. The mass of the sample in milligram (mg) is measured as a function of temperature ramp and is represented by the TG curve. The derivative of the TG curve in μg/min represents the rate of decomposition reaction and is referred to as the DTG curve. The DTA curve in μV represents the heat flow. The TG/DTA curves together depict the thermal behaviour of the ceramics.

When a weight change occurs on the sample side, the beam is displaced and this movement is detected optically and the drive coil current is changed to return the displacement to zero position. The detected drive coil current change is proportional to the sample weight change and is output as the TG signal. The DTA detects the temperature difference between the sample holder and the reference holder using electromotive force of thermocouple, which are attached to the holder. The differential is output as the DTA signal [24-26]. The powder sample is taken in stoichiometric proportions and mixed thoroughly. A definite amount of initial mass is taken and the TGA curves are recorded with a temperature ramp from room temperature to the required temperature at a rate of 10°C/min in air atmosphere. The DTG curve of the sample shows peaks at temperatures corresponding to mass loss. Endotherms are observed in the DTA curves at corresponding temperatures. Total mass loss is obtained from the difference in initial mass and the mass of the final residue. The mass loss can be due to desorption or drying, the release of CO_2, removal of volatile components and the intermediate reaction products. The temperature of complete phase formation can be inferred very clearly from the TGA curves and the calcination temperatures can be chosen appropriately.
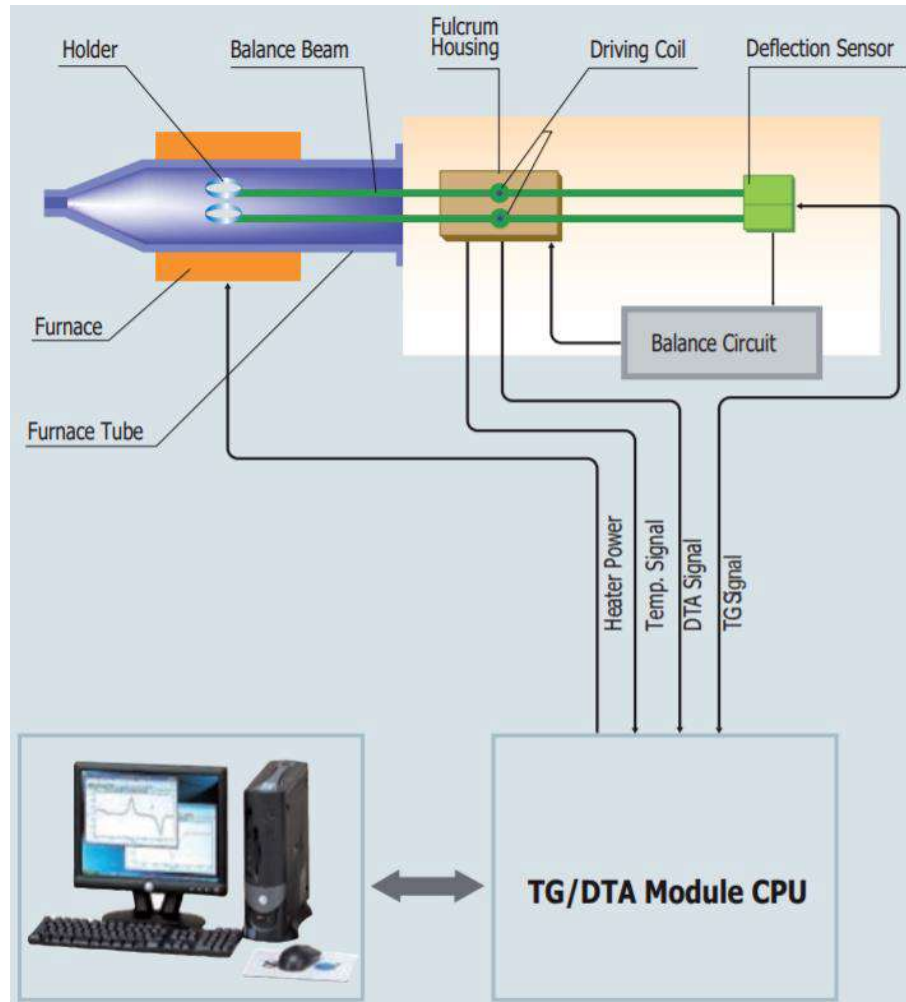
Figure 2.15 Schematic representation of a typical TG/DTA equipment [Ref. 24]

2.8 ThermoMechanical Analyzer (TMA)

Thermomechanical analyzer measures the changes in length and volume of a sample as a function of temperature. TMA is used for the measurement of coefficients of thermal expansion, thermal shrinkage as a function of temperature, glass transition temperature etc. TMA measures material deformation under controlled conditions of load, sample length, atmosphere, time and temperature. Coefficient of thermal expansion CTE is an intrinsic material property showing the expansion and shrinkage characteristic during thermal excursion. Coefficient of thermal expansion (CTE) is calculated using the Equation 2.18, where (L_{final} - $L_{initial}$) is the change in thickness in μm, $L_{initial}$ the initial thickness of the sample in μm and (T_{final} - $T_{initial}$) the change in temperature [27-30].

$$CTE = \frac{(L_{final} - L_{initial})}{L_{initial}(T_{final} - T_{initial})}$$ (2.18)

The shrinkage behaviour of the ceramic is a significant parameter for the fabrication of LTCC and ULTCC tapes. Most of the sintered ceramics and ceramic/polymer composites exhibit thermal expansion. CTE of the LTCC and ULTCC substrates must match with the CTE of the silicon based electronic components which are mounted on them. Most of the sintered ceramic samples show low CTE value (less than +10 ppm/^{o}C) and the CTE of the polymer ceramic composites is determined by the themal behaviour of the polymer as well as the ceramic filler.

In the present study TMA measurements were done using high performance thermal analyzer Model EXSTAR 6000 manufactured by SII Nano Technology INC., Japan. The TMA consists of a furnace with a thermocouple that could accurately measure the temperature of the sample and the sample holder, along with a linear variable differential transformer (LVDT) to convert the mechanical displacements into electrical signals. A schematic representation of the TMA equipment is shown in Figure 2.16. The working temperature is from -150 to 600°C. The sample cylinder and the TMA probe are made of quartz which has a very low CTE. The TMA measurement range is ±5 mm and sensitivity is 0.02 μm, which enables accurate measurements of sample displacement with very high resolution. The sample is placed on a quartz glass probe which is connected to a position sensor. Expansion or contraction of the sample on heating moves the probe and these small variations in the thickness of the sample with temperature is accurately detected and converted into electrical signals by the linear variable differential transformer (LVDT) [27].

For shrinkage measurements, green pellets of the ceramic with 7 mm diameter are loaded in the TMA. The initial thickness of the sample is noted at the beginning of the experiment. Temperature is varied from room temperature to the required value at the rate of 10°C/min and the change in length (in μm) is measured at regular intervals. The temperature at which the sample exhibits maximum shrinkage can be chosen as the most appropriate temperature for sintering of green tapes.
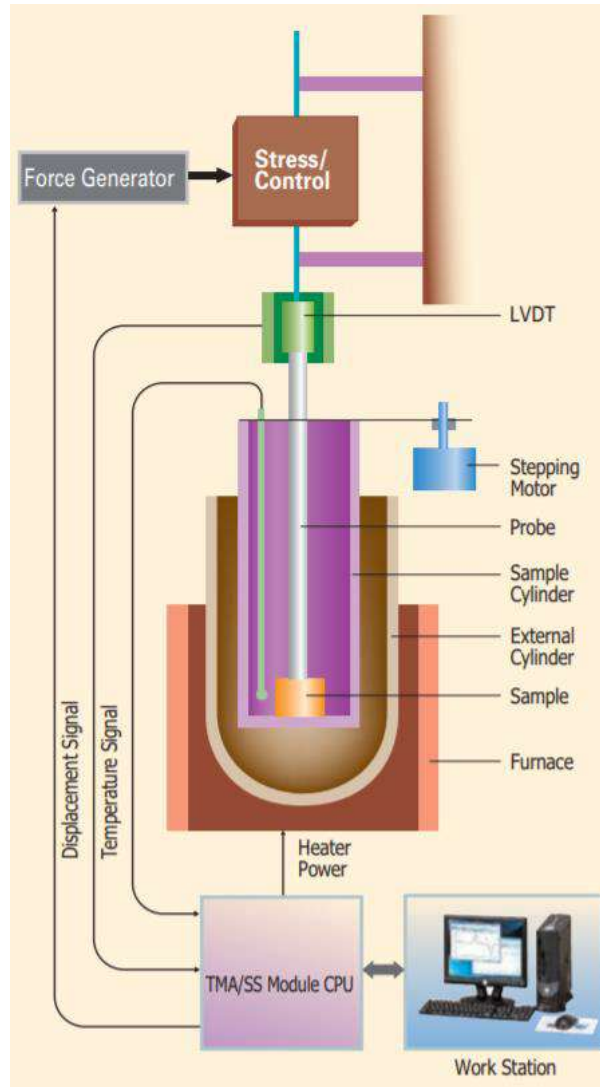
Figure 2.16 Schematic representation of TMA instrument [Ref. 27]

CTE measurements utilize sintered pellets (7 mm diameter, 1-5 mm thickness) and ceramic/polymer composite samples (8 mm length, 1-1.5 mm thickness) are used. The initial thickness of the sample is noted at the beginning of the experiment. Temperature is varied from room temperature to the required value at the rate of 10°C/min and the change in length (in μm) is measured at regular intervals and the CTE is calculated.

2.9 Ultimate tensile strength measurement

The Ultimate tensile strength is the maximum stress that a material can withstand before breaking when it is stretched or pulled by a force. The mechanical strength of the polymer/ceramic composites at different filler loadings were measured using a Universal Testing Machine (UTM, Shimadzu-1000G). The equipment consists

of a testing frame that provides the motion control for force measuring, control and analysis software to input the operating parameters, display unit to show the measured results, load cell to measure force and extensometer to measure deformation. The composite samples are held firmly between the grips and extensometer for measurements maintaining constant effective initial length for all the samples. The measurement was carried out at a constant load of 500 N at room temperature. The lower end of the sample is fixed whereas the upper end is pulled upward at an appropriate drawing speed. The sample undergoes elongation and breaks beyond the peak value of load. The measurement is stopped on sample breakage and the peak load is noted. The area of cross-section of the composite sample at the region of breakage is calculated from the measured values of width and thickness of the sample. The ultimate tensile strength of the material is calculated by dividing the peak load (in N) by the area of cross-section (in mm^2), which is usually expressed in MPa.

In the present study, the error bars are incorporated in the measurement results to understand how the results are spread around the mean value based on the resolution/accuracy of the various characterization techniques used. Repeated measurements carried out using each test procedure and average values obtained are found to be well within the permissible limit of the respective methodology adopted and the same are reported in the thesis.

References

[1] W. D. Kingery, H. K. Bowen, D. R. Uhlmann, *Introduction to Ceramics,* NY, John Wiley & Sons (1976).

[2] S. J. L. Kang, *Sintering: densification, grain growth and microstructure*, Elsevier (2004).

[3] D. Segal, *Chemical synthesis of advanced ceramic materials* (Vol. 1), Cambridge University Press (1991).

[4] M. N. Rahaman, *Sintering of ceramics*, CRC press (2007).

[5] R. Jenkins, R. L. Snyder, *Introduction to X-ray Powder Diffractometry* (Vol. 138), NY, John Wiley & Sons (1996).

[6] B. D. Cullity, S. R. Stock, *Elements of X-ray Diffraction*, Pearson Education (2014).

[7] R. Guinebretière, *X-ray diffraction by polycrystalline materials*, John Wiley & Sons (2013).

[8] R. E. Dinnebier, S. J. L. Billinge, *Powder Diffraction: Theory and Practice*, Royal Society of Chemistry (2008).

[9] M. Lee, *X-Ray Diffraction for Materials Research: From Fundamentals to Applications*, CRC Press (2016).

[10] C. Suryanarayana, M. G. Norton, *X-ray diffraction: a practical approach*, Springer (1998).

[11] E. Smith, G. Dent, *Modern Raman spectroscopy: a practical approach*, John Wiley & Sons (2013).

[12] D. J. Gardiner, P. R. Graves, *Practical Raman Spectroscopy*, Springer-Verlag (1989).

[13] D. A. Long, D. A. Long, *Raman spectroscopy* (Vol. 276), New York: McGraw-Hill (1977).

[14] J. R. Ferraro, *Introductory Raman spectroscopy*, Elsevier (2003).

[15] Instruction manual of Carl Zeiss EVO18 SEM.

(www.scribd.com/document/364248527/Instruction-Manual-EVO)

[16] J. I. Goldstein, D. E. Newbury, J. R. Michael, N. W. Ritchie, J. H. J. Scott, D. C. Joy, *Scanning electron microscopy and X-ray microanalysis*, Springer (2017).

[17] L. Reimer, *Scanning electron microscopy: physics of image formation and microanalysis* (Vol. 45), Springer (2013).

[18] D. Kajfez, Q-factor measurement with a scalar network analyser, IEE Proc. Microw Antennas Propag., 142 [5] (1995) 369-372.

[19] B. W. Hakki, P. D. Coleman, A dielectric resonator method of measuring inductive capacities in the millimeter range, IRE Trans. Microwave Theory Tech., 8 [4] (1960) 402-410.

[20] W. E. Courtney, Analysis and evaluation of a method of measuring the complex permittivity and permeability microwave insulators, IEEE Trans. Microw. Theory Tech., 18 [8] (1970) 476-485.

[21] J. Krupka, K. Derzakowski, B. Riddle, J. B. Jarvis, A dielectric resonator for measurements of complex permittivity of low loss dielectric materials as a function of temperature, Meas. Sci. Technol., 9 [10] 1751-1756.

[22] M. T. Sebastian, *Dielectric materials for wireless communication*, Elsevier (2008).

[23]   M. T. Sebastian, H. Jantunen, High Temperature Cofired Ceramic (HTCC), Low Temperature Cofired Ceramic (LTCC), and Ultralow Temperature Cofired Ceramic (ULTCC) Materials, *Microwave Materials and Applications,* 2V Set, (2017) 355-425.

[24]   Instruction manual of TG/DTA instrument SII Nano Technology INC., Japan.

(www.masterlabsrl.it/wp-content/uploads/2012/11/Exstar-series.pdf)

[25]   P. J. Haines, *Thermal methods of analysis: principles, applications and problems*, Springer Science & Business Media (2012).

[26]   M. E. Brown, Differential thermal analysis (DTA) and differential scanning calorimetry (DSC). In: *Introduction to Thermal Analysis*, Springer, Dordrecht (1988).

[27]   Instruction manual of Model EXSTAR 6000 manufactured by SII Nano Technology INC., Japan.

(www.masterlabsrl.it/wpcontent/uploads/2012/11/Exstar-series.pdf)

[28]   E. G. Wolff, *Introduction to the dimensional stability of composite materials*. DEStech Publications, Inc (2004).

[29]   S. Z. Cheng, (Ed.) *Handbook of thermal analysis and calorimetry: applications to polymers and plastics* (Vol. 3), Elsevier (2002).

[30]   Y. C. Lee, B. A. Parviz, J. A. Chiou, S. Chen, Packaging for microelectromechanical and nanoelectromechanical systems, IEEE Trans. Adv. Packag., 26 [3] (2003) 217-226.

Chapter 3

Crystal structure and microwave dielectric properties of ultra low temperature co-firable double sodium-lanthanide tetramolybdate $Na_5R(MoO_4)_4$ (R = La, Pr, Nd, Sm, Y and Yb) ceramics

3.1 Introduction

3.2 Materials and methods

3.3 Results and discussion

3.4 Conclusions

Some of the contents of this chapter have been published in

3.1 Introduction

Sodium molybdate based compositions are widely reported as ULTCC and LTCC materials [1-5]. Sodium molybdate - rare earth molybdate phase diagrams consist of $NaR(MoO_4)_2$ and $Na_5R(MoO_4)_4$ type compositions which are formed by rare earth elements from La-Lu and Y. In addition to these compositions, another composition with structure type $NaR_5(MoO_4)_8$ is reported for rare earth elements from La to Eu [6-10]. Interestingly, the crystal structure of all the three phases are related to the scheelite structure of $CaWO_4$. $NaR(MoO_4)_2$ compositions exhibit pure scheelite structure whereas $Na_5R(MoO_4)_4$ compositions exhibit modulated scheelite-like structure and that of $NaR_5(MoO_4)_8$ type compositions are reported to have incommensurately modulated scheelite structure [11-14]. Klevtsova et al. have compared the atomic arrangements in the crystal structure of scheelite $CaWO_4$ with that of the scheelite-like structure of $Na_5Lu(WO_4)_4$, which are isostructural to the compositions under study. Scheelite like structured $Na_5Lu(WO_4)_4$ belongs to tetragonal structure with space group $I4_1/a$ having 4 number of formula unit cells per unit cell. Both the structures contain the same number of cations. The Ca atoms in $CaWO_4$ structure are substituted by Na and Lu atoms in the $Na_5Lu(WO_4)_4$ structure [13].

Rybakova et al. has reported the phase diagrams of sodium molybdate - rare earth molybdate systems [7]. Mokhosoev et al. has reported the synthesis of $Na_5R(MoO_4)_4$ (R = La-Lu) by solid-state ceramic route and correlated the lattice parameters with ionic radii [8,9]. Though the series is reported to be isostructural with identical structural units, the bond lengths and molecular arrangements are varied with respect to the rare earth ions, which are attributed to the electronegativity differences in the trivalent cations in these compositions [10-12].

In the present study double sodium-lanthanide tetramolybdate $Na_5R(MoO_4)_4$ ceramics are prepared and studied their structure-property correlation to establish their suitability for LTCC and ULTCC applications. Stedman et al. has reported the detailed crystal structure of $Na_5Y(MoO_4)_4$ and compared it with that of the scheelite structure of $NaY(MoO_4)_2$ [14]. The unit cell of $Na_5Y(MoO_4)_4$ is given in Figure 3.1 which consists of Mo atoms occupying the Wyckoff position 16(f) with approximately regular tetrahedral coordination with Mo-O bond lengths varying from 1.741 Å to 1.796 Å. The unit cell contains two types of Na atoms of which one forms a regular NaO_4 tetrahedron and the other forms a highly irregular NaO_6 octahedron. The crystal structure also

contains yttrium atoms occupying Wyckoff position 4(a) forming a slightly distorted YO_8 dodecahedron with two Y-O bond lengths 2.362 Å and 2.366 Å [14]. $NaY(MoO_4)_2$ consists of regular average Mo-O bond length of 1.733 Å and Y-O bond length of 2.511 Å.
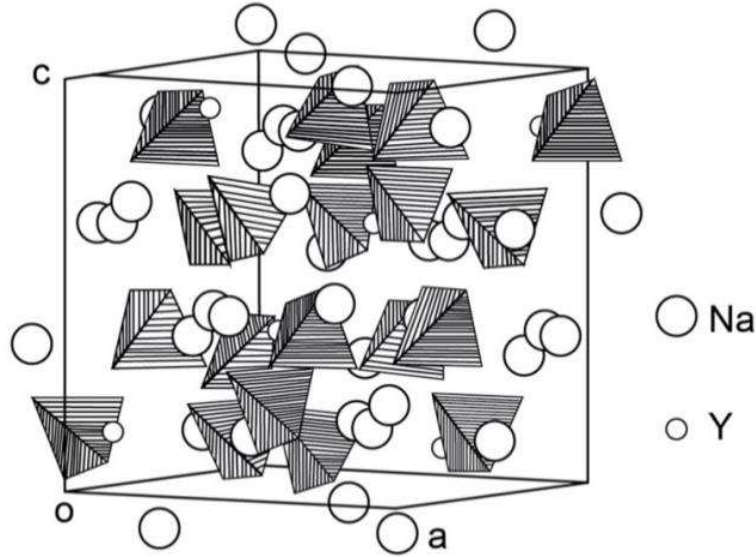
Figure 3.1 Crystal structure of $Na_5Y(MoO_4)_4$ [Ref. 14]

In the present work, $Na_5La(MoO_4)_4$, $Na_5Pr(MoO_4)_4$, $Na_5Nd(MoO_4)_4$, $Na_5Sm(MoO_4)_4$, $Na_5Y(MoO_4)_4$ and $Na_5Yb(MoO_4)_4$ ceramics have been prepared by solid-state ceramic route. The detailed crystal structure of these compositions are studied using powder X-ray diffraction and laser Raman spectroscopic techniques. The microwave dielectric properties and chemical compatibility of the compositions with aluminium metal electrode are also investigated using XRD and energy dispersive X-ray spectroscopy with a view to use them for ultra low temperature co-firable applications.

3.2 Materials and methods

$Na_5R(MoO_4)_4$ (R = La, Pr, Nd, Sm, Y and Yb) ceramics were prepared by the conventional solid-state ceramic route. The starting materials used were Na_2CO_3 (99.9%, Merck), La_2O_3 (99.9%, Sigma Aldrich), Pr_6O_{11} (99.9%, Aldrich), Nd_2O_3 (99.9%, Aldrich), Sm_2O_3 (99.9%, Sigma Aldrich), Y_2O_3 (99.9%, Star Rare Earth), Yb_2O_3 (99.9%, Treibacher) and MoO_3 (99%, Himedia). Stoichiometric proportions of these chemicals were accurately weighed and thoroughly mixed in an agate mortar using double distilled water as the mixing medium. The resultant slurry was dried inside

a hot air oven at 100°C and ground well. These powders were calcined at 500°C for an hour in a programmable SiC furnace. The calcined powders were ground well again into fine powder and 5 wt% of polyvinyl alcohol (PVA) solution was added to it as binder and then dried. The granulated powders were uniaxially pressed into cylindrical compacts using a 11 mm diameter tungsten carbide die under a pressure of 250 MPa in a hydraulic hand press and sintered at various temperatures in the range 510-610°C for one hour. The bulk density values of the sintered samples were determined accurately using dimensional methods. Powder X-ray diffraction (XRD) measurements of the samples were carried out with CuKα radiation using a Brucker Model 5005 X-ray diffractometer, Germany. The Raman spectra of the compositions under study were recorded using a Thermo Scientific DXR with Nd:YVO$_4$ DPSS laser of 532 nm. The surface morphology of the sintered samples were studied using a scanning electron microscope (Carl Zeiss, Model No: EVO18 Research, Germany). The energy dispersive X-ray spectroscopy (EDS) technique was used for analysing the chemical compatibility of the ceramic samples with aluminium metal electrode. A Vector Network Analyzer (Agilent make PNA E8362B, Bayan Lepas, Malaysia) was used to measure the microwave dielectric properties of the well sintered ceramics. The dielectric constant values of the samples were measured by Hakki and Coleman post resonator technique [15] and the quality factor by resonant cavity method [16]. The temperature coefficient of resonant frequency τ_f of the ceramics was determined from the TE$_{01\delta}$ mode frequency variation with temperature in the range 30-100°C.

3.3 Results and discussion

3.3.1 Powder X-ray diffraction studies

The X-ray diffraction patterns of Na$_5$R(MoO$_4$)$_4$ (R = La, Pr, Nd, Sm, Y and Yb) ceramics sintered at optimum temperatures are given in Figure 3.2 a-f. The compositions of structure type Na$_5$R(MoO$_4$)$_4$ are reported to be isostructural for all rare earth ions and yttrium. Na$_5$R(MoO$_4$)$_4$ ceramics crystallize in the tetragonal structure with space group I4$_1$/a having four molecules in crystallographical unit cell (Z= 4) [14]. The X-ray diffraction patterns of Na$_5$R(MoO$_4$)$_4$ (R = La, Pr, Nd, Sm, Y and Yb) compositions are indexed according to the standard ICDD files 72-2158, 61-0723, 55-0689, 23-0697, 82-2368 and 56-1487 corresponding to Na$_5$La(MoO$_4$)$_4$, Na$_5$Pr(MoO$_4$)$_4$, Na$_5$Nd(MoO$_4$)$_4$, Na$_5$Sm(MoO$_4$)$_4$, Na$_5$Y(MoO$_4$)$_4$ and Na$_5$Yb(MoO$_4$)$_4$ respectively.

The lattice parameters and the unit cell volume of $Na_5R(MoO_4)_4$ (R = La, Pr, Nd, Sm, Y and Yb) compositions are calculated using the equations 3.1 and 3.2 respectively.

$$\frac{1}{d_{hkl}^2} = \frac{h^2+k^2}{a^2} + \frac{l^2}{c^2}$$

(3.1)

$$V = a^2c$$

(3.2)

The calculated lattice parameters are comparable with that of the reported values and are given in Table 3.1. Figure 3.3 shows the variation of lattice parameters a, c and unit cell volume V as a function of ionic radii of the eight coordinated R^{3+} ions [17].
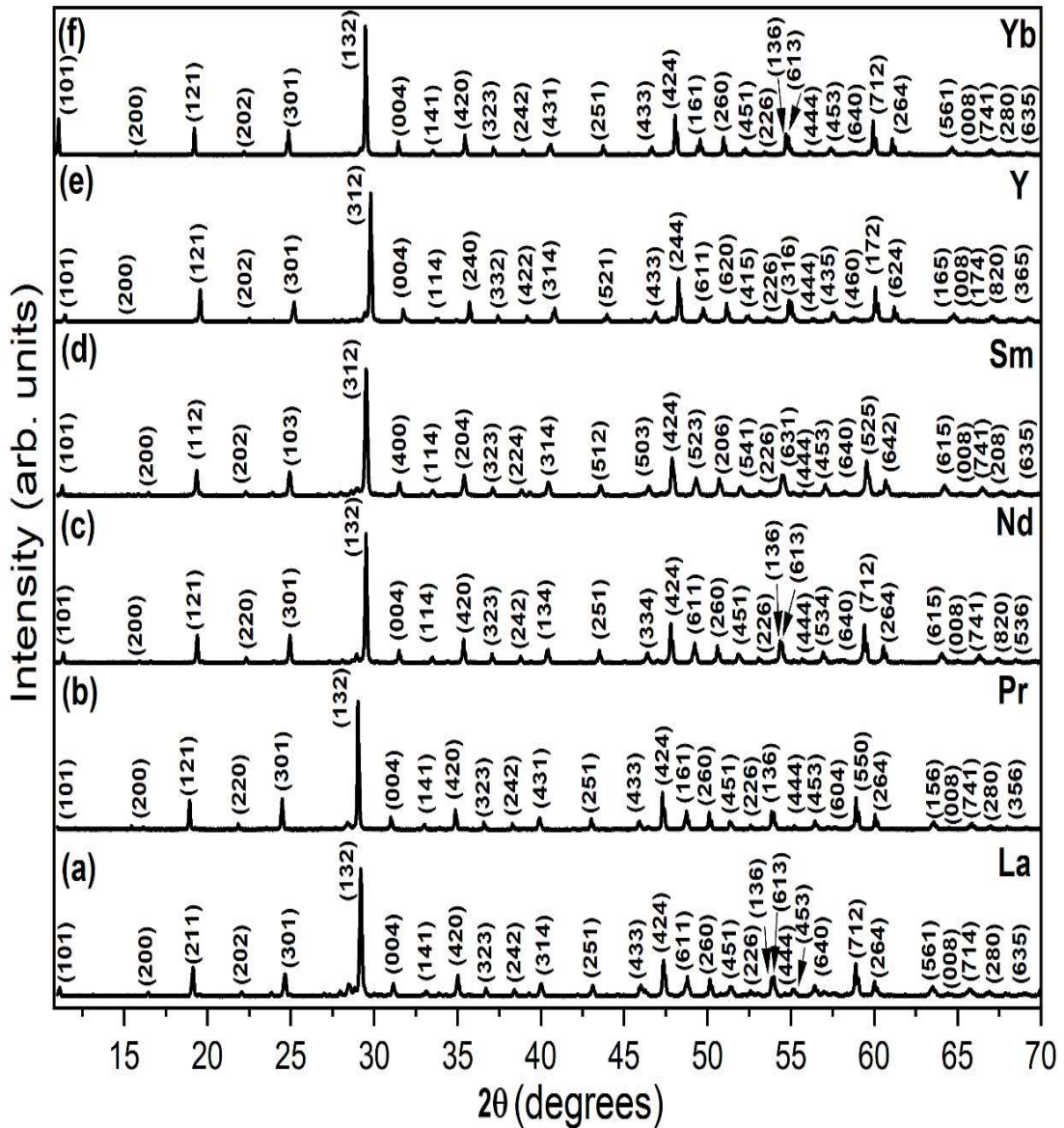
Figure 3.2 XRD patterns of $Na_5R(MoO_4)_4$ (R = La, Pr, Nd, Sm, Y and Yb) sintered ceramics

Table 3.1 Comparison of calculated and reported lattice parameters of $Na_5R(MoO_4)_4$
(R = La, Pr, Nd, Sm,Y and Yb) ceramics

R^{3+} ions	Crystal structure	Z	Calculated lattice parameters (Å)		Reported lattice parameters (Å)		Unit cell volume (Å)^3	ICDD card nos
			a	*c*	*a*	*c*		
La	Tetragonal	4	11.54	11.61	11.57	11.62	1546.12	72-2158
Pr	Tetragonal	4	11.52	11.55	11.52	11.56	1532.8	61-0723
Nd	Tetragonal	4	11.50	11.53	11.50	11.54	1522.84	55-0689
Sm	Tetragonal	4	11.49	11.46	11.51	11.46	1512.95	23-0697
Y	Tetragonal	4	11.37	11.43	11.37	11.44	1477.63	82-2368
Yb	Tetragonal	4	11.32	11.39	11.34	11.40	1459.54	56-1487
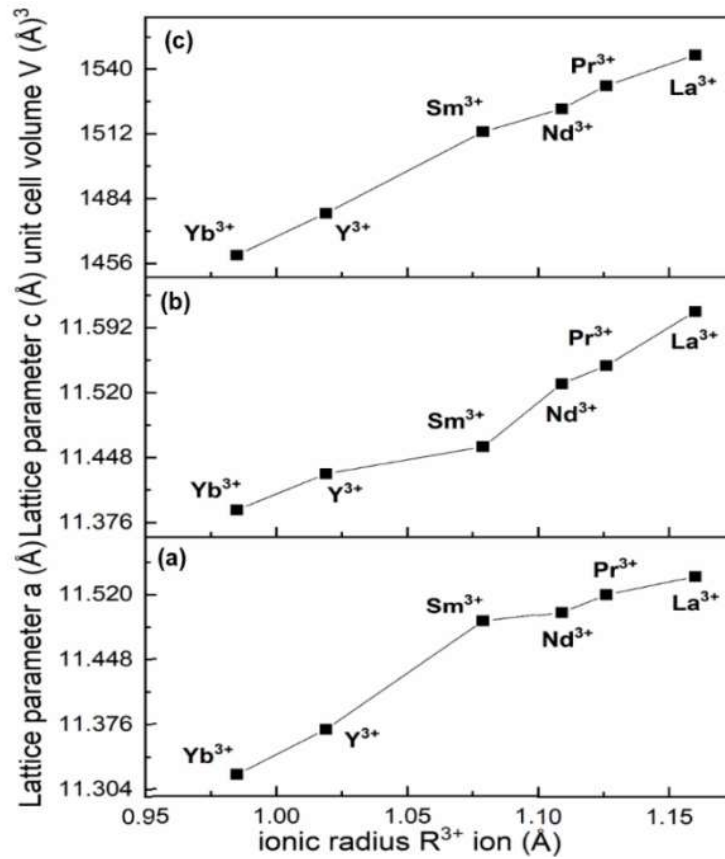
Figure 3.3 (a) Lattice parameter a; (b) Lattice parameter c and (c) unit cell volume of $Na_5R(MoO_4)_4$ (R = La, Pr, Nd, Sm, Y and Yb) ceramics as a function of ionic radii of R^{3+} ions

3.3.2 Raman spectroscopic studies

The crystal structure of $Na_5R(MoO_4)_4$ (R = La, Pr, Nd, Sm, Y and Yb) ceramics are investigated in detail using laser Raman spectroscopic studies. The Raman spectra of $Na_5R(MoO_4)_4$ ceramics are shown in Figure 3.4 a-f and the band assignments are given in Table 3.2. The Raman bands occur at similar wavenumbers for all the ceramics under study and this is a conclusive evidence for the identical molecular arrangements in the structure of these compositions. The Raman spectra exhibit bands corresponding to the internal vibrations of $(MoO_4)^{2-}$ tetrahedra. The four fundamental modes of vibration of $(MoO_4)^{2-}$ tetrahedra include a non-degenerate symmetric stretching mode at 894 cm^{-1}, a doubly degenerate symmetric bending mode at 318 cm^{-1}, triply degenerate asymmetric stretching and asymmetric bending modes at 833 and 381 cm^{-1}, respectively [18-21].
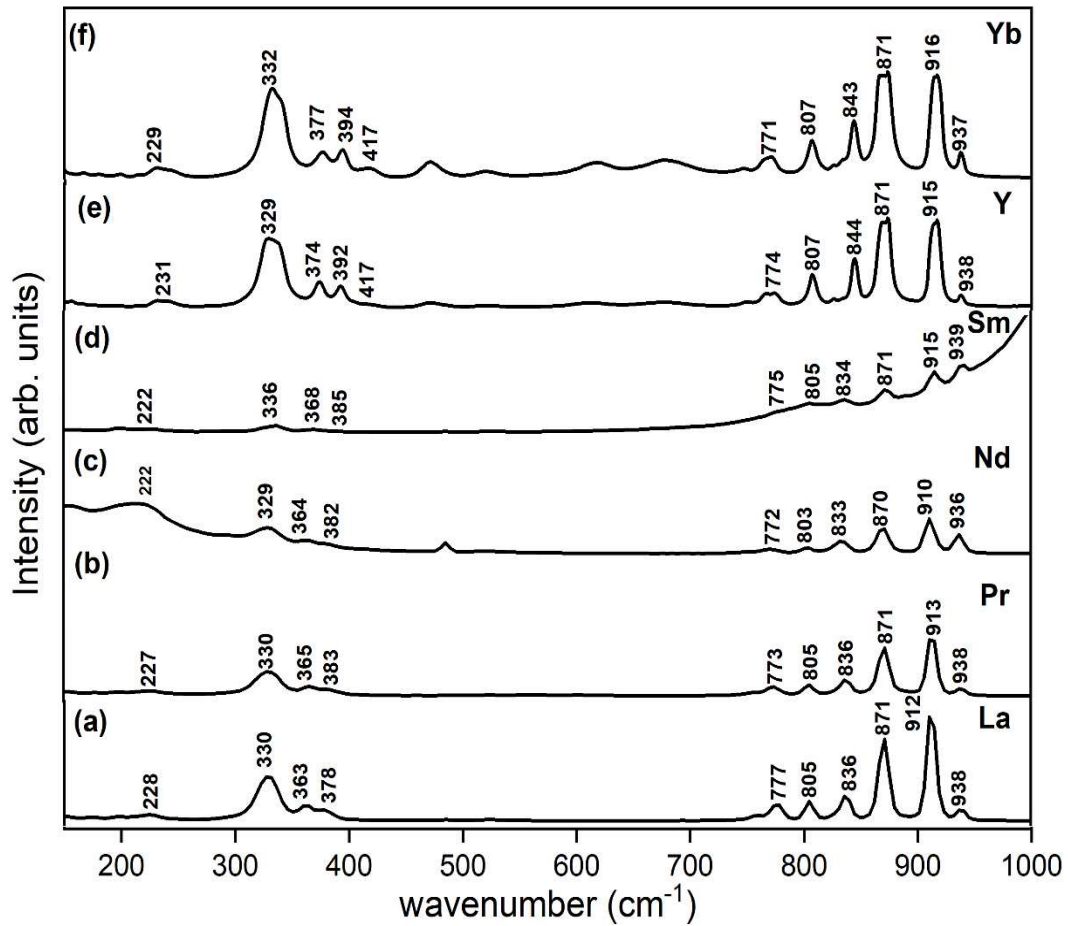
Figure 3.4 Raman spectra of $Na_5R(MoO_4)_4$ (R = La, Pr, Nd, Sm, Y and Yb) sintered ceramics

Table 3.2 Raman mode assignments of $Na_5R(MoO_4)_4$ (R = La, Pr, Nd, Sm, Y and Yb) ceramics

La (cm)$^{-1}$	Pr (cm)$^{-1}$	Nd (cm)$^{-1}$	Sm (cm)$^{-1}$	Y (cm)$^{-1}$	Yb (cm)$^{-1}$	Assignments[*1,2]
938 vw	938 vw	936 w	939 vw	938 w	937 w	
912 vs	913 s	910 s	915 m	915 vs	916 vs	$\nu_s(MoO_4)^{2-}$
871 vs	871 s	870 mbr	871wbr	871vs br	871 vs br	
836 mbr	836 mbr	833 w	834 vw	844 m	843 m	
805 m	805 w	803 vw	805 vw	807 m	807 m	$\nu_{as}(MoO_4)^{2-}$
777 wbr	773 wbr	772 vw	775 vw	774 wbr	771 wbr	
378 vw	383 vw	382 vw	385 vw	417 vw	417 w	
363 w	365 w	364 vw	368 vw	392 m	394m	$\delta_{as}(MoO_4)^{2-}$
				374 m	377 m	
330 mbr	330 mbr	329 mbr	336 w	329 sbr	332 sbr	$\delta_s(MoO_4)^{2-}$
228 vw	227 vw	222 vw	222 vw	231 vw	229 vw	Lattice-mode vibrations

[*1] ν_s – symmetric stretching ν_{as} – asymmetric stretching δ_{as} – asymmetric bending

δ_s – symmetric bending

[*2] vs very strong; s strong; m medium; w weak; br broad; vw very weak

The symmetric stretching vibrations of $(MoO_4)^{2-}$ tetrahedra are observed as very strong peaks at 871 cm^{-1} and 916 cm^{-1} together with weak shoulder at 937 cm^{-1} and the prominent bands observed in the range 843 cm^{-1} to 771 cm^{-1} correspond to the asymmetric stretching vibrations of $(MoO_4)^{2-}$ ions. The asymmetric bending vibrations of $(MoO_4)^{2-}$ tetrahedra appear at 377 cm^{-1} and 394 cm^{-1} for $Na_5Yb(MoO_4)_4$ ceramic. The symmetric bending vibrations of $(MoO_4)^{2-}$ tetrahedra are observed at 332 cm^{-1} for $Na_5Yb(MoO_4)_4$ ceramic. The lattice-mode vibrations are observed below 250 cm^{-1} and an unambiguous assignment of these modes is difficult. The Raman bands of $Na_5R(MoO_4)_4$ (R = La, Pr, Nd, Sm, Y and Yb) ceramics are compared with that of $CaMoO_4$ with pure scheelite structure having $\nu_s(MoO_4)^{2-}$ at 875 cm^{-1}, $\nu_{as}(MoO_4)^{2-}$ at 843 cm^{-1} and 791 cm^{-1}, $\delta_{as}(MoO_4)^{2-}$ at 389 cm^{-1} and $\delta_s(MoO_4)^{2-}$ at 320 cm^{-1} [22]. The Raman spectra of modulated scheelite structure exhibit additional bands compared to

pure scheelite which are brought about by atomic rearrangements of Ca atoms with Na and R atoms and cationic vacancies.

The Raman bands of $Na_5R(MoO_4)_4$ (R = La, Pr, Nd, Sm) ceramics corresponding to asymmetric stretching and bending mode regions are less resolved compared to that of $Na_5R(MoO_4)_4$ (R = Y and Yb) ceramics. The FWHM values of the Raman modes are correlated with the quality factor in microwave dielectric samples [23-26]. The Raman spectra of $Na_5R(MoO_4)_4$ (R = La, Pr, Nd, Sm, Y and Yb) ceramics in the wavenumber range 1300 to 2400 cm^{-1} are shown in Figure 3.5 a-f.
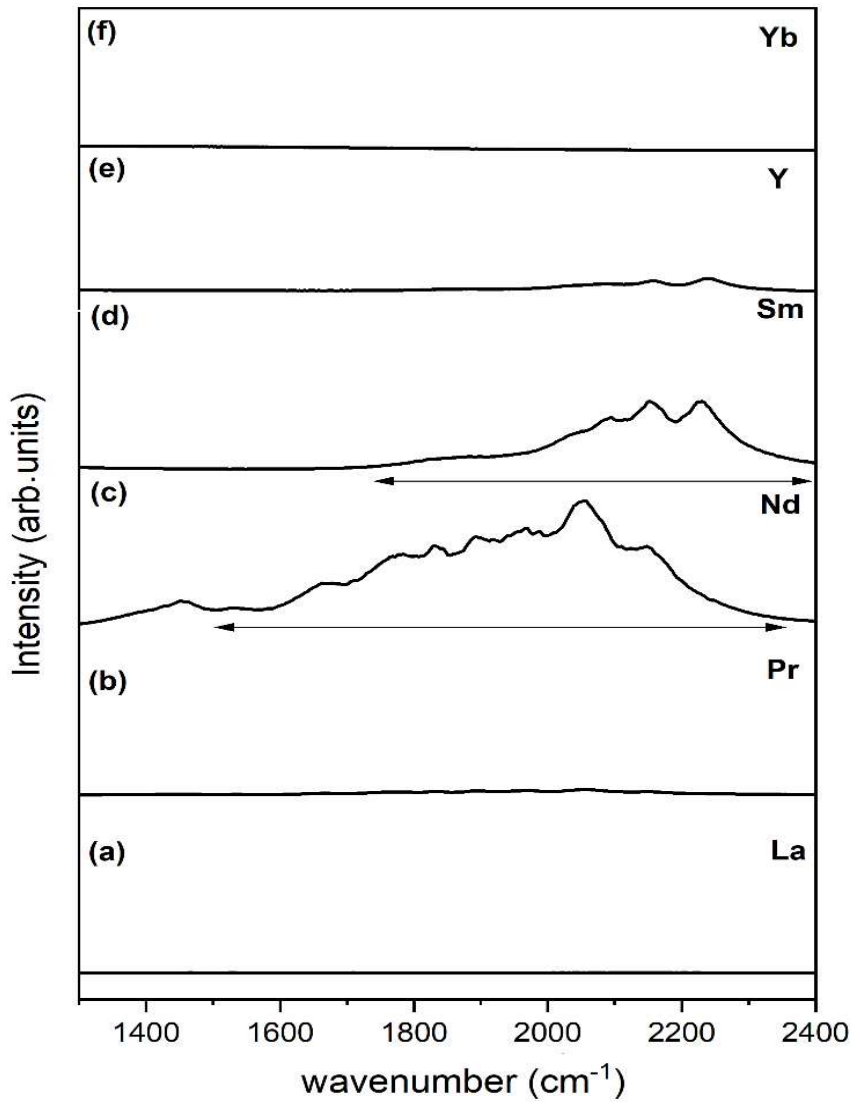
Figure 3.5 Raman spectra for wavenumber range 1300-2400 cm^{-1} of $Na_5R(MoO_4)_4$ (R = La, Pr, Nd, Sm, Y and Yb) ceramics

The Raman spectra of $Na_5Nd(MoO_4)_4$ and $Na_5Sm(MoO_4)_4$ compositions clearly manifest high intensity bands in the wavenumber region from 1300 to 2400 cm^{-1},

whereas very weak bands appear for $Na_5Yb(MoO_4)_4$. These high intensity bands mask the fine structure of the Raman bands in the lower wavenumber region as seen in Figures 3.5 (c) and (d). $Na_5Nd(MoO_4)_4$ is reported as a potential laser material [27-29]. These bands are attributed to the fluorescence emissions caused by the 532 nm visible light laser irradiation of the sample.

3.3.3 Morphological studies

The SEM micrographs of $Na_5R(MoO_4)_4$ (R = La, Pr, Nd, Sm, Y and Yb) ceramics are shown in Figure 3.6 a-f. The sintered ceramic samples show dense microstructure with polygonal grains of size 1 to 3 μm which are evenly distributed. Phase homogeneity of the ceramics are further ascertained by SEM investigation. $Na_5Y(MoO_4)_4$ and $Na_5Yb(MoO_4)_4$ ceramics exhibit compact microstructure with larger well-defined grain boundaries compared to other compositions, which can be correlated with the quality factor of the ceramics.
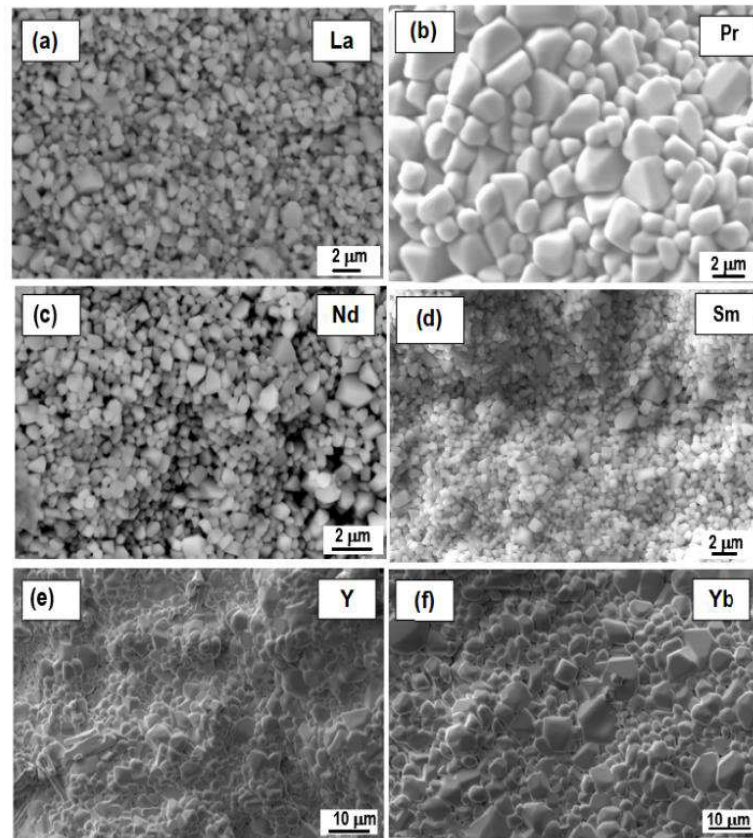
Figure 3.6 SEM micrographs of (a) $Na_5La(MoO_4)_4$ ceramic sintered at 530°C/1h, (b) $Na_5Pr(MoO_4)_4$ ceramic sintered at 540°C/1h, (c) $Na_5Nd(MoO_4)_4$ ceramic sintered at 550°C/1h, (d) $Na_5Sm(MoO_4)_4$ ceramic sintered at 560°C/1h, (e) $Na_5Y(MoO_4)_4$ ceramic sintered at 600°C/1h and (f) $Na_5Yb(MoO_4)_4$ ceramic sintered at 570°C/1h

3.3.4 Microwave dielectric studies

The $Na_5R(MoO_4)_4$ (R = La, Pr, Nd, Sm, Y and Yb) ceramics are calcined at 500°C for 1h and sintered in the temperature range from 510°C to 610°C for 1 h to obtain maximum density. The density of the sintered samples are measured using dimensional methods. The microwave dielectric properties of the $Na_5R(MoO_4)_4$ (R = La, Pr, Nd, Sm, Y and Yb) ceramics are given in Table 3.3.

The dielectric constant ε_r of the $Na_5R(MoO_4)_4$ (R = La, Pr, Nd, Sm, Y and Yb) ceramics varies from 6.2 to 7.8, whereas the quality factor $Q_u \times f$ values ranges from 18,800 to 56,800 GHz. The $Na_5Y(MoO_4)_4$ ceramic shows a maximum sintered density of 3.6 g/cm^3 with 95% densification at 600°C having dielectric constant ε_r of 7.8, quality factor $Q_u \times f$ of 56,800 GHz and temperature coefficient of resonant frequency τ_f of -83 ppm/°C. The $Na_5Yb(MoO_4)_4$ ceramic shows a maximum sintered density of 3.9 g/cm^3 with 93% densification at 570°C having dielectric constant ε_r of 6.9, quality factor $Q_u \times f$ of 43,400 GHz and temperature coefficient of resonant frequency τ_f of -68 ppm/°C.

Table 3.3 Sintering temperature, maximum sintered density and microwave dielectric properties of $Na_5R(MoO_4)_4$ (R = La, Pr, Nd, Sm, Y and Yb) ceramics

Compositions	Sintering temperature (°C)/1h	Density (g/cm³)	ε_r @ GHz	$Q_u \times f$ (GHz)
$Na_5La(MoO_4)_4$	530	3.47	6.2	18,800
$Na_5Pr(MoO_4)_4$	540	3.50	6.4	19,900
$Na_5Nd(MoO_4)_4$	550	3.43	7.1	21,250
$Na_5Sm(MoO_4)_4$	560	3.53	6.3	26,800
$Na_5Y(MoO_4)_4$	600	3.60	7.8	56,800
$Na_5Yb(MoO_4)_4$	570	3.90	6.9	43,400

The variation of resonant frequency with temperature for $Na_5Yb(MoO_4)_4$ ceramic sintered at 570°C/1h and that of $Na_5Y(MoO_4)_4$ ceramic sintered at 600°C/1h is shown in Figure 3.7. The variation of sintered density, dielectric constant ε_r and the

quality factor $Q_u \times f$ of Na$_5$Yb(MoO$_4$)$_4$ ceramic with sintering temperature is shown in Figure 3.8.
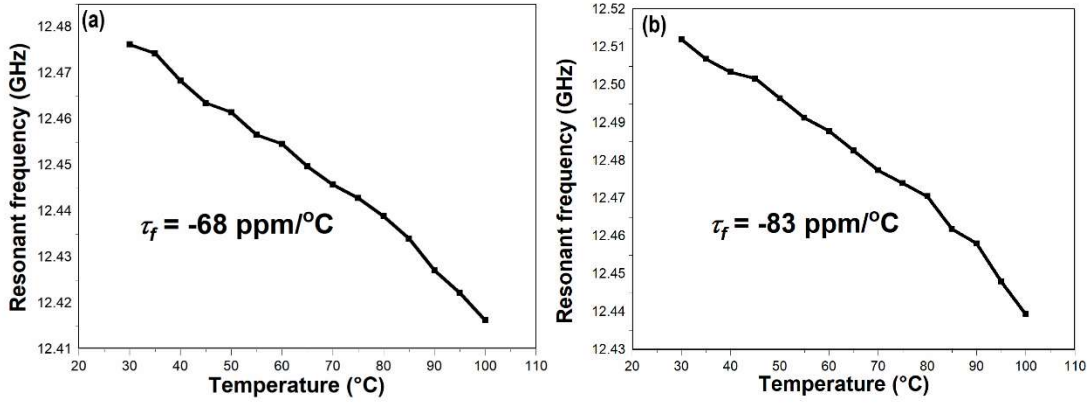
Figure 3.7 Variation of resonant frequency with temperature of (a) Na$_5$Yb(MoO$_4$)$_4$ ceramic sintered at 570°C/1h and (b) Na$_5$Y(MoO$_4$)$_4$ ceramic sintered at 600°C/1h
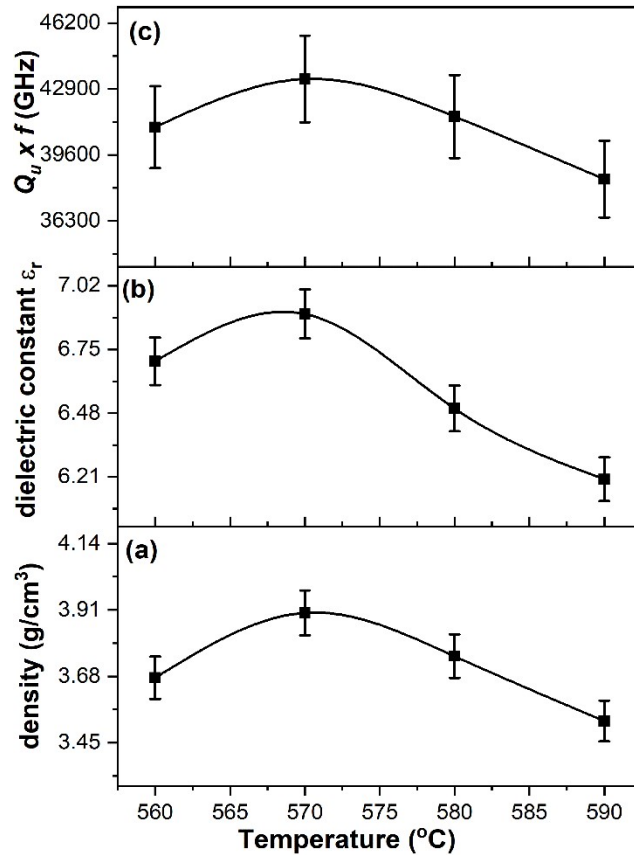
Figure 3.8 Variation of (a) density, (b) dielectric constant ε_r and (c) quality factor $Q_u \times f$ of Na$_5$Yb(MoO$_4$)$_4$ ceramic with sintering temperature

Na$_5$Yb(MoO$_4$)$_4$ ceramic has a theoretical dielectric constant of 6.82 calculated by Clausius-Mossotti equation using the molar volume V$_m$ and the sum of dielectric polarizabilities α$_D$ of the individual ions [30,31]. The effect of porosity on dielectric

constant can be eliminated by applying Bosman and Having's porosity correction to the measured dielectric constant [32,33].

$$(\varepsilon_r)_{corrected} = (\varepsilon_r)_{measured} (1 + 1.5\ P) \qquad (3.3)$$

where, $(\varepsilon_r)_{corrected}$ and $(\varepsilon_r)_{measured}$ are the corrected and measured values of dielectric constant and P the fractional porosity. $Na_5Yb(MoO_4)_4$ ceramic has a porosity corrected dielectric constant of 7.4.

$Na_5R(MoO_4)_4$ (R = La, Pr, Nd and Sm) compositions achieve only around 90% of the theoretical density and exhibit weak microwave resonance with relatively lower quality factor compared to $Na_5Y(MoO_4)_4$ and $Na_5Yb(MoO_4)_4$ ceramics [23-26]. This can be attributed to their lower densification as well as smaller grain sizes as revealed in SEM micrographs compared to $Na_5Y(MoO_4)_4$ and $Na_5Yb(MoO_4)_4$ ceramics. The quality factor is inversely related to the FWHM value of the Raman bands and hence the large quality factor $Q_u \times f$ of 56,800 GHz of $Na_5Y(MoO_4)_4$ ceramic and 43,400 GHz of $Na_5Yb(MoO_4)_4$ ceramic can be attributed to the lower FWHM of the Raman bands as compared to the broader Raman bands of $Na_5R(MoO_4)_4$ (R = La, Pr, Nd and Sm) compositions. The weaker microwave resonance exhibited by $Na_5R(MoO_4)_4$ (R = La, Pr, Nd and Sm) samples limit the accurate measurement of the temperature variation of the $TE_{01\delta}$ mode frequency and hence the τ_f values of these compositions are not reported in this work.

3.3.5 Compatibility studies

The chemical compatibility with aluminium electrode is evaluated by powder X-ray diffraction and energy dispersive X-ray spectroscopy (EDS) analyses of the $Na_5R(MoO_4)_4$ (R = La, Pr, Nd, Sm, Y and Yb) ceramics co-fired with 20 wt% aluminium powder at optimum sintering temperatures. The effect of R^{3+} ion substitution on the co-firability of these compositions is investigated in detail. The XRD patterns and the EDS point analysis results of the Al co-fired samples of $Na_5R(MoO_4)_4$ (R = La and Pr) ceramics are given in Figures 3.9 and 3.10 respectively.

The XRD patterns of both $Na_5La(MoO_4)_4$ and $Na_5Pr(MoO_4)_4$ ceramics reveal the presence of Al marked with '*', however few extra peaks marked with 'x' are also formed. The backscattered SEM images of the samples show the presence of multiple phases although their manifestation in XRD is very weak. The EDS point analysis also

confirms the secondary phase formation on co-firing. The probable additional phases identified are $Al_2(MoO_4)_3$ along with Na_2MoO_4.

The XRD patterns and the EDS point analysis results of the Al co-fired samples of $Na_5Nd(MoO_4)_4$ are given in Figures 3.11 and 3.12 respectively and that of $Na_5Sm(MoO_4)_4$ are given in Figures 3.13 and 3.14 respectively.
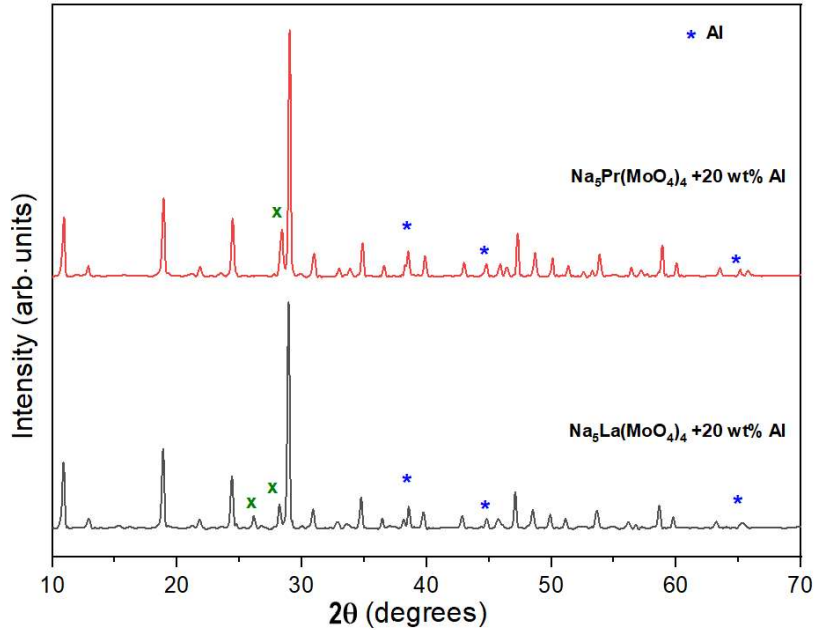
Figure 3.9 XRD patterns of (a) $Na_5La(MoO_4)_4$ and (b) $Na_5Pr(MoO_4)_4$ ceramics co-fired with 20 wt% Al at optimum sintering temperatures
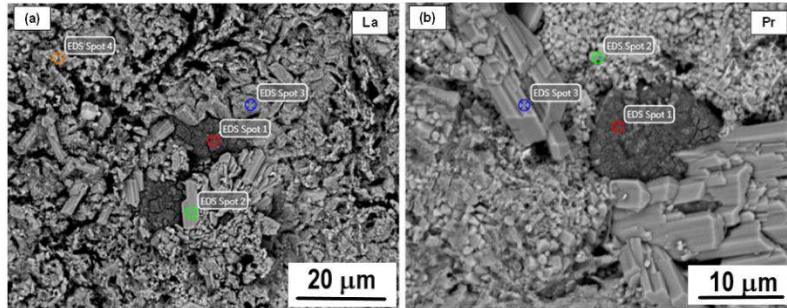
EDS point analysis spectra of 20 wt% Al co-fired sample of $Na_5La(MoO_4)_4$					
Element Atomic %	O K	NaK	AlK	MoL	LaL	probable phase identified
EDS Spot 1	57.34	0	39.04	3.62	0	$Al_2(MoO_4)_3$
EDS Spot 2	75.82	4.50	0	19.68	0	Na_2MoO_4
EDS Spot 3	52.01	26.25	1.36	20.38	0	x
EDS Spot 4	56.48	15.37	0	21.88	6.27	$Na_5La(MoO_4)_4$

EDS point analysis spectra of 20 wt% Al co-fired sample of $Na_5Pr(MoO_4)_4$					
Element Atomic %	O K	NaK	AlK	MoL	PrL	probable phase identified
EDS Spot 1	33.15	1.58	62.86	2.42	0	x
EDS Spot 2	6.01	0.96	1.83	34.43	56.76	x
EDS Spot 3	72.98	7.47	0	19.55	0	Na_2MoO_4

Figure 3.10 Backscattered SEM image and EDS point analysis results of (a) $Na_5La(MoO_4)_4$ and (b) $Na_5Pr(MoO_4)_4$ ceramics co-fired with 20 wt% Al at optimum sintering temperature
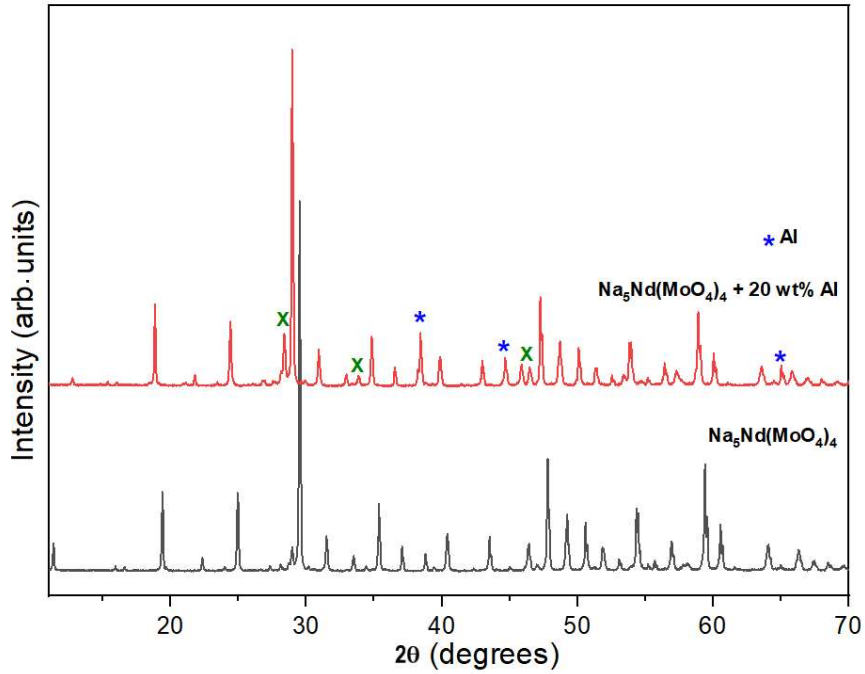
Figure 3.11 XRD patterns of $Na_5Nd(MoO_4)_4$ ceramic and $Na_5Nd(MoO_4)_4$ ceramic co-fired with 20 wt% Al at 550°C/1h
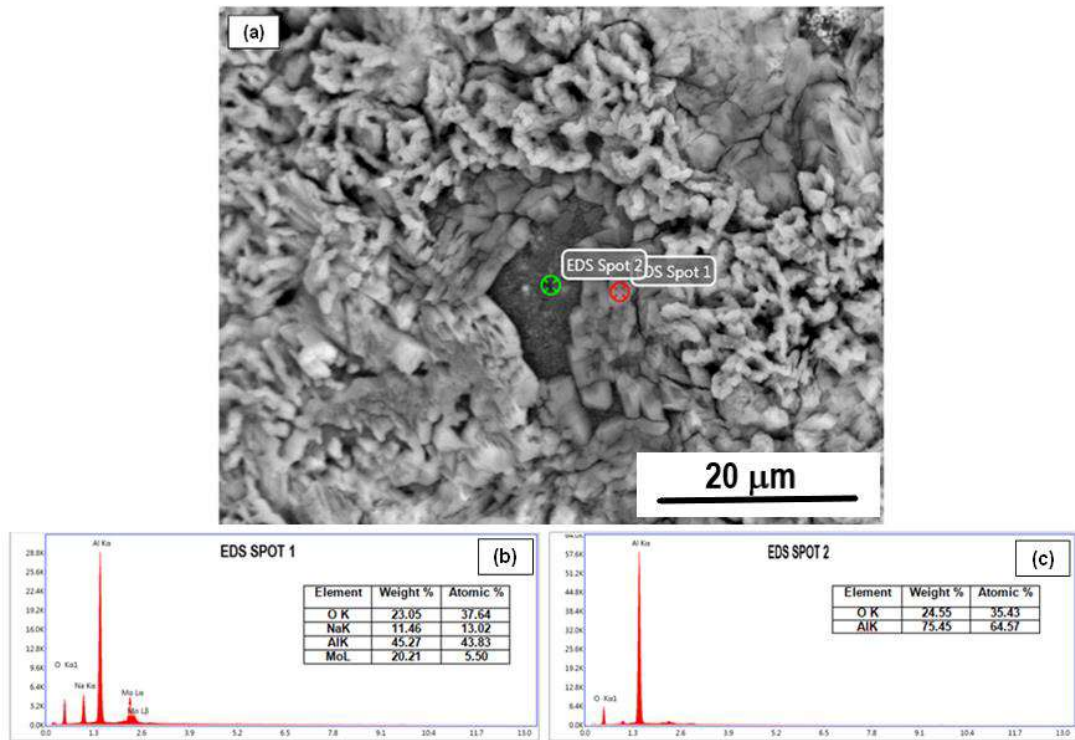
Figure 3.12 (a) Backscattered SEM image; EDS point analysis spectra at (b) spot 1 and (c) spot 2 of $Na_5Nd(MoO_4)_4$ ceramic co-fired with 20 wt% Al at 550°C/1h
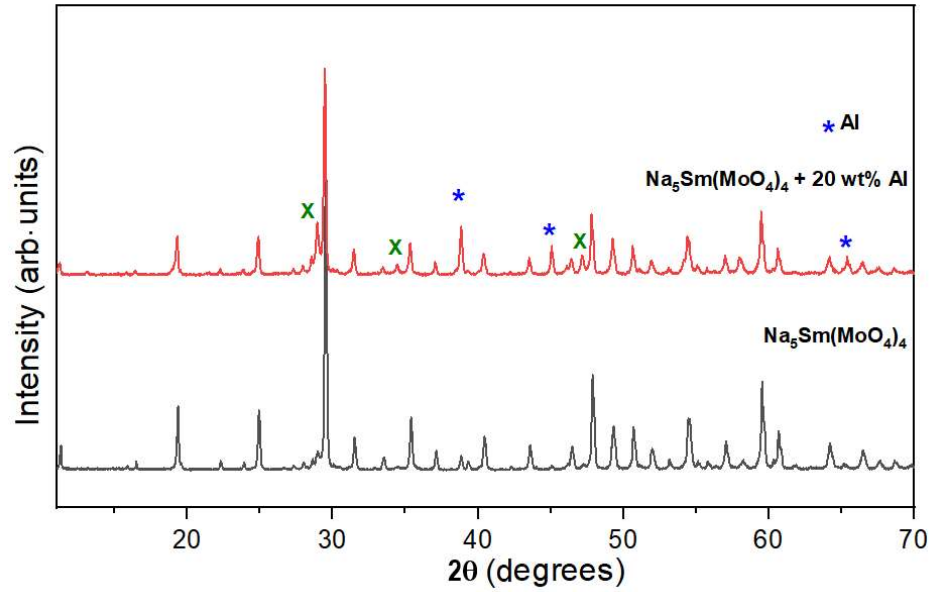
Figure 3.13 XRD patterns of Na$_5$Sm(MoO$_4$)$_4$ ceramic and Na$_5$Sm(MoO$_4$)$_4$ ceramic co-fired with 20 wt% Al at 560°C/1h
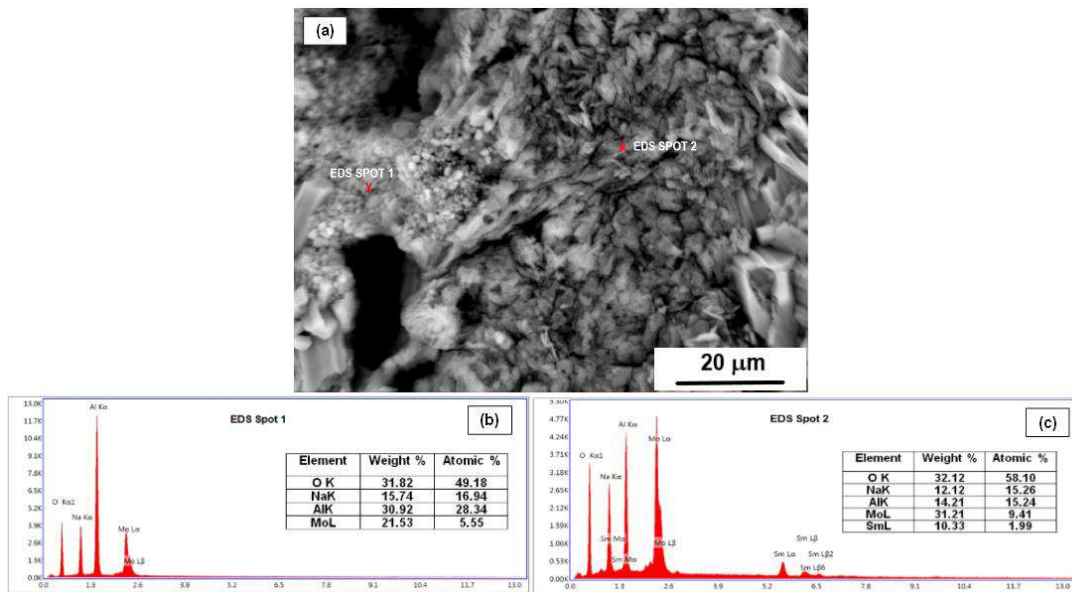
Figure 3.14 (a) Backscattered SEM image; EDS point analysis results (b) spot 1 and (c) spot 2 of Na$_5$Sm(MoO$_4$)$_4$ ceramic co-fired with 20 wt% Al at 560°C/1h

The XRD patterns of both Na$_5$Nd(MoO$_4$)$_4$ and Na$_5$Sm(MoO$_4$)$_4$ reveal the presence of Al marked with '*' along with secondary phase formation marked with 'x'. The EDS point analysis of Na$_5$Nd(MoO$_4$)$_4$ ceramic shows the presence of oxidised aluminium along with sodium aluminium molybdate phase formation. The EDS point analysis of Na$_5$Sm(MoO$_4$)$_4$ ceramic also reveals the chemical reactivity between the co-fired ceramic and aluminium.

The XRD patterns and the EDS analysis results of the Al co-fired samples of $Na_5Y(MoO_4)_4$ are given in Figures 3.15 and 3.16 respectively and that of $Na_5Yb(MoO_4)_4$ are given in Figures 3.17 and 3.18 respectively.
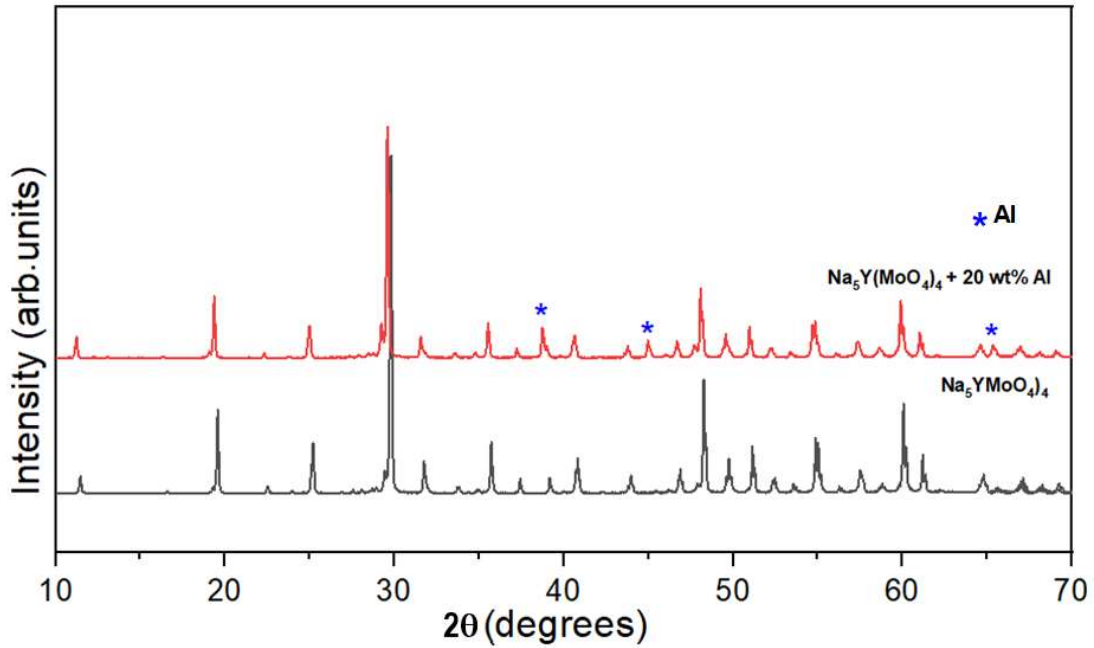
Figure 3.15 XRD patterns of $Na_5Y(MoO_4)_4$ ceramic and $Na_5Y(MoO_4)_4$ ceramic co-fired with 20 wt% Al at 600°C/1h
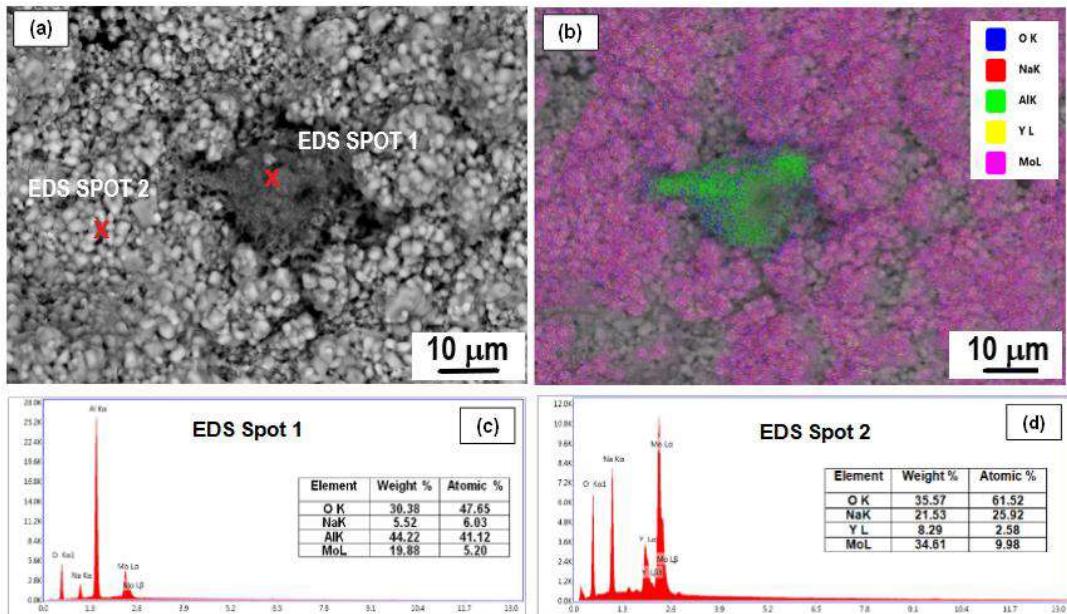
Figure 3.16 (a) Backscattered SEM image; (b) EDS phase map; EDS point analysis spectra at (c) spot 1 and (d) spot 2 of $Na_5Y(MoO_4)_4$ ceramic co-fired with 20 wt% Al at 600°C/1h
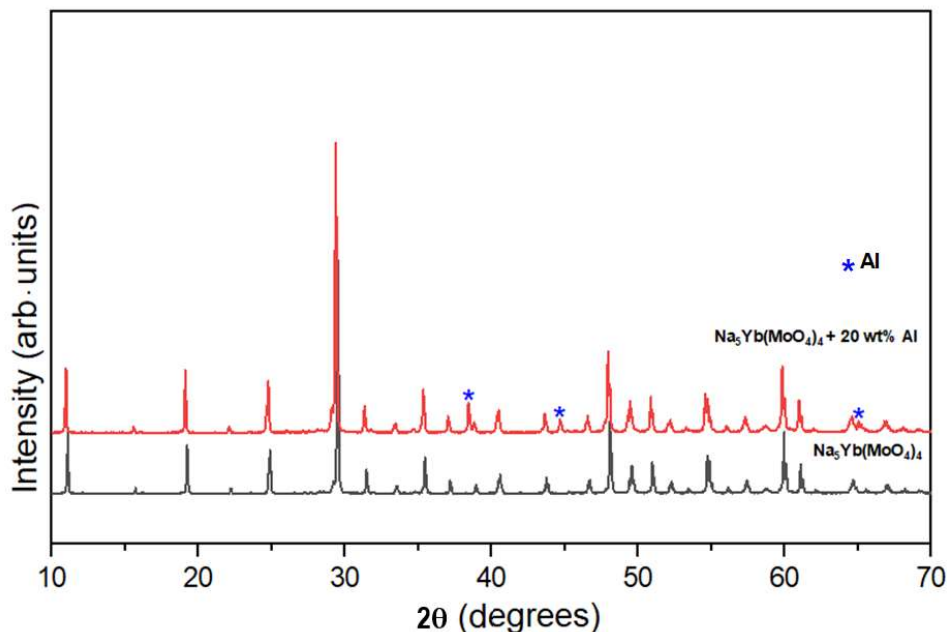
Figure 3.17 XRD patterns of $Na_5Yb(MoO_4)_4$ ceramic and $Na_5Yb(MoO_4)_4$ ceramic co-fired with 20 wt% Al at 570ºC/1h

Among the XRD patterns of the co-fired samples, $Na_5Yb(MoO_4)_4$ ceramic co-fired with aluminium exhibits well defined peaks of aluminium at 2θ values 38.5°, 44.7° and 65.1° are marked with '*', in addition to the characteristic peaks of the ceramics. The elemental phase map of both $Na_5Y(MoO_4)_4$ and $Na_5Yb(MoO_4)_4$ samples show co-fired aluminium as an island surrounded by the sintered ceramic. However, the EDS point analysis at the aluminium region in the co-fired $Na_5Y(MoO_4)_4$ shows traces of Na, Mo and O along with Al. In the case of co-fired $Na_5Yb(MoO_4)_4$ ceramic, EDS point analysis shows the presence of metal aluminium only at EDS spot 1 as shown in Figure 3.18 (b), which clearly indicates that $Na_5Yb(MoO_4)_4$ ceramic exhibits better co-firability with aluminium electrode material. The co-firability of $Na_5Yb(MoO_4)_4$ ceramic with aluminium is further ascertained by the nature of the EDS line scan of $Na_5Yb(MoO_4)_4$ ceramic as shown in Figure 3.19. The EDS line scan across the co-fired aluminium region shows a sharp decrease in the aluminium content at the interface of co-fired ceramic and aluminium. The elemental mapping for each constituent element is also given in Figure 3.20. The complementary nature of the images clearly confirms the co-firability of the ceramics with aluminium metal.
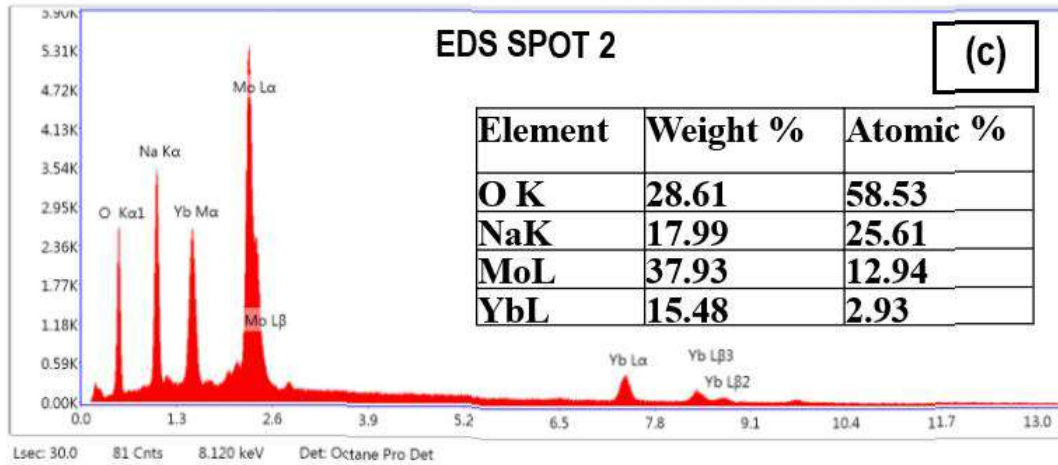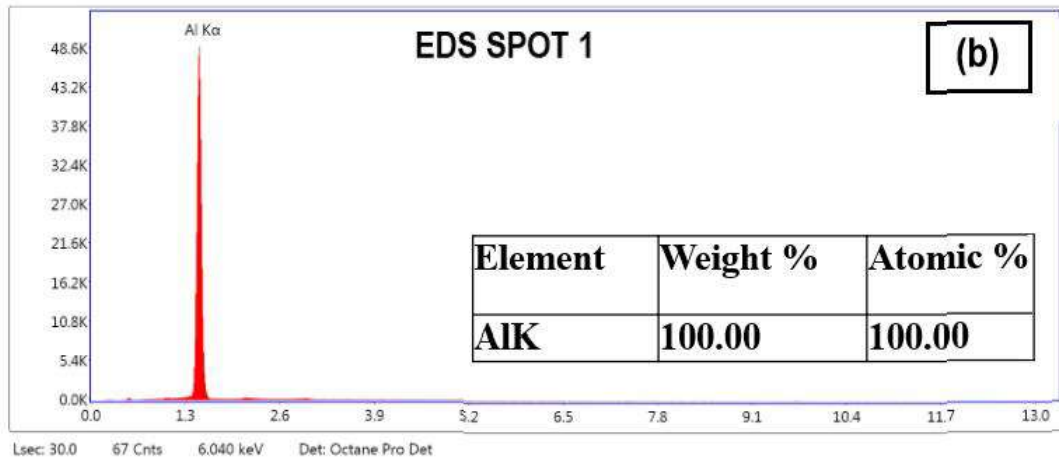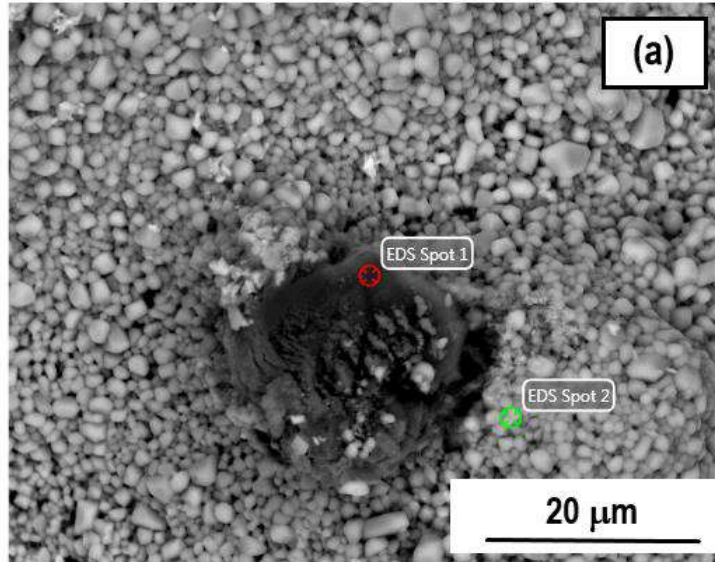
Figure 3.18 (a) Backscattered SEM image; EDS point analysis results (b) spot 1 and (c) spot 2 of $Na_5Yb(MoO_4)_4$ ceramic co-fired with 20 wt% Al at 570°C/1h
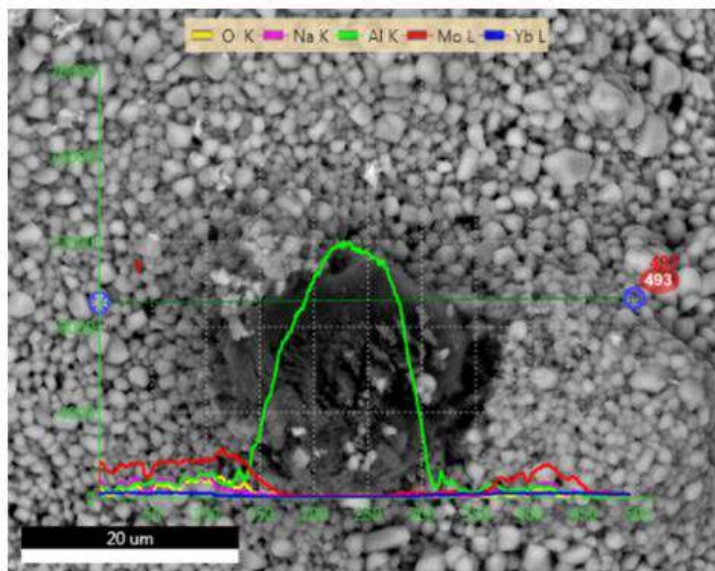
Figure 3.19 EDS line scan of Na$_5$Yb(MoO$_4$)$_4$ ceramic co-fired with 20 wt% Al at 570°C/1h
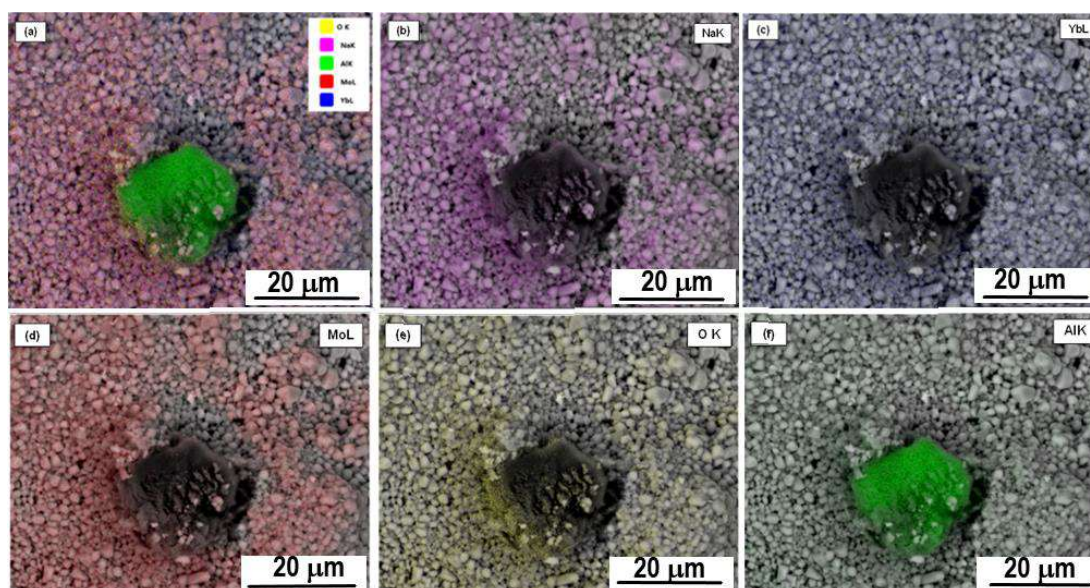
Figure 3.20 (a) EDS elemental mapping overlay on image; Elemental mapping of b) Na, c) Yb, d) Mo, e) O and f) Al elements in Na$_5$Yb(MoO$_4$)$_4$ ceramic co-fired with 20 wt% Al at 570°C/1h

3.4 Conclusions

The Na$_5$R(MoO$_4$)$_4$ (R = La, Pr, Nd, Sm, Y and Yb) ceramics have been prepared through conventional solid-state ceramic method. The phase purity of the samples is studied by powder X-ray diffraction technique. The presence of (MoO$_4$)$^{2-}$ tetrahedra in the crystal structure of these compositions is confirmed using laser Raman

spectroscopic studies. The scanning electron microscopic investigations reveal that the microstructure of the sintered ceramic compacts are dense in nature with grain size ranging from 1 to 3 µm. Present study shows, $Na_5R(MoO_4)_4$ (R = Y and Yb) ceramics have excellent microwave dielectric properties. $Na_5Y(MoO_4)_4$ ceramic has a dielectric constant of 7.8, quality factor $Q_u \times f$ of 56,800 GHz, and temperature coefficient of resonant frequency τ_f of -83 ppm/°C whereas a dielectric constant of 6.9, quality factor $Q_u \times f$ of 43,400 GHz, and temperature coefficient of resonant frequency τ_f of -68 ppm/°C are obtained for $Na_5Yb(MoO_4)_4$ ceramic. Powder X-ray diffraction and energy dispersive X-ray spectroscopy analyses have been used as tools to analyse the chemical compatibility of these ceramics with aluminium metal electrode. Among the compositions studied, $Na_5Yb(MoO_4)_4$ ceramic shows excellent chemical compatibility with aluminium electrode and is a potential candidate material for ULTCC applications.

References

[1] Z. Di, P. Li-Xia, Q. Ze-Ming, J. Biao-Bing, Y. Xi, Novel ultra-low temperature co-fired microwave dielectric ceramic at 400 degrees and its chemical compatibility with base metal, Sci. Rep., 4 (2014) 5980.

[2] G. Q. Zhang, H. Wang, J. Guo, L. He, D. D. Wei, Q. B. Yuan, Ultra-low sintering temperature microwave dielectric ceramics based on Na_2O-MoO_3 binary system, J. Am. Ceram. Soc., 98 [2] (2015) 528-533.

[3] D. Zhou, C. A. Randall, L. X. Pang, H. Wang, J. Guo, G. Q. Zhang, Y. Wu, K. T. Guo, L. Shui, X. Yao, Microwave dielectric properties of $(ABi)_{1/2}$ MoO_4 (A = Li, Na, K, Rb, Ag) type ceramics with ultra-low firing temperatures, Mater. Chem. Phys., 129 [3] (2011) 688-692.

[4] H. Xi, D. Zhou, H. Xie, W. Li, Microwave dielectric properties of low firing scheelite-related $(Na_{0.5}La_{0.5})MoO_4$ ceramic, Mater. Lett., 142 (2015) 221-224.

[5] H. H. Xi, D. Zhou, H. D. Xie, W. B. Li, Microwave dielectric properties of low firing $(Na_{0.5}Ln_{0.5})MoO_4$ (Ln = Nd and Ce) ceramics, Ceram. Int., 41 [4] (2015) 6103-6107.

[6] O. M. Basovich, A. A. Uskova, S. F. Solodovnikov, Z. A. Solodovnikova, E. G. Haykina, Phase-formation in the systems of Na_2MoO_4-Cs_2MoO_4-$Ln_2(MoO_4)_3$ and the crystalline structure of the new triple molybdate $Cs_7Na_5Yb_2(MoO_4)_9$, Vestnik. Buryat. State. Univ., 3 (2011) 24-29.

[7] T. P. Rybakova, V. K. Trunov, The sodium molybdate-rare earth molybdate systems, Russ. J. Inorg. Chem., 19 [6] (1974) 888-890.

[8] M. V. Mokhosoev, F. P. Alekseev, E. I. Get'man, Double molybdates of the rare-earth elements and sodium of composition $Na_5Ln(MoO_4)_4$, Russ. J. Inorg. Chem., 14 [2] (1969) 310-311.

[9] M. V. Mokhosoev, I. F. Kokot, V. I. Lutsyk, I. S. Kononenko, Interaction in melts between double lanthanum alkali metal molybdates and alkali metal molybdates, Russ. J. Inorg. Chem., 15 [1] (1970) 142-144.

[10] V. A. Efremov, T. A. Berezina, I. M. Averina, V. K. Trunov, Structure of $Na_5Tb(MoO_4)_4$, $Na_5Lu(MoO_4)_4$, and $Na_5Lu(WO_4)_4$, Sov. Phys. Crystallogr., 25 [2] (1980) 146-150.

[11] V. A. Efremov, V. K. Trunov, T. A. Berezina, Fine changes in the structure of scheelite-like $Na_5TR(EO_4)_4$ with a variation in their elemental composition, Sov. Phys. Crystallogr., 27 [1] (1982) 77-81.

[12] V. K. Trunov, T. A. Berezina, A. A. Evdokimov, V. K. Ishunin, V. G. Krongauz, Sodium rare-earth-element double molybdates and tungstates, Russ. J. Inorg. Chem., 23 [10] (1978) 1465-1467.

[13] R. F. Klevtsova, L. A. Glinskaya, L. P. Kozeeva, P. V. Klevtsov, The double sodium lutetium tungstates, $NaLu(WO_4)_2$ and $Na_5Lu(WO_4)_4$, and their crystal structures, Sov. Phys. Crystallogr., 17 [4] (1973) 672-676.

[14] N. J. Stedman, A. K. Cheetham, P. D. Battle, Crystal structures of two sodium yttrium molybdates: $NaY(MoO_4)_2$ and $Na_5Y(MoO_4)_4$, J. Mater. Chem., 4 [5] (1994) 707-711.

[15] B. W. Hakki, P. D. Coleman, A dielectric resonator method of measuring inductive capacities in the millimeter range, IRE Trans. Microwave Theory Tech., 8 [4] (1960) 402-410.

[16]   J. Krupka, K. Derzakowski, B. Riddle, J. B. Jarvis, A dielectric resonator for measurements of complex permittivity of low loss dielectric materials as a function of temperature., Meas. Sci. Technol., 9 [10] (1998) 1751-1756.

[17]   R. D. Shannon, Revised effective ionic radii and systematic studies of interatomic distances in halides and chalcogenides, Acta crystallogr. A, 32 [5] (1976) 751-767.

[18]   F. D. Hardcastle, I. E. Wachs, Molecular structure of molybdenum oxide in bismuth molybdates by Raman spectroscopy, J. Phys. Chem. 95 [26] (1991) 10763-10772.

[19]   F. D. Hardcastle, I. E. Wachs, Determination of molybdenum–oxygen bond distances and bond orders by Raman spectroscopy, J. Raman Spectrosc., 21 [10] (1990) 683-691.

[20]   N. K. James, R. Ratheesh, Microwave dielectric properties of low-temperature sinterable $BaCe_2(MoO_4)_4$ ceramics, J. Am. Ceram. Soc., 93 [4] (2010) 931-933.

[21]   A. Surjith, R. Ratheesh, High Q ceramics in the $ACe_2(MoO_4)_4$ (A= Ba, Sr and Ca) system for LTCC applications, J. Alloys Compd., 550, (2013) 169-172.

[22]   E. Sinha, P. Yadav, Study of structural and optical properties of $CaMoO_4$ ceramic synthesized by solid state reaction route, Ferroelectrics, 517 [1] (2017) 1-7.

[23]   V. L. Vilesh, G. Subodh, Crystal structure, phonon modes and dielectric properties of B site ordered $ABiLiTeO_6$ (A= Ba, Sr) double perovskites, Ceram. Int., 44 [11] (2018) 12036-12041.

[24]   M. Y. Chen, C. T. Chia, I. N. Lin, L. J. Lin, C. W. Ahn, S. Nahm, Microwave properties of $Ba(Mg_{1/3}Ta_{2/3})O_3$, $Ba(Mg_{1/3}Nb_{2/3})O_3$ and $Ba(Co_{1/3}Nb_{2/3})O_3$ ceramics revealed by Raman scattering, J. Eur. Ceram. Soc., 26 [10-11] (2006) 1965-1968.

[25]   J. Zhang, J. Zhai, J. Wang, J. Shao, X. Lu, X. Yao, Infrared dielectric response and Raman spectra of tunable $Ba_{0.5}Sr_{0.5}TiO_3$–Mg_2TiO_4 composite ceramics, J. Appl. Phys., 107 [1] (2010) 014106.

[26]   F. Shi, H. Dong, Correlation of crystal structure, dielectric properties and lattice vibration spectra of $(Ba_{1−x}Sr_x)(Zn_{1/3}Nb_{2/3})O_3$ solid solutions, Dalton Trans., 40 [25] (2011) 6659-6667.

[27]   V. M. Markushev, N. É. Ter-Gabriélyan, C. M. Briskina, V. R. Belan, V. F. Zolin, Stimulated emission kinetics of neodymium powder lasers, Sov. J. Quant. Electron., 20 [7] (1990) 773.

[28]   F. Auzel, P. Goldner, Coherent light sources with powder: Stimulated amplification versus super-radiance, J. Alloys Compd., 300 (2000) 11-17.

[29]   N. E. Ter-Gabrielian, V. M. Markushev, V. R. Belan, C. M. Briskina, V. F. Zolin, Spectra of stimulated emission from powders of dual sodium and neodymium tetramolybdate, Kvantovaya Elektron. (Moscow), 18 (1991) 38.

[30]   M. T. Sebastian, *Dielectric materials for wireless communication*, Elsevier (2008).

[31]   R. D. Shannon, Dielectric polarizabilities of ions in oxides and fluorides, J. Appl. Phys., 73 [1] (1993) 348-366.

[32]   A. J. Bosman, E. E. Havinga, Temperature dependence of dielectric constants of cubic ionic compounds, Phys. Rev., 129 [4] (1963) 1593.

[33]   W. Wen, C. Li, Y. Sun, Y. Tang, L. Fang, $Cu_3Mo_2O_9$: An Ultralow-Firing Microwave Dielectric Ceramic with Good Temperature Stability and Chemical Compatibility with Aluminum, J. Electron. Mater., 47 [2] (2018) 1003-1008.

Chapter 4

Structure and microwave dielectric properties of NaR$_5$(MoO$_4$)$_8$ (R = La, Pr, Nd and Sm) molybdate microwave ceramics for LTCC applications

4.1 Introduction

4.2 Materials and methods

4.3 Results and discussion

4.4 Conclusions

Some of the contents of this chapter have been accepted for publication in

4.1 Introduction

Classical crystals show lattice periodicity, whereas aperiodic crystals exhibit long range order without lattice periodicity. Incommensurately modulated (IM) structures form a class of aperiodic crystals, which are studied using the concept of superspace. The symmetry of the modulated structure of mineral natrite γ Na_2CO_3 is the first incommensurately modulated compound explained using superspace approach by P M De Wolff et al. [1-5]. The study of IM structures help to understand the atomic interactions in crystals. Cation-cation interactions are identified as the driving forces for incommensurability in crystals. The study of IM structures, helps to characterize chemical bonds, study phase transitions, physical properties like luminescence, classify, describe, predict structure families and their stabilization conditions [6-10].

Scheelite, glasserite and palmierite are some of the mineralogical families studied using the (3+1)D superspace approach. The scheelite structure $CaWO_4$ has tetragonal symmetry with space group $I4_1/a$. The scheelite structure of composition ABO_4 can accommodate A and B cations with various oxidation states. The ABO_4 structure has AO_8 polyhedra and BO_4 tetrahedra sharing common vertices. If the cation and anion substitution gives composition $(A_1,A_2)_n[(B_1,B_2)O_4]_n$ with cation to anion ratio $(A_1+A_2)/[B_1O_4 + B_2O_4)]$ 1:1, there is no cationic or anionic vacancies in the structure. $KNd(MoO_4)_2$, $KSm(MoO_4)_2$, $KYb(MoO_4)_2$ are some of the well-studied incommensurately modulated scheelite-like structures [11-14]. $Na_{2/7}Gd_{4/7}MoO_4$ is a cation deficient incommensurately modulated scheelite-type structure with tetragonal (3+2)D super space symmetry [15]. $Ag_{1/8}Pr_{5/8}MoO_4$ is the first representative in a large family of IM scheelite-type structures, described by (3+1)D superspace. The incommensurately modulated scheelite-type structure of $Ag_{1/8}Pr_{5/8}MoO_4$ is shown in Figure 4.1. $Ag_{1/8}Pr_{5/8}MoO_4$ structure consists of groups of 5 AO_8 (Pr,Ag) polyhedra alternating with two cation vacancies [16].

The $NaR_5(MoO_4)_8$ type compounds exhibit incommensurately modulated scheelite structure and crystallizes in monoclinic system with four-dimensional space group `I2/b`($\alpha\beta0$)00 having Z = 0.5 [16]. The $Na_{1/8}R_{5/8}MoO_4$ structure type reported to be isostructural to $Ag_{1/8}Pr_{5/8}MoO_4$ is a cation deficient phase with 1/4th of cation positions vacant [16,17]. These scheelite type compounds show occupancy modulation and displacive modulation with the arrangement of Na/R atoms and the vacancies being the cause of incommensurate modulation. In the case of $Na_{1/8}R_{5/8}MoO_4$ composition

with scheelite-type structures the cation to anion vacancies are not necessarily integers. The cation (Na^+, R^{3+}) - cation vacancy ordering influence the catalytic and luminescent properties of these compounds [18-20].
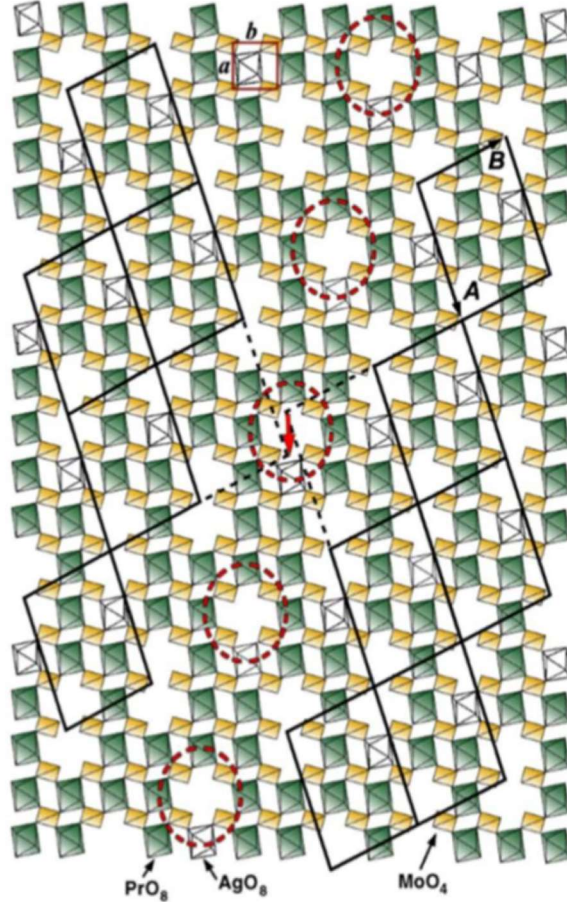
Figure 4.1 Crystal structure of $Ag_{1/8}Pr_{5/8}MoO_4$ [Ref. 16]

Rybakova et al. reported the double molybdate compositions with Na:R ratio 1:5 for Pr^{3+} and Sm^{3+} rare earth ions. The Na_2MoO_4-$Pr_2(MoO_4)_3$ phase diagram is given in Figure 4.2. The phase formation of $NaR_5(MoO_4)_8$ type is reported only for rare earth ions from lanthanum to europium [17,21]. Sodium molybdate - rare earth molybdate based binary compositions with commensurately modulated scheelite structure have been identified as ultra low temperature co-firable ceramics in the previous chapter [22]. Incommensurately modulated scheelite structures with structural formula $NaR_5(MoO_4)_8$ reported in the Na_2MoO_4-$R_2(MoO_4)_3$ (R = La, Pr, Nd and Sm) systems are investigated in the present chapter.
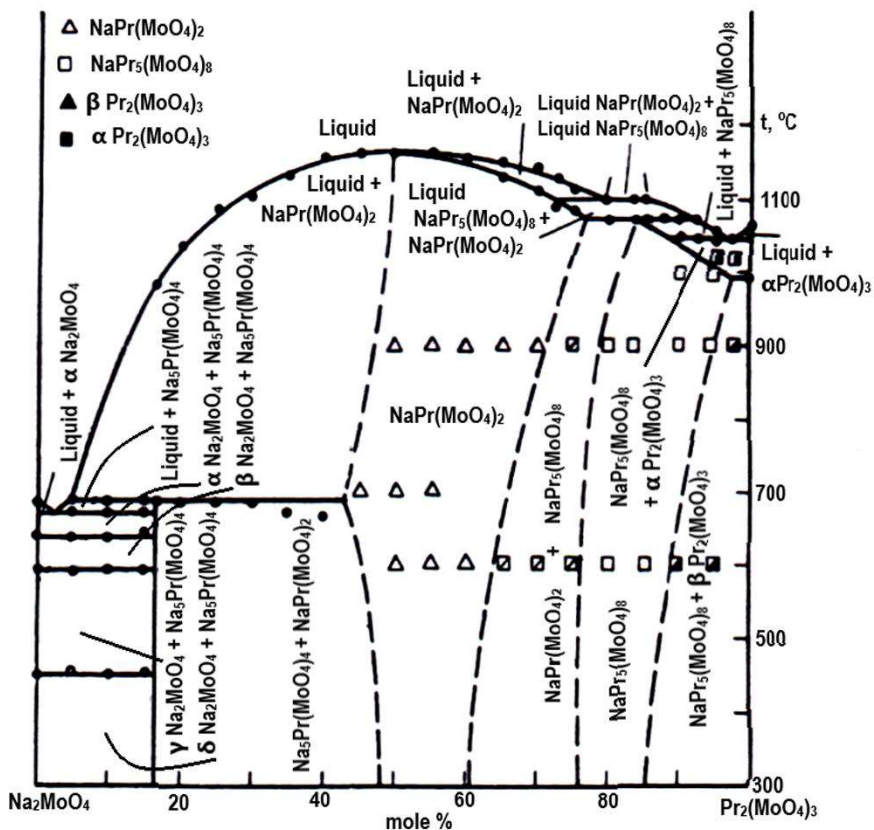
Figure 4.2 The Na_2MoO_4-$Pr_2(MoO_4)_3$ phase diagram [Ref. 17]

In the present study, $NaR_5(MoO_4)_8$ (R = La, Pr, Nd and Sm) ceramics are prepared by solid-state ceramic route. The phase purity of the compounds are studied using powder X-ray diffraction technique. The microwave dielectric properties of the ceramics have been studied for their use as dielectric resonators. Further, the co-firability of the compositions with silver metal electrode is evaluated using powder X-ray diffraction and energy dispersive X-ray spectroscopy to ascertain the feasibility of using these ceramics for LTCC applications.

4.2 Materials and methods

$NaR_5(MoO_4)_8$ (R = La, Pr, Nd and Sm) ceramics were prepared by conventional solid-state ceramic route using Na_2CO_3 (99.9%, Merck), La_2O_3 (99.9%, Sigma Aldrich), Pr_6O_{11} (99.9%, Aldrich), Nd_2O_3 (99.9%, Aldrich), Sm_2O_3 (99.9%, Sigma Aldrich) and MoO_3 (99%, Himedia). The constituent chemicals in stoichiometric proportions were mixed in double distilled water thoroughly and dried in a hot air oven at 100^oC. The dried sample was calcined at $550^oC/1h$ in a programmable SiC furnace. The calcined sample was ground well and mixed with 5 wt% polyvinyl alcohol (PVA) solution as binder and dried. The dried powder was pelletized in a hydraulic hand press

87

at 250 MPa using a 11 mm tungsten carbide die and sintered to get maximum density in the range 740°C to 800°C for one hour. The density of the sintered samples were determined using dimensional methods. Powder X-ray diffraction (XRD) measurement of the samples were carried out with CuKα radiation using a Brucker Model 5005, X-ray diffractometer, Germany. Carl Zeiss, Model No: EVO18 Research (Germany) scanning electron microscope with energy dispersive X-ray spectroscopy (EDS) facility was used to study the surface morphology and chemical compatibility of the ceramic samples with silver metal electrode. The Raman spectra of the compositions under study were recorded using a Thermo Scientific DXR with Nd:YVO4 DPSS laser of 532 nm. A Vector Network Analyzer (Agilent make PNA E8362B, Bayan Lepas, Malaysia) was used to evaluate the microwave dielectric properties. Dielectric constant and temperature coefficient of resonant frequency τ_f of the ceramics under study were measured using Hakki and Coleman post resonator technique [23]. The quality factor of the ceramics were measured using resonant cavity method (Krupka cavity) [24].

4.3 Results and discussion

4.3.1 Powder X-ray diffraction studies

The XRD patterns of the $NaLa_5(MoO_4)_8$, $NaPr_5(MoO_4)_8$, $NaNd_5(MoO_4)_8$ and $NaSm_5(MoO_4)_8$ ceramics are given in Figure 4.3 a-d. The X-ray diffraction patterns show isomorphous nature and matches with the ICDD (International Centre for Diffraction Data) files 61-0722 for $NaLa_5(MoO_4)_8$ ceramic, 30-1238 for $NaPr_5(MoO_4)_8$ ceramic, 61-0724 for $NaNd_5(MoO_4)_8$ ceramic and 60-0804 for $NaSm_5(MoO_4)_8$ ceramic. Thus the phase purity of the compounds are confirmed using powder X-ray diffraction studies. The XRD pattern of $NaPr_5(MoO_4)_8$ ceramic is isomorphous with that of the other compositions and hence is indexed using the ICDD file 61-0722 of $NaLa_5(MoO_4)_8$. Miller indices are not provided in the ICDD pattern of $NaLa_5(MoO_4)_8$ for 2θ reflections having intensity less than 5% of the maximum intensity and those peaks are left unindexed. However to get better clarity the unindexed peaks in the XRD pattern of $NaLa_5(MoO_4)_8$ ceramic are matched with the standard ICDD pattern. Similar observations are found in other compositions as well. The lattice parameters calculated from the indexed XRD patterns match with the reported values and are given in Table. 4.1.
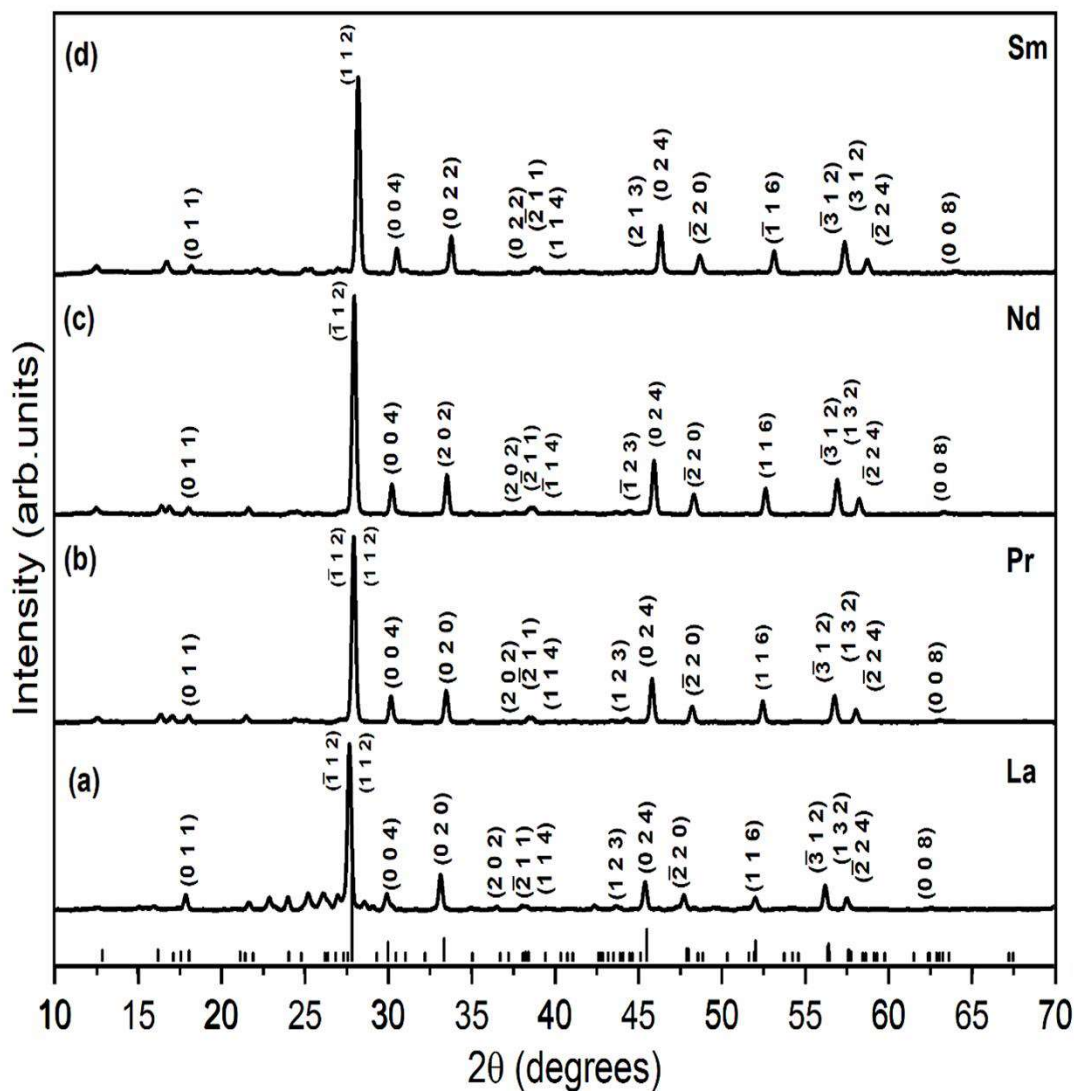
Figure 4.3 XRD patterns of $NaR_5(MoO_4)_8$ (R = La, Pr, Nd and Sm) sintered ceramics

Table 4.1 Comparison of calculated and reported lattice parameters of $NaR_5(MoO_4)_8$
(R= La, Pr, Nd and Sm) ceramics

Compositions	Ionic radii R^{3+} ions (Å)	Crystal structure	Calculated lattice parameters (Å)			Reported lattice parameters (Å)			ICDD card nos
			a	*b*	*c*	*a*	*b*	*c*	
$NaLa_5(MoO_4)_8$	1.16	Monoclinic	5.45	5.37	11.93	5.36	5.35	11.88	61-0722
$NaPr_5(MoO_4)_8$*	1.126	Monoclinic	5.43	5.32	11.84	-----	----	----	30-1238
$NaNd_5(MoO_4)_8$	1.109	Monoclinic	5.40	5.31	11.82	5.29	5.28	11.68	61-0724
$NaSm_5(MoO_4)_8$	1.079	Monoclinic	5.35	5.26	11.71	5.25	5.251	11.56	60-0804

* Lattice parameters are not provided in the ICDD file

4.3.2 Raman spectroscopic studies

The laser Raman spectra of the compositions are given in Figure 4.4 a-d. The vibrations corresponding to $(MoO_4)^{2-}$ tetrahedra are identified in the laser Raman spectra of the samples. The $(MoO_4)^{2-}$ tetrahedra in the free-state has four fundamental modes of vibrations, namely, a nondegenerate symmetric stretching mode $v_1(A)$ at 894 cm^{-1}, a doubly degenerate symmetric bending mode $v_2(E)$ at 318 cm^{-1}, triply degenerate asymmetric stretching $v_3(F_2)$, and asymmetric bending $v_4(F_2)$ modes at 833 cm^{-1} and 381 cm^{-1}, respectively [25]. The deconvoluted Raman spectra are given in Figure 4.5 a-d.

The wavenumbers of the Raman bands and the assignment of stretching and bending modes of $(MoO_4)^{2-}$ tetrahedra are given in Table 4.2. The stretching vibrations of $(MoO_4)^{2-}$ tetrahedra are observed in the wavenumber range above 818 cm^{-1} and the bending vibrations in the wavenumber range from 314 cm^{-1} to 387 cm^{-1} for the ceramics under study. In the case of $NaLa_5(MoO_4)_8$ ceramic, the symmetric stretching vibrations (v_1) of $(MoO_4)^{2-}$ tetrahedra are observed as very strong broad band at 890 cm^{-1} together with a shoulder peak at 902 cm^{-1} and additional modes at 939 cm^{-1} and 967 cm^{-1} which clearly indicates the distortion of $(MoO_4)^{2-}$ molecules with distinct Mo-O bond lengths in the crystal structure. The bands corresponding to asymmetric stretching vibrations of $(MoO_4)^{2-}$ ions are found at 831 cm^{-1} and 750 cm^{-1}. The symmetric (v_2) and asymmetric (v_4) bending vibrations of $(MoO_4)^{2-}$ tetrahedra appeared at 317 cm^{-1} and 374 cm^{-1} respectively.
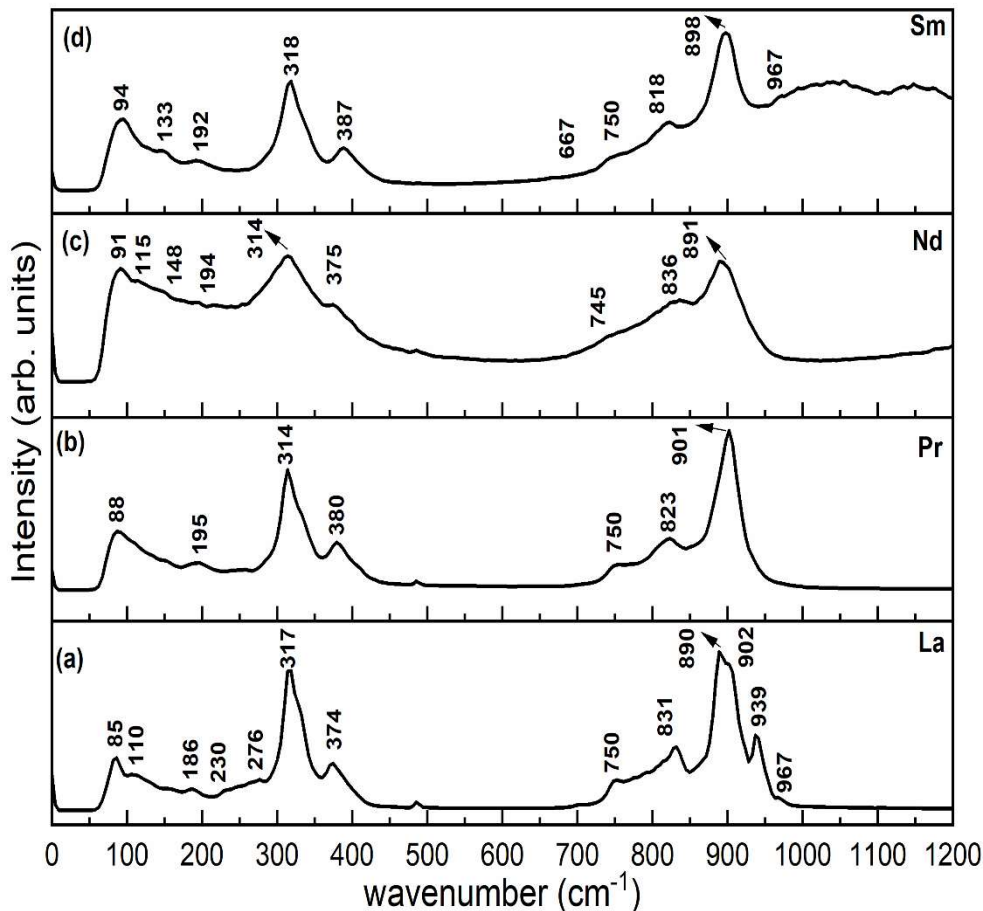
Figure 4.4 Laser Raman spectra of NaR$_5$(MoO$_4$)$_8$ (R = La, Pr, Nd and Sm) sintered ceramics

The presence of strong sharp symmetric stretching mode at 901 cm^{-1} for NaPr$_5$(MoO$_4$)$_8$ ceramic without additional modes is an indication of regular (MoO$_4$)$^{2-}$ group in the crystal structure. The bands corresponding to asymmetric stretching vibrations of (MoO$_4$)$^{2-}$ ions are found at 823 cm^{-1} and 750 cm^{-1}. The symmetric (υ_2) and asymmetric (υ_4) bending vibrations of (MoO$_4$)$^{2-}$ tetrahedra are appeared at 314 cm^{-1} and 380 cm^{-1} respectively. The symmetric stretching vibrations (υ_1) of (MoO$_4$)$^{2-}$ tetrahedra are observed as very broad peak at 891 cm^{-1} for the NaNd$_5$(MoO$_4$)$_8$ ceramic together with asymmetric stretching vibrations at 836 cm^{-1} and 745 cm^{-1}. The symmetric (υ_2) and asymmetric (υ_4) bending vibrations of (MoO$_4$)$^{2-}$ tetrahedra are appeared at 314 cm^{-1} and 375 cm^{-1} respectively.
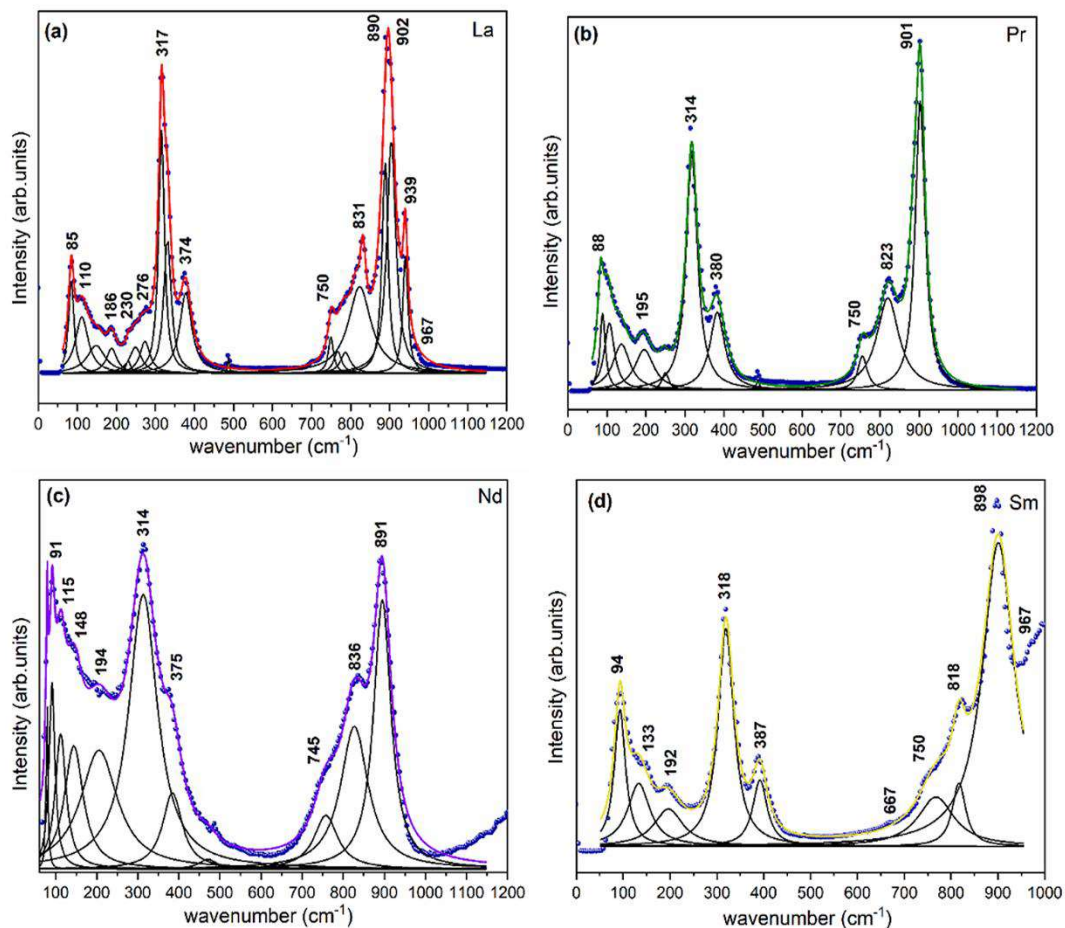
Figure 4.5 Deconvoluted Raman spectra of NaR$_5$(MoO$_4$)$_8$ (R = La, Pr, Nd and Sm) sintered ceramics

The symmetric stretching vibrations (υ_1) of (MoO$_4$)$^{2-}$ tetrahedra are observed as very strong band at 898 cm^{-1} for the NaSm$_5$(MoO$_4$)$_8$ ceramic together with weak modes above 967 cm^{-1}. The bands corresponding to asymmetric stretching vibrations of (MoO$_4$)$^{2-}$ tetrahedra are found at 818 cm^{-1} and 750 cm^{-1}. The symmetric (υ_2) bending vibrations of (MoO$_4$)$^{2-}$ tetrahedra appeared at 318 cm^{-1} and that of asymmetric (υ_4) bending vibrations at 387 cm^{-1}. The Raman bands below 250 cm^{-1} correspond to lattice-mode region and an unambiguous assignment of these bands are not possible [25-28].

Table 4.2 Raman mode assignments of $NaR_5(MoO_4)_8$ (R= La, Pr, Nd and Sm) ceramics

La (cm⁻¹)	Pr (cm⁻¹)	Nd (cm⁻¹)	Sm (cm⁻¹)	Assignments[*1,2]
967 vw 939 m 902 vs 890 vsbr	901 vs	891 sbr	967 w 898 vs	$\nu_s\,(MoO_4)^{2-}$
831 m 750 w	823 m 750 w	836 s 745 w	818 s 750 vw 667 vw	$\nu_{as}\,(MoO_4)^{2-}$
374 m	380 m	375 msh	387 mbr	$\delta_{as}\,(MoO_4)^{2-}$
317 sbr 276 w	314 s	314 sbr	318 s	$\delta_s\,(MoO_4)^{2-}$
230 w 186 w 110 w 85 m	195 w 88 m	194 w 148 w 115 w 91 m	192 w 133 w 94 m	Lattice-mode vibrations

[*1] ν_s – symmetric stretching ν_{as} – asymmetric stretching δ_{as} – asymmetric bending δ_s – symmetric bending

[*2] vs very strong; s strong; m medium; w weak; br broad; vw very weak; sh shoulder

4.3.3 Morphological studies

The secondary electron micrographs of the $NaR_5(MoO_4)_8$ (R = La, Pr, Nd and Sm) ceramics are given in Figure 4.6 a-d. These images show dense, uniform microstructure with polygonal grains of size 1 to 5 μm.
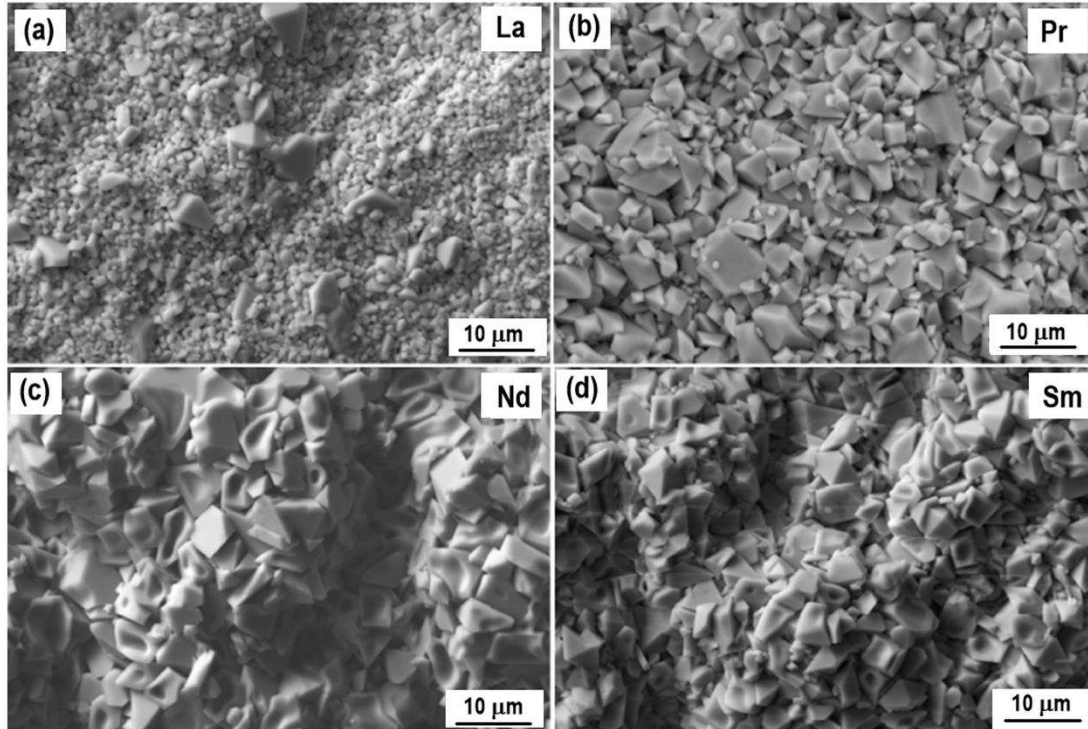
Figure 4.6 SEM micrographs of (a) $NaLa_5(MoO_4)_8$ ceramic sintered at 780°C/1h, (b) $NaPr_5(MoO_4)_8$ ceramic sintered at 780°C/1h, (c) $NaNd_5(MoO_4)_8$ ceramic sintered at 770°C/1h and (d) $NaSm_5(MoO_4)_8$ ceramic sintered at 760°C/1h

4.3.4 Microwave dielectric studies

$NaR_5(MoO_4)_8$ (R = La, Pr, Nd and Sm) ceramics exhibit excellent resonance at microwave frequencies. The sintering temperature, maximum sintered density and the microwave dielectric properties of the ceramics under study are given in Table 4.3. The variation of density and dielectric constant with sintering temperature for $NaR_5(MoO_4)_8$ (R = La, Pr, Nd and Sm) ceramics are shown in Figure 4.7 a-d. $NaLa_5(MoO_4)_8$ ceramic has a maximum sintered density of 4.3 g/cm^3 which is 91% of the theoretical density. $NaPr_5(MoO_4)_8$, $NaNd_5(MoO_4)_8$ and $NaSm_5(MoO_4)_8$ samples attain 94% of their theoretical density. The highest quality factor is obtained for $NaNd_5(MoO_4)_8$ ceramic with a $Q_u \times f$ value of 78,600 GHz and the lowest for $NaLa_5(MoO_4)_8$ ceramic with a $Q_u \times f$ value of 56,200 GHz. Maximum temperature coefficient of resonant frequency is exhibited by $NaLa_5(MoO_4)_8$ ceramic with a τ_f value of -72 ppm/°C and the lowest by $NaNd_5(MoO_4)_8$ ceramic with a τ_f value of -42 ppm/°C.

Table 4.3 Sintering temperature, maximum sintered density and microwave dielectric properties of $NaR_5(MoO_4)_8$ (R= La, Pr, Nd and Sm) ceramics

Compositions	Sintering temperature (ºC)/1h	Density (g/cm³)	ε_r @ GHz	$Q_u \times f$ (GHz)	τ_f (ppm/ºC)
$NaLa_5(MoO_4)_8$	780	4.3	11.5	56,200	-72
$NaPr_5(MoO_4)_8$	780	4.8	11.4	71,900	-52
$NaNd_5(MoO_4)_8$	770	4.8	11.1	78,600	-42
$NaSm_5(MoO_4)_8$	760	4.7	10.6	59,400	-51

The vibrational coherency and the strength of Mo-O bonds are reported to have a decisive role in determining the quality factor of the ceramics. A rigid atomic framework with less rattling of atoms increase the decay time of microwave energy in the material. The $NaLa_5(MoO_4)_8$ ceramic has additional modes in the symmetric stretching region of Raman spectra showing the presence of irregular $(MoO_4)^{2-}$ tetrahedra in the crystal structure. The low quality factor can be attributed to the disorder in the $(MoO_4)^{2-}$ structural unit. Whereas, the high quality factor obtained for $NaPr_5(MoO_4)_8$ ceramic can be attributed to the regular $(MoO_4)^{2-}$ tetrahedral arrangements in the crystal structure, which is evident from the presence of the sharp symmetric stretching modes in the Raman spectrum. $NaSm_5(MoO_4)_8$ ceramic has symmetric bell shaped curve for the stretching mode, but few additional modes can be seen at higher wavenumbers and hence has lesser quality factor compared to $NaPr_5(MoO_4)_8$ ceramic [29-33].
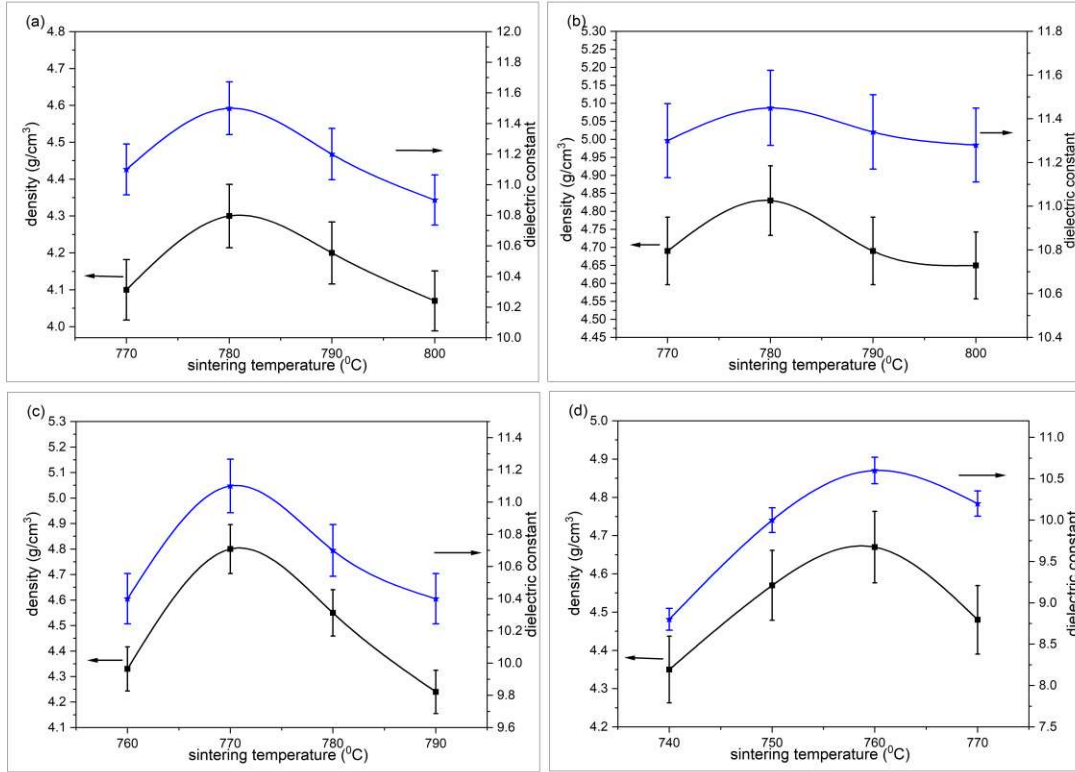
Figure 4.7 Variation of density and dielectric constant with sintering temperature for NaR$_5$(MoO$_4$)$_8$ (R = La, Pr, Nd and Sm) ceramics

The dielectric constant ε_r is correlated with the total ionic polarizability α_D and the variation of the same with the effective ionic radii [34] of the eight coordinated R^{3+} rare earth ion is given in Figure 4.8. The total ionic polarizability of NaR$_5$(MoO$_4$)$_8$ compositions are evaluated by the formula α_D (NaR$_5$(MoO$_4$)$_8$ = α_D (Na$^+$) + 5α_D (R^{3+}) + 8α_D (Mo^{6+}) + 32α_D (O^{2-}) taking into account the ionic polarizability values of the individual ions using Shannon additive rule. The ionic polarizability values are Na$^+$ (1.8 Å^3), La^{3+} (6.07 Å^3), Pr^{3+} (5.32 Å^3), Nd^{3+} (5.01 Å^3), Sm^{3+} (4.74 Å^3), Mo^{6+} (3.28 Å^3) and O^{2-} (2.01 Å^3) [35,36]. The dielectric constant ε_r decreases with the decrease in total ionic polarizability α_D of the constituent ions. The variation of resonant frequency with temperature for NaR$_5$(MoO$_4$)$_8$ (R= La, Pr, Nd, Sm) ceramics sintered at optimum sintering temperatures are given in Figure 4.9 a-d.
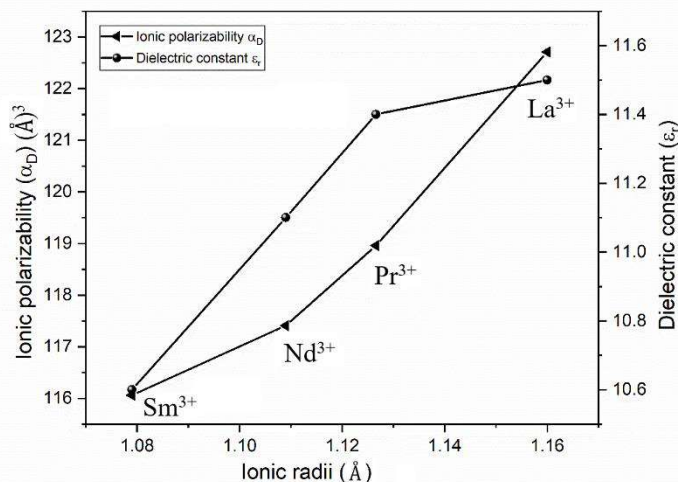
Figure 4.8 Variation of dielectric constant ε_r and total ionic polarizability α_D with ionic radii of R^{3+} rare earth ions in $NaR_5(MoO_4)_8$ (R = La, Pr, Nd, Sm) ceramics
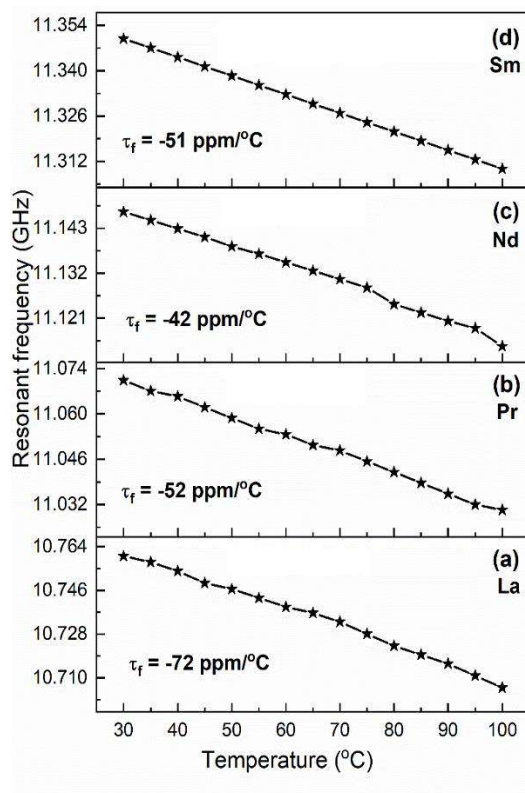
Figure 4.9 Variation of resonant frequency with temperature for $NaR_5(MoO_4)_8$ (R= La, Pr, Nd, Sm) ceramics sintered at optimum sintering temperature

4.3.5 Compatibility studies

The ceramics are co-fired with 20 wt% Ag at their respective optimum sintering temperatures. X-ray diffraction and energy dispersive X-ray spectroscopy analyses are used to determine the silver co-firability of these ceramics. The XRD patterns of

NaR$_5$(MoO$_4$)$_8$ (R = La, Pr, Nd and Sm) silver co-fired ceramics are given in Figure 4.10 a-d. The XRD patterns of the co-fired samples clearly show all the characteristic peaks of the ceramic, in addition to the peaks of silver marked with '*'. The co-firability of the ceramics are further ascertained by energy dispersive X-ray spectroscopy of the silver co-fired samples. The backscattered SEM micrograph of the NaLa$_5$(MoO$_4$)$_8$ ceramic co-fired with 20 wt% Ag at 780°C for 1h is shown in Figure 4.11 (a). The EDS point analysis spectra done at the silver region, marked as spot 1 and the ceramic region, marked as spot 2 are shown in Figure 4.11 (b) and (c). The spot 1 shows the presence of Ag alone whereas the EDS point analysis at spot 2 reveals the presence of Ag indicating the diffusion of silver into the ceramic matrix during co-firing. The EDS elemental mapping overlay on the image and the mapping of each element is given in Figure 4.12 and the EDS line scan is given in Figure 4.13. The co-fired silver is present as an island surrounded by the ceramic and the elemental colour mapping of Ag and Mo shows complementary appearance. The EDS line scan done across the silver region for the co-fired sample of NaLa$_5$(MoO$_4$)$_8$ ceramic shows rapid decrease of silver content at the interface between ceramic and silver.
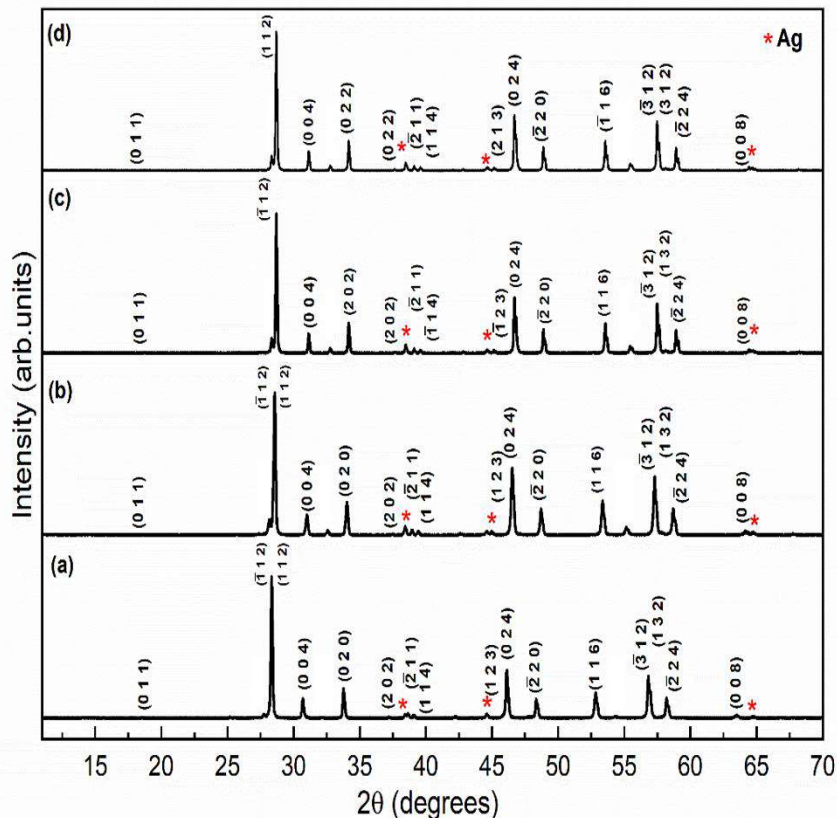
Figure 4.10 XRD patterns of 20 wt% Ag co-fired samples of NaR$_5$(MoO$_4$)$_8$

(R = La, Pr, Nd, Sm) ceramics
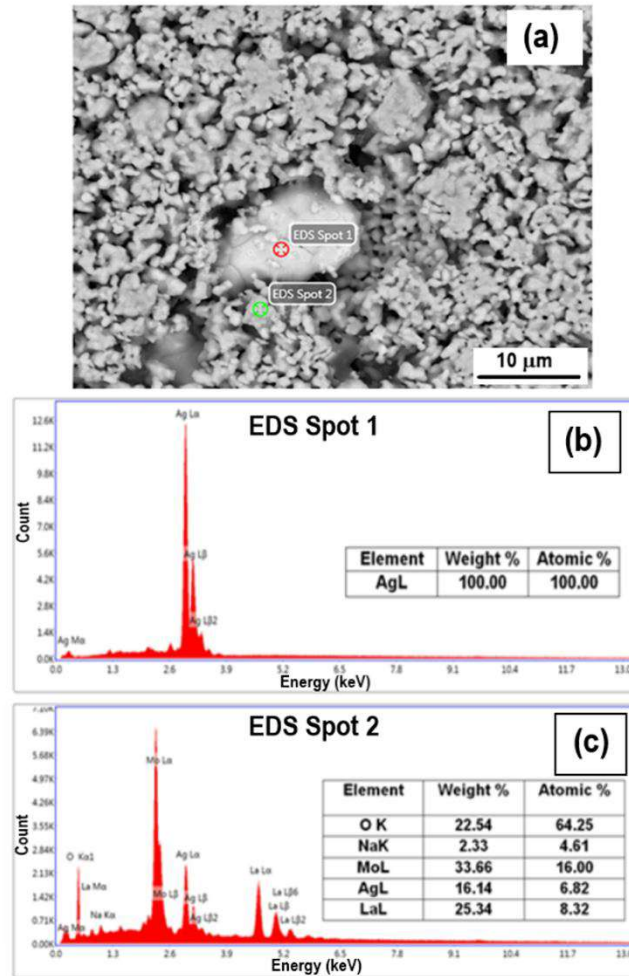
Figure 4.11 (a) Backscattered SEM image; EDS point analysis spectra at (b) spot 1 and (c) spot 2 of $NaLa_5(MoO_4)_8$ ceramic co-fired with 20 wt% Ag at optimum sintering temperature
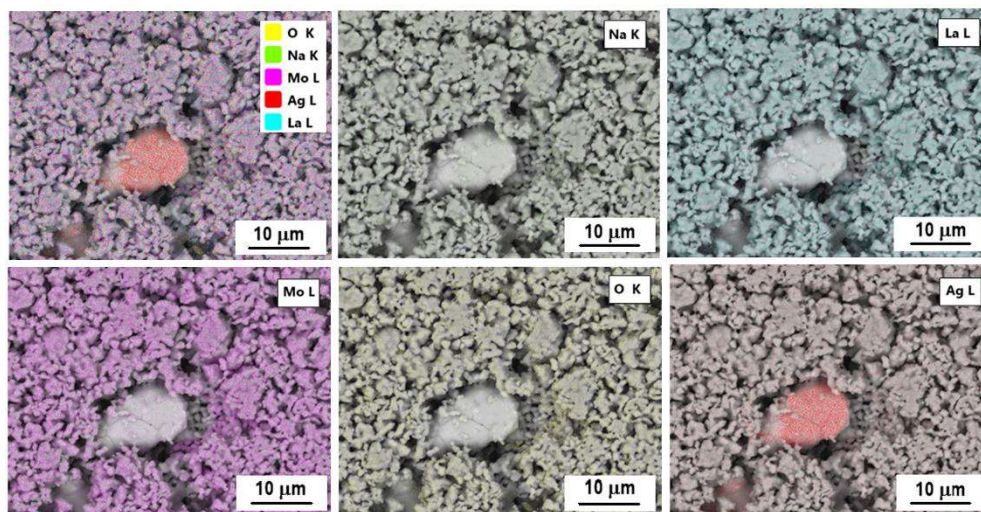
Figure 4.12 EDS elemental mapping of $NaLa_5(MoO_4)_8$ ceramic co-fired with 20 wt% Ag at optimum sintering temperature
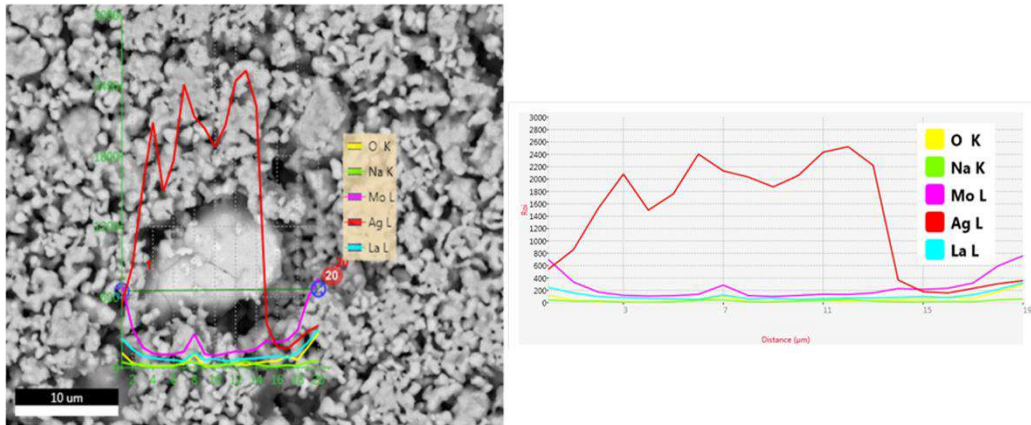
Figure 4.13 EDS line scan of $NaLa_5(MoO_4)_8$ ceramic co-fired with 20 wt% Ag at optimum sintering temperature

The backscattered SEM micrograph of the $NaPr_5(MoO_4)_8$ ceramic co-fired with silver along with the EDS point analysis results are given in Figure 4.14 a-c. The EDS elemental mapping image along with the mapping of each element is given in Figure 4.15 and the EDS line scan is given in Figure 4.16.
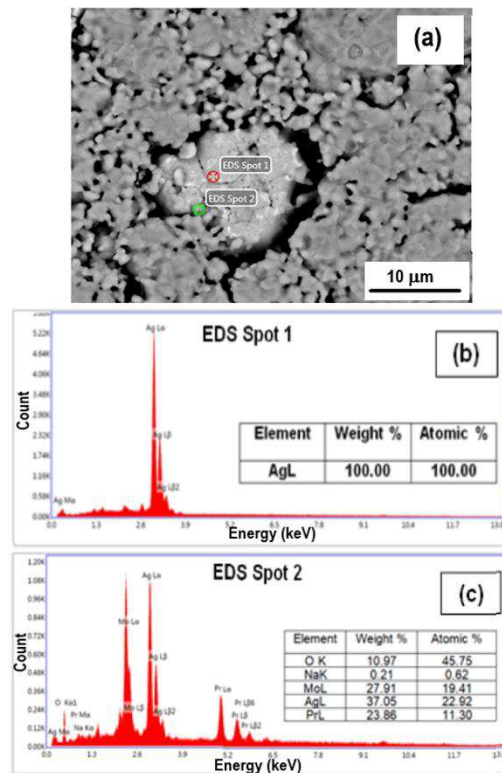
Figure 4.14 (a) Backscattered SEM image; EDS point analysis spectra at (b) spot 1 and (c) spot 2 of $NaPr_5(MoO_4)_8$ ceramic co-fired with 20 wt% Ag at optimum sintering temperature
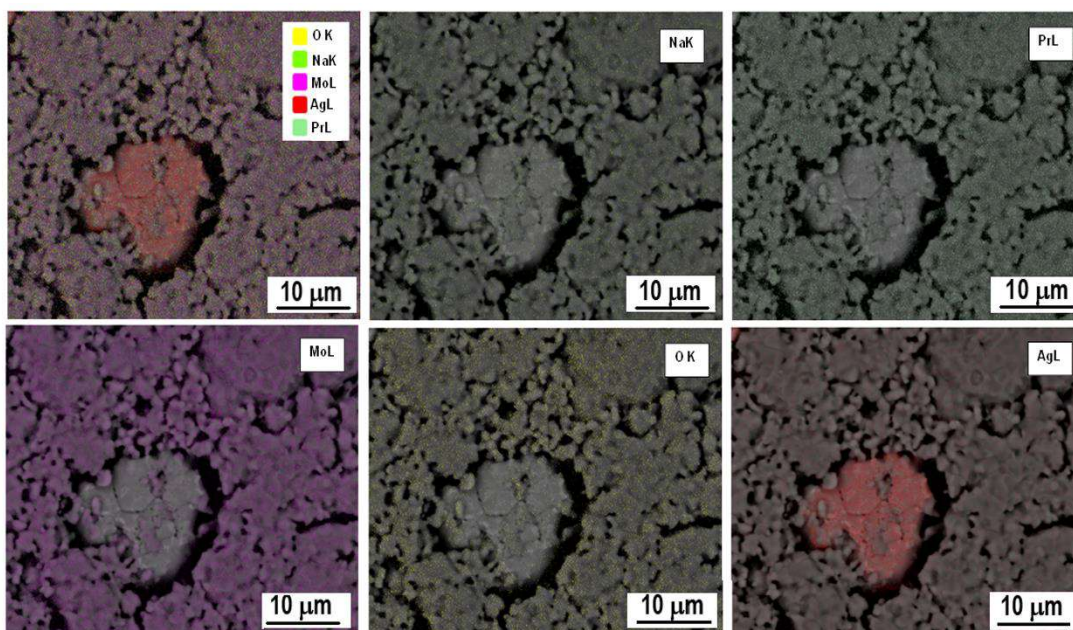
Figure 4.15 EDS elemental mapping of NaPr$_5$(MoO$_4$)$_8$ ceramic co-fired with 20 wt% Ag at optimum sintering temperature
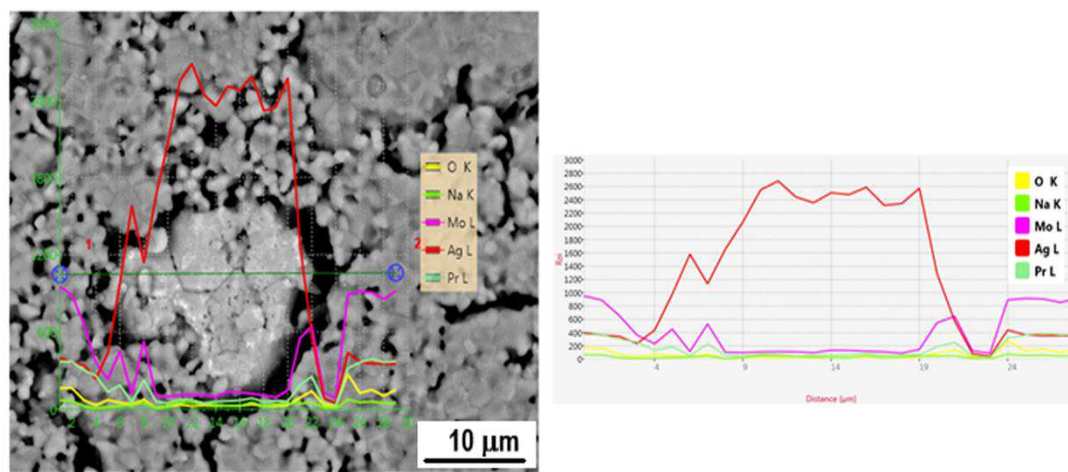
Figure 4.16 EDS line scan of NaPr$_5$(MoO$_4$)$_8$ ceramic co-fired with 20 wt% Ag at optimum sintering temperature

The backscattered SEM micrograph of the NaNd$_5$(MoO$_4$)$_8$ ceramic co-fired with silver along with the EDS point analysis results are given in Figure 4.17 a-c. The EDS elemental mapping image along with the mapping of each element is given in Figure 4.18 and the EDS line scan is given in Figure 4.19.
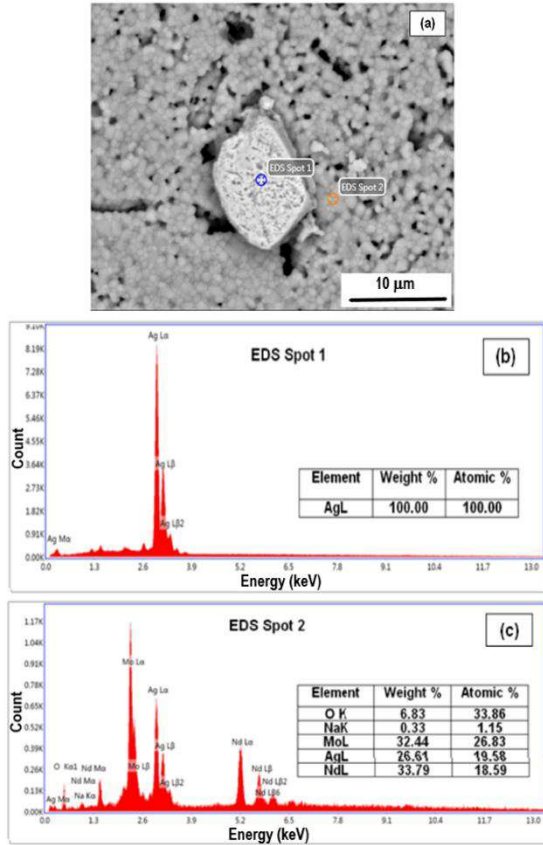
Figure 4.17 (a) Backscattered SEM image; EDS point analysis spectra at (b) spot 1 and (c) spot 2 of NaNd$_5$(MoO$_4$)$_8$ ceramic co-fired with 20 wt% Ag at optimum sintering temperature
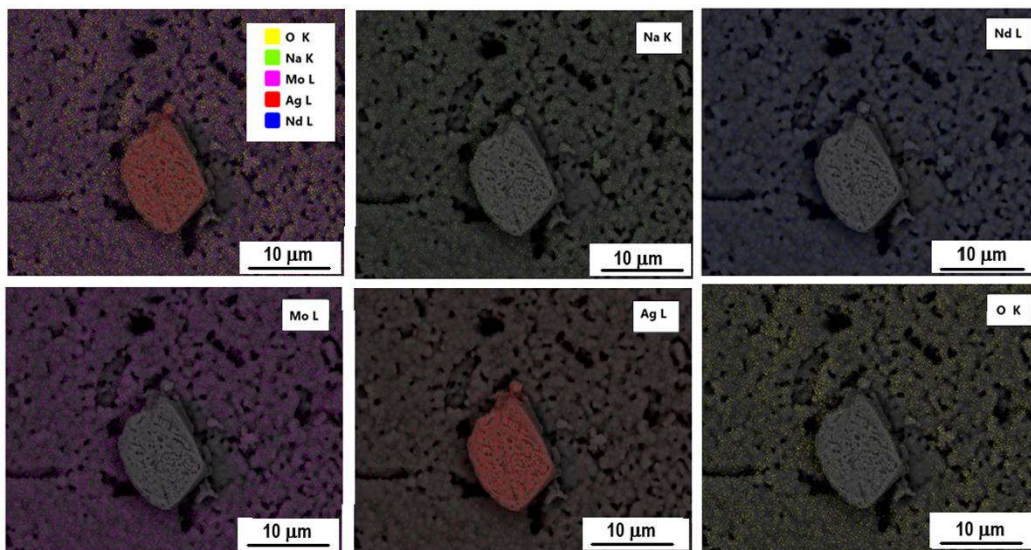
Figure 4.18 EDS elemental mapping of NaNd$_5$(MoO$_4$)$_8$ ceramic co-fired with 20 wt% Ag at optimum sintering temperature
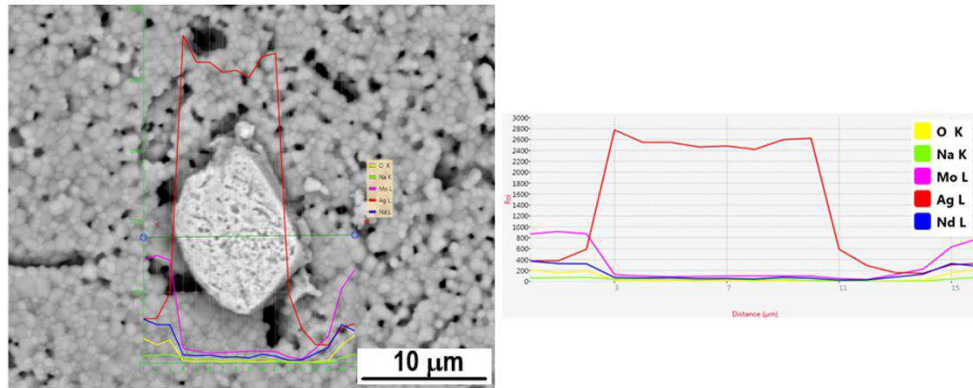
Figure 4.19 EDS line scan of NaNd$_5$(MoO$_4$)$_8$ ceramic co-fired with 20 wt% Ag at optimum sintering temperature

The backscattered SEM micrograph of the NaSm$_5$(MoO$_4$)$_8$ ceramic co-fired with silver along with the EDS point analysis results are given in Figure 4.20 a-c. The EDS elemental mapping overlay on image along with the mapping of each element is given in Figure 4.21 and the EDS line scan is given in Figure 4.22.
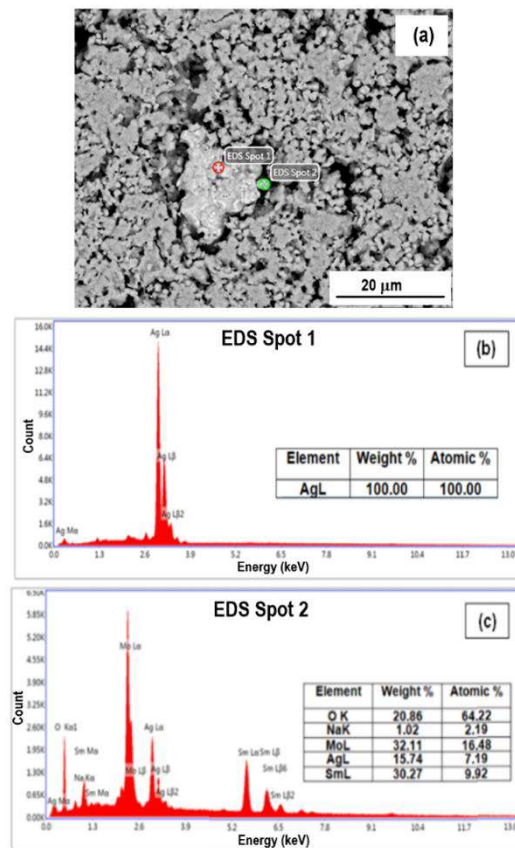
Figure 4.20 (a) Backscattered SEM image; EDS point analysis spectra at (b) spot 1 and (c) spot 2 of NaSm$_5$(MoO$_4$)$_8$ ceramic co-fired with 20 wt% Ag at optimum sintering temperature
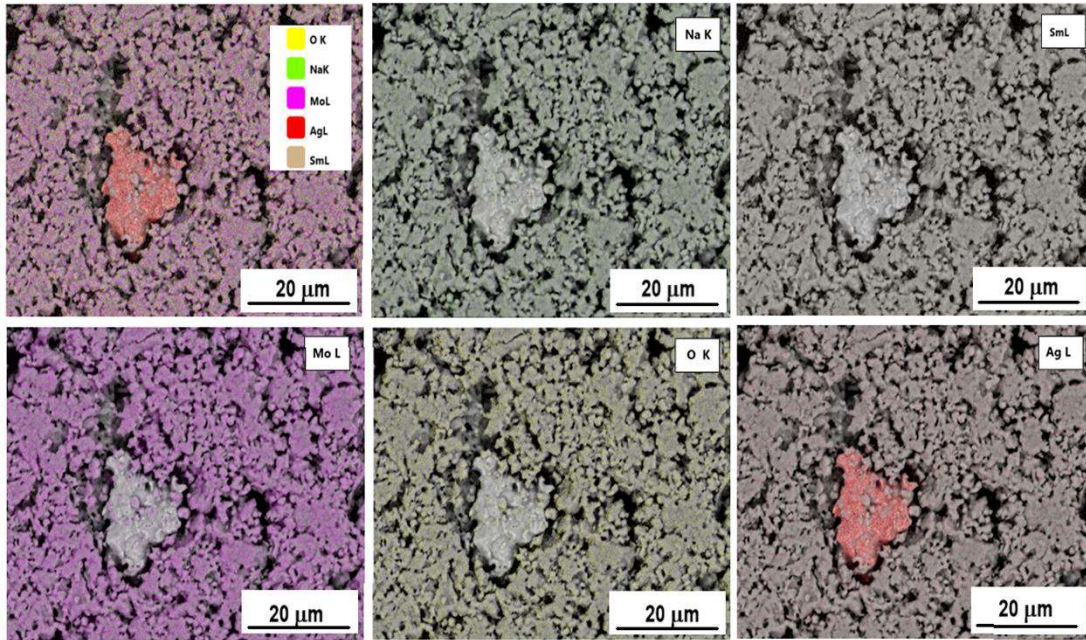
Figure 4.21 EDS elemental mapping of NaSm$_5$(MoO$_4$)$_8$ ceramic co-fired with 20 wt% Ag at optimum sintering temperature
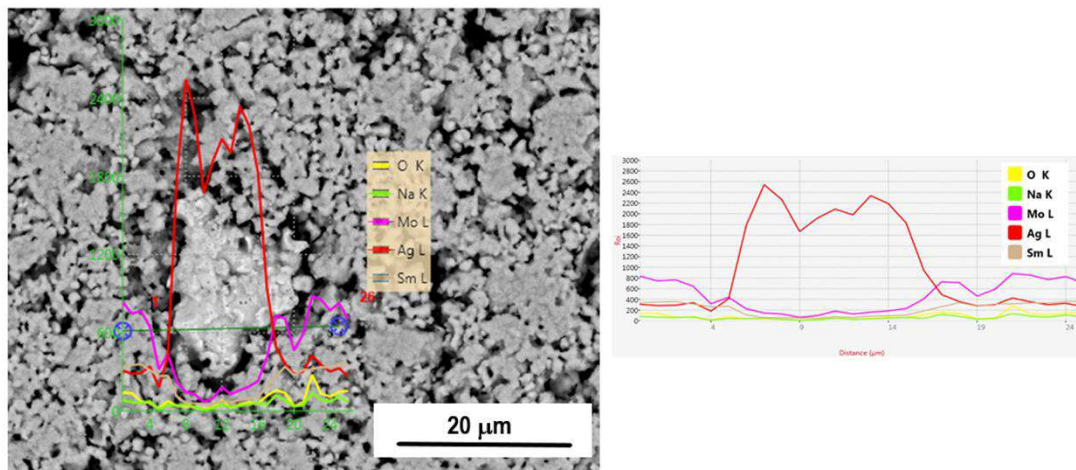
Figure 4.22 EDS line scan of NaSm$_5$(MoO$_4$)$_8$ ceramic co-fired with 20 wt% Ag at optimum sintering temperature

The EDS analysis clearly shows that the co-fired samples exhibit silver as an island surrounded by ceramic. The EDS point analysis at EDS spot 1 silver region of all the four co-fired samples shows the presence of silver alone, whereas the point analysis at ceramic region shows presence of silver in addition to ceramic. However, the EDS line scan shows sharp fall in silver content at the ceramic-silver interface. The silver diffusion into the ceramic on co-firing hinders the utility of these ceramics for

LTCC applications. However, owing to their excellent dielectric properties, the ceramics under study are ideal candidate materials for microwave circuit applications.

4.4 Conclusions

Phase pure $NaLa_5(MoO_4)_8$, $NaPr_5(MoO_4)_8$, $NaNd_5(MoO_4)_8$ and $NaSm_5(MoO_4)_8$ ceramics have been prepared by conventional solid-state ceramic route. The XRD patterns show isomorphous nature for the rare earth elements from La to Sm. The powder X-ray diffraction patterns exactly match with the ICDD data and the lattice parameters are calculated. The laser Raman spectral studies confirmed the presence of $(MoO_4)^{2-}$ tetrahedra in the molecular structure. The scanning electron micrographs show compact microstructure with phase homogeneity. All the samples show excellent microwave dielectric properties. $NaLa_5(MoO_4)_8$ ceramic shows ε_r of 11.5, Q_u x f of 56,200 GHz and τ_f of -72 ppm/°C whereas $NaPr_5(MoO_4)_8$ ceramic shows ε_r of 11.4, Q_u x f of 71,900 GHz and τ_f of -52 ppm/°C at maximum sintered density. $NaNd_5(MoO_4)_8$ ceramic shows ε_r of 11.1, Q_u x f of 78,600 GHz and τ_f of -42 ppm/°C whereas $NaSm_5(MoO_4)_8$ ceramic shows ε_r of 10.6, Q_u x f of 59,400 GHz and τ_f of -51 ppm/°C at maximum sintered density. X-ray diffraction and EDS analyses of the ceramics co-fired with 20 wt% silver show diffusion of silver into the ceramic. Hence, it can be concluded from the present study that $NaR_5(MoO_4)_8$ (R = La, Pr, Nd, Sm) ceramics are not suitable for LTCC applications. However considering their excellent microwave dielectric properties these materials can be used as substrates for microwave circuit applications.

References

[1]   P. M. De Wolff, The pseudo-symmetry of modulated crystal structures, Acta Crystallogr. A, 30 [6] (1974) 777-785.

[2]   W. Van Aalst, J. Den Holander, W. J. A. M. Peterse, P. M. De Wolff, The modulated structure of γ-Na_2CO_3 in a harmonic approximation, Acta Crystallogr. B, 32 [1] (1976) 47-58.

[3]   A. Arakcheeva, G. Chapuis, A reinterpretation of the phase transitions in Na_2CO_3, Acta Crystallogr. B, 61 [6] (2005) 601-607.

[4]   E. Brouns, J. W. Visser, P. M. De Wolff, An anomaly in the crystal structure of Na_2CO_3, Acta Cryst., 17 [5] (1964) 614-614.

[5]   M. Dušek, G. Chapuis, M. Meyer, V. Petricek, Sodium carbonate revisited, Acta Crystallogr. B, 59 [3] (2003) 337-352.

[6]   G. Chapuis, Crystallographic excursion in superspace, Cryst. Eng., 6 [4] (2003) 187-195.

[7]   T. Janssen, G. Chapuis, M. De Boissieu, *Aperiodic Crystals: From Modulated Phases to Quasicrystals: Structure and Properties*, Oxford University Press (2018).

[8]   A. Arakcheeva, G. Chapuis, V. Petricek, V. Morozov, The role of second coordination-sphere interactions in incommensurately modulated structures, using β-$K_5Yb(MoO_4)_4$ as an example, Acta Crystallogr. B, 61 [4] (2005) 400-406.

[9]   S. Van Smaalen, Incommensurate crystal structures, Crystallogr. Rev., 4 [2] (1995) 79-202.

[10]   A. Arakcheeva, L. Bindi, P. Pattison, N. Meisser, G. Chapuis, I. Pekov, The incommensurately modulated structures of natural natrite at 120 and 293 K from synchrotron X-ray data, Am. Mineral., 95 [4] (2010) 574-581.

[11]   V. A. Morozov, A. V. Arakcheeva, G. Chapuis, N. Guiblin, M. D. Rossell, G. Van Tendeloo, $KNd(MoO_4)_2$: a new incommensurate modulated structure in the scheelite family, Chem. Mater., 18 [17] (2006) 4075-4082.

[12]   A. Arakcheeva, P. Pattison, G. Chapuis, M. Rossell, A. Filaretov, V. Morozov, G. Van Tendeloo, $KSm(MoO_4)_2$, an incommensurately modulated and partially disordered scheelite-like structure, Acta Crystallogr. B, 64 [2] (2008) 160-171.

[13]   A. Arakcheeva, G. Chapuis, Getting more out of an incommensurately modulated structure: the example of $K_5Yb(MoO_4)_4$, Acta Crystallogr. B, 62 [1] (2006) 52-59.

[14]   A. Arakcheeva, G. Chapuis, Capabilities and limitations of a (3+d)-dimensional incommensurately modulated structure as a model for the derivation of an extended family of compounds: example of the scheelite-like structures, Acta Crystallogr. B, 64 [1] (2008) 12-25.

[15]   V. Morozov, A. Arakcheeva, B. Redkin, V. Sinitsyn, S. Khasanov, E. Kudrenko, M. Raskina, O. Lebedev, G. Van Tendeloo, $Na_{2/7}Gd_{4/7}MoO_4$: a modulated scheelite-type structure and conductivity properties, Inorg. Chem., 51 [9] (2012) 5313-5324.

[16]   V. A. Morozov, A. V. Mironov, B. I. Lazoryak, E. G. Khaikina, O. M. Basovich, M. D. Rossell, G. Van Tendeloo, $Ag_{1/8}Pr_{5/8}MoO_4$: An incommensurately modulated scheelite-type structure, J. Solid State Chem., 179 [4] (2006) 1183-1191.

[17]   T. P. Rybakova, V. K. Trunov, The sodium molybdate-rare earth molybdate systems, Russ. J. Inorg. Chem., 19 [6] (1974) 888-890.

[18]   P. Jiang, W. Gao, R. Cong, T. Yang, Structural investigation of the A-site vacancy in scheelites and the luminescence behavior of two continuous solid solutions $A_{1-1.5x}Eu_x\square_{0.5x}WO_4$ and $A_{0.64-0.5y}Eu_{0.24}Li_y\square_{0.12-0.5y}WO_4$ (A= Ca,Sr; $\square$= vacancy), Dalton Trans., 44 [13] (2015) 6175-6183.

[19]   V. A. Morozov, A. V. Arakcheeva, P. Pattison, K. W Meert, P. F. Smet, D. Poelman, N. Gauquelin, J. Verbeeck, A. M. Abakumov, J. Hadermann, $KEu(MoO_4)_2$: polymorphism, structures, and luminescent properties, Chem. Mater., 27 [16] (2015) 5519-5530.

[20]   A. Arakcheeva, D. Logvinovich, G. Chapuis, V. Morozov, S. V. Eliseeva, J. C. G. Bünzli, P. Pattison, The luminescence of $Na_xEu^{3+}_{(2-x)/3}MoO_4$ scheelites depends on the number of Eu-clusters occurring in their incommensurately modulated structure, Chem. Sci., 3 [2] (2012) 384-390.

[21]   V. K. Trunov, A. A. Evdokimov, T. P. Rybakova, T. A. Berezina, Double tungstates and molybdates of lithium and sodium with the rare earth elements having the scheelite structure, Russ. J. Inorg. Chem., 24 [1] (1979) 93-97.

[22]   J. Dhanya, E. K. Suresh, R. Naveenraj, R. Ratheesh, Synthesis and characterization of $Na_5M(MoO_4)_4$ (M=Y,Yb) microwave ceramics for ULTCC applications, Ceram. Int., 44 [6] (2018) 6699-6704.

[23]   B. W. Hakki, P. D. Coleman, A dielectric resonator method of measuring inductive capacities in the millimeter range, IRE Trans. Microwave Theory Tech., 8 [4] (1960) 402-410.

[24]   J. Krupka, K. Derzakowski, B. Riddle, J. B. Jarvis, A dielectric resonator for measurements of complex permittivity of low loss dielectric materials as a function of temperature, Meas. Sci. Technol., 9 [10] (1998) 1751-1756.

[25]   N. K. James, R. Ratheesh, Microwave dielectric properties of low-temperature sinterable $BaCe_2(MoO_4)_4$ ceramics, J. Am. Ceram. Soc., 93 [4] (2010) 931-933.

[26]   F. D. Hardcastle, I. E. Wachs, Determination of molybdenum–oxygen bond distances and bond orders by Raman spectroscopy, J. Raman Spectrosc., 21 [10] (1990) 683-691.

[27]   F. D. Hardcastle, I. E. Wachs, Molecular structure of molybdenum oxide in bismuth molybdates by Raman spectroscopy, J. Phys. Chem., 95 [26] (1991) 10763-10772.

[28]   A. Surjith, R. Ratheesh, High Q ceramics in the $ACe_2(MoO_4)_4$ (A= Ba, Sr and Ca) system for LTCC applications, J. Alloys Compd., 550 (2013) 169-172.

[29]   V. L. Vilesh, G. Subodh, Crystal structure, phonon modes and dielectric properties of B site ordered $ABiLiTeO_6$ (A= Ba, Sr) double perovskites, Ceram. Int., 44 [11] (2018) 12036-12041.

[30]   S. D. Ramarao, S. R. Kiran, V. R. K. Murthy, Structural, lattice vibrational, optical and microwave dielectric studies on $Ca_{1-x}Sr_xMoO_4$ ceramics with scheelite structure, Mater. Res. Bull., 56 (2014) 71-79.

[31]   M. Y. Chen, C. T. Chia, I. N. Lin, L. J. Lin, C. W. Ahn, S. Nahm, Microwave properties of $Ba(Mg_{1/3}Ta_{2/3})O_3$, $Ba(Mg_{1/3}Nb_{2/3})O_3$ and $Ba(Co_{1/3}Nb_{2/3})O_3$ ceramics revealed by Raman scattering, J. Eur. Ceram. Soc., 26 [10-11] (2006)1965-1968.

[32]   J. Zhang, J. Zhai, J. Wang, J. Shao, X. Lu, X. Yao, Infrared dielectric response and Raman spectra of tunable $Ba_{0.5}Sr_{0.5}TiO_3$–Mg_2TiO_4 composite ceramics, J. Appl. Phys. 107 [1] (2010) 014106.

[33]   F. Shi, H. Dong, Correlation of crystal structure, dielectric properties and lattice vibration spectra of $(Ba_{1-x}Sr_x)(Zn_{1/3}Nb_{2/3})O_3$ solid solutions, Dalton Trans., 40 [25] (2011) 6659-6667.

[34]   R. D. Shannon, Revised effective ionic radii and systematic studies of interatomic distances in halides and chalcogenides, Acta Crystallogr. A, 32 [5] (1976) 751-767.

[35]   S. D. Ramarao, V. R. K. Murthy, Structural, Raman spectroscopic and microwave dielectric studies on $Ni_{1-x}(Zn_{1/2}Zr_{1/2})_xW_{1-x}Nb_xO_4$ ceramic compounds with wolframite structure, Dalton Trans., 44 [5] (2015) 2311-2324.

[36]   R. D. Shannon, Dielectric polarizabilities of ions in oxides and fluorides, J. Appl. Phys., 73 [1] (1993) 348-366.

Chapter 5

Structure and microwave dielectric properties of $Na_2A_5(MoO_4)_6$ (A = Zn, Mg, Ca, Sr and Ba) ultra low temperature co-firable ceramics

5.1 Introduction

5.2 Materials and methods

5.3 Results and discussion

5.4 Conclusions

Some of the contents of this chapter have been published in

5.1 Introduction

Klevtsova et al. have reported the preparation of single crystals of double molybdates $Na_2A_5(MoO_4)_6$ (A = Mg, Zn, Co) and studied the X-ray diffraction patterns in detail [1-3]. $Na_2Zn_5(MoO_4)_6$ and $Na_2Mg_5(MoO_4)_6$ are isostructural and belong to triclinic crystal structure with space group $P\bar{1}$. The reported crystal structure data of $Na_2Zn_5(MoO_4)_6$ and $Na_2Mg_5(MoO_4)_6$ are given in Table 5.1. The crystal structure of $Na_2Mg_5(MoO_4)_6$ is shown in Figure 5.1. The crystal structure of $Na_2Mg_5(MoO_4)_6$ is reported to have NaO_6 octahedra, two types of Mg atoms forming distorted octahedra with Mg-O distances varying in the range 2.003-2.175 Å. Mo atoms occupy three different crystallographical positions with tetrahedral coordination [3].
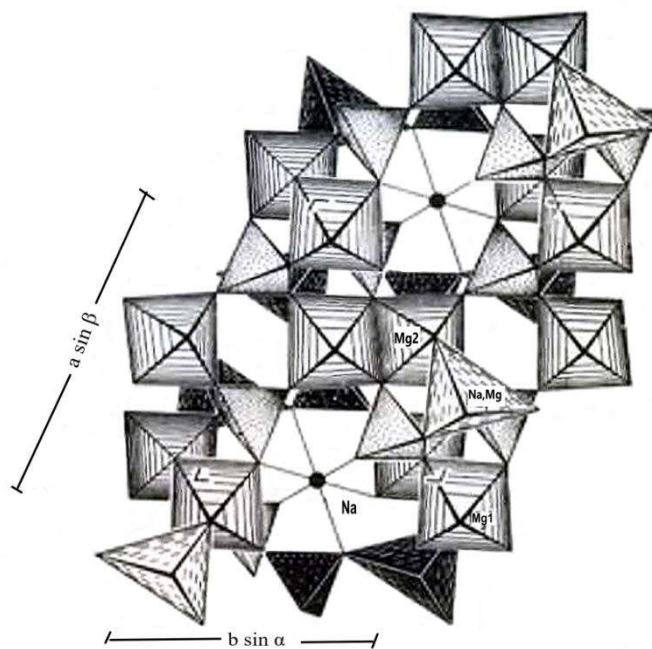
Figure 5.1 Structure of $Na_2Mg_5(MoO_4)_6$ along the c axis [Ref. 3]

The pairs of MgO_6 octahedra have shared common edges and are linked by the MoO_4 tetrahedra to form a 3D framework. The seven cation positions are fully occupied and there are no cation vacancies. The electrical neutrality of the molecule is maintained by the statistical distribution of 1 Na and 1 Mg atom in the general position, forming five-pointed polyhedron [3-9]. Zhang et al. have reported the optical properties of Cr^{3+} doped $Na_2Mg_5(MoO_4)_6$ single crystals [5].

Table 5.1 Crystal structure data of $Na_2A_5(MoO_4)_6$ (A = Zn, Mg) compositions

Compositions	Crystal structure	Space group	Z	a(Å)	b(Å)	c(Å)	ICDD card nos
$Na_2Zn_5(MoO_4)_6$	Triclinic	$P\bar{1}$	6	10.70	8.610	6.99	35-0312
$Na_2Mg_5(MoO_4)_6$	Triclinic	$P\bar{1}$	6	10.57	8.617	6.951	73-0003

The phase diagrams of Na_2MoO_4-$CaMoO_4$, Na_2MoO_4-$SrMoO_4$ and Na_2MoO_4-$BaMoO_4$ systems are reported by Petrosyan et al. [10]. The Na_2MoO_4-$CaMoO_4$, Na_2MoO_4-$SrMoO_4$ and Na_2MoO_4-$BaMoO_4$ systems are reported to behave as a simple eutectic with composition 92, 96.5 and 91 mole% of Na_2MoO_4 with eutectic melting points 685°C, 687°C and 714°C respectively. The melting point of Na_2MoO_4, $CaMoO_4$, $SrMoO_4$ and $BaMoO_4$ are 690°C, 1445°C, 1460°C and 1460°C respectively. The eutectic melting point is lower than the melting point of the constituent compounds. The polymorphism of Na_2MoO_4 plays an important role in the feasibility of phase formations in the $Na_2A_5(MoO_4)_6$ (A = Ca, Sr and Ba) system. Compositions analogous to $Na_2A_5(MoO_4)_6$ are not reported in the Na_2MoO_4-$CaMoO_4$, Na_2MoO_4 -$SrMoO_4$ and Na_2MoO_4-$BaMoO_4$ phase diagrams. Finite solid solutions are formed in the Na_2MoO_4-$CaMoO_4$ phase diagram with maximum of 9% solubility of $CaMoO_4$ in δ-Na_2MoO_4 and 3% in γ-Na_2MoO_4. These solid solutions are reported to decompose to initial phases on cooling [10].

In the present study, $Na_2A_5(MoO_4)_6$ (A = Zn, Mg, Ca, Sr and Ba) ceramics are prepared by solid-state ceramic route and structural and microwave dielectric characterizations have been done. The chemical compatibility of these ceramics with Al is determined using XRD and EDS analyses to understand their suitability for multilayer circuit applications.

5.2 Materials and methods

$Na_2A_5(MoO_4)_6$ (A = Zn, Mg, Ca, Sr and Ba) ceramics were prepared by conventional solid-state ceramic route. The starting materials Na_2CO_3 (99%, Merck), ZnO (99%, Sigma Aldrich), MgO (99%, Aldrich), $CaCO_3$ (99+%, Sigma Aldrich), $SrCO_3$ (99.9%, Himedia), $BaCO_3$ (99+%, Sigma Aldrich) and MoO_3 (99%, Himedia) were taken in stoichiometric proportions and mixed thoroughly in an agate mortar using

distilled water as medium for an hour. The slurry was dried at 100°C in a hot air oven and ground well. The powder samples were then transferred into an alumina crucible and calcined at 500°C for one hour in a programmable SiC furnace. 5 wt% PVA (Polyvinyl alcohol) solution was added to the finely ground calcined powder as binder, dried and pressed into pellets in a 11 mm tungsten carbide die using a hydraulic hand press under a pressure of 250 MPa. The green pellets were sintered at appropriate temperatures in the range 510 to 650°C for an hour to get maximum experimental density. The bulk density of the sintered samples were determined from dimensional methods. Crystal structure and phase purity of the samples were studied by powder X-ray diffraction (XRD) measurement using CuKα radiation with Brucker Model 5005 X-ray diffractometer, Germany. Carl Zeiss, Model No: EVO18 Research, Germany scanning electron microscope with energy dispersive X-ray spectroscopy (EDS) facility was used to study the surface morphology as well as the chemical compatibility of the ceramic samples with Al electrode. The TGA/DTA measurements were carried out by high performance simultaneous TGA & DTA/DSC equipment setsys evolution par setaram. The shrinkage behaviour was determined using thermomechanical analyzer Model EXSTAR 6000 manufactured by SII Nano Technology INC., Japan. Raman spectra of the compositions were recorded using a Thermo Scientific DXR with Nd:YVO$_4$ DPSS laser of 532 nm. A Vector Network Analyzer (Agilent make PNA E8362B, Bayan Lepas, Malaysia) was used to measure the microwave dielectric properties of the well sintered ceramics. The dielectric constant of the sample was measured by Hakki and Coleman post resonator technique [11] and the quality factor was measured by resonant cavity method [12]. The temperature coefficient of resonant frequency τ_f of the ceramics was also measured in the temperature range 30–100°C by noting the variation of the TE$_{01\delta}$ mode frequency with temperature.

5.3 Results and discussion

5.3.1 TG/DTA studies

The phase formation in the Na$_2$MoO$_4$-AMoO$_4$ (A = Zn, Mg, Ca, Sr, Ba) systems can be ascertained by Thermogravimetry and Differential thermal analysis (TG/DTA). The TG/DTA curves of the Na$_2$Zn$_5$(MoO$_4$)$_6$ and Na$_2$Mg$_5$(MoO$_4$)$_6$ ceramics are shown in Figures 5.2 and Figure 5.3 respectively.
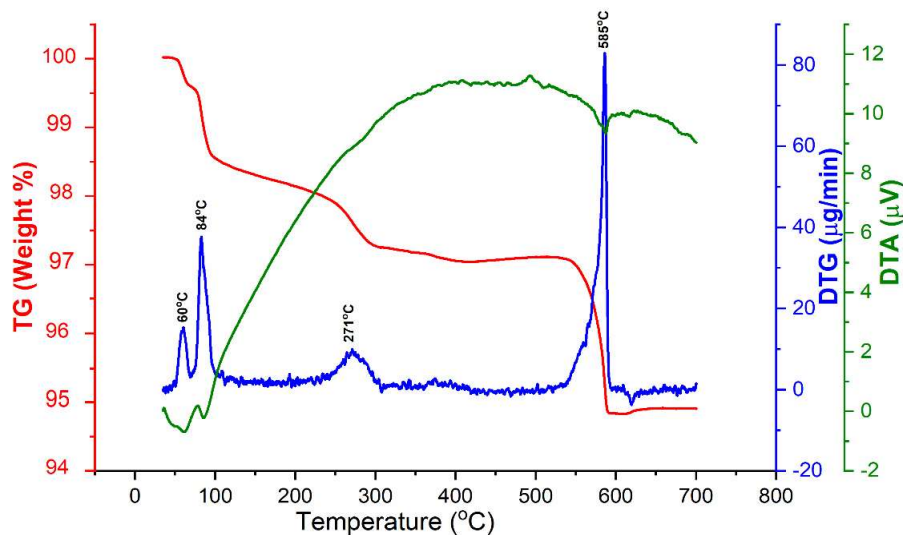
Figure 5.2 TG/DTA curves of $Na_2Zn_5(MoO_4)_6$ ceramic

Figure 5.2 depicts TG curve showing weight percentage of the sample as a function of temperature ramp representing the rate of decomposition reaction and DTG curve which is a derivative of the TG curve in μg/min, representing the rate of decomposition reaction. The TG/DTA curves of $Na_2Zn_5(MoO_4)_6$ ceramic was recorded from room temperature 30°C to 700°C at a rate of 10°C/min in air atmosphere. The TG curve of the sample manifests multistage decomposition with relatively stable intermediate products. The DTG curve of the sample shows peaks at 60°C, 84°C, 271°C and 585°C. Endotherms are observed in the DTA curve at corresponding temperatures. The sample showed rapid initial mass loss due to desorption of water molecules at 60°C and 84°C. The peak at 271°C represents an intermediate reaction stage followed by removal of CO_2 and phase formation at 585°C.
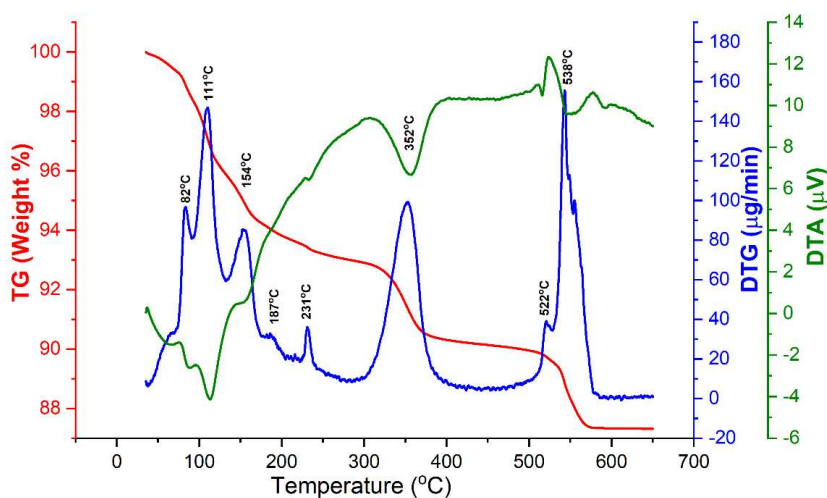
Figure 5.3 TG/DTA curves of $Na_2Mg_5(MoO_4)_6$ ceramic

The TG/DTA curves of $Na_2Mg_5(MoO_4)_6$ ceramic was recorded from room temperature 30°C to 650°C at a rate of 10°C/min in air atmosphere. The mass loss pattern followed by $Na_2Mg_5(MoO_4)_6$ is different compared to $Na_2Zn_5(MoO_4)_6$. The DTG curve of the sample showed peaks at 82°C, 111°C, 154°C, 187°C, 231°C, 352°C, 522°C and 538°C. Unlike $Na_2Zn_5(MoO_4)_6$, $Na_2Mg_5(MoO_4)_6$ showed a peak at 352°C which can be attributed to the release of hydroxyl groups adsorbed by MgO. MgO is reported to have hydrophilic nature and adsorbs water and form $Mg(OH)_2$ phase, which decomposes on heating [13]. The sharp DTG peak at 538°C shows the removal of CO_2 followed by phase formation.

The TG/DTA curves of the $Na_2Ca_5(MoO_4)_6$, $Na_2Sr_5(MoO_4)_6$ and $Na_2Ba_5(MoO_4)_6$ ceramics are shown in Figures 5.4, 5.5 and 5.6 respectively.
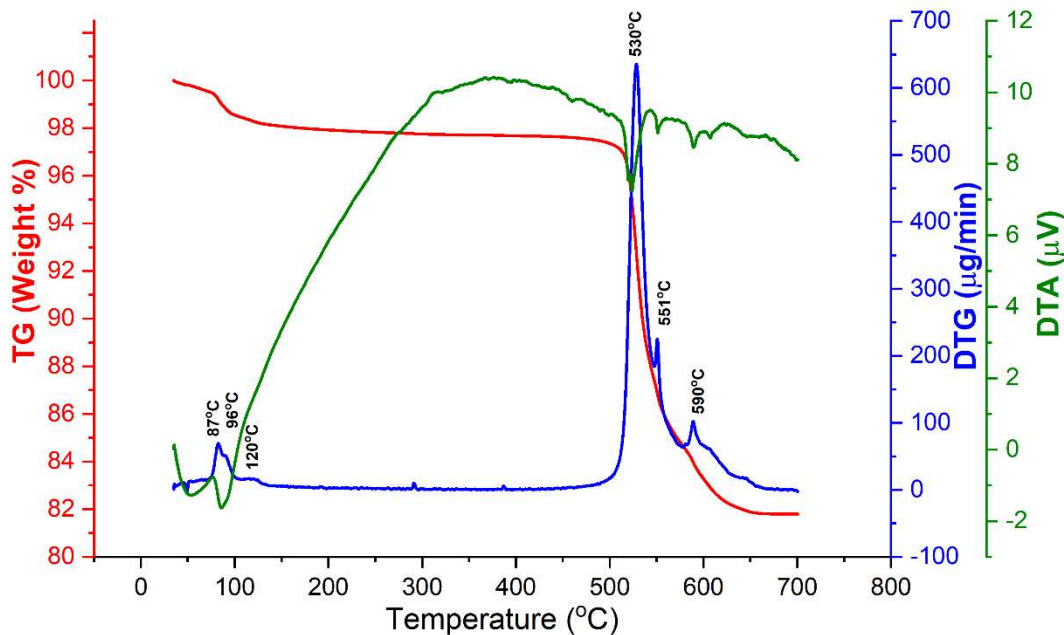
Figure 5.4 TG/DTA curves of $Na_2Ca_5(MoO_4)_6$ ceramic

Figure 5.4 shows the TG/DTA curves of $Na_2Ca_5(MoO_4)_6$ recorded from room temperature 30°C to 700°C at a rate of 10 °C/min in air atmosphere. The DTG curve of the sample shows peaks at 87°C, 96°C, 120°C, 530°C, 551°C and 590°C.
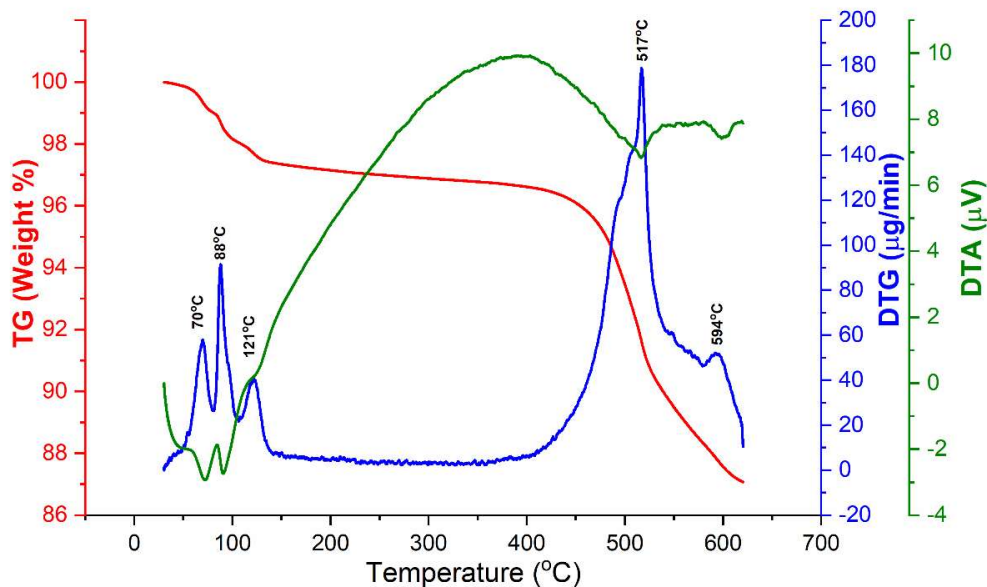
Figure 5.5 TG/DTA curves of $Na_2Sr_5(MoO_4)_6$ ceramic

Figure 5.5 shows the TG/DTA curves of $Na_2Sr_5(MoO_4)_6$ recorded from room temperature 30°C to 620°C at a rate of 10°C/min in air atmosphere. The DTG curve of the sample shows peaks at 70°C, 88°C, 121°C, 517°C and 594°C.
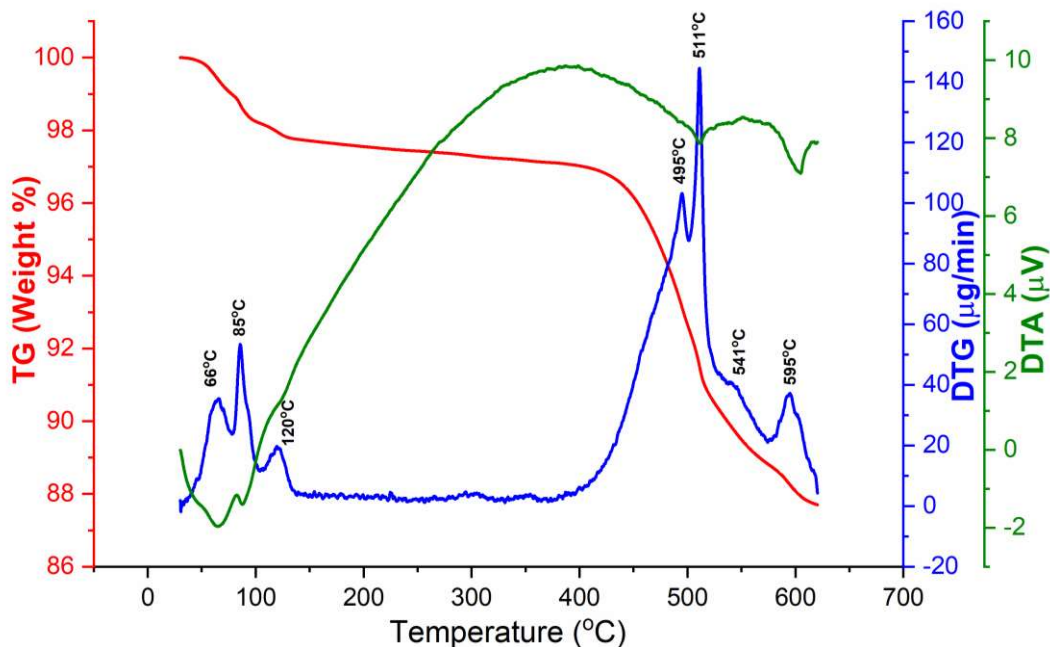
Figure 5.6 TG/DTA curves of $Na_2Ba_5(MoO_4)_6$ ceramic

Figure 5.6 shows the TG/DTA curves of $Na_2Ba_5(MoO_4)_6$ recorded from room temperature 30°C to 620°C at a rate of 10°C/min in air atmosphere. The DTG curve of the sample shows peaks at 66°C, 85°C, 120°C, 495°C, 511°C, 541°C and 595°C. These peaks represent multiple phase formation during heating cycle.

5.3.2 Powder X-ray diffraction studies

The powder X-ray diffraction patterns of $Na_2Zn_5(MoO_4)_6$ and $Na_2Mg_5(MoO_4)_6$ ceramics are shown in Figures 5.7 and 5.8 respectively. $Na_2Zn_5(MoO_4)_6$ and $Na_2Mg_5(MoO_4)_6$ have triclinic crystal structure with space group $P\bar{1}$. The XRD pattern of $Na_2Zn_5(MoO_4)_6$ is indexed using standard ICDD file no. 35-0312 which has structure data only upto 2θ value of $41°$ and that of $Na_2Mg_5(MoO_4)_6$ matches with the standard ICDD file no. 73-0003 which has structure data only upto 2θ value of $58°$.
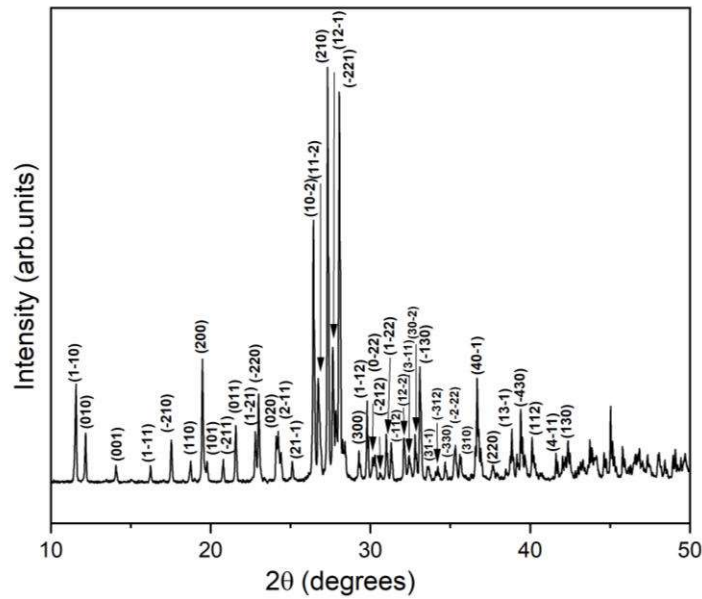
Figure 5.7 XRD pattern of $Na_2Zn_5(MoO_4)_6$ sintered ceramic
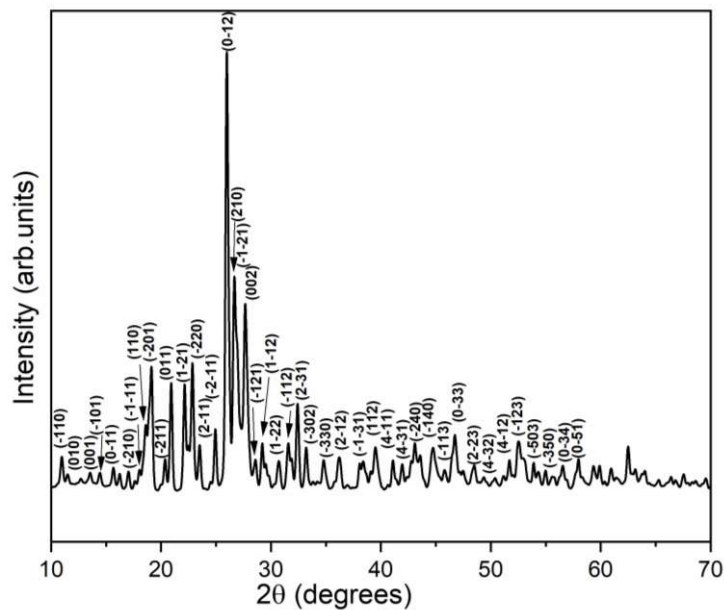
Figure 5.8 XRD pattern of $Na_2Mg_5(MoO_4)_6$ sintered ceramic

116

The powder X-ray diffraction patterns of $Na_2A_5(MoO_4)_6$ (A = Ca, Sr and Ba) ceramics are shown in Figure 5.9 a-c.
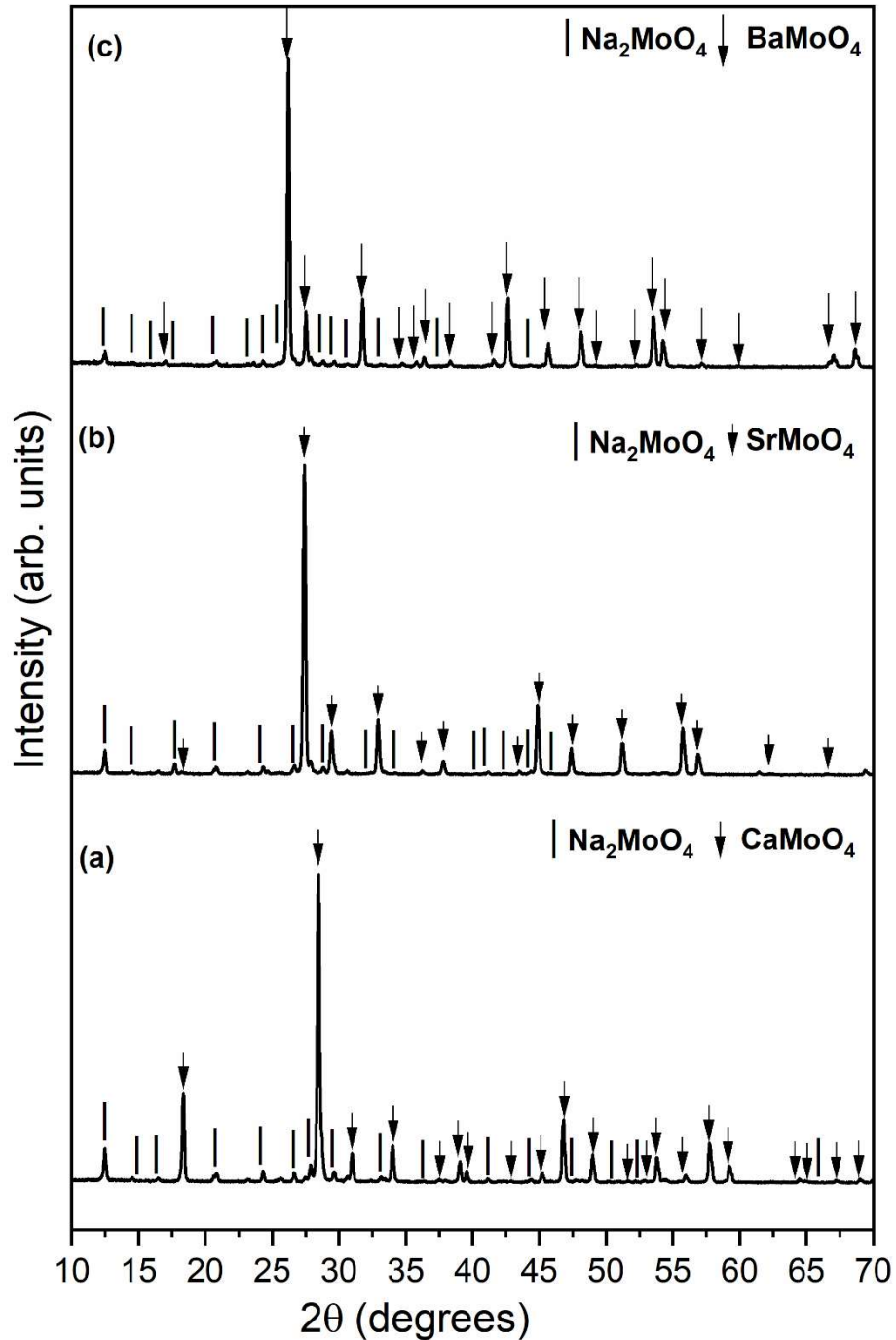
Figure 5.9 XRD patterns of (a) $Na_2Ca_5(MoO_4)_6$, (b) $Na_2Sr_5(MoO_4)_6$ and (c) $Na_2Ba_5(MoO_4)_6$ sintered ceramics

There are no reported literature on single phase compositions in the Na_2MoO_4-$BaMoO_4$, Na_2MoO_4-$SrMoO_4$ and Na_2MoO_4-$CaMoO_4$ systems. The XRD patterns of $Na_2A_5(MoO_4)_6$ (A = Ca, Sr and Ba) compositions resemble with respective alkaline

earth molybdates, viz CaMoO$_4$ (ICDD file 01-081-9937), SrMoO$_4$ (ICDD file 01-083-6703) and BaMoO$_4$ (ICDD file 01-083-6705) together with additional peaks corresponding to Na$_2$MoO$_4$ (ICDD file 26-0967). The XRD peaks are found to shift to higher diffraction angles with substitution of Sr^{2+} and Ca^{2+} for Ba^{2+}. This is an indication of the lowering of cell volume with Sr^{2+} ion and Ca^{2+} ion substitution, which have lower ionic radii than Ba^{2+} ion [14].

The inferences drawn from above results are further ascertained by the Raman analysis and SEM studies in the following sections.

5.3.3 Raman spectroscopic studies

The laser Raman spectrum of the Na$_2$Zn$_5$(MoO$_4$)$_6$ ceramic sintered at 590°C for 1hr is given in Figure 5.10 (a) and that of Na$_2$Mg$_5$(MoO$_4$)$_6$ ceramic sintered at 540°C for 1 h is given in Figure 5.10 (b). The crystal structures of Na$_2$A$_5$(MoO$_4$)$_6$ (A = Zn, Mg) are reported to have Mo atoms in tetrahedral coordination. The free state (MoO$_4$)$^{2-}$ tetrahedra have four fundamental modes of vibration, namely, a non-degenerate symmetric stretching mode ν_1(A) at 894 cm^{-1}, a doubly degenerate symmetric bending mode ν_2(E) at 318 cm^{-1}, triply degenerate asymmetric stretching ν_3(F$_2$), and asymmetric bending ν_4(F$_2$) modes at 833 cm^{-1} and 381 cm^{-1}, respectively [15-17]. The symmetric stretching vibrations (υ_1) of (MoO$_4$)$^{2-}$ tetrahedra are observed as very strong peak at 937 cm^{-1} together with shoulder peak at 962 cm^{-1} and a weak mode at 917 cm^{-1} for Na$_2$Zn$_5$(MoO$_4$)$_6$ ceramic. Four bands are observed in the 789 to 888 cm^{-1} which corresponds to asymmetric stretching vibrations of (MoO$_4$)$^{2-}$ ions. The symmetric (υ_2) and asymmetric (υ_4) bending vibrations of (MoO$_4$)$^{2-}$ tetrahedra are appeared at 336 and 375 cm^{-1} respectively. The bands observed below 250 cm^{-1} can be attributed to lattice-mode vibrations and an unambiguous assignment of these modes are not possible. The symmetric stretching vibrations (υ_1) of (MoO$_4$)$^{2-}$ tetrahedra are observed as very strong peak at 934 cm^{-1} together with shoulder peaks at 954 cm^{-1} and 966 cm^{-1} and weak modes at 907 cm^{-1} and 916 cm^{-1} for Na$_2$Mg$_5$(MoO$_4$)$_6$ ceramic. The bands observed in the 813 to 869 cm^{-1} correspond to asymmetric stretching vibrations of (MoO$_4$)$^{2-}$ ions. The prominent bands corresponding to symmetric (υ_2) and asymmetric (υ_4) bending vibrations of (MoO$_4$)$^{2-}$ tetrahedra are present at 332 cm^{-1} and 366 cm^{-1} respectively. The bands observed below 250 cm^{-1} can be attributed to lattice-mode vibrations and an unambiguous assignment of these modes are not possible.
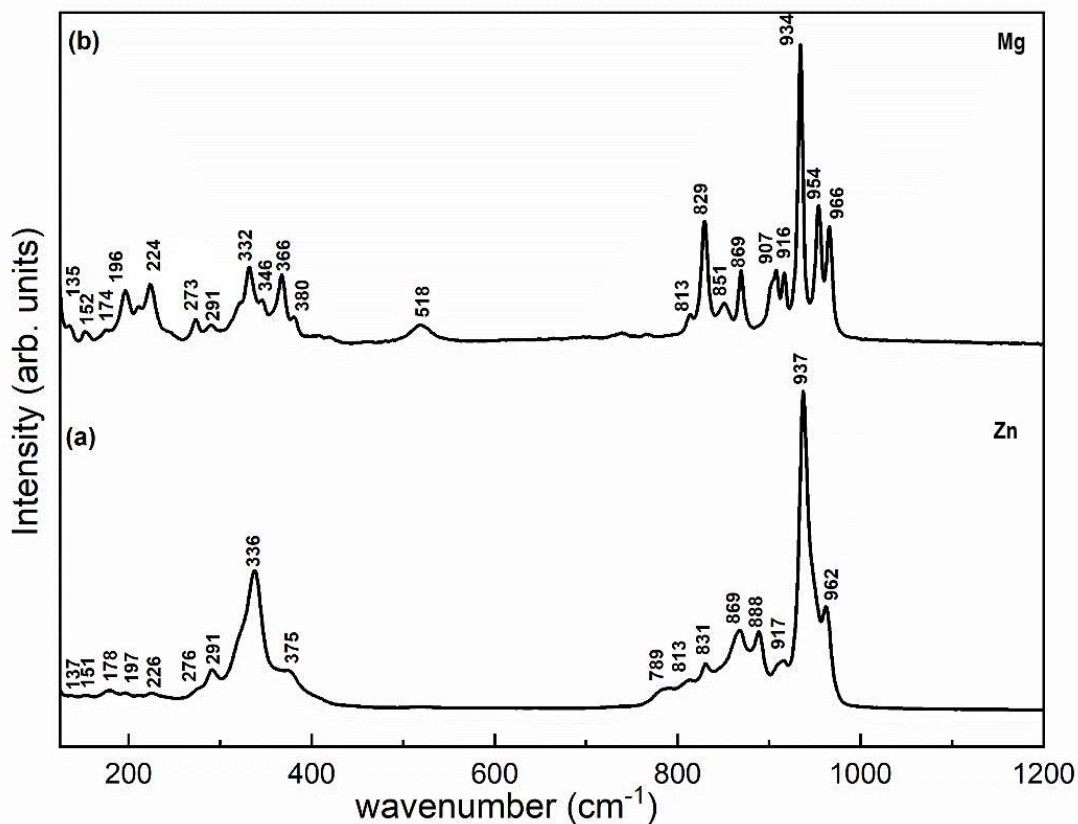
Figure 5.10 Laser Raman spectra of $Na_2A_5(MoO_4)_6$ (A = Zn, Mg) sintered ceramics

The laser Raman spectra of the $Na_2A_5(MoO_4)_6$ (A = Ca, Sr, Ba) ceramics are given in Figure 5.11 a-c. The bands of $(MoO_4)^{2-}$ tetrahedra are present in the Raman spectra of $Na_2A_5(MoO_4)_6$ (A = Ca, Sr, Ba) ceramics and exhibit lower number of Raman bands compared to Zn and Mg compositions. The Raman spectra of the $Na_2A_5(MoO_4)_6$ (A = Ca, Sr, Ba) ceramics reaffirm the multiphase nature of these compositions, which is earlier identified through the XRD studies. The Raman modes of $Na_2A_5(MoO_4)_6$ (A = Ca, Sr and Ba) ceramics match with that of the reported Raman modes of $CaMoO_4$, $SrMoO_4$ and $BaMoO_4$ [18] which are intercalated with the Raman bands of Na_2MoO_4 [19]. $Na_2Ba_5(MoO_4)_6$ ceramic has a very sharp symmetric stretching mode at 889 cm^{-1}, asymmetric stretching modes at 837 cm^{-1} and 790 cm^{-1}, symmetric bending mode at 324 cm^{-1} and asymmetric bending modes at 345 cm^{-1} and 359 cm^{-1}. $Na_2Sr_5(MoO_4)_6$ ceramic has symmetric stretching mode of $(MoO_4)^{2-}$ tetrahedra at 885 cm^{-1}, asymmetric stretching modes at 844 cm^{-1} and 794 cm^{-1}, symmetric bending mode at 326 cm^{-1} and asymmetric bending modes at 366 cm^{-1} and 382 cm^{-1}. $Na_2Ca_5(MoO_4)_6$ ceramic has symmetric stretching mode of $(MoO_4)^{2-}$ tetrahedra at 878 cm^{-1}, asymmetric stretching modes at 846 cm^{-1} and 793 cm^{-1}, symmetric bending mode at 322 cm^{-1} and asymmetric bending modes at 391 cm^{-1} and 404 cm^{-1}. The bands observed below 250

119

cm^{-1} can be attributed to lattice-mode vibrations and an unambiguous assignment of these modes is not possible.
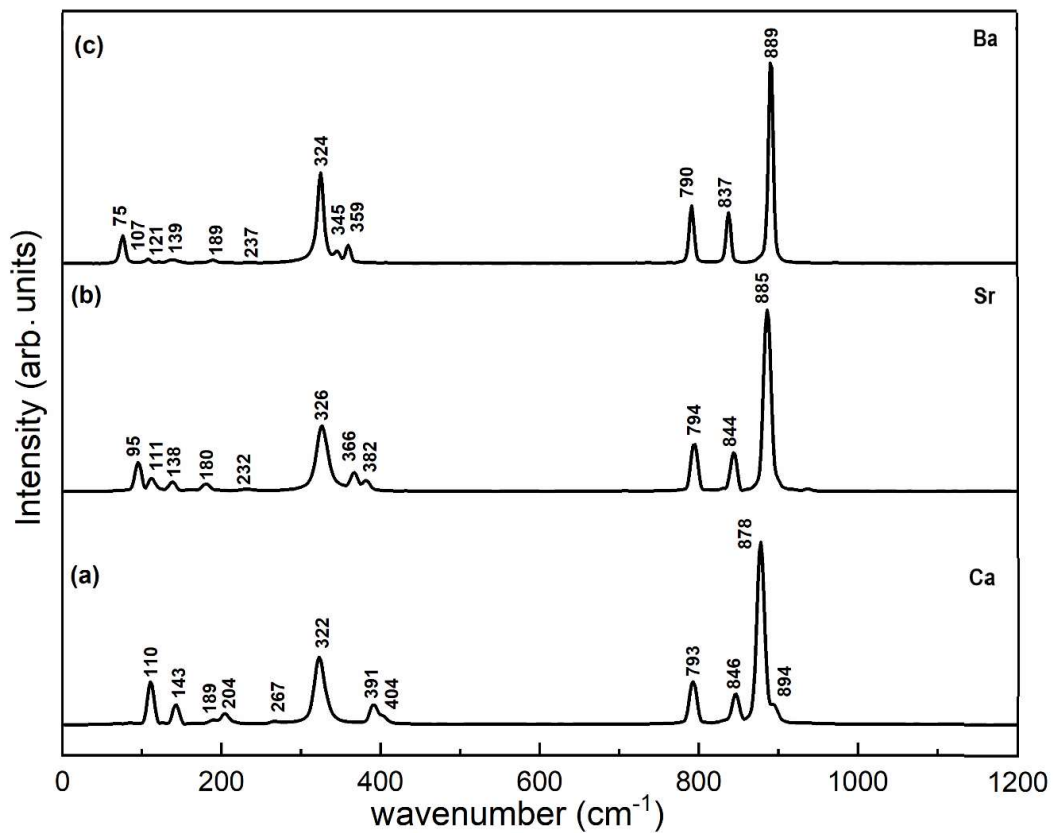
Figure 5.11 Laser Raman spectra of Na$_2$A$_5$(MoO$_4$)$_6$ (A = Ca, Sr and Ba) sintered ceramics

The Raman mode assignments of the Na$_2$A$_5$(MoO$_4$)$_6$ (A = Zn, Mg, Ca, Sr and Ba) ceramics are given in Table 5.2.

Table 5.2 Raman mode assignments of $Na_2A_5(MoO_4)_6$ (A = Zn, Mg, Ca, Sr and Ba) ceramics

Zn (cm^{-1})	Mg (cm^{-1})	Ca (cm^{-1})	Sr (cm^{-1})	Ba (cm^{-1})	Assignments *1,2
962 w sh	966 m				
	954 m				
937 vs	934 vs				
917 vw	916 w				
	907 w	894vw sh			
		878 vs	885 vs	889 vs	$\nu_s(MoO_4)^{2-}$
888 m	869 m				
869 m	851 vw	846 m	844 m	837 m	
	829 s				$\nu_{as}(MoO_4)^{2-}$
831 w	813 wsh				
813 vw		793 m	794 m	790 m	
789 vw					
	518 w	404 vw	382 vw	359 w	
375 w	380 wsh	391 w	366 w	345 vw	$\delta_{as}(MoO_4)^{2-}$
	366 m				
	346 vw				
336 m	332 m	322 m	326 m	324 m	$\delta_s(MoO_4)^{2-}$
291 w	291 w	267 vw			
276 vw	273 w				
226 vw	224 m	204 vw	232 vw	237 vw	Lattice-mode
197 vw	196 m	189 vw	180 w	189 vw	vibrations
178 vw	174 vw	143 m	138 w	139 vw	
151 vw	152 vw	110 m	111 w	121 vw	
137 vw	135 vw		95 m	107 vw	
				75 m	

[*1] ν_s – symmetric stretching ν_{as} – asymmetric stretching δ_{as} – asymmetric bending

δ_s – symmetric bending

[*2] vs very strong; s strong; m medium; w weak; br broad; vw very weak; sh shoulder

5.3.4 Morphological studies

The SEM micrographs of $Na_2Zn_5(MoO_4)_6$ and $Na_2Mg_5(MoO_4)_6$ ceramics are shown in Figure 5.12 (a) and (b) respectively.
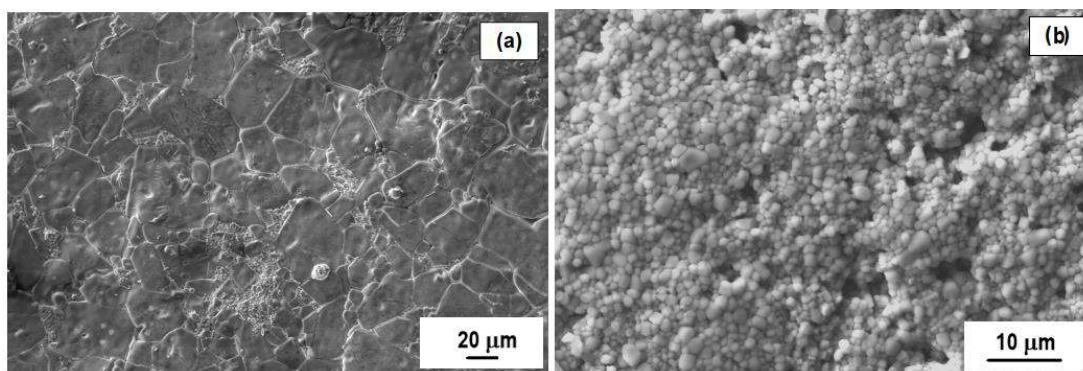
Figure 5.12 SEM micrographs of (a) $Na_2Zn_5(MoO_4)_6$ ceramic sintered at 590°C/1h and (b) $Na_2Mg_5(MoO_4)_6$ ceramic sintered at 540°C/1h

$Na_2A_5(MoO_4)_6$ (A = Zn, Mg) compositions exhibit densely packed microstructure. $Na_2Zn_5(MoO_4)_6$ ceramic exhibits exaggerated grain growth comprising of polygonal grains of size as large as 180 μm and the microstructure is correlated with the microwave dielectric properties. The SEM micrograph of $Na_2Mg_5(MoO_4)_6$ also exhibits phase homogeneity of the ceramic with smaller grains of size 1-3 μm. The SEM micrographs and the EDS point analysis of $Na_2A_5(MoO_4)_6$ (A = Ca, Sr, Ba) ceramics are given in Figures 5.13, 5.14 and 5.15 respectively.

The backscattered SEM micrograph of $Na_2Ca_5(MoO_4)_6$ ceramic given in Figure 5.13 (a) exhibits multiphase nature. The EDS point analysis at spot 1, Figure 5.13 (b) reveals the presence of Na, Mo and O, whereas that at spot 2, Figure 5.13 (c) contains Ca in addition to Na, Mo and O. The backscattered SEM image of $Na_2Sr_5(MoO_4)_6$ ceramic is shown in Figure 5.14 (a). The EDS point analysis at spot 1, Figure 5.14 (b) reveals the presence of Sr, Mo and O, whereas that at spot 2, Figure 5.14 (c) contains Na, Sr, Mo and O. The backscattered SEM micrograph of $Na_2Ba_5(MoO_4)_6$ ceramic given in Figure 5.15 (a) exhibits multiphase nature comprising of Na_2MoO_4 and $BaMoO_4$. The EDS point analysis at spot 1, Figure 5.15 (b) reveals the presence of Ba, Mo and O, whereas that at spot 2, Figure 5.15 (c) contains Na, Mo and O. Alkaline earth metal molybdates $BaMoO_4$, $SrMoO_4$ and $CaMoO_4$ have scheelite structure and belong to tetragonal crystal system whereas the $ZnMoO_4$ and $MgMoO_4$ have wolframite structure belonging to monoclinic crystal system [20]. The formation of $BaMoO_4$, $SrMoO_4$ and $CaMoO_4$ compositions through solid-state route are reported at temperatures in the range 800-1100°C [21]. The sodium based compounds in the reaction pathway of the systems under study facilitate the low temperature formation of the corresponding alkaline earth metal molybdates. Based on the above

investigations, it can be inferred that among the samples studied $Na_2A_5(MoO_4)_6$ (A = Zn and Mg) form phase pure compositions. $Na_2A_5(MoO_4)_6$ (A = Ba, Sr and Ca) compositions exists as Na_2MoO_4 and the respective alkaline earth molybdate.
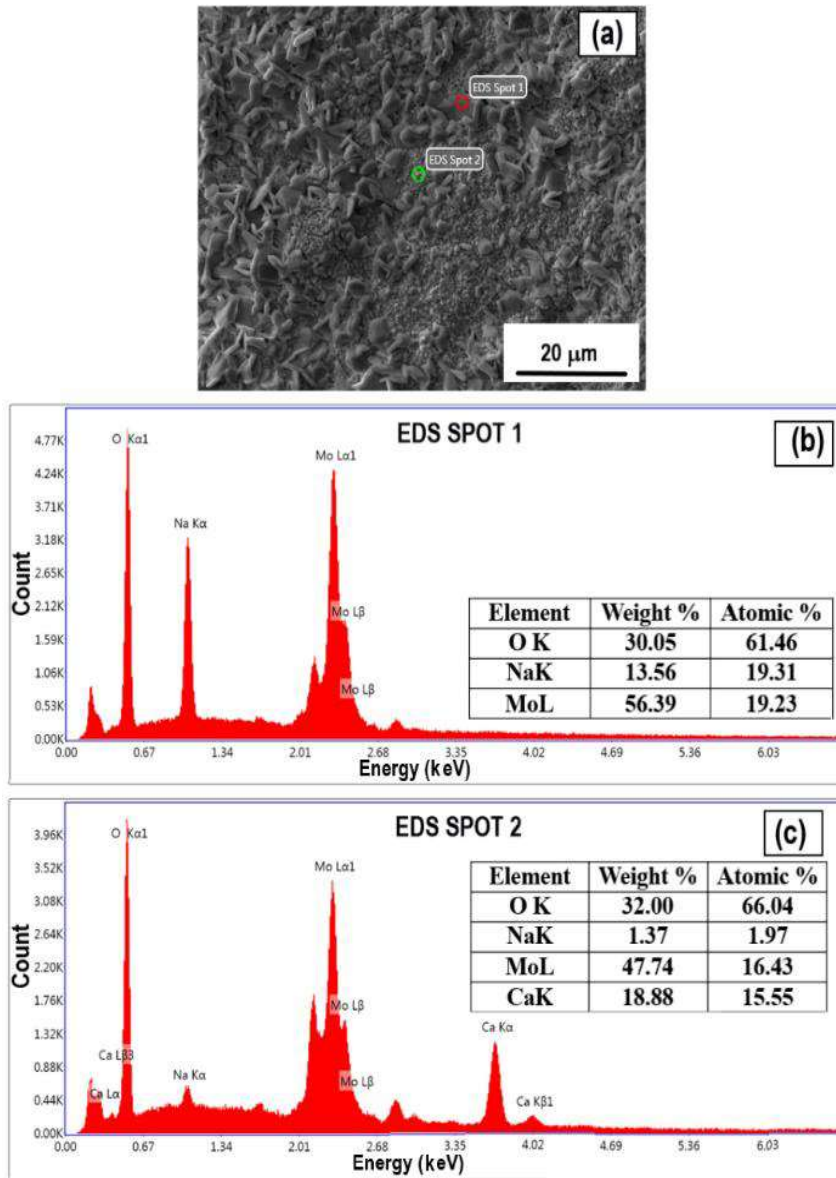
Figure 5.13 (a) Backscattered SEM image; EDS point analysis spectra at (b) spot 1 and (c) spot 2 of $Na_2Ca_5(MoO_4)_6$ ceramic sintered at 640°C/1h
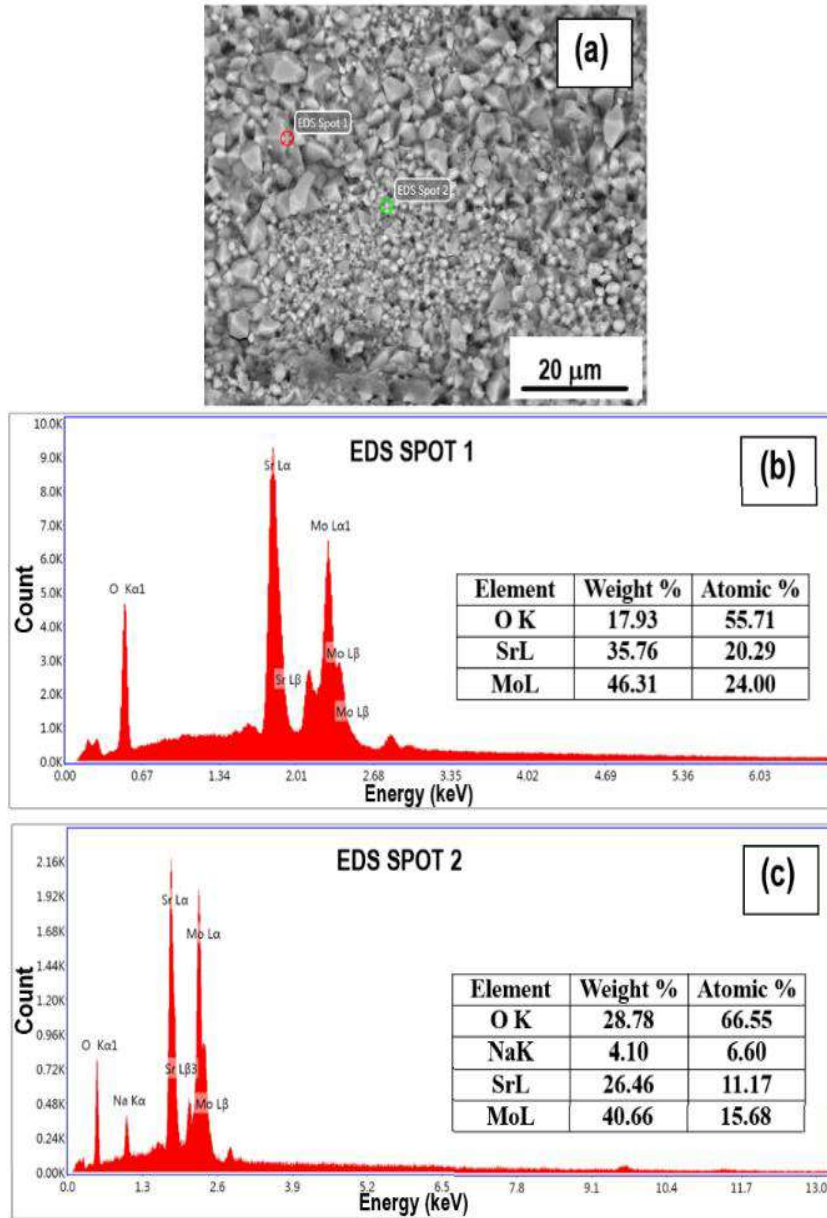
Figure 5.14 (a) Backscattered SEM image; EDS point analysis at (b) spot 1 and (c) spot 2 of $Na_2Sr_5(MoO_4)_6$ ceramic sintered at 620°C/1h

Figure 5.15 (a) Backscattered SEM image; EDS point analysis at (b) spot 1 and (c) spot 2 of $Na_2Ba_5(MoO_4)_6$ ceramic sintered at 610°C/1h

5.3.5 Microwave dielectric studies

The $Na_2A_5(MoO_4)_6$ (A = Zn, Mg, Ca, Sr and Ba) ceramics exhibit excellent microwave properties. The sintering temperature, maximum sintered density, dielectric constant ε_r, quality factor $Q_u \times f$ and temperature coefficient of resonant frequency τ_f of the compositions are given in Table. 5.3.

Table 5.3 Sintering temperature, maximum sintered density and microwave dielectric properties of $Na_2A_5(MoO_4)_6$ (A = Zn, Mg, Ca, Sr and Ba) ceramics

Compositions	Sintering temperature (ºC) /1h	Density (g/cm³)	ε_r @ GHZ	$Q_u \times f$ (GHz)	τ_f (ppm/ºC)
$Na_2Zn_5(MoO_4)_6$	590	3.7	8.1	35,800	-95
$Na_2Mg_5(MoO_4)_6$	540	3.3	7.8	37,600	-87
$Na_2Ca_5(MoO_4)_6$	640	3.9	8.1	28,500	-67
$Na_2Sr_5(MoO_4)_6$	620	3.8	7.6	20,500	-44
$Na_2Ba_5(MoO_4)_6$	610	3.6	6.1	43,000	-74

Among the compositions studied, $Na_2Zn_5(MoO_4)_6$ ceramic has a dielectric constant $\varepsilon_r = 8.1$, quality factor $Q_u \times f = 35,800$ GHz, and temperature coefficient of resonant frequency $\tau_f = -95$ ppm/°C. Although $Na_2Mg_5(MoO_4)_6$ ceramic exhibits higher quality factor and lower τ_f, the hygroscopic nature of this composition limits its practical applications as a microwave material.

The variation of dielectric constant, quality factor and temperature coefficient of resonant frequency has been studied for all the ceramics under study as a function of sintering temperature. Typical results obtained for $Na_2Zn_5(MoO_4)_6$ ceramic are shown in Figures 5.16 to 5.18. The variation of density and dielectric constant of $Na_2Zn_5(MoO_4)_6$ ceramic as a function of temperature is shown in Figure 5.16. The variation of quality factor with temperature is shown in Figure 5.17. It is clear from the graph that as the sintering temperature increases both density and dielectric constant increases up to optimum sintering temperature and thereafter both the properties decreases because of melting as well as evaporation of the some of the constituents,

which in turn introduces porosity in the ceramic materials. However, $Q_u \times f$ increases beyond 590°C due to the influence of exaggerated grain growth in the $Na_2Zn_5(MoO_4)_6$ ceramics [22-26].
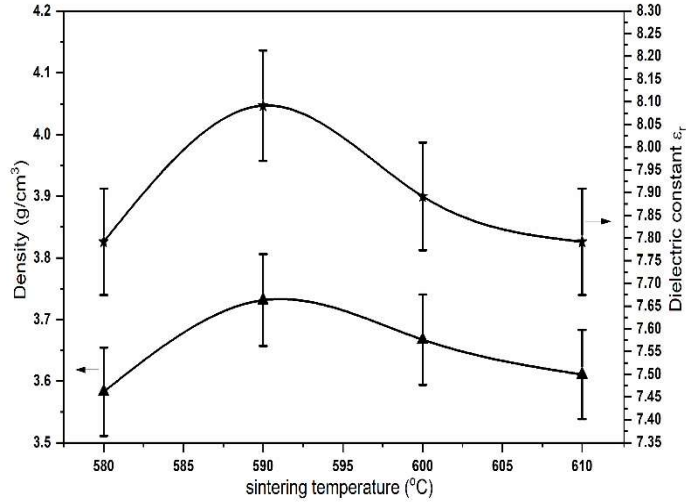
Figure 5.16 Variation of density and dielectric constant of $Na_2Zn_5(MoO_4)_6$ ceramic with sintering temperature
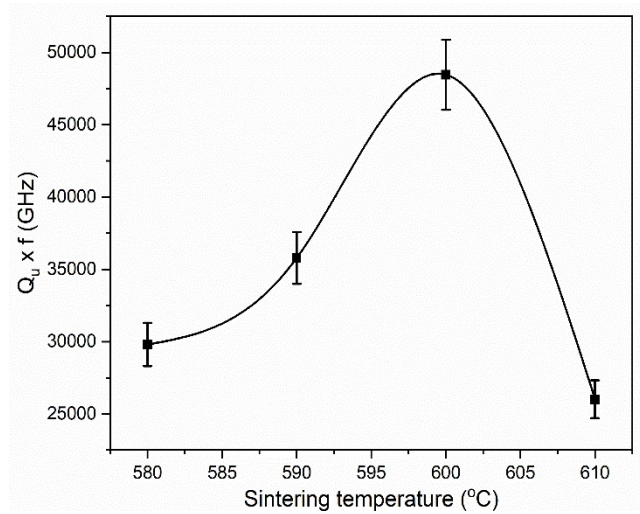
Figure 5.17 Variation of quality factor of $Na_2Zn_5(MoO_4)_6$ ceramic with sintering temperature

The temperature coefficient of resonant frequency for the $Na_2Zn_5(MoO_4)_6$ ceramic sintered at various temperatures are given in Figure 5.18. The variation of resonant frequency with temperature for the $Na_2A_5(MoO_4)_6$ (A = Zn, Mg, Ca, Sr and Ba) ceramics sintered at optimum temperature are given in Figure 5.19 a-e.
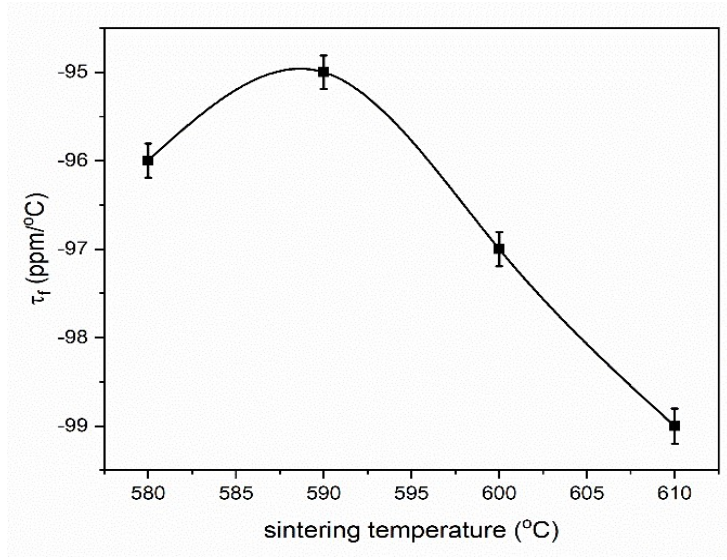
Figure 5.18 Variation of temperature coefficient of resonant frequency of Na$_2$Zn$_5$(MoO$_4$)$_6$ ceramic for different sintering temperatures
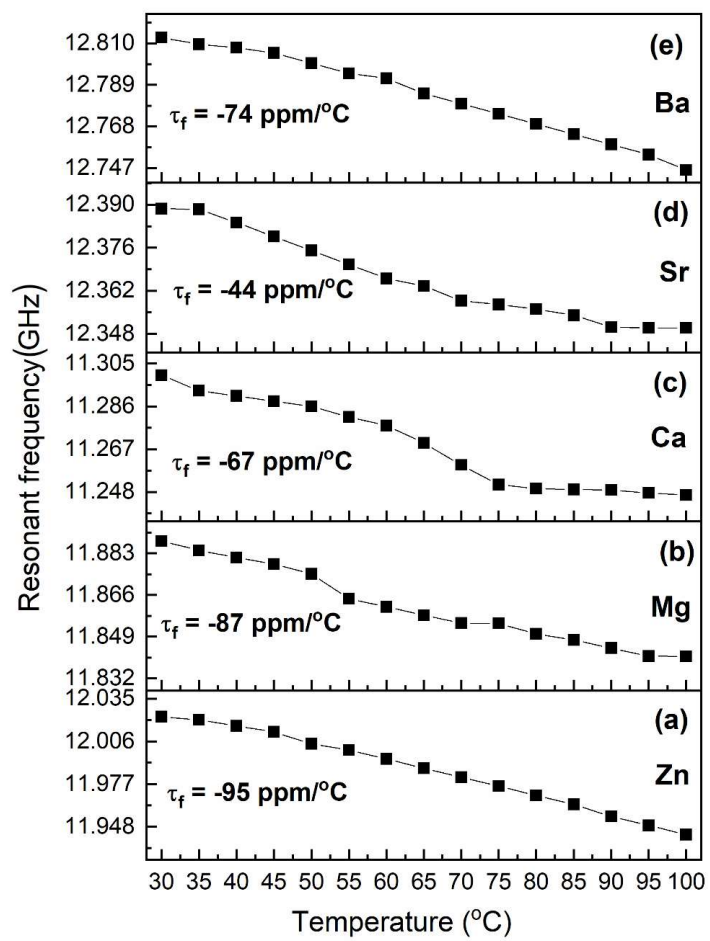
Figure 5.19 Variation of resonant frequency with temperature for Na$_2$A$_5$(MoO$_4$)$_6$ (A = Zn, Mg, Ca, Sr and Ba) ceramics sintered at optimum temperatures

The shrinkage behaviour of $Na_2A_5(MoO_4)_6$ (A = Zn, Ca, Sr and Ba) ceramics are studied using a thermomechanical analyzer and the shrinkage curves are shown in Figure 5.20 a-d. The ceramics show rapid shrinkage near to 400°C which further ascertain their suitability for ULTCC applications. The $Na_2Mg_5(MoO_4)_6$ sample did not yield a proper shrinkage behaviour and hence the results are not included in the study. This could be due to the hygroscopic nature of the sample.
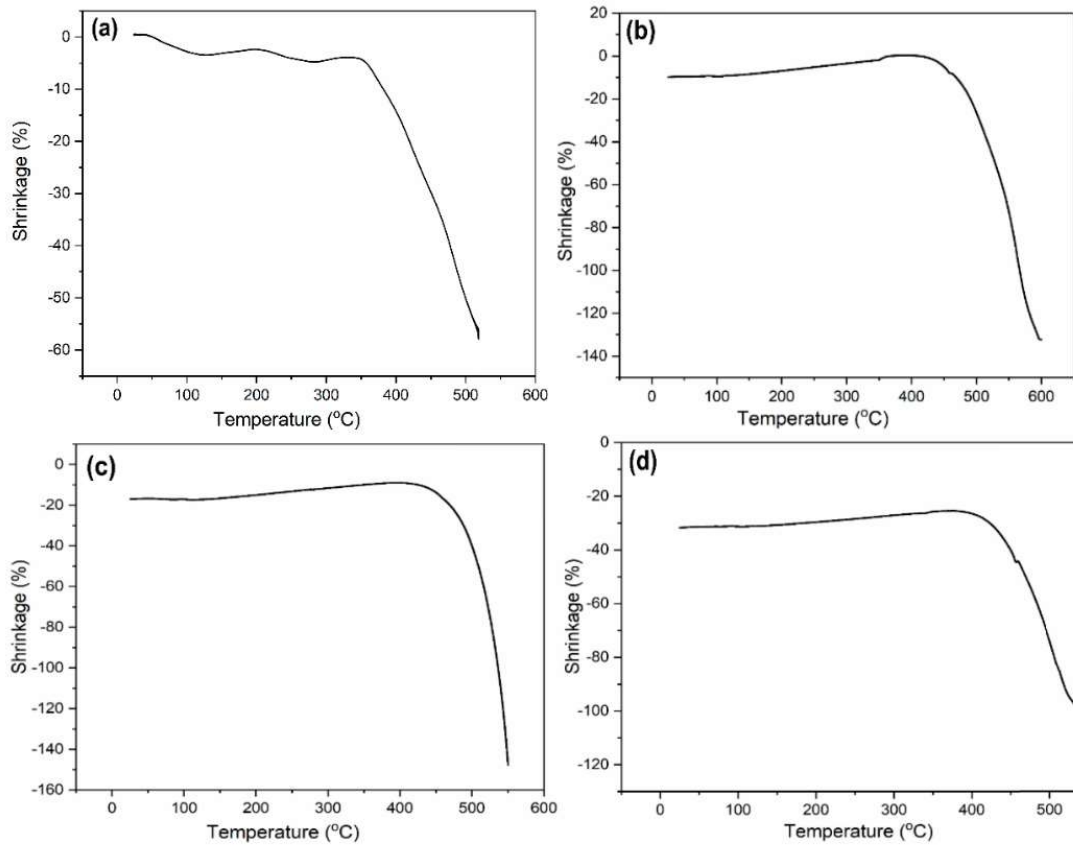
Figure 5.20 Shrinkage curves of (a) $Na_2Zn_5(MoO_4)_6$, (b) $Na_2Ca_5(MoO_4)_6$, (c) $Na_2Sr_5(MoO_4)_6$ and (d) $Na_2Ba_5(MoO_4)_6$ ceramics

5.3.6 Compatibility studies

The chemical compatibility of $Na_2A_5(MoO_4)_6$ (A = Zn, Mg, Ca, Sr and Ba) ceramics with aluminium electrode has been determined by XRD and EDS analyses of the ceramic co-fired with 20 wt% of aluminium powder at appropriate sintering temperatures for 1h. The XRD pattern of $Na_2Zn_5(MoO_4)_6$ ceramic co-fired with aluminium along with the XRD pattern of the $Na_2Zn_5(MoO_4)_6$ ceramic are given in Figure 5.21. The XRD pattern clearly exhibits the characteristic peaks of aluminium,

as per ICDD file no. 89-2769 at 2θ values 38.5°, 44.7° and 65.1° marked with '*'. The pattern also contains all the peaks manifested in the XRD pattern of the corresponding ceramic, with no extra peaks as a result of Al addition, which clearly indicates the chemical compatibility of the ceramics with Al metal.
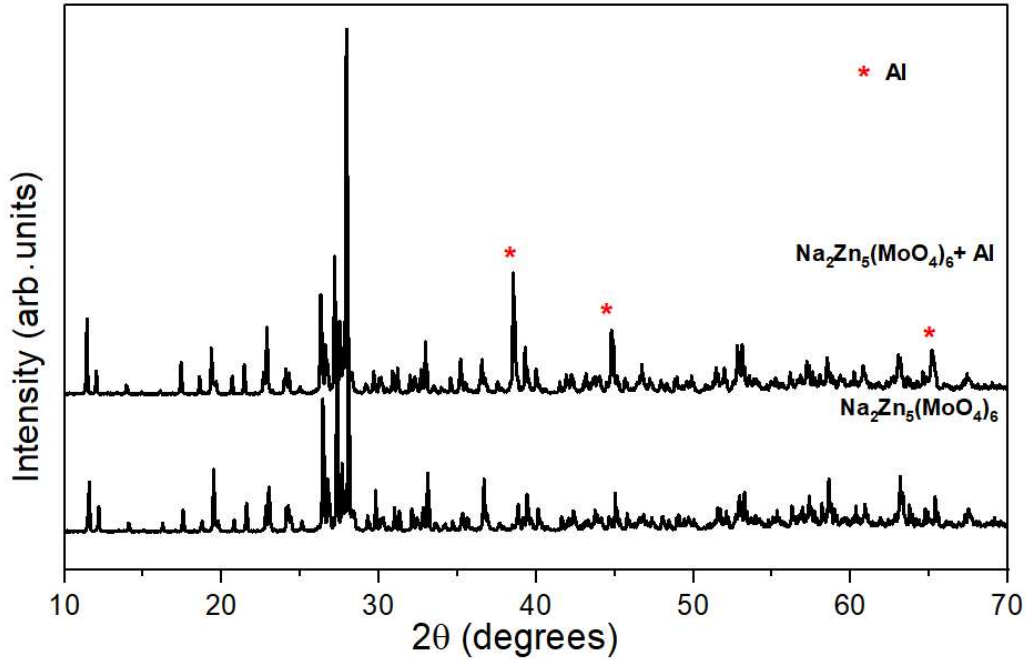
Figure 5.21 XRD patterns of $Na_2Zn_5(MoO_4)_6$ ceramic and $Na_2Zn_5(MoO_4)_6$ ceramic co-fired with 20 wt% Al at 590°C/1h

The co-firability of the $Na_2Zn_5(MoO_4)_6$ ceramic was further ascertained by energy dispersive X-ray spectroscopy. The backscattered SEM micrograph of the $Na_2Zn_5(MoO_4)_6$ ceramic co-fired with aluminium along with EDS point analysis results are given in Figure 5.22 a-c. The EDS spectra taken at spots 1 and 2 are shown in Figures 5.22(b) and 5.22(c) respectively. The atomic percentage and weight percentage of each element are also given in inset. The point analysis at the aluminium region clearly shows that the ceramic under study is compatible with aluminium electrode. The EDS elemental mapping overlay on image and mapping for each element is given in Figure 5.23 a-f. The aluminium region shown in green colour clearly depicts island formation surrounded by the ceramic grains and did not show any evidence of diffusion of aluminium into the ceramic region.
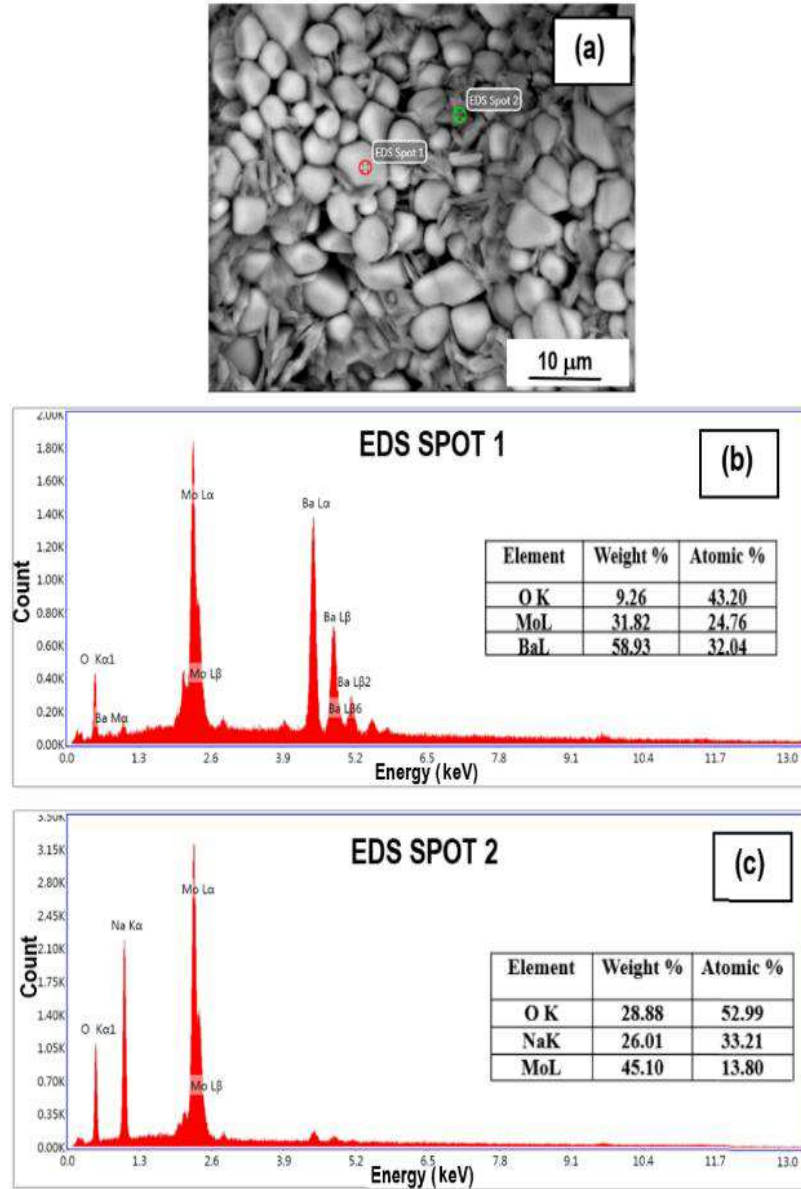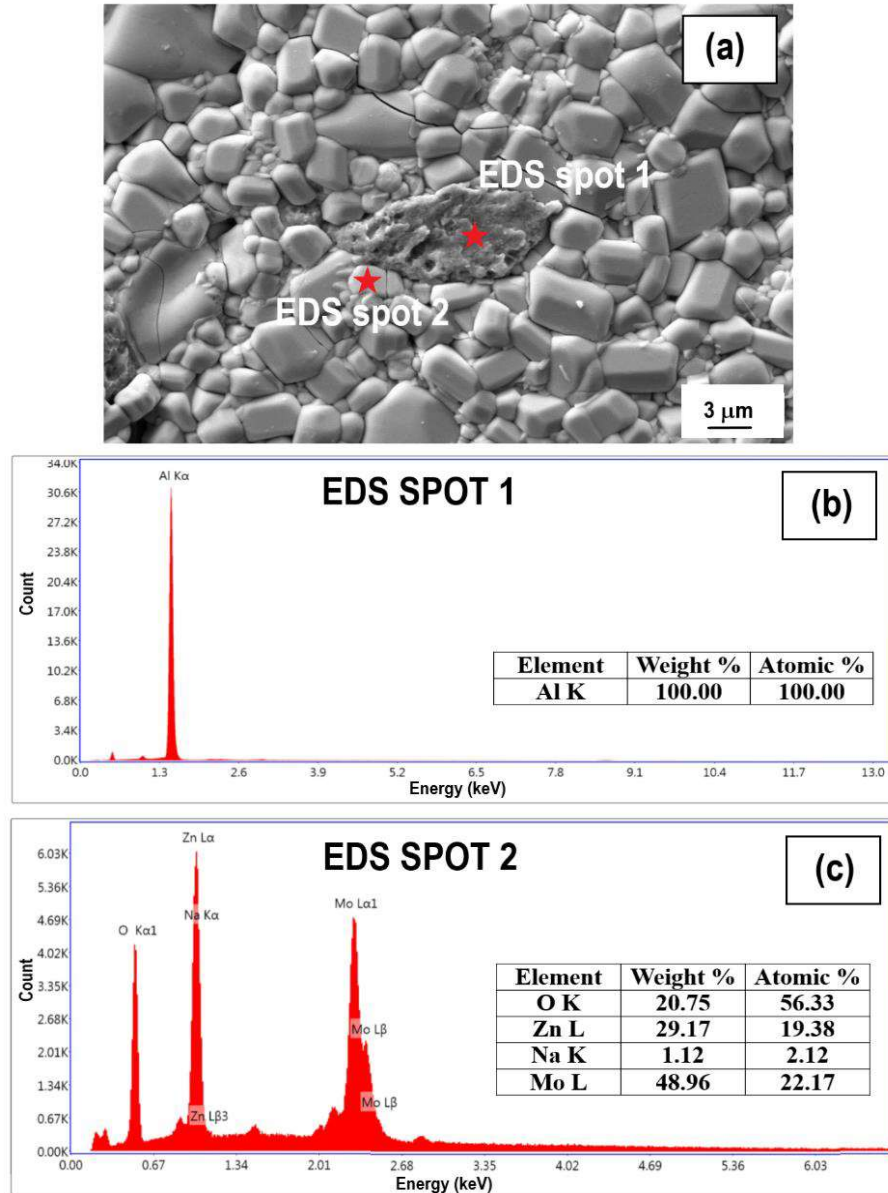
Figure 5.22 (a) Backscattered SEM image; EDS point analysis spectra at (b) spot 1 and (c) spot 2 of $Na_2Zn_5(MoO_4)_6$ ceramics co-fired with 20 wt% Al at 590°C/1h

The XRD pattern of $Na_2Mg_5(MoO_4)_6$ ceramic co-fired with aluminium is given in Figure 5.24 and is compared with the XRD pattern of $Na_2Mg_5(MoO_4)_6$ ceramic. The XRD pattern of the co-fired sample clearly exhibits the characteristic peaks of aluminium as per ICDD file no. 89-2769 at 2θ values 38.5°, 44.7° and 65.1° marked with '*'. The backscattered SEM micrographs of the $Na_2Mg_5(MoO_4)_6$ ceramic co-fired with aluminium along with the EDS point analysis results are given in Figure 5.25 a-c.
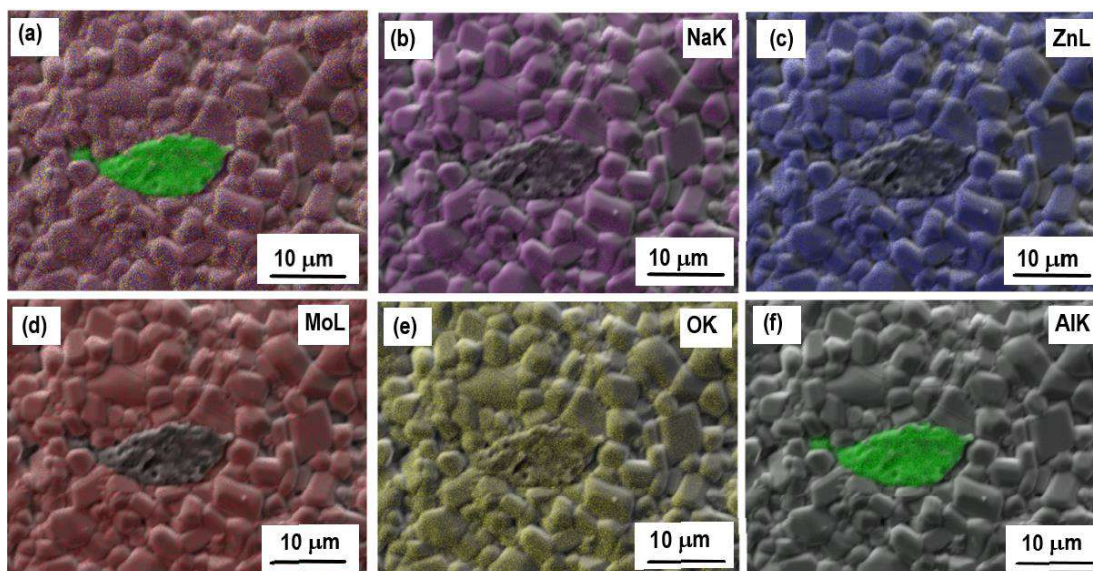
Figure 5.23 (a) EDS elemental mapping overlay on image; Elemental mapping of b) Na, c) Zn, d) Mo, e) O and f) Al elements in $Na_2Zn_5(MoO_4)_6$ ceramics co-fired with 20 wt% Al at 590°C/1h
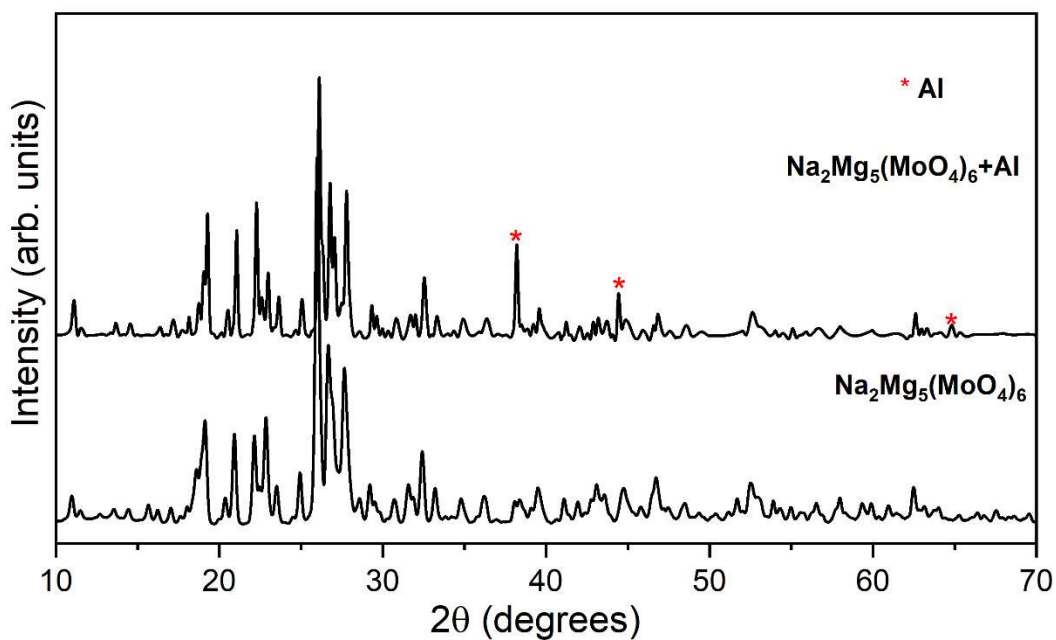
Figure 5.24 XRD patterns of $Na_2Mg_5(MoO_4)_6$ ceramic and $Na_2Mg_5(MoO_4)_6$ ceramic co-fired with 20 wt% Al sintered at 540°C/1h
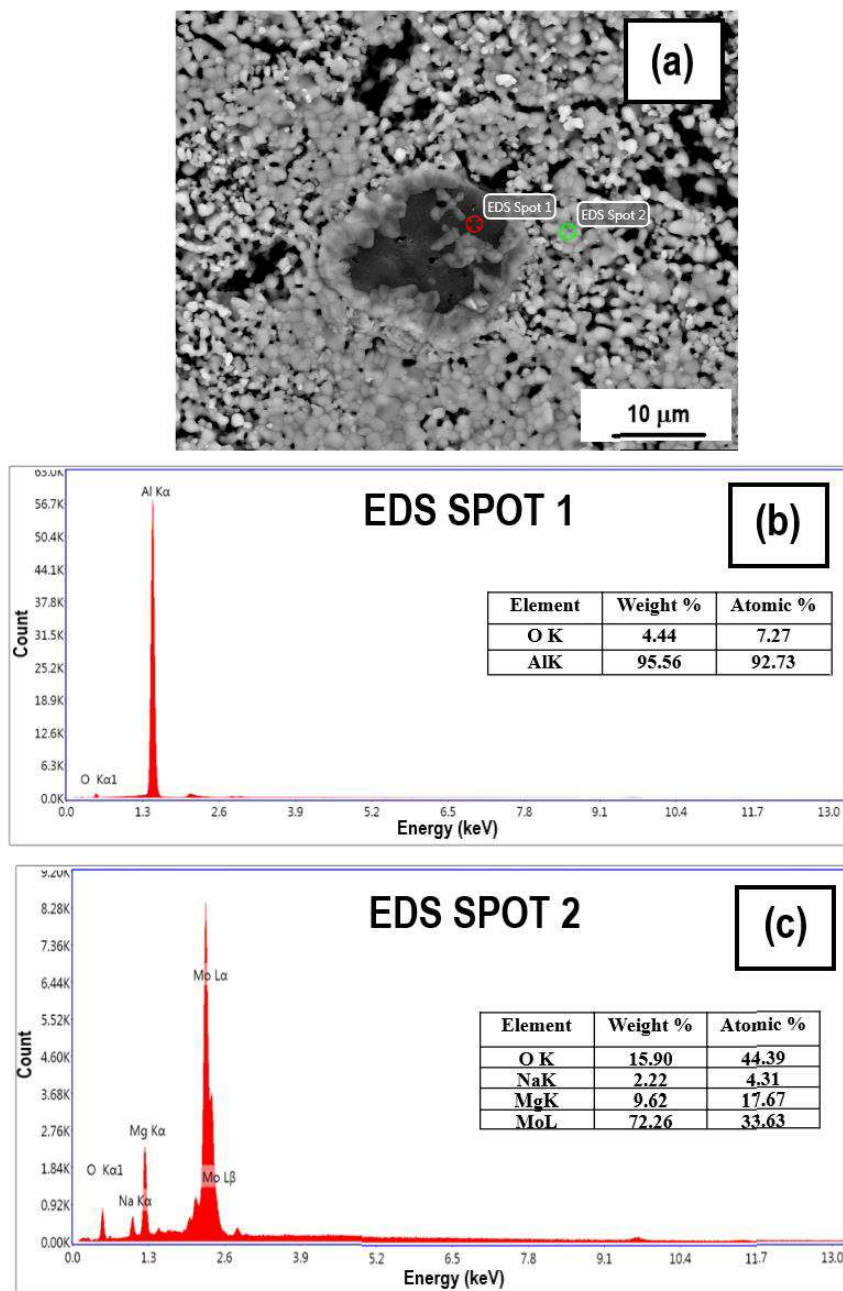
Figure 5.25 (a) Backscattered SEM image; EDS point analysis spectra at (b) spot 1 and (c) spot 2 of $Na_2Mg_5(MoO_4)_6$ ceramic co-fired with 20 wt% Al at 540°C/1h

The XRD patterns of $Na_2A_5(MoO_4)_6$ (A = Ca, Sr and Ba) ceramics co-fired with aluminium are given in Figure 5.26 and are compared with the corresponding XRD patterns of the ceramics. The XRD patterns clearly exhibit the characteristic peaks of aluminium as per ICDD file no. 89-2769 at 2θ values 38.5°, 44.7° and 65.1° which are marked with '*'.
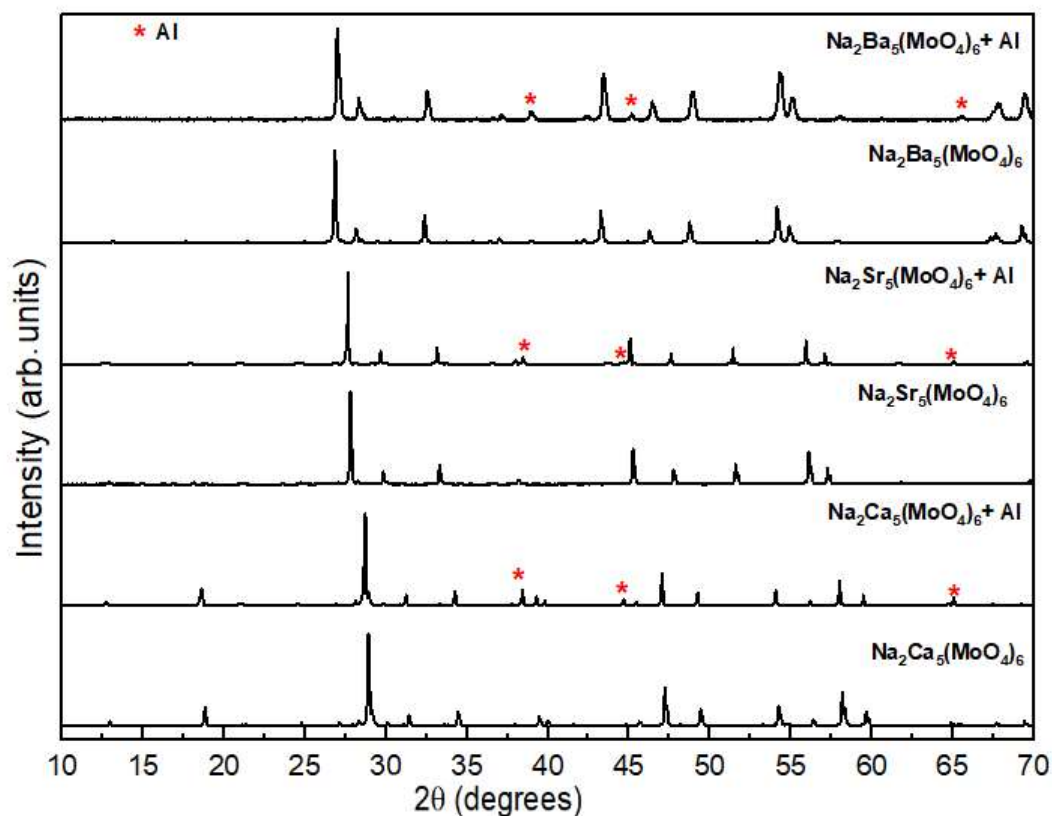
Figure 5.26 XRD patterns of $Na_2A_5(MoO_4)_6$ (A = Ca, Sr and Ba) ceramics co-fired with 20 wt% Al at optimum sintering temperature

The backscattered SEM micrograph of the $Na_2Ca_5(MoO_4)_6$ ceramic co-fired with aluminium is shown in Figure 5.27 (a). The EDS point analysis results at spot 1 and spot 2 (Figures 5.27 (b) and (c)) reveal the presence of Mo, O along with small quantities of Na and Ca at the Al region of the co-fired sample.
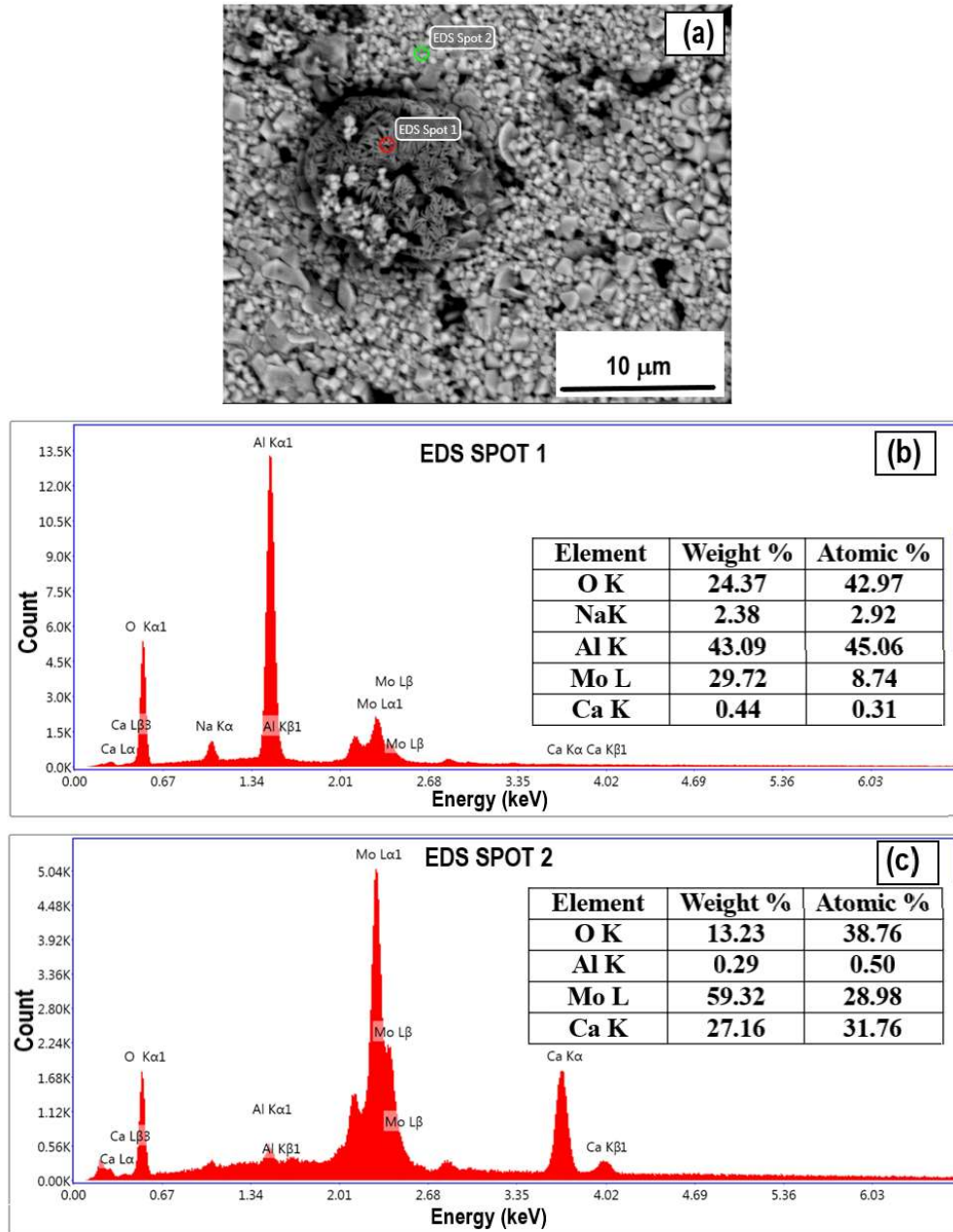
Figure 5.27 (a) Backscattered SEM image; EDS point analysis spectra at (b) spot 1 and (c) spot 2 of $Na_2Ca_5(MoO_4)_6$ ceramic co-fired with 20 wt% Al at 640°C/1h

The backscattered SEM micrographs of the $Na_2Sr_5(MoO_4)_6$ ceramic co-fired with aluminium and EDS point analysis results are given in Figure 5.28. The EDS point analysis ascertains the compatibility of the ceramics with aluminium.
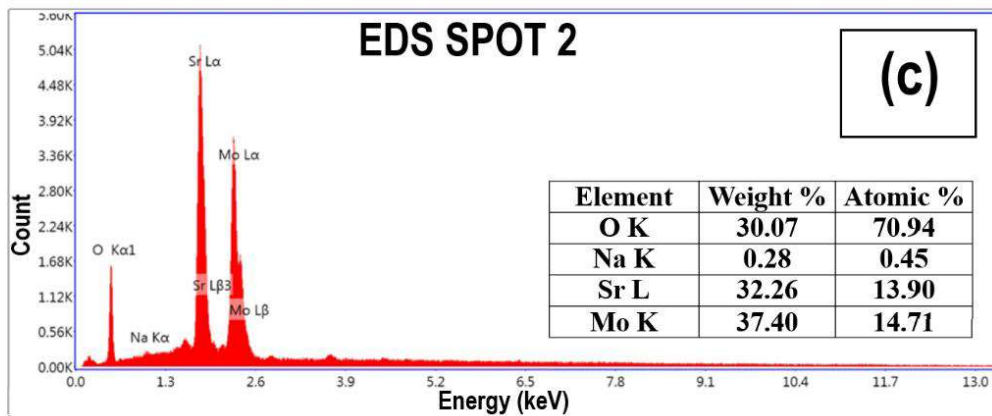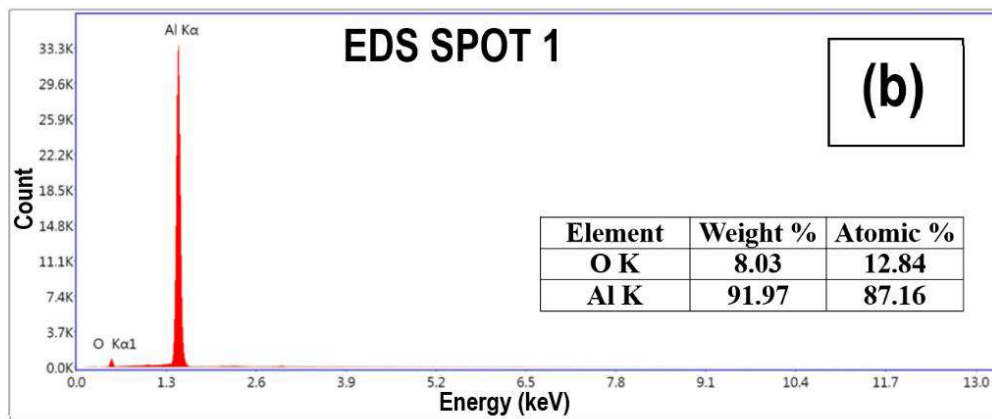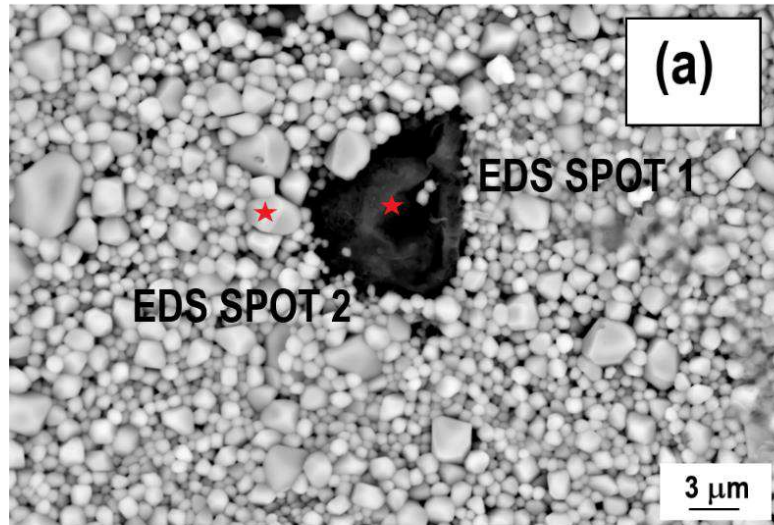
Figure 5.28 (a) Backscattered SEM image; EDS point analysis spectra at (b) spot 1 and (c) spot 2 of $Na_2Sr_5(MoO_4)_6$ ceramic co-fired with 20 wt% Al at 620°C/1h

The backscattered SEM micrographs of the $Na_2Ba_5(MoO_4)_6$ ceramic co-fired with aluminium and EDS point analysis results are given in Figure 5.29.
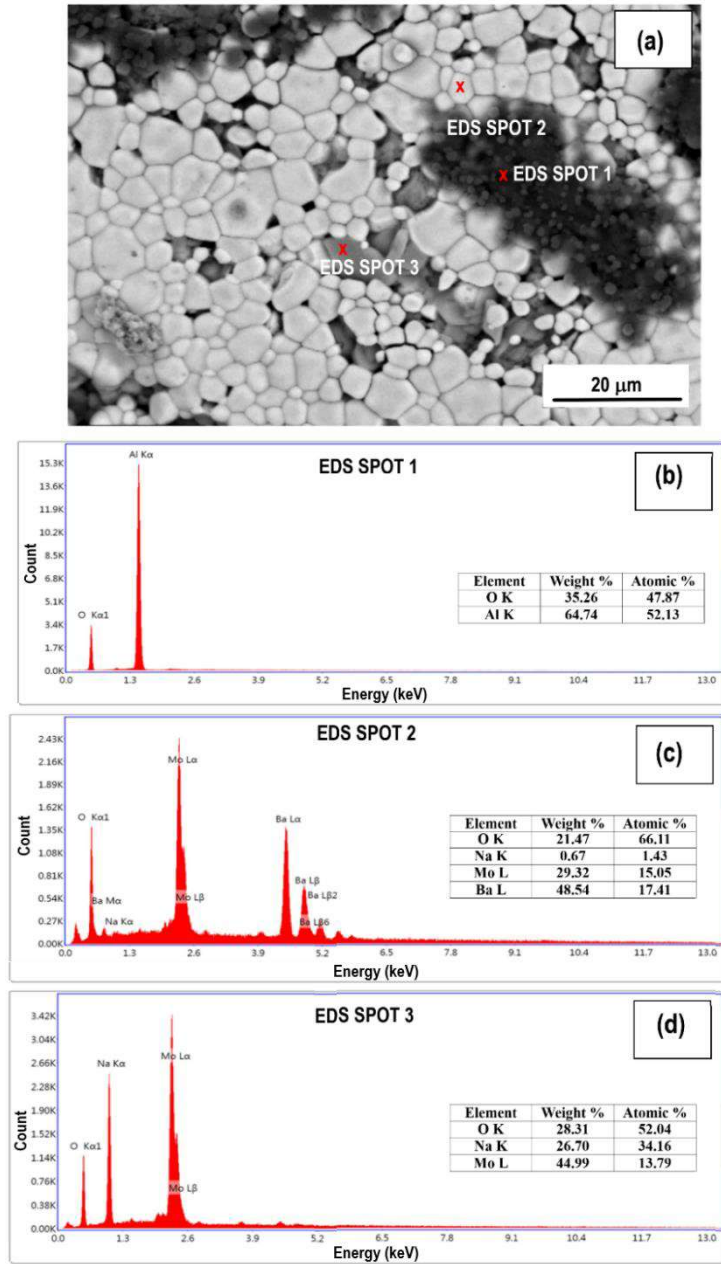
Figure 5.29 (a) Backscattered SEM image; EDS point analysis spectra at (b) spot 1, (c) spot 2 and (d) spot 3 of $Na_2Ba_5(MoO_4)_6$ ceramic co-fired with Al at 610°C/1h

5.4 Conclusions

$Na_2A_5(MoO_4)_6$ (A = Zn, Mg, Ca, Sr and Ba) ceramics are prepared by solid-state ceramic route. Phase formation of these ceramic compositions has been studied using TG/DTA analyses. Powder X-ray diffraction studies reveal that $Na_2Zn_5(MoO_4)_6$ and $Na_2Mg_5(MoO_4)_6$ ceramics are phase pure whereas their Ca, Sr and Ba analogues exhibit multiphase nature with Na_2MoO_4 and alkaline earth molybdate phases. Laser Raman spectroscopy has been employed to understand the molecular structure of the compositions. The prominent bands observed in the Raman spectrum are attributed to the normal modes of vibration of $(MoO_4)^{2-}$ tetrahedra. The Raman bands of $Na_2A_5(MoO_4)_6$ (A = Ca, Sr and Ba) ceramics are similar to those of $CaMoO_4$, $SrMoO_4$ and $BaMoO_4$. The microstructure of the sintered ceramics are studied using scanning electron microscopy. The multiphase nature of $Na_2A_5(MoO_4)_6$ (A = Ca, Sr and Ba) ceramics is further ascertained by EDS point analysis. Among the ceramics studied, $Na_2Zn_5(MoO_4)_6$ ceramic sintered at 590°C shows promising dielectric properties with ε_r = 8.1, Q_u x f = 35,800 GHz and τ_f = −95 ppm/°C at microwave frequencies. The hygroscopic nature of $Na_2Mg_5(MoO_4)_6$ limits its use as a ULTCC material. $Na_2A_5(MoO_4)_6$ (A = Zn, Ca, Sr and Ba) ceramics show good shrinkage at ultra low temperatures. The chemical compatibility of $Na_2A_5(MoO_4)_6$ (A = Zn, Mg, Ca, Sr and Ba) ceramics with Al metal electrode is studied using powder X-ray diffraction and energy dispersive X-ray spectroscopy. All the compositions except Ca showed good Al compatibility. The present study reveals that among the samples studied $Na_2Zn_5(MoO_4)_6$ is a glass free, phase pure and cost effective microwave ceramic system ideal for ULTCC applications.

References

[1]   V. A. Efremov, V. M. Zhukovskij, Y. G. Petrosyan, Phase diagram of Na_2MoO_4-$MgMoO_4$ system, Zh. Neorg. Khim., 21 [1] (1976) 209-213.

[2]   A. L. Kruglyashov, E. M. Skou, Ionic conductivity of compounds in the system Na_2MoO_4-$ZnMoO_4$, Solid State Ion., 28, (1988) 233-236.

[3]   R. F. Klevtsova, V. G. Kim, P. V. Klevtsov, X-ray diffraction investigation of double molybdates $Na_2R_5^{2+}(MoO_4)_6$, R= Mg, Co, Zn, Sov. Phys. Crystallogr. 25 [6] (1980) 657-660.

[4]   S. F. Solodovnikov, R. F. Klevtsova, P. V. Klevtsov, A correlation between the structure and some physical properties of binary molybdates (Tungstates) of uni- and bivalent metals, J. Struct. Chem., 35 [6] (1994) 879-889.

[5]   L. Zhang, L. Li, Y. Huang, S. Sun, Z. Lin, G. Wang, Growth, spectral property and crystal field analysis of Cr^{3+}-doped $Na_2Mg_5(MoO_4)_6$ crystal, Opt. Mater., 49 (2015) 75-78.

[6]   G. D. Tsyrenova, S. F. Solodovnikov, E. G. Khaikina, E. T. Khobrakova, Z. G. Bazarova, Z. A. Solodovnikova, Phase formation in the systems Ag_2MoO_4–MO–MoO_3 (M= Ca, Sr, Ba, Pb, Cd, Ni, Co, Mn) and crystal structures of $Ag_2M_2(MoO_4)_3$ (M= Co, Mn), J. Solid State Chem., 177 [6] (2004) 2158-2167.

[7]   S. F. Solodovnikov, Z. A. Solodovnikova, I. A. Gudkova, E. S. Zolotova, V. N. Yudin, Homogeneity regions of double molybdates in the Na_2MoO_4-$MgMoO_4$ system and structures of triclinic $Na_{1.51}Mg_{2.245}(MoO_4)_3$ and $Na_{1.66}Mn_{2.17}(MoO_4)_3$, J. Struct. Chem., 54 [5] (2013) 917-925.

[8]   E. Ines, M. F. Zid, A. Driss, Synthesis, Crystal Structure and Electrical Properties of the Molybdenum Oxide $Na_{1.92}Mg_{2.04}Mo_3O_{12}$, J. Crystallogr., 2013. (http://dx.doi.org/10.1155/2013/146567)

[9]   C. Gicquel-Mayer, M. Mayer, Etude structurale du molybdate double $Na_{0.5}Zn_{2.75}(MoO_4)_3$. Revue De Chimie. Minérale, 19 (1982) 91-98.

[10] Y. G. Petrosyan, E. V. Tkachenko, V. M. Zhukovskij, Phase diagrams of Na_2MoO_4-$MMoO_4$ (M-Ca,Sr,Ba), Izv. Akad. Nauk SSSR, Neorg. Mater., 11 [9] (1975) 1618-1621.

[11] B. W. Hakki, P. D. Coleman, A dielectric resonator method of measuring inductive capacities in the millimeter range, IRE Trans. Microwave Theory Tech., 8 [4] (1960) 402-410.

[12] J. Krupka, K. Derzakowski, B. Riddle, J. B. Jarvis, A dielectric resonator for measurements of complex permittivity of low loss dielectric materials as a function of temperature, Meas. Sci. Technol., 9 [10] (1998) 1751-1756.

[13] K. P. Murali, S. Rajesh, O. Prakash, A. R. Kulkarni, R. Ratheesh, Comparison of alumina and magnesia filled PTFE composites for microwave substrate applications, Mater. Chem. Phys., 113 [1] (2009) 290-295.

[14] R. D. Shannon, Revised effective ionic radii and systematic studies of interatomic distances in halides and chalcogenides, Acta crystallogr. A, 32 [5] (1976) 751-767.

[15] F. D. Hardcastle, I. E. Wachs, Molecular structure of molybdenum oxide in bismuth molybdates by Raman spectroscopy, J. Phys. Chem., 95 [26] (1991) 10763-10772.

[16] F. D. Hardcastle, I. E. Wachs, Determination of molybdenum–oxygen bond distances and bond orders by Raman spectroscopy, J. Raman Spectrosc., 21 [10] (1990) 683-691.

[17] N. K. James, R. Ratheesh, Microwave dielectric properties of low-temperature sinterable $BaCe_2(MoO_4)_4$ ceramics, J. Am. Ceram. Soc., 93 [4] (2010) 931-933.

[18] B. P. Singh, P. V. Ramakrishna, S. Singh, V. K. Sonu, S. Singh, P. Singh, A. Bahadur, R. A. Singh, S. B. Rai, Improved photo-luminescence behaviour of Eu^{3+} activated $CaMoO_4$ nanoparticles via Zn^{2+} incorporation, RSC Adv., 5 [69] (2015) 55977-55985.

[19] R. H. Busey, O. L. Keller Jr, Structure of the aqueous pertechnetate ion by Raman and infrared spectroscopy. Raman and infrared spectra of crystalline $KTcO_4$, $KReO_4$, Na_2MoO_4, Na_2WO_4, $Na_2MoO_4 \cdot 2H2O$, and $Na_2WO_4 \cdot 2H2O$, J. Che. Phys., 41 [1] (1964) 215-225.

[20] A. W. Sleight, Accurate cell dimensions for ABO_4 molybdates and tungstates, Acta Crystallogr. B, 28 [10] (1972) 2899-2902.

[21] G. K. Choi, J. R. Kim, S. H. Yoon, K. S. Hong, Microwave dielectric properties of scheelite (A= Ca, Sr, Ba) and wolframite (A= Mg, Zn, Mn) $AMoO_4$ compounds, J. Eur. Ceram. Soc., 27 [8-9] (2007) 3063-3067.

[22] V. L. Vilesh, G. Subodh, Crystal structure, phonon modes and dielectric properties of B site ordered $ABiLiTeO_6$ (A= Ba, Sr) double perovskites, Ceram. Int., 44 [11] (2018) 12036-12041.

[23] S. D. Ramarao, S. R. Kiran, V. R. K. Murthy, Structural, lattice vibrational, optical and microwave dielectric studies on $Ca_{1-x}Sr_xMoO_4$ ceramics with scheelite structure, Mater. Res. Bull., 56 (2014) 71-79.

[24] M. Y. Chen, C. T. Chia, I. N. Lin, L. J. Lin, C. W. Ahn, S. Nahm, Microwave properties of $Ba(Mg_{1/3}Ta_{2/3})O_3$, $Ba(Mg_{1/3}Nb_{2/3})O_3$ and $Ba(Co_{1/3}Nb_{2/3})O_3$ ceramics revealed by Raman scattering, J. Eur. Ceram. Soc., 26 [10-11] (2006) 1965-1968.

[25] J. Zhang, J. Zhai, J. Wang, J. Shao, X. Lu, X. Yao, Infrared dielectric response and Raman spectra of tunable $Ba_{0.5}Sr_{0.5}TiO_3$–Mg_2TiO_4 composite ceramics, J. Appl. Phys., 107 [1] (2010) 014106.

[26] F. Shi, H. Dong, Correlation of crystal structure, dielectric properties and lattice vibration spectra of $(Ba_{1-x}Sr_x)(Zn_{1/3}Nb_{2/3})O_3$ solid solutions, Dalton Trans., 40 [25] (2011) 6659-6667.

Chapter 6

Structure and microwave dielectric properties of new molybdate $AR_4(MoO_4)_7$ (A = Ba, Sr and Ca; R = La, Pr, Nd and Sm) ceramics for LTCC applications

6.1 Introduction

6.2 Materials and methods

6.3 Results and discussion

6.4 Conclusions

6.1 Introduction

The single phase binary molybdate compositions with scheelite based structures in the Na_2MoO_4-$AMoO_4$ and Na_2MoO_4-$R_2(MoO_4)_3$ systems are investigated in the previous chapters. In the present chapter, the crystal structure, microwave dielectric properties and co-firability of compositions with formula $AR_4(MoO_4)_7$ in the $AMoO_4$-$R_2(MoO_4)_3$ system having scheelite derived structure is investigated in detail. Several alkaline earth lanthanide double molybdates have been reported as excellent ceramics for LTCC applications. Single phase compositions with structure type $BaR_2(MoO_4)_4$ are reported as ceramics for low temperature co-firing applications [1-3]. A. A. Evdokimov and V. K. Trunov have extensively studied the $SrWO_4$-$R_2(WO_4)_3$ (R = La, Nd, or Sm) and part of $BaWO_4$-$La_2(WO_4)_3$ phase diagrams and reported the formation of a single phase composition with structural formula $BaLa_4(WO_4)_7$ and $SrR_4(WO_4)_7$ (R = La, Pr, Nd, Sm, Eu and Gd) with monoclinic unit cell [4]. The vectors $\vec{a}$, $\vec{b}$ and $\vec{c}$ of the $BaLa_4(WO_4)_7$ unit cell are related to that of the scheelite cell [4]. The luminescence properties of $BaLa_4(WO_4)_7$ has been widely reported [5-7]. Vakulyuk et al. have studied the $BaMoO_4$-$R_2(MoO_4)_3$ (R = La-Lu) systems and reported that the phase relationships in the $BaMoO_4$-$La_2(MoO_4)_3$ system are different from other lanthanides [8,9]. The equilibrium phase diagram of $BaMoO_4$-$La_2(MoO_4)_3$ is given in Figure 6.1.

$BaMoO_4$ has scheelite structure and $La_2(MoO_4)_3$ has scheelite-like structure with an ordered distribution of cations and cationic vacancies. In the $BaMoO_4$-$La_2(MoO_4)_3$ system, two ordered phases with superstructure other than that of $BaMoO_4$ and $La_2(MoO_4)_3$ are reported with structural formulae $BaLa_2(MoO_4)_4$ and $BaLa_4(MoO_4)_7$ [8]. The $SrMoO_4$-$R_2(MoO_4)_3$ and $CaMoO_4$-$R_2(MoO_4)_3$ systems are broadly classified into three categories ie. R = La-Sm, Eu-Tb and Ho-Lu, among which the compositions of structure type $AR_4(MoO_4)_7$ are reported only with rare earth elements from La to Sm [10,11]. The phase diagrams of $SrMoO_4$-$Sm_2(MoO_4)_3$ and $CaMoO_4$-$Nd_2(MoO_4)_3$ systems are reported by Vakulyuk et al. [11]. The $AR_4(MoO_4)_7$ are reported as an ordered phase on the basis of scheelite structure and are formed by ordered arrangement of cations and cationic vacancies with respect to Ca atoms in the $CaMoO_4$ structure. The phase relationships in the alkaline earth molybdate - rare earth molybdate phase diagrams are reported to be largely influenced by the crystal structure of lanthanide molybdate.
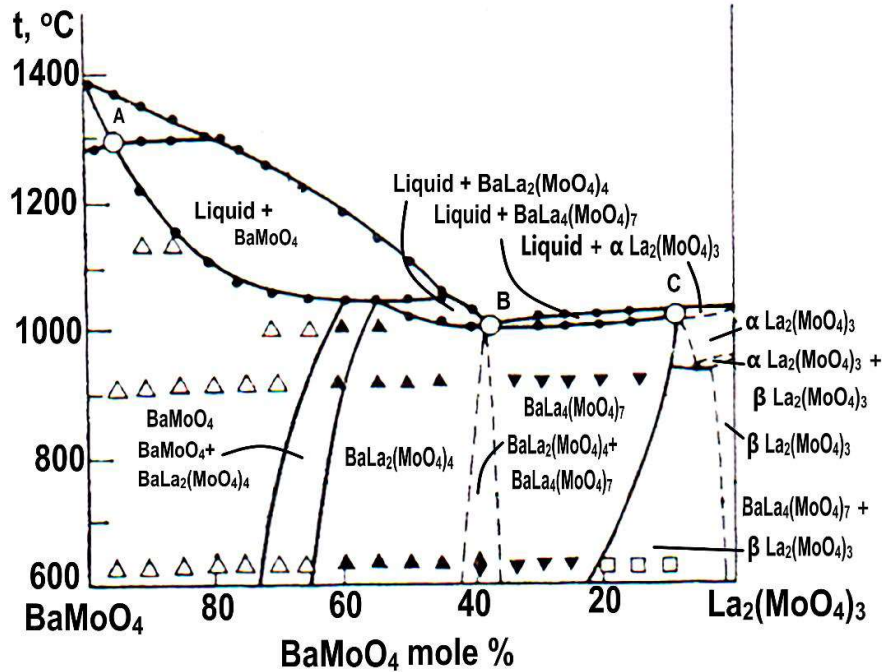
Figure 6.1 $BaMoO_4$-$La_2(MoO_4)_3$ phase diagram [Ref. 8]

The microwave dielectric properties of $ALa_4(MoO_4)_7$ (A = Ba, Sr, Ca) ceramics have been reported by our research group [12]. This chapter investigates the synthesis, structural characterization and microwave dielectric properties of $AR_4(MoO_4)_7$ (A = Ba, Sr, Ca; R = La, Pr, Nd, Sm) ceramics and their suitability for LTCC applications.

6.2 Materials and methods

$BaLa_4(MoO_4)_7$, $BaPr_4(MoO_4)_7$, $BaNd_4(MoO_4)_7$, $BaSm_4(MoO_4)_7$, $SrLa_4(MoO_4)_7$, $SrPr_4(MoO_4)_7$, $SrNd_4(MoO_4)_7$, $SrSm_4(MoO_4)_7$, $CaLa_4(MoO_4)_7$, $CaPr_4(MoO_4)_7$, $CaNd_4(MoO_4)_7$ and $CaSm_4(MoO_4)_7$ ceramics were prepared by the conventional solid-state ceramic route. The starting materials used were $BaCO_3$ (99+%, Sigma Aldrich), $SrCO_3$ (99.9%, Himedia), $CaCO_3$ (99+%, Sigma Aldrich), La_2O_3 (99.9%, Sigma Aldrich), Pr_6O_{11} (99.9%, Aldrich), Nd_2O_3 (99.9%, Aldrich), Sm_2O_3 (99.9%, Sigma Aldrich) and MoO_3 (99%, Himedia).The stoichiometric proportions of these chemicals were accurately weighed and thoroughly mixed in an agate mortar using double distilled water as the mixing medium. The resultant slurry was dried inside a hot air oven and calcined at 600°C for 1h in a programmable SiC furnace. The calcined powder was ground into fine powder and 5 wt% polyvinyl alcohol (PVA) solution was added to it as binder and dried. These samples were again ground well and made into cylindrical compacts using an 11 mm tungsten carbide die under a pressure of 250 MPa in a hydraulic hand press and sintered at appropriate temperatures in the

143

range 670 to 760°C to get maximum density. The dimensions of the sintered pellets were accurately measured and the bulk density values of the sintered samples were determined.

Structural characterization and phase purity of the samples were investigated by powder X-ray diffraction measurement using a Brucker Model 5005 X-ray diffractometer, Germany with CuKα radiation. Surface morphology and microstructure of the well sintered samples were studied by scanning electron microscopic (SEM) investigation using Carl Zeiss, Model No: EVO18 Research, Germany. The energy dispersive X-ray spectroscopy (EDS) analysis was employed to check the chemical compatibility of the ceramics with silver electrodes. Laser Raman spectra of these compositions were recorded using Thermo Scientific DXR with Nd:YVO4 DPSS laser of 532 nm to understand the molecular structure. A Vector Network Analyzer (Agilent make PNA E8362B, Bayan Lepas, Malaysia) was used to measure the microwave dielectric properties of the well sintered ceramics. The dielectric constant of the samples was measured by Hakki and Coleman post resonator technique [13] and the quality factor was measured by resonant cavity method [14]. The temperature coefficient of resonant frequency τ_f of the ceramics was also measured in the temperature range 30–100ºC.

6.3 Results and discussion

6.3.1 Powder X-ray diffraction studies

The powder X-ray diffraction patterns of the well sintered ceramic samples of $BaR_4(MoO_4)_7$ (R = La, Pr, Nd and Sm) ceramics are shown in Figure 6.2 a-d. The ICDD files of these compositions are not available and hence these XRD patterns are indexed according to the standard ICDD pattern of $BaLa_4(WO_4)_7$ with file no. 29-0177, which is reported to be isostructural with that of the corresponding molybdates under study. $BaLa_4(WO_4)_7$ has monoclinic structure with the lattice parameters a =12.18 Å, b = 12.03 Å and c = 33.77 Å, unit cell volume of 4895.46 Å^3 with 8 formula units per unit cell having a β value of 98.37º.

$BaLa_4(MoO_4)_7$ is formed as a single phase composition, whereas $BaR_4(MoO_4)_7$ (R = Pr, Nd, Sm) compositions are multiphase in nature. The standard ICDD peak positions of $BaLa_4(WO_4)_7$ are represented in Figure 6.2. The XRD patterns of $BaR_4(MoO_4)_7$ (R = Pr, Nd, Sm) ceramics contain phases of $BaR_2(MoO_4)_4$ and

$R_2(MoO_4)_3$ (R= Pr, Nd, Sm) respectively. The peaks corresponding to $BaPr_2(MoO_4)_4$ phase in the XRD pattern of $BaPr_4(MoO_4)_7$ ceramics marked with '|' are identified using the ICDD pattern of $BaLa_2(MoO_4)_4$ (file no. 35-0365) since ICDD file is not available for $BaPr_2(MoO_4)_4$. The peaks corresponding to $BaNd_2(MoO_4)_4$ and $BaSm_2(MoO_4)_4$ phases are indexed according to ICDD files 36-0193 and 67-0483 respectively and are marked with '|'. $Pr_2(MoO_4)_3$, $Nd_2(MoO_4)_3$ and $Sm_2(MoO_4)_3$ respectively are marked with '*' in the XRD patterns and are shown in Figure 6.2 as per the ICDD files 28-0861, 19-0817 and 24-1000 for the respective compositions.

The powder X-ray diffraction patterns of $SrR_4(MoO_4)_7$ (R= La, Pr, Nd and Sm) ceramics and that of $CaR_4(MoO_4)_7$ (R= La, Pr, Nd and Sm) ceramics show isomorphous nature and are given in Figures 6.3 a-d and 6.4 a-d respectively.
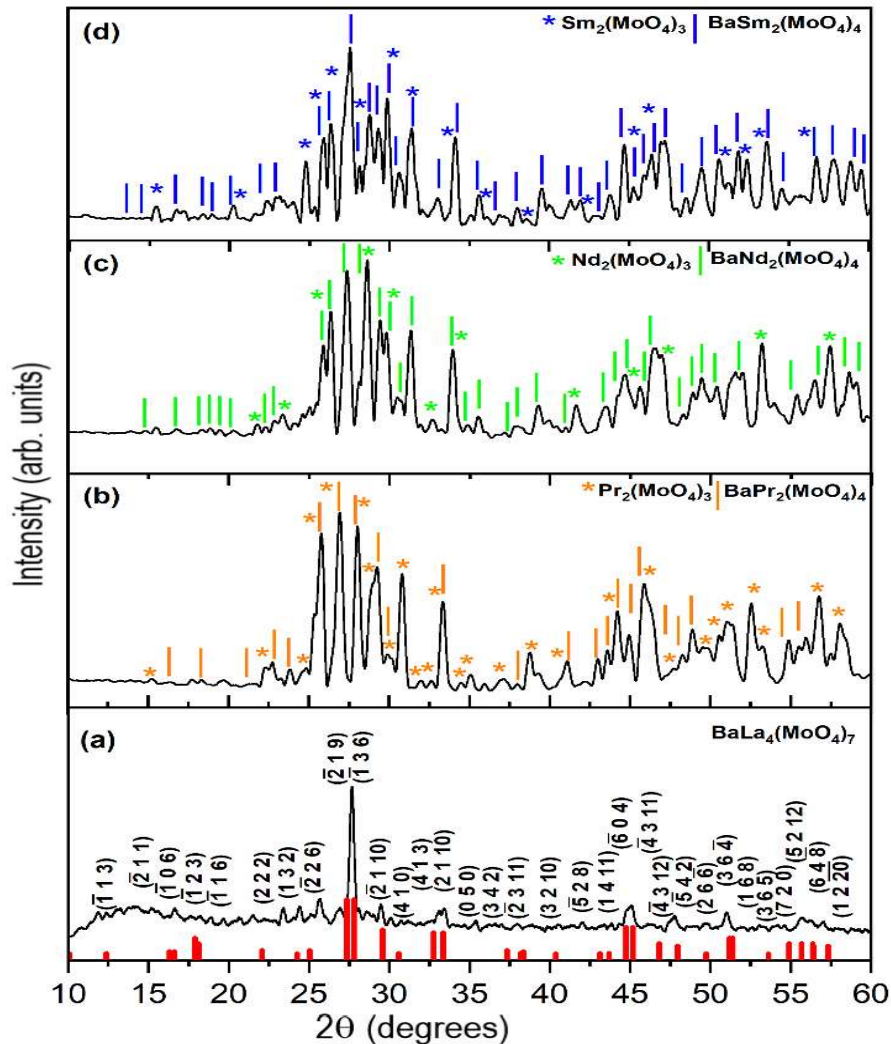
Figure 6.2 XRD patterns of $BaR_4(MoO_4)_7$ (R = La, Pr, Nd and Sm) sintered ceramics
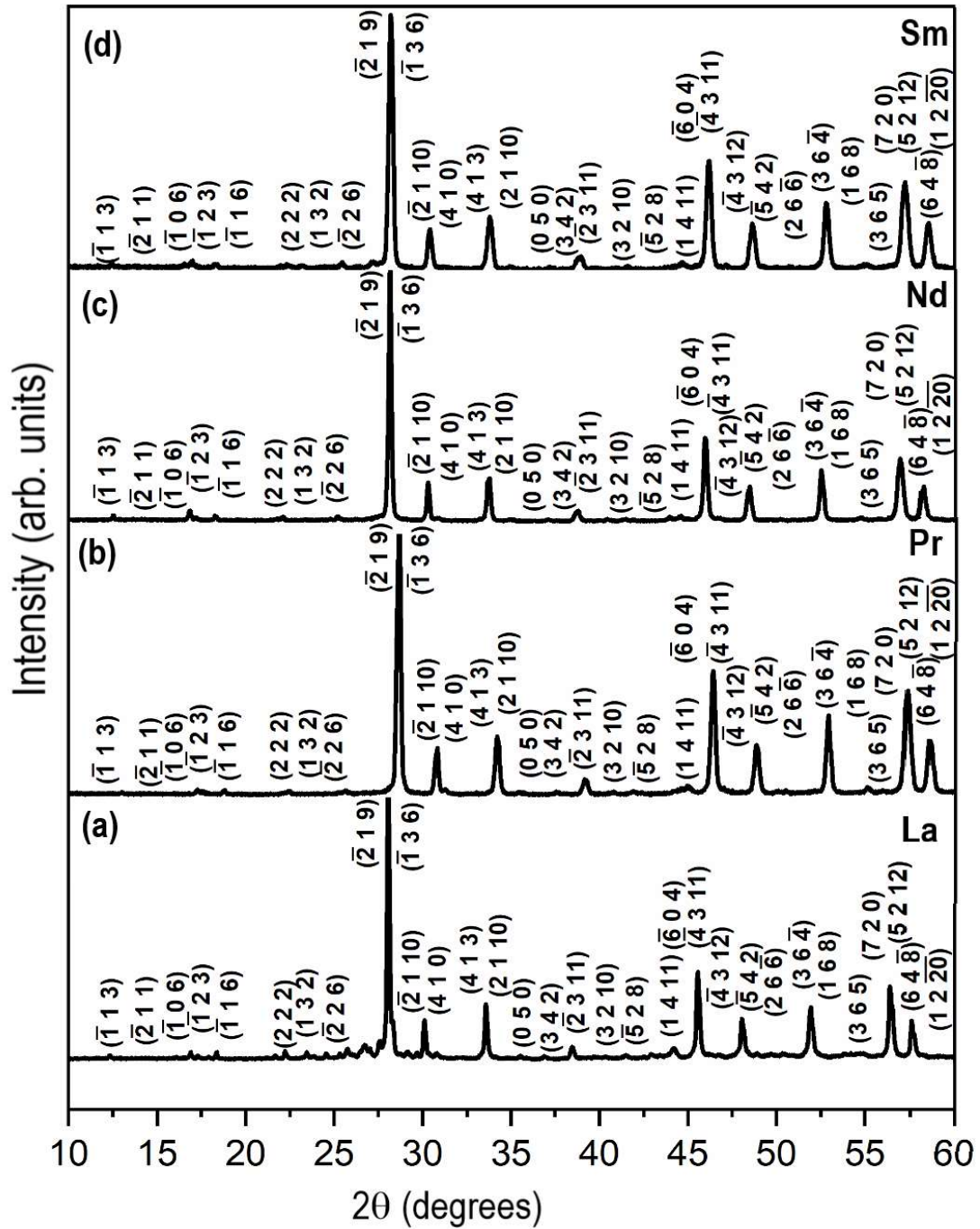
Figure 6.3 XRD patterns of SrR$_4$(MoO$_4$)$_7$ (R = La, Pr, Nd and Sm) sintered ceramics
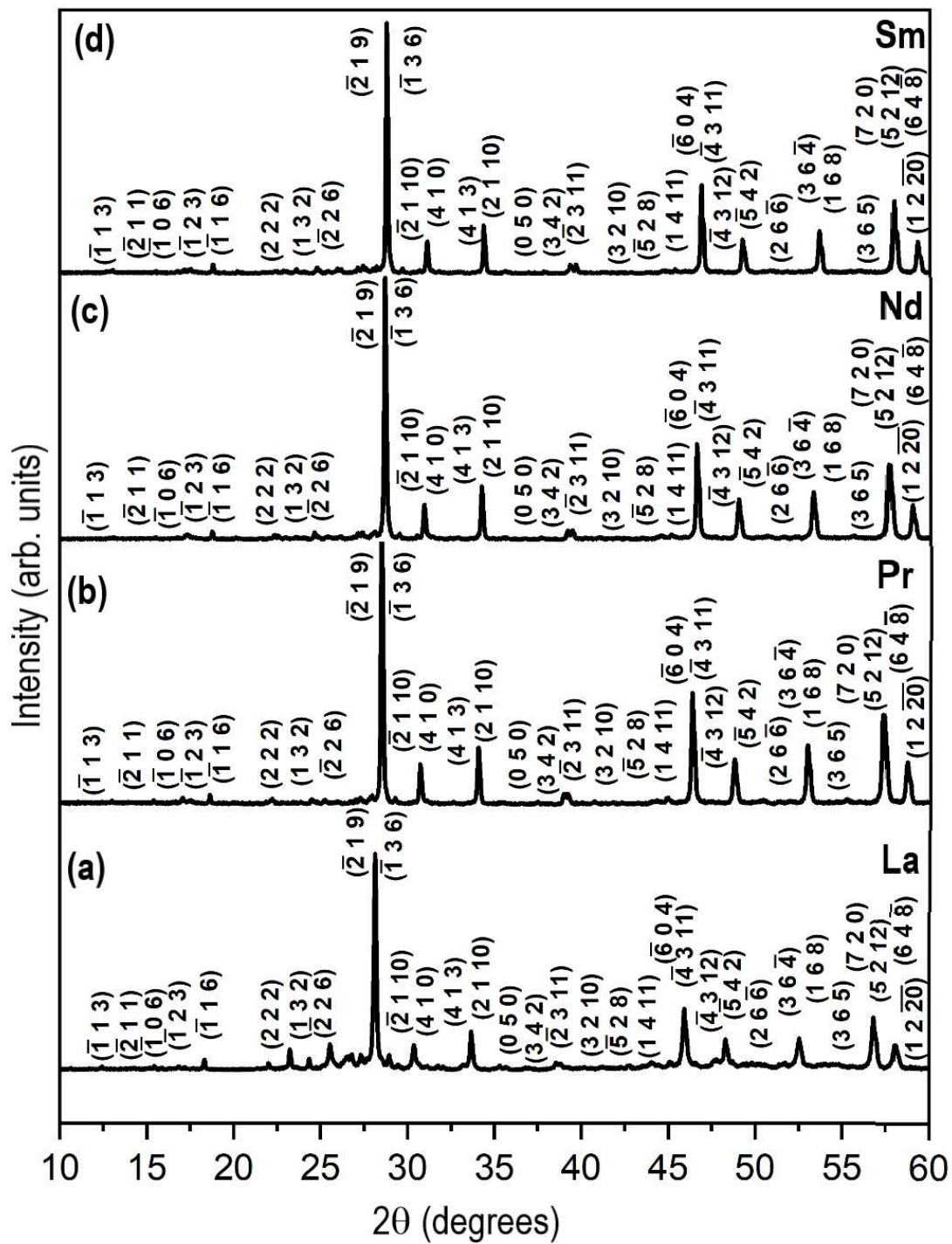
Figure 6.4 XRD patterns of $CaR_4(MoO_4)_7$ (R = La, Pr, Nd and Sm) sintered ceramics

The lattice parameters, unit cell volume, c/a ratio and theoretical density calculated from the X-ray diffraction patterns for the phase pure compositions are given in Table 6.1.

Table 6.1 Calculated lattice parameters, c/a ratio, unit cell volume and theoretical density of $AR_4(MoO_4)_7$ (A = Ba, Sr and Ca; R = La, Pr, Nd and Sm) ceramics

Compositions	Lattice parameters (Å)			c/a ratio	Unit cell volume (Å)³	Theoretical density (g/cm³)
	a	*b*	*c*			
$BaLa_4(MoO_4)_7$	12.184	12.393	32.238	2.64	4815	5.0
$SrLa_4(MoO_4)_7$	11.961	11.405	37.075	3.09	5003	4.7
$SrPr_4(MoO_4)_7$	11.737	11.018	37.708	3.21	4825	4.9
$SrNd_4(MoO_4)_7$	11.849	11.347	37.242	3.14	4954	4.8
$SrSm_4(MoO_4)_7$	11.796	11.313	37.313	3.16	4926	4.9
$CaLa_4(MoO_4)_7$	11.857	11.226	38.519	3.24	5073	4.5
$CaPr_4(MoO_4)_7$	11.755	11.036	38.293	3.25	4915	4.7
$CaNd_4(MoO_4)_7$	11.686	10.982	38.158	3. 26	4845	4.8
$CaSm_4(MoO_4)_7$	11.640	10.812	39.417	3.38	4908	4.8

6.3.2 Raman spectroscopic studies

Laser Raman spectra of the $BaR_4(MoO_4)_7$ (R = La, Pr, Nd and Sm) ceramics are given in Figure 6.5 a-d, that of $SrR_4(MoO_4)_7$ (R = La, Pr, Nd and Sm) ceramics are given in Figure 6.6 a-d and that of $CaR_4(MoO_4)_7$ (R = La, Pr, Nd and Sm) ceramics are given in Figure 6.7 a-d. Symmetric stretching vibrations of $(MoO_4)^{2-}$ tetrahedra are observed at 906 cm^{-1} and 937 cm^{-1} for $BaLa_4(MoO_4)_7$ ceramic together with asymmetric stretching vibrations at 859 cm^{-1} and 831 cm^{-1}. The asymmetric bending vibrations are observed for $BaLa_4(MoO_4)_7$ at 363 cm^{-1} and that of symmetric bending are observed at 310 cm^{-1} with a shoulder peak at 324 cm^{-1}. The bands in the region below 250 cm^{-1} belong to the lattice-mode vibrations and an unambiguous assignment of these modes is not possible [15-17]. The $SrLa_4(MoO_4)_7$ and $CaLa_4(MoO_4)_7$ ceramics also show Raman bands at identical wavenumbers as that of $BaLa_4(MoO_4)_7$ which ascertain that the compositions are isomorphous with similar molecular arrangement. The symmetric stretching vibrations of $(MoO_4)^{2-}$ tetrahedra are observed at 903 cm^{-1} together with a weak band at 937 cm^{-1} for $SrPr_4(MoO_4)_7$ and asymmetric stretching vibrations are observed at 819 cm^{-1}. The symmetric bending vibrations are observed at 316 cm^{-1} with a shoulder peak at 334 cm^{-1} and asymmetric bending vibrtations are observed at 378 cm^{-1}. The Raman spectrum of $CaPr_4(MoO_4)_7$ ceramic consists of a very sharp

symmetric stretching band at 901 cm^{-1} and asymmetric stretching bands at 823 cm^{-1} and 759 cm^{-1}. The symmetric bending vibrations are observed at 320 cm^{-1} and asymmetric bending vibrations at 383 cm^{-1}. Compared to La and Sm analogues, SrPr$_4$(MoO$_4$)$_7$ and CaPr$_4$(MoO$_4$)$_7$ ceramics have lower FWHM for the symmetric stretching mode and lesser number of additional modes in the stretching and bending vibrations. The multiphase nature of BaR$_4$(MoO$_4$)$_7$ (R = Pr, Nd, Sm) compositions are evident from the increased number of Raman modes present in the spectra.

The FWHM of the prominent Raman bands corresponding to symmetric stretching mode can be correlated with the quality factor of these ceramics. Among SrR$_4$(MoO$_4$)$_7$ (R = La, Pr, Nd and Sm) and CaR$_4$(MoO$_4$)$_7$ (R = La, Pr, Nd and Sm) ceramics, praseodymium compositions have sharp symmetric stretching mode. The Raman modes of SrNd$_4$(MoO$_4$)$_7$ and CaNd$_4$(MoO$_4$)$_7$ contain peaks corresponding to the vibrations of (MoO$_4$)$^{2-}$ tetrahedra, however the peak intensity is largely masked by the presence of prominent Raman bands at higher wavenumbers (1300-2400 cm^{-1}), which is a clear manifestation of fluorescence absorption by the material. These materials properties have the potential to establish the correlation between quantum yield of photoluminescence and quality factor of ceramic. In order to show the fluoroscence effect of ANd$_4$(MoO$_4$)$_7$ (A = Ba, Sr, Ca) compositions, the Raman spectra in the wavenumber range 1300-2400 cm^{-1} are shown in Figure 6.8.
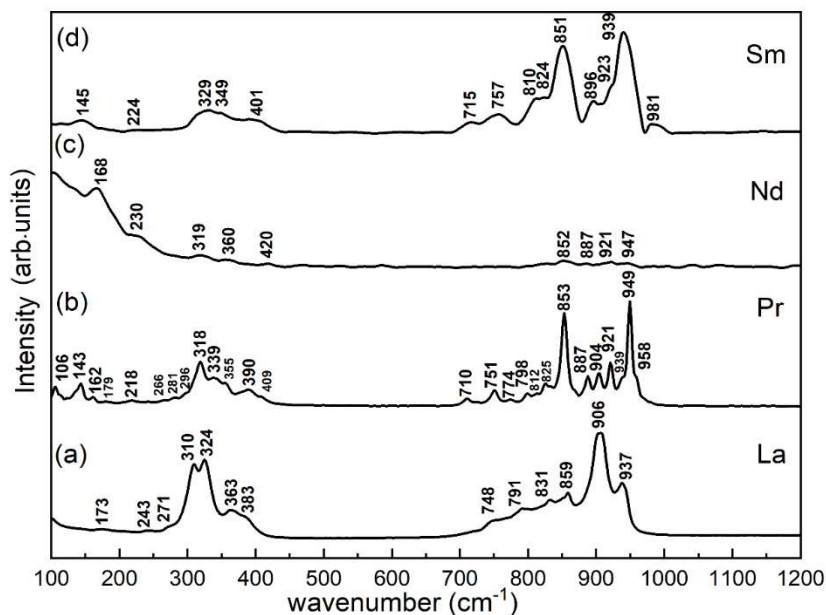
Figure 6.5 Laser Raman spectra of BaR$_4$(MoO$_4$)$_7$ (R = La, Pr, Nd and Sm) sintered ceramics
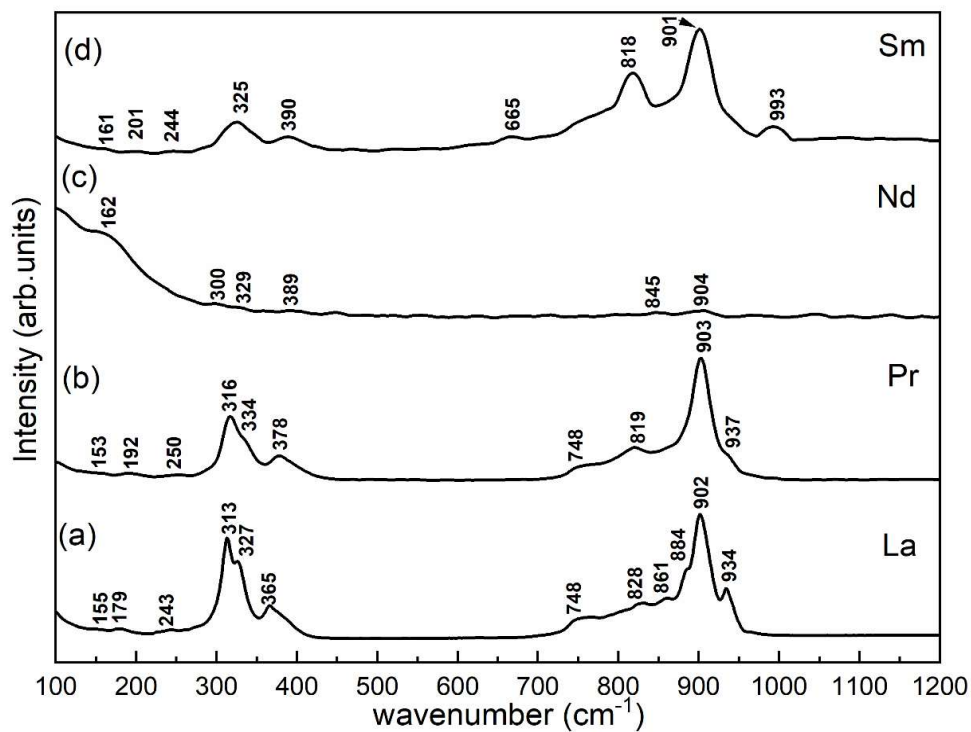
Figure 6.6 Laser Raman spectra of $SrR_4(MoO_4)_7$ (R = La, Pr, Nd and Sm) sintered ceramics
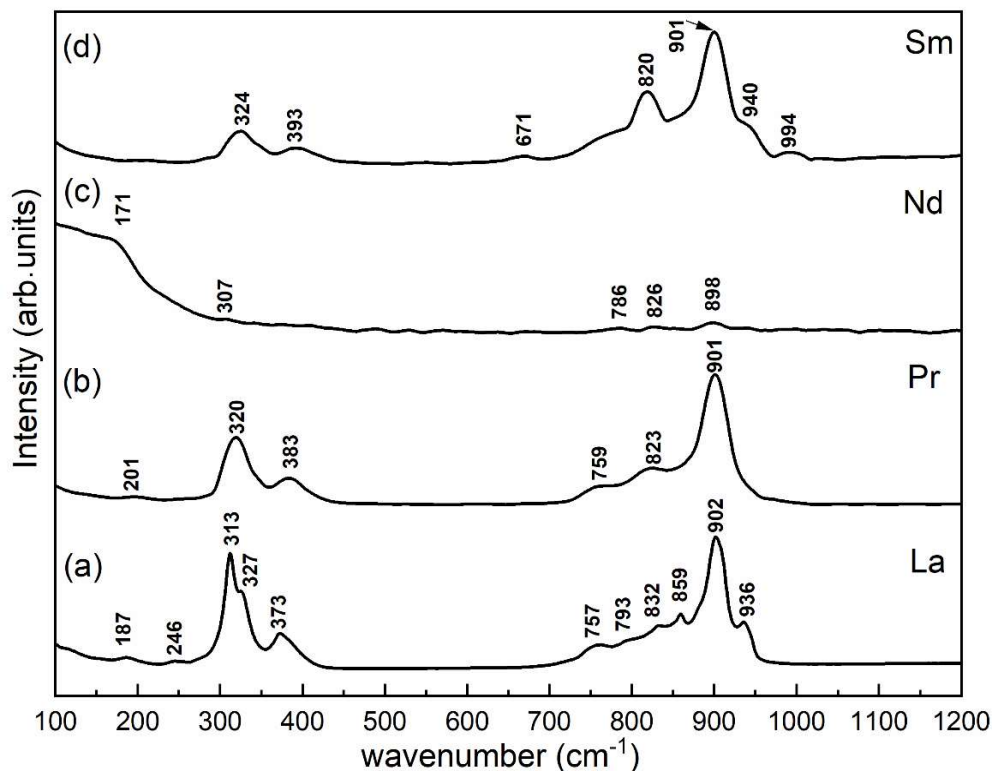
Figure 6.7 Laser Raman spectra of $CaR_4(MoO_4)_7$ (R = La, Pr, Nd and Sm) sintered ceramics
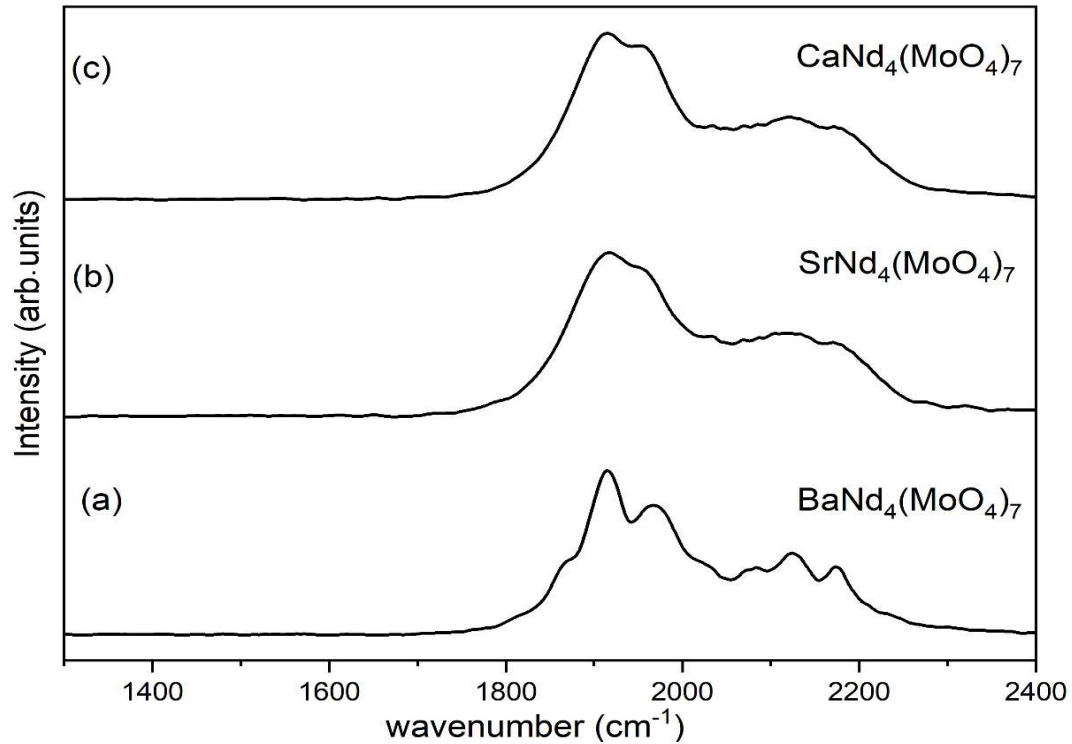
Figure 6.8 Laser Raman spectra of $ANd_4(MoO_4)_7$ (A = Ba, Sr and Ca) sintered ceramics

6.3.3 Morphological studies

The backscattered scanning electron micrographs of $BaR_4(MoO_4)_7$ (R = La, Pr, Nd and Sm) ceramics sintered at 710 °C/1h are shown in Figure 6.9. The sintered samples show dense morphology with polygonal grains with 1 to 5 µm size. Among the $BaR_4(MoO_4)_7$ (R = La, Pr, Nd, Sm) ceramics, $BaLa_4(MoO_4)_7$ ceramic alone shows phase homogeneity. The SEM micrographs of $BaPr_4(MoO_4)_7$, $BaNd_4(MoO_4)_7$ and $BaSm_4(MoO_4)_7$ ceramics clearly show the presence of two types of grain morphologies, the chemical composition of which is analysed using the energy dispersive X-ray spectroscopic analysis.
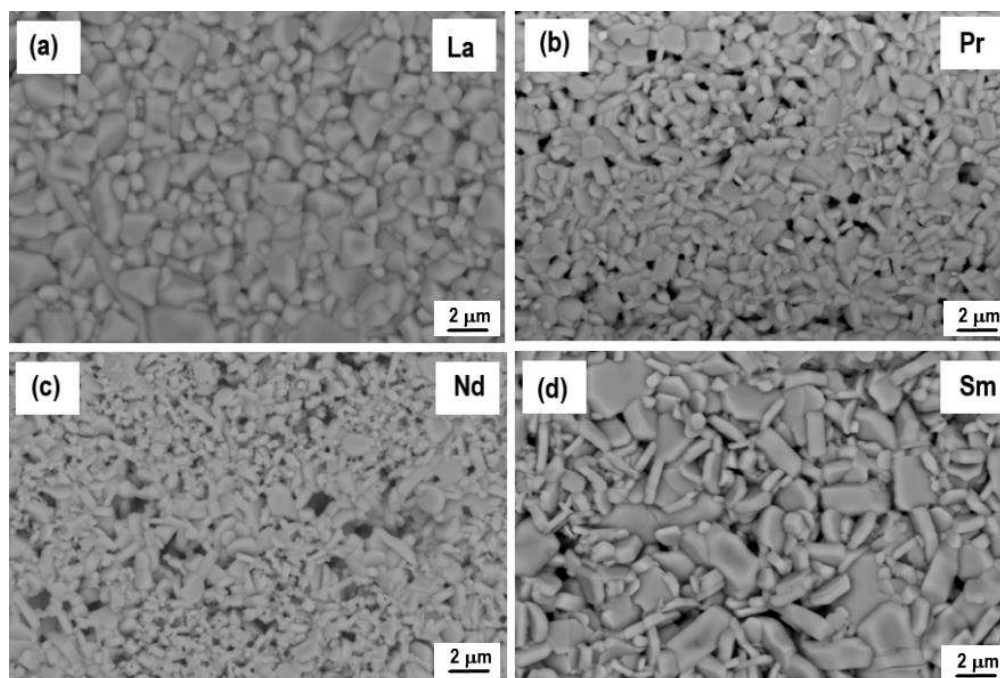
Figure 6.9 Backscattered SEM micrographs of (a) $BaLa_4(MoO_4)_7$, (b) $BaPr_4(MoO_4)_7$, (c) $BaNd_4(MoO_4)_7$ and (d) $BaSm_4(MoO_4)_7$ ceramics sintered at 710°C/1h

The EDS point analysis of $BaNd_4(MoO_4)_7$ sample carried out at two different grain types marked as EDS spot 1 and EDS spot 2 is shown in Figure 6.10. The EDS point analysis spectrum at spot 1 shows the presence of Ba, Nd, Mo and O, whereas that at spot 2 contains only Nd, Mo and O. The EDS point analysis results confirm that the $BaNd_4(MoO_4)_7$ sample is not phase pure, instead $BaNd_2(MoO_4)_4$ and $Nd_2(MoO_4)_3$ phases co-exist in the sample. Similarly, $BaPr_4(MoO_4)_7$ sample consists of $BaPr_2(MoO_4)_4$ and $Pr_2(MoO_4)_3$ phases and $BaSm_4(MoO_4)_7$ sample consists of $BaSm_2(MoO_4)_4$ and $Sm_2(MoO_4)_3$ phases. The EDS point analysis results further confirm the results obtained from XRD analysis. Hence, it can be concluded that among the $BaR_4(MoO_4)_7$ (R = La, Pr, Nd and Sm) compositions, only $BaLa_4(MoO_4)_7$ is phase pure. Crystal structure and thermodynamic stability of the compositions could be the possible reasons for the non-existence of $BaR_4(MoO_4)_7$ (R = Pr, Nd and Sm) phases.
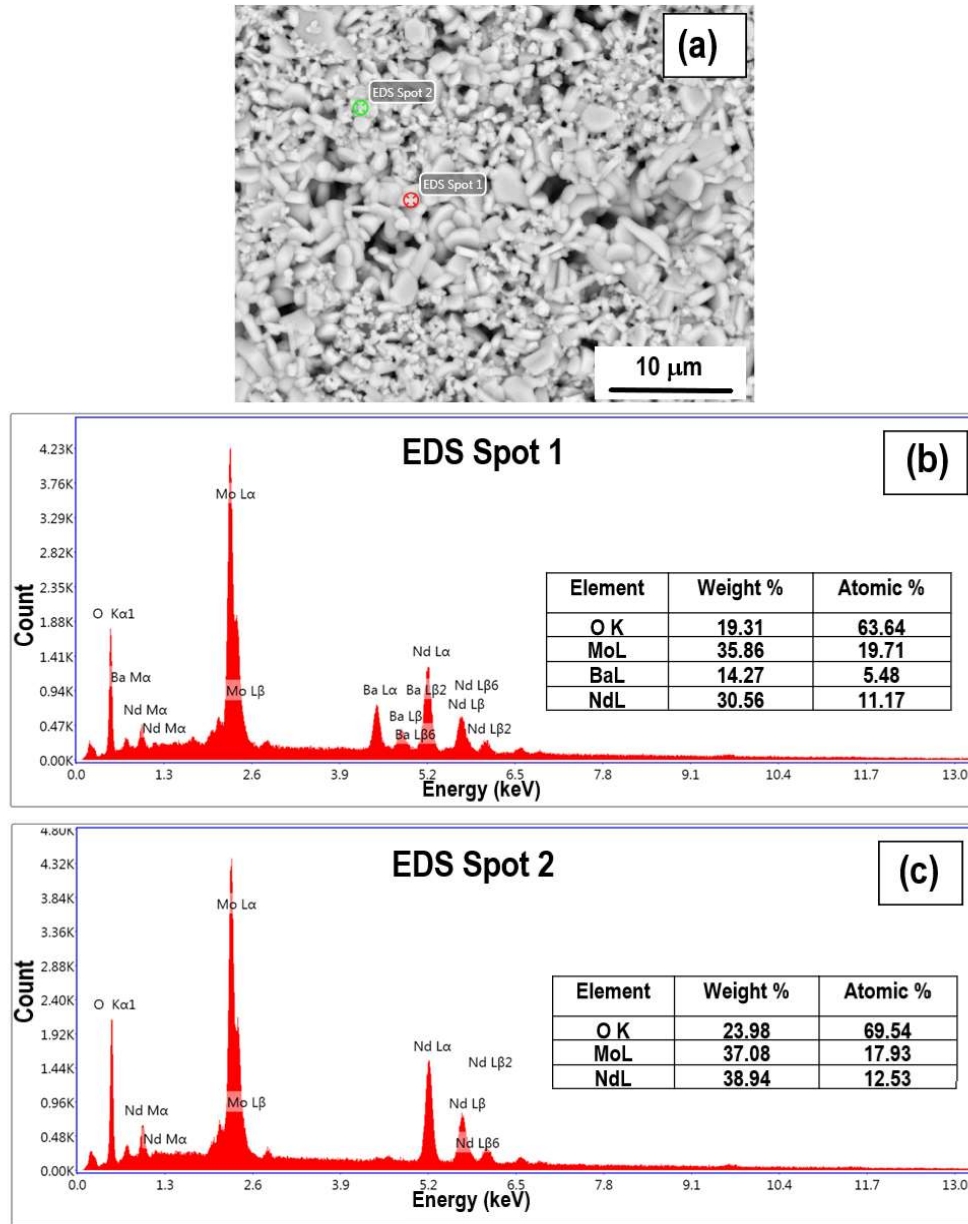
Figure 6.10 EDS point analysis spectra at EDS spot 1 and spot 2 of multiphase BaNd$_4$(MoO$_4$)$_7$ ceramic sintered at 710°C/1h

The SEM micrographs of SrR$_4$(MoO$_4$)$_7$ (R = La, Pr, Nd) ceramics sintered at 740°C/1h and SrSm$_4$(MoO$_4$)$_7$ ceramic sintered at 730°C/1h are given in Figure 6.11. The SEM micrographs of CaR$_4$(MoO$_4$)$_7$ (R = La, Pr, Nd) ceramics sintered at 750°C/1h and CaSm$_4$(MoO$_4$)$_7$ ceramic sintered at 740°C/1h are given in Figure 6.12.
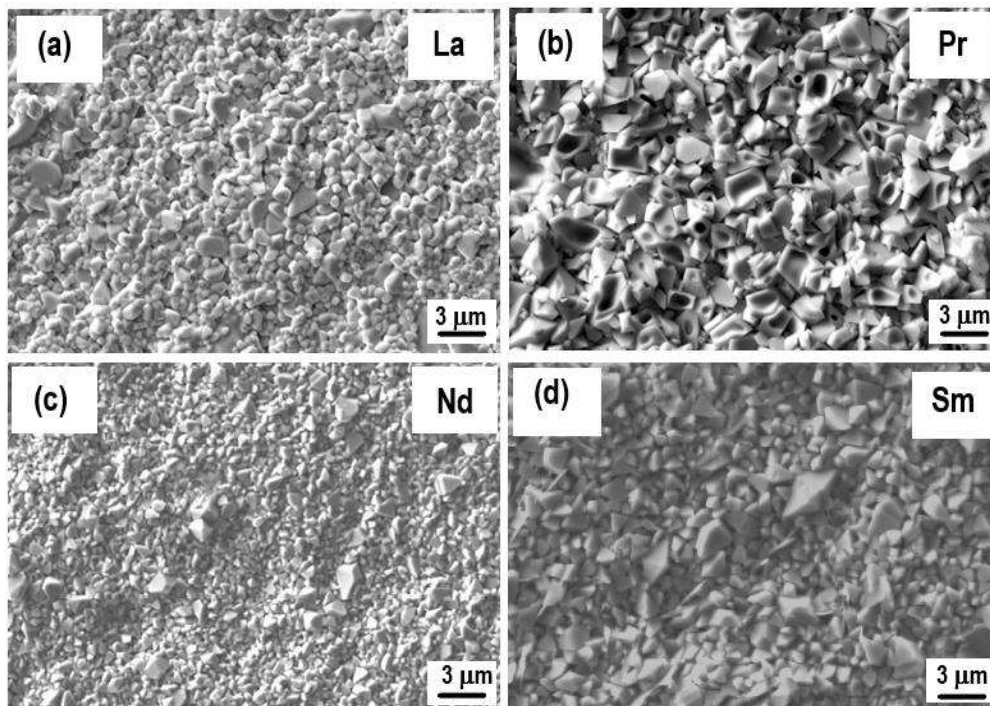
Figure 6.11 SEM micrographs of (a) SrLa$_4$(MoO$_4$)$_7$, (b) SrPr$_4$(MoO$_4$)$_7$, (c)SrNd$_4$(MoO$_4$)$_7$ ceramics sintered at 740°C/1h and (d) SrSm$_4$(MoO$_4$)$_7$ ceramics sintered at 730°C/1h
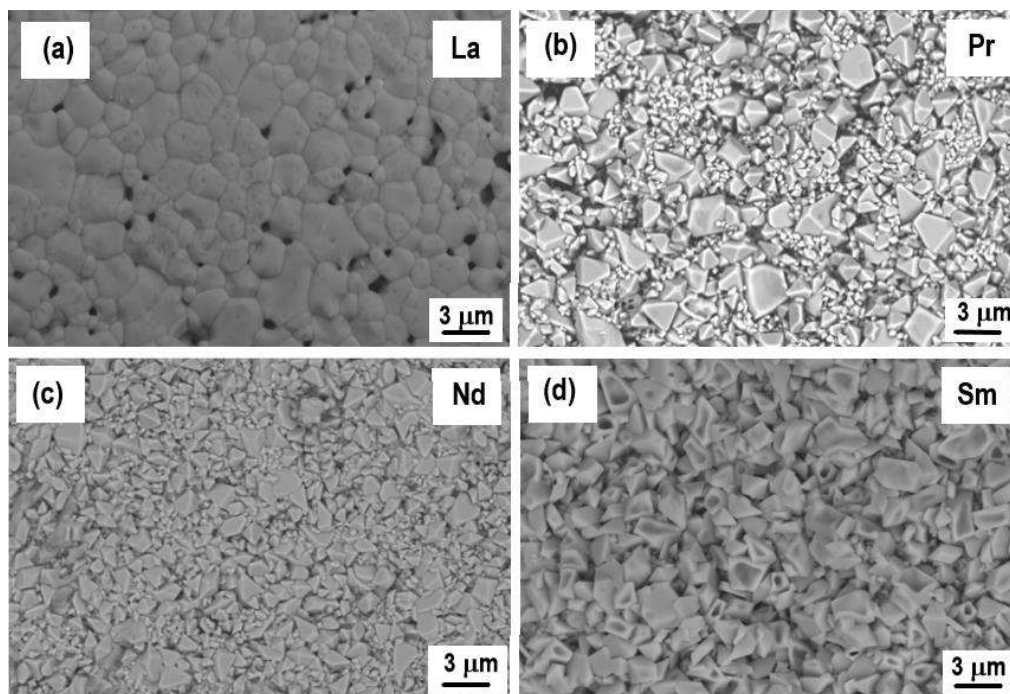
Figure 6.12 SEM micrographs of (a) CaLa$_4$(MoO$_4$)$_7$, (b) CaPr$_4$(MoO$_4$)$_7$, (c) CaNd$_4$(MoO$_4$)$_7$ ceramics sintered at 750°C/1h and (d) CaSm$_4$(MoO$_4$)$_7$ ceramics sintered at 740°C/1h

6.3.4 Microwave dielectric studies

The optimised sintering temperature, sintered density, dielectric constant, quality factor and temperature coefficient of resonant frequency of the $AR_4(MoO_4)_7$ (A = Ba, Sr, Ca; R = La, Pr, Nd, Sm) ceramics under study are given in Table 6.2. Among the $CaR_4(MoO_4)_7$ (R = La, Pr, Nd, Sm) ceramics, $CaPr_4(MoO_4)_7$ shows very high quality factor $Q_u \times f$ of 91,000 GHz with a dielectric constant of 10.6 and τ_f of -39 ppm/°C. Similar trend is shown by the $SrR_4(MoO_4)_7$ (R = La, Pr, Nd, Sm) system also wherein $SrPr_4(MoO_4)_7$ exhibiting the maximum quality factor $Q_u \times f$ of 78,600 GHz, dielectric constant of 9.6 and τ_f of -73 ppm/°C.

Table 6.2 Sintering temperature, maximum sintered density and microwave dielectric properties of $AR_4(MoO_4)_7$ (A = Ba, Sr, Ca; R = La, Pr, Nd, Sm) ceramics

Compositions	Sintering temperature (°C)/1h	Density (g/cm³)	ε_r @ GHz	$Q_u \times f$ (GHz)	τ_f (ppm/°C)
$BaLa_4(MoO_4)_7$	710	4.5	11.8	39,300	-68
$BaPr_4(MoO_4)_7$	710	3.9	8.7	30,500	-41
$BaNd_4(MoO_4)_7$	710	4.1	9.5	31,700	-35
$BaSm_4(MoO_4)_7$	710	3.7	8.1	27,500	-34
$SrLa_4(MoO_4)_7$	740	4.4	11.7	44,200	-83
$SrPr_4(MoO_4)_7$	740	4. 5	9.6	78,600	-73
$SrNd_4(MoO_4)_7$	740	4.4	9	39,400	-90
$SrSm_4(MoO_4)_7$	730	4.5	9.5	30,500	-79
$CaLa_4(MoO_4)_7$	750	4.2	11.4	30,200	-90
$CaPr_4(MoO_4)_7$	750	4.4	10.6	91,000	-39
$CaNd_4(MoO_4)_7$	750	4.5	10.4	68,400	-44
$CaSm_4(MoO_4)_7$	740	4.3	9.7	34,000	-48

6.3.5 Compatibility studies

The chemical compatibility of the ceramics with silver metal electrode is a pre-requisite for LTCC materials. The ceramics under study are co-fired with 20 wt% Ag at their optimum sintering temperatures for 1h. Powder X-ray diffraction and energy dispersive X-ray Spectroscopy (EDS) analyses have been carried out to check the reactivity of Ag with the host ceramic matrix. The XRD patterns of the co-fired samples of $BaLa_4(MoO_4)_7$, $SrLa_4(MoO_4)_7$ and $CaLa_4(MoO_4)_7$ ceramics are given in Figure 6.13. The XRD patterns of the Ag co-fired samples of $SrR_4(MoO_4)_7$ (R = La, Pr, Nd and Sm) ceramics and that of $CaR_4(MoO_4)_7$ (R = La, Pr, Nd and Sm) ceramics are given in Figures 6.14 and 6.15 respectively. The XRD patterns of co-fired samples contain peaks corresponding to Ag and the ceramic. However, the Ag peaks are manifested in all the XRD patterns with low intensity. The compatibility of the ceramics with Ag was further evaluated using EDS analysis.
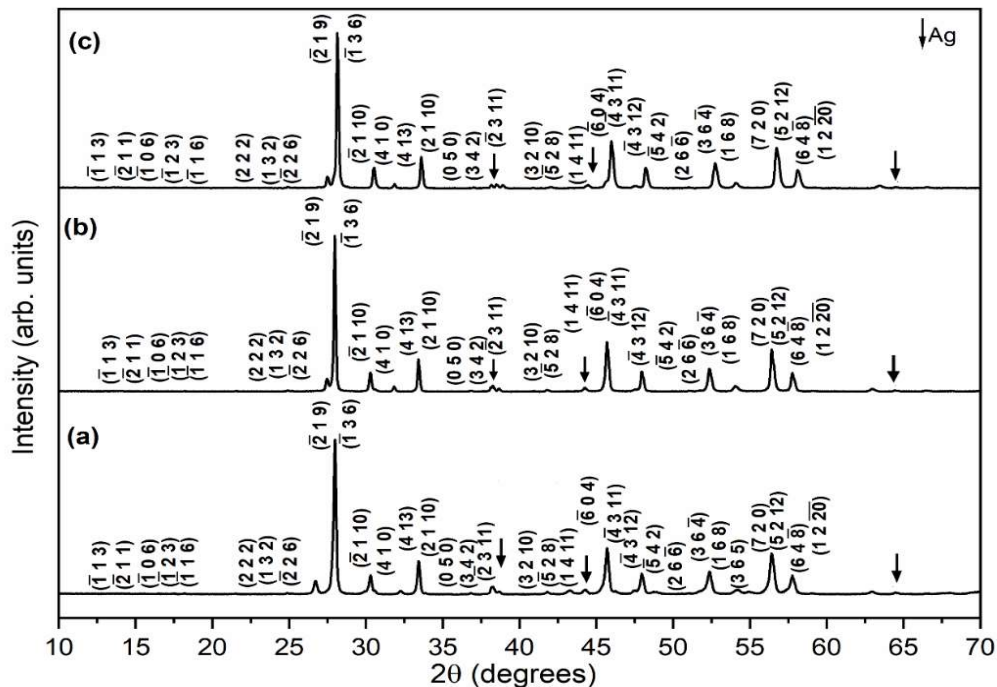
Figure 6.13 XRD patterns of a) $BaLa_4(MoO_4)_7$, b) $SrLa_4(MoO_4)_7$ and c) $CaLa_4(MoO_4)_7$ ceramics co-fired with 20 wt% Ag at optimum sintering temperature
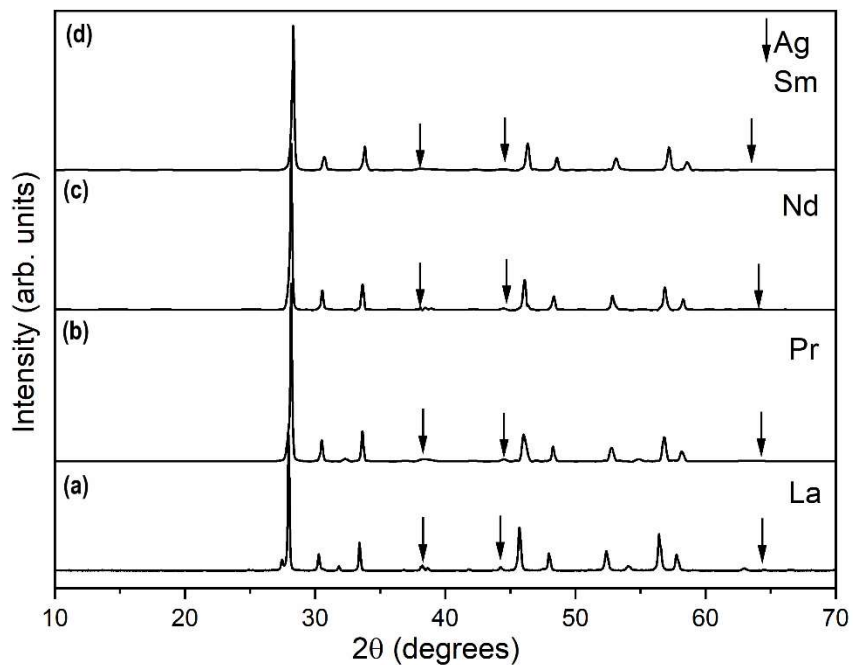
Figure 6.14 XRD patterns of 20 wt% Ag co-fired samples of $SrR_4(MoO_4)_7$ (R = La, Pr, Nd and Sm) ceramics
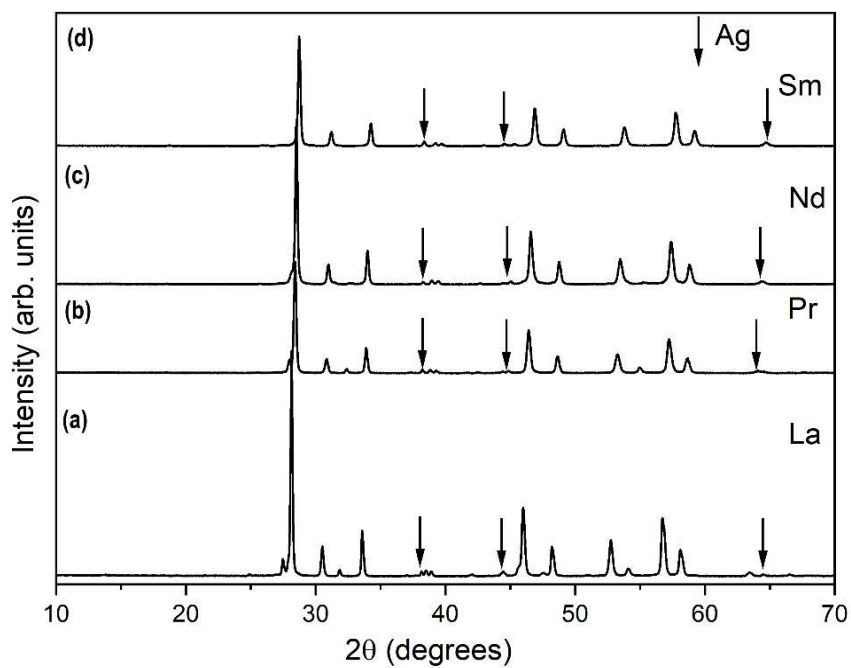
Figure 6.15 XRD patterns of 20 wt% Ag co-fired samples of $CaR_4(MoO_4)_7$ (R = La, Pr, Nd and Sm) ceramics

The backscattered SEM micrographs of the 20 wt% Ag co-fired samples of all the ceramics contain co-fired silver as a distinct region separated from the ceramic. EDS point analysis is done at silver region (spot 1) as well as ceramic region (spot 2) and the results are compiled in Table 6.3.

Among $SrR_4(MoO_4)_7$ (R = La, Pr, Nd and Sm) ceramics, better co-firability is obtained for $SrPr_4(MoO_4)_7$. A typical representation of the backscattered SEM image of 20 wt% Ag co-fired sample of $SrPr_4(MoO_4)_7$ is given in Figure 6.16 (a). The EDS point analysis results at spot 1 (silver region) and spot 2 (ceramic region) are illustrated in Figures 6.16 (b) and (c) respectively. The EDS point analysis done at silver region exhibits only silver whereas the analysis at the ceramic region shows the presence of small amount of Ag as well. The elemental mapping corresponding to elements Sr, Pr, Mo, O and Ag are shown in Figure 6.17. The EDS analysis show that 20 wt% Ag co-fired sample of $SrNd_4(MoO_4)_7$ and $SrSm_4(MoO_4)_7$ have Mo and O traces along with Ag in the silver region, unlike their La and Pr analogues.

The backscattered SEM image, EDS elemental mapping, EDS point analysis spectra at spot 1 and spot 2 of the co-fired sample of the $CaNd_4(MoO_4)_7$ are shown in Figure 6.18 a-d respectively. The EDS point analysis done at silver region exhibits only silver whereas the analysis at the ceramic region shows the presence of small amount of Ag as well. The EDS point analysis shows that Ag co-fired samples of $AR_4(MoO_4)_7$ (A = Ba, Sr, Ca; R = La, Pr, Nd and Sm) ceramics contain presence of Ag in the ceramic region which limits the use of these ceramics for LTCC applications. However, the excellent quality factor exhibited by these ceramics make them very promising candidate materials for other potential microwave circuit applications.

Table 6.3 EDS point analysis results of $AR_4(MoO_4)_7$ (A = Ba, Sr, Ca; R = La, Pr, Nd, Sm) ceramics co-fired with 20 wt% Ag at optimum sintering temperatures

Composition AR$_4$(MoO$_4$)$_7$	EDS point spectrum	Weight % of each element				
		A	R	Mo	O	Ag
BaLa$_4$(MoO$_4$)$_7$	Spot 1*	0	0	0	0	100.00
	Spot 2*	1.70	24.77	32.60	24.64	16.28
SrLa$_4$(MoO$_4$)$_7$	Spot 1	0	0	0	10.38	89.62
	Spot 2	3.20	24.94	32.79	24.67	14.41
SrPr$_4$(MoO$_4$)$_7$	Spot 1	0	0	0	0	100.00
	Spot 2	4.86	25.93	34.36	20.58	14.28
SrNd$_4$(MoO$_4$)$_7$	Spot 1	0	0	4.19	11.31	84.50
	Spot 2	5.12	25.97	37.34	16.12	15.45
SrSm$_4$(MoO$_4$)$_7$	Spot 1	0	0	5.89	8.77	85.34
	Spot 2	6.20	9.08	44.53	20.72	19.46
CaLa$_4$(MoO$_4$)$_7$	Spot 1	0	0	0	0	100.0
	Spot 2	2.89	25.90	37.42	17.27	16.52
CaPr$_4$(MoO$_4$)$_7$	Spot 1	3.12	24.29	36.38	20.10	16.12
	Spot 2	2.56	23.04	35.38	22.99	16.03
CaNd$_4$(MoO$_4$)$_7$	Spot 1	0	0	0	0	100.00
	Spot 2	1.68	27.80	35.63	16.70	18.19
CaSm$_4$(MoO$_4$)$_7$	Spot 1	0	0	0	11.34	88.66
	Spot 2	1.96	34.06	38.64	7.78	17.55

*Spot 1- silver region and Spot 2 – ceramic region in the 20 wt% Ag co-fired ceramics
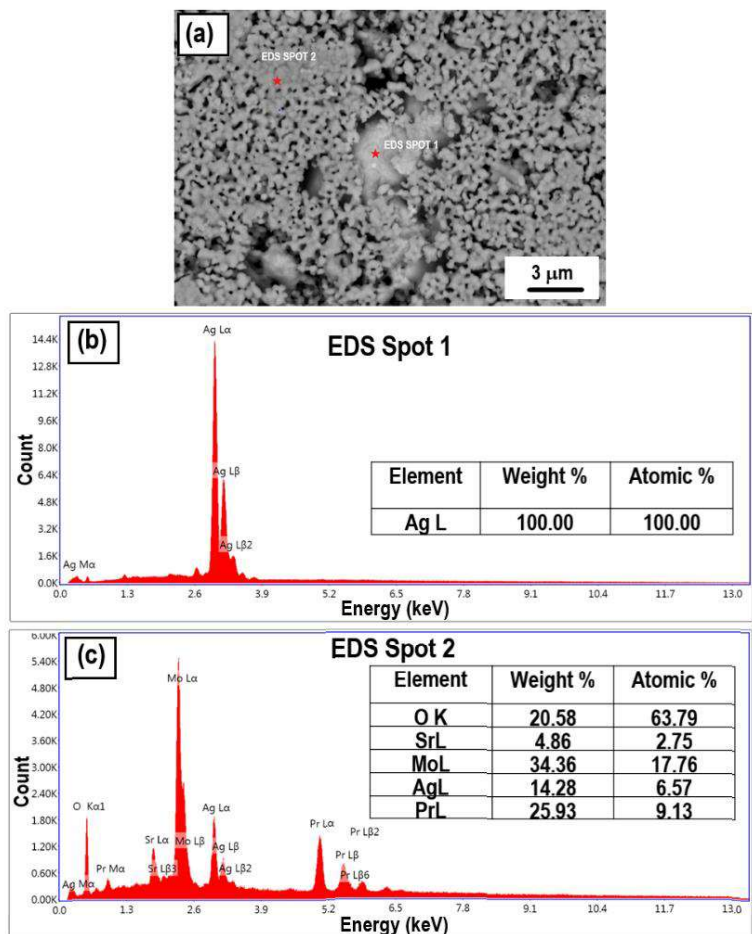
Figure 6.16 a) Backscattered SEM micrograph; EDS point analysis spectra at b) spot 1 and c) spot 2 of SrPr$_4$(MoO$_4$)$_7$ ceramic co-fired with 20 wt% Ag at 740°C/1h
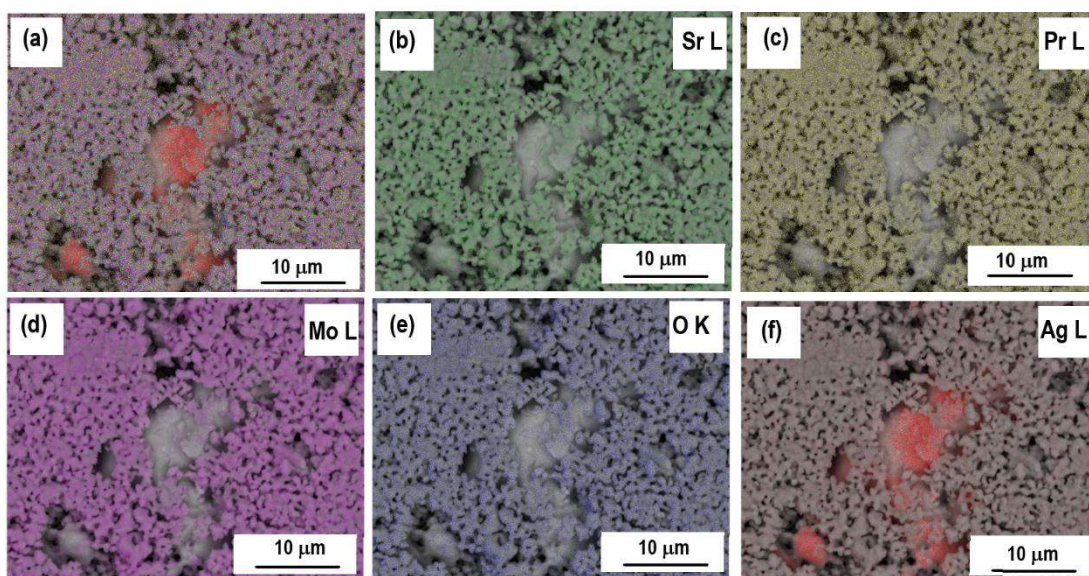
Figure 6.17 (a) EDS elemental mapping overlay on image; Elemental mapping of b) Sr, c) Pr, d) Mo, e) O and f) Ag elements in SrPr$_4$(MoO$_4$)$_7$ ceramic co-fired with 20 wt% Ag at 740°C/1h
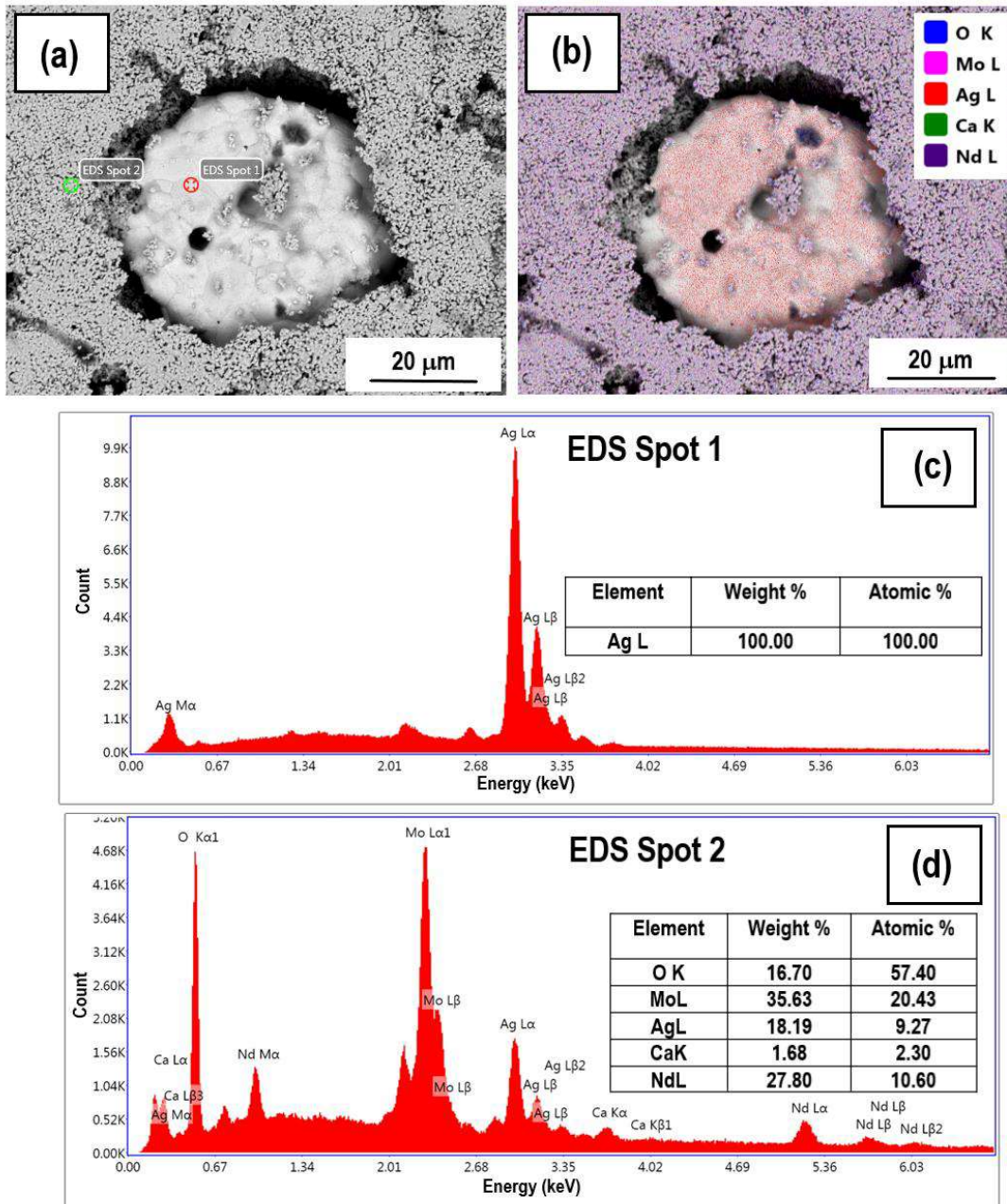
Figure 6.18 a) Backscattered SEM micrograph; b) EDS elemental mapping overlay on image; c) EDS spectrum at spot 1 and d) EDS spectrum at spot 2 of CaNd$_4$(MoO$_4$)$_7$ ceramic co-fired with 20 wt% Ag at 750°C/1h

6.4 Conclusions

$AR_4(MoO_4)_7$ (A = Ba, Sr, Ca; R = La, Pr, Nd and Sm) ceramics have been prepared by solid-state ceramic route. The isostructural nature of the phase pure compositions are confirmed by XRD and laser Raman spectra. The ceramics show excellent microwave dielectric properties with dielectric constant of phase pure compositions ranges from 9 to 11.8. Among the ceramics studied, $CaPr_4(MoO_4)_7$ exhibits the highest quality factor Q_u x f of 91,000 GHz and lowest τ_f of -39 ppm/^{o}C. The higher quality factor is correlated with the sharp symmetric stretching mode of the $CaPr_4(MoO_4)_7$ ceramics. The co-firability of these samples with Ag is determined by XRD and EDS analyses of the 20 wt% silver co-fired samples. The backscattered SEM images of the co-fired samples show the presence of silver and ceramic as distinct regions. The EDS point analysis at the ceramic region reveals the presence of Ag in addition to the constituent elements. The diffusion of silver into the ceramic on co-firing limits the applicability of these ceramics for LTCC applications. The $AR_4(MoO_4)_7$ (A = Ba, Sr, Ca; R = La, Pr, Nd and Sm) ceramics exhibit excellent microwave dielectric properties. However, the compatibility of the ceramics with Ag electrodes needs to be improved by varying the processing temperature and sintering atmosphere. The ceramic systems with low sintering temperatures investigated in this work offer possibilities for fabrication of various microwave circuit devices including substrate integrated waveguides.

References

[1] A. Surjith, R. Ratheesh, High Q ceramics in the $ACe_2(MoO_4)_4$ (A= Ba, Sr and Ca) system for LTCC applications, J. Alloys Compd., 550 (2013) 169-172.

[2] D. Zhou, L. X. Pang, J. Guo, Y. Wu, G. Q. Zhang, W. Dai, H. Wang, X. Yao, New microwave dielectric ceramics $BaLn_2(MoO_4)_4$ (Ln = Nd and Sm) with low loss, J. Am. Ceram. Soc., 94 [9] (2011) 2800-2803.

[3] W. B. Li, H. H. Xi, D. Zhou, Microwave dielectric properties of $BaY_2(MoO_4)_4$ ceramic with low sintering temperature, J. Mater. Sci.: Mater. Electron, 26 [3] (2015) 1608-1611.

[4] A. A. Evdokimov, V. K. Trunov, Investigation of certain tungstate systems, Russ. J. Inorg. Chem., 18 [10] (1973) 1506-1510.

[5] S. A. Yan, Y. S. Chang, J. W. Wang, W. S. Hwang, Y. H. Chang, Synthesis and luminescence properties of color-tunable $Ba_{1-y}Sr_yLa_{4-x}Tb_x(WO_4)_7$ (x= 0.02–1.2, y= 0–0.4) phosphors, Mater. Res. Bull., 46 [8] (2011) 1231-1236.

[6] S. A. Yan, J. W. Wang, Y. S. Chang, W. S. Hwang, Y. H. Chang, Synthesis and photoluminescence properties of $Ba_{1-y}Sr_yLa_{4-x}Dy_x(WO_4)_7$ (x= 0.04–0.2, y= 0–0.4) phosphors, Ceram. Int., 38 [3] (2012) 2569-2574.

[7] G. Blasse, G. J. Dirksen, L. H. Brixner, The luminescence of Eu^{3+}-activated $BaLa_4(WO_4)_7$, Mater. Chem. Phys., 21 [3] (1989) 293-299.

[8] V. V. Vakulyuk, A. A. Evdokimov, G. P. Khomchenko, The $BaMoO_4$-$Ln_2(MoO_4)_3$ systems (Ln = Nd, Sm, Yb), Russ. J. Inorg. Chem., 27 [7] (1982) 1016-1019.

[9] N. F. Fedorov, V. V. Ipatov, G. I. Rozhnovskaya, Phase equilibria in $BaMoO_4$-$Ln_2(MoO_4)_3$ systems (Ln = Nd or Gd), Russ. J. Inorg. Chem., 27 [7] (1982) 1019-1022.

[10] V. P. Sirotinkin, A. A. Evdokimov, V. K. Trunov, Equilibrium diagrams of the $AMoO_4$-$La_2(MoO_4)_3$ systems (A = Ca-Ba, Pb), Russ. J. Inorg. Chem., 26 [7] (1981) 1018-1020.

[11] V. V. Vakulyuk, A. A. Evdokimov, T. A. Berezina, Phase relationships in the $CaMoO_4$-$Ln_2(MoO_4)_3$ and $SrMoO_4$-$Ln_2(MoO_4)_3$ systems (Ln = Pr- Lu), Russ. J. Inorg. Chem., 27 [7] (1982) 1022-1024.

[12] P. V. Sarika (2015) Preparation and characterization of $ALa_4Mo_7O_{28}$ [A = Ba, Sr, Ca] ceramics for LTCC applications, (Unpublished master's thesis) C-MET, Thrissur, Kerala.

[13] B. W. Hakki, P. D. Coleman, A dielectric resonator method of measuring inductive capacities in the millimeter range, IRE Trans. Microwave Theory Tech., 8 [4] (1960) 402-410.

[14] J. Krupka, K. Derzakowski, B. Riddle, J. B. Jarvis, A dielectric resonator for measurements of complex permittivity of low loss dielectric materials as a function of temperature, Meas. Sci. Technol., 9 [10] (1998) 1751-1756.

[15] F. D. Hardcastle, I. E. Wachs, Determination of molybdenum–oxygen bond distances and bond orders by Raman spectroscopy, J. Raman Spectrosc., 21 [10] (1990) 683-691.

[16] N. K. James, R. Ratheesh, Microwave dielectric properties of low-temperature sinterable $BaCe_2(MoO_4)_4$ ceramics, J. Am. Ceram. Soc., 93 [4] (2010) 931-933.

[17] F. D. Hardcastle, I. E. Wachs, Molecular structure of molybdenum oxide in bismuth molybdates by Raman spectroscopy, J. Phys. Chem., 95 [26] (1991) 10763-10772.

Chapter 7

Effect of Ti^{4+} substitution on the structure and microwave dielectric properties of low temperature sinterable Pr$_2$Zr$_3$(MoO$_4$)$_9$ ceramics

7.1 Introduction

7.2 Materials and methods

7.3 Results and discussion

7.4 Conclusions

7.1 Introduction

Recently a few binary molybdates in the Ln_2O_3-ZrO_2-MoO_3 phase diagram (Ln = La, Nd, Sm) were reported as low temperature sintering ceramics with good microwave dielectric properties [1,2]. Ln_2O_3-ZrO_2-MoO_3 phase diagram is reported to have three binary molybdate structure types of formula $Ln_2Zr_3(MoO_4)_9$ (Ln = La-Tb), $Ln_2Zr_2(MoO_4)_7$ (Ln=Sm-Ho,Y) and $Ln_2Zr(MoO_4)_5$ (Ln=Tb-Lu,Y) [3-9]. $Ln_2(Zr/Hf)_3(MoO_4)_9$ compositions form a large family of isostructural compounds reported to be derived from a natural mineral called kosnarite with chemical formula $KZr_2(PO_4)_3$ which exhibits large isomorphic capacity to cation and anion substitutions [10,11]. The compounds in this series crystallize in the trigonal symmetry with space group $R\overline{3}c$ having 6 formula units per unit cell. The $Ln_2(Zr/Hf)_3(MoO_4)_9$ compounds have cage structure formed by the mixed framework of polyhedra and are ideal host ceramic matrices for nuclear waste containment. These materials are also reported as luminophores and also as solid state electrolytes in oxide fuel cells [12,13].

The compounds of $Pr_2Zr_3(MoO_4)_9$ type are reported to have a cage structure formed by the mixed framework of tricapped PrO_9 polyhedra, hexadentate ZrO_6 octahedra and bidentate MoO_4 tetrahedra. The crystal structure of $Pr_2Hf_3(MoO_4)_9$ is shown in Figure 7.1 [4].
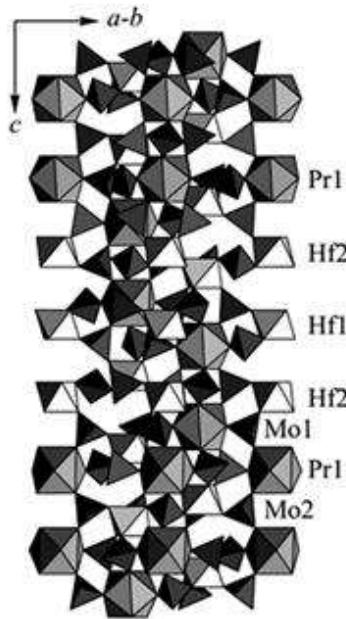
Figure 7.1 Crystal structure of $Pr_2Hf_3(MoO_4)_9$ [Ref. 4]

In this chapter, $Pr_2Zr_3(MoO_4)_9$ ceramic is prepared by solid-state ceramic route and the structure-property relationship has been established. The effect of Ti^{4+} ion substitution for Zr^{4+} ion is investigated and associated crystal structure and properties of the $Pr_2Zr_{(3-x)}Ti_x(MoO_4)_9$ (x = 0,1,2,3) compositions are studied in detail. The compatibility of these compositions with Ag/Al metal electrodes are also ascertained by XRD and EDS analyses.

7.2 Materials and methods

Conventional solid-state ceramic route was employed for the preparation of $Pr_2Zr_{(3-x)}Ti_x(MoO_4)_9$ (x = 0,1,2,3) ceramics from the starting materials Pr_6O_{11} (99.9%, Aldrich), ZrO_2 (99.9%, Aldrich), TiO_2 (99.9%, Merck) and MoO_3 (99%, Himedia). The stoichiometric quantities of the constituent chemicals were mixed thoroughly in double distilled water medium and the slurry was dried in a hot air oven. The dried samples were calcined at appropriate temperatures in a programmable SiC furnace. The calcined samples were ground well and mixed with 5 wt% poly vinyl alcohol (PVA) solution as binder and dried. The dried powder was pelletized in a hydraulic hand press at 250 MPa using a 11 mm tungsten carbide die and sintered at appropriate temperatures to get maximum density. The bulk density of the sintered samples were accurately determined from the dimensions of the sintered samples. Powder X-ray diffraction (XRD) patterns of the sintered samples were recorded using CuKα radiation with Brucker Model 5005 X-ray diffractometer, Germany. The Raman spectra of the compositions under study were recorded using a Thermo Scientific DXR with Nd:YVO$_4$ DPSS laser of 532 nm. Carl Zeiss, Model No: EVO18 Research (Germany) scanning electron microscope was used to study the microstructure of the sintered ceramic samples. A Vector Network Analyzer (Agilent make PNA E8362B, Bayan Lepas, Malaysia) was employed to determine the microwave dielectric properties of the sintered ceramic compacts. Dielectric constant of the sintered pellets were studied using Hakki and Coleman post resonator technique [14] whereas the quality factor using the resonant cavity method (Krupka cavity) [15]. The temperature coefficient of resonant frequency τ_f of the ceramic was measured in the temperature range 30-100ºC using Hakki and Coleman post resonator technique.

7.3 Results and discussion

7.3.1 Powder X-ray diffraction studies

The X-ray diffraction patterns of $Pr_2Zr_{(3-x)}Ti_x(MoO_4)_9$ (x = 0,1,2,3) ceramics are given in Figure 7.2 a-d. The powder X-ray diffraction pattern of $Pr_2Zr_3(MoO_4)_9$ ceramic exactly matches with the standard ICDD file no. 51-1851. $Pr_2Zr_3(MoO_4)_9$ is reported to have trigonal unit cell with space group $R\bar{3}c$. The phase purity of the $Pr_2Zr_3(MoO_4)_9$ composition was confirmed by the XRD analysis. Zr^{4+} and Ti^{4+} ions have comparable radii of 0.86 Å and 0.745 Å respectively and hence Ti^{4+} ion can fit into the Zr^{4+} site [16].

The XRD patterns of $Pr_2Zr_2Ti(MoO_4)_9$, $Pr_2ZrTi_2(MoO_4)_9$ and $Pr_2Ti_3(MoO_4)_9$ ceramics also resemble with that of $Pr_2Zr_3(MoO_4)_9$ phase exhibiting a uniform shift towards higher diffraction angles with increasing Ti^{4+} substitution. However, except $Pr_2Zr_2Ti(MoO_4)_9$, the XRD patterns of $Pr_2ZrTi_2(MoO_4)_9$ and $Pr_2Ti_3(MoO_4)_9$ ceramics contain additional peaks corresponding to α-MoO_3. The calculated lattice parameters of $Pr_2Zr_3(MoO_4)_9$ ceramic are a = 9.854 Å , c = 58.732 Å , c/a ratio 5.960 and unit cell volume 4938.44 Å^3 , which matches with the ICDD values, a = 9.820 Å , c = 58.666 Å, c/a ratio 5.974 and unit cell volume 4899.87 Å^3 . The lattice parameters and the unit cell volume decrease and c/a ratio increase as a result of Ti^{4+} substitution. The calculated lattice parameters for $Pr_2Ti_3(MoO_4)_9$ ceramics are a = 9.535 Å , c = 57.751 Å , c/a ratio 6.057 and unit cell volume of 4547.47 Å^3. The shift of XRD peaks towards the higher diffraction angles with increasing Ti^{4+} substitution can be attributed to the decrease in unit cell volume. The calculated lattice parameters, c/a ratio and unit cell volume are given in Table 7.1.
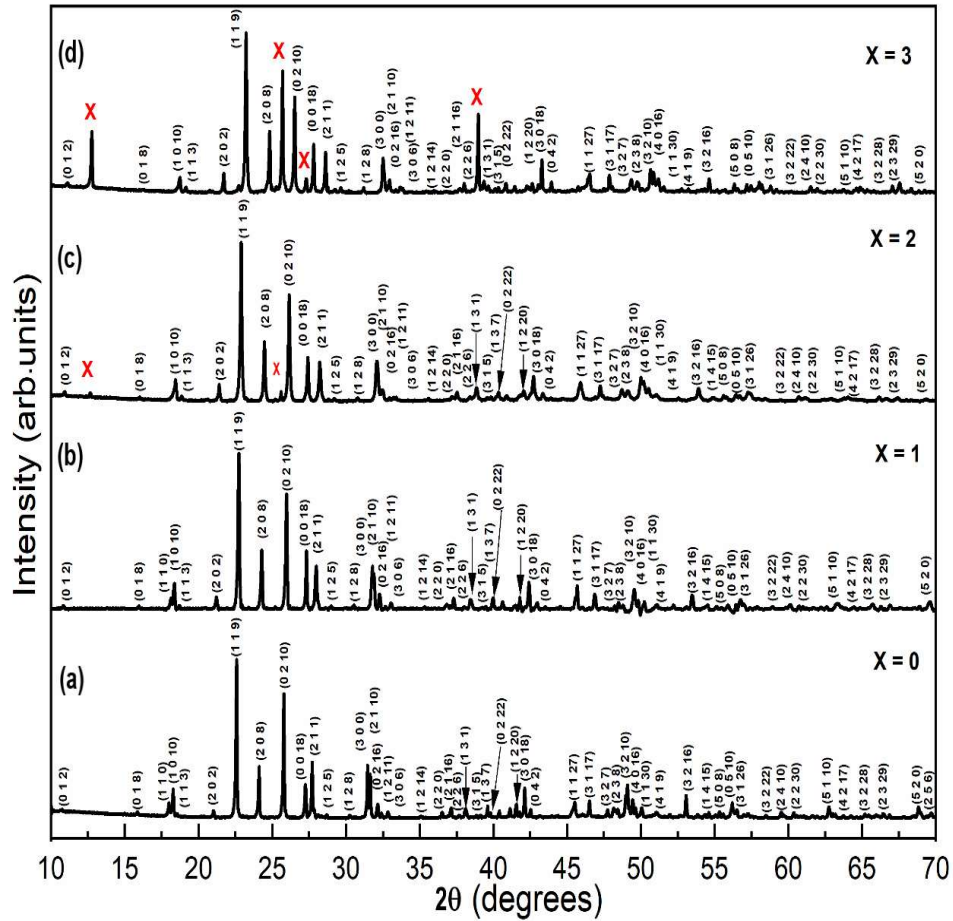
Figure 7.2 XRD patterns of $Pr_2Zr_{(3-x)}Ti_x(MoO_4)_9$ sintered ceramics with
(a) x =0, (b) x = 1, (c) x = 2 and (d) x = 3 (x= 0,1,2,3)

Table 7.1 Calculated lattice parameters, c/a ratio and unit cell volume of

$Pr_2Zr_{(3-x)}Ti_x(MoO_4)_9$ (x = 0,1,2,3) ceramics

Compositions	a=b (Å)	c (Å)	c/a	Unit cell volume $a^2c \sin60^o$ (Å)^3
$Pr_2Zr_3(MoO_4)_9$	9.854	58.732	5.960	4938.44
$Pr_2Zr_2Ti(MoO_4)_9$	9.758	58.654	6.011	4837.06
$Pr_2ZrTi_2(MoO_4)_9$	9.678	58.451	6.039	4741.46
$Pr_2Ti_3(MoO_4)_9$	9.535	57.751	6.057	4547.47

168

7.3.2 Raman spectroscopic studies

The laser Raman spectra of the $Pr_2Zr_{(3-x)}Ti_x(MoO_4)_9$ (x = 0,1,2,3) ceramics are shown in Figure 7.3 a-d. The Raman mode assignments of the $Pr_2Zr_{(3-x)}Ti_x(MoO_4)_9$ (x= 0,1,2,3) ceramics are given in Table 7.2. $Pr_2Zr_3(MoO_4)_9$ ceramic is reported to consist of two types of Mo atoms forming tetrahedra with average Mo-O bond lengths varying from 1.755 Å to 1.763 Å. The symmetric stretching modes of $(MoO_4)^{2-}$ tetrahedra occur at 876 cm^{-1} along with a shoulder peak at 892 cm^{-1} in the Raman spectrum of $Pr_2Zr_3(MoO_4)_9$ ceramic. The structure of $Pr_2Zr_3(MoO_4)_9$ consists of large voids within the three dimensional 'subnet' of $\{[Zr(MoO_4)_3]^{2-}\}_{3\infty}$ occupied by the Pr atom, which coordinate with the free vertices of $(MoO_4)^{2-}$ tetrahedra [4].The Raman spectrum of $Pr_2Zr_3(MoO_4)_9$ ceramic consists of additional bands at higher wavenumbers from 936 cm^{-1} to 986 cm^{-1} which are attributed to the presence of three dimensional 'subnet' of $\{[Zr(MoO_4)_3]^{2-}\}_{3\infty}$ in the structure. The prominent asymmetric stretching modes of $(MoO_4)^{2-}$ tetrahedra occur at 817 cm^{-1} and the symmetric and asymmetric bending modes at 338 cm^{-1} and 400 cm^{-1} respectively. Similar observations are found in other compositions under study also. The symmetric stretching modes of $(MoO_4)^{2-}$ tetrahedra occur at 878 cm^{-1}, along with a peak at 896 cm^{-1} in the Raman spectrum of the $Pr_2Ti_3(MoO_4)_9$ ceramic. The prominent asymmetric stretching modes of $(MoO_4)^{2-}$ tetrahedra occur at 818 cm^{-1} and 799 cm^{-1}. The symmetric bending mode occur at 347 cm^{-1} and the asymmetric bending mode is present as a broad peak at 400 cm^{-1} [17-20]. The symmetric stretching modes of ZrO_6 exist in the wavenumber region between 400 and 500 cm^{-1} are more prominent in the Raman spectrum of $Pr_2Zr_3(MoO_4)_9$. The free state TiO_6 octahedral Raman modes are at v_1 639 cm^{-1}, v_2 519 cm^{-1}, v_5 197 cm^{-1} and v_6 144 cm^{-1}. The bands of TiO_6 octahedra are present at 633 cm^{-1}, 513 cm^{-1}, 196 cm^{-1} and 143 cm^{-1} and is seen with maximum intensity in the $Pr_2Ti_3(MoO_4)_9$ ceramic. In the lattice mode region, a band at 143 cm^{-1} shows a gradual increase in intensity with Ti substitution from x = 1 to 3 and can be assigned to vibrations involving Ti atoms substituting Zr atoms in the complex crystal structure [21-25]. The other Raman bands below 250 cm^{-1} correspond to the lattice mode region and cannot be assigned unambiguously.
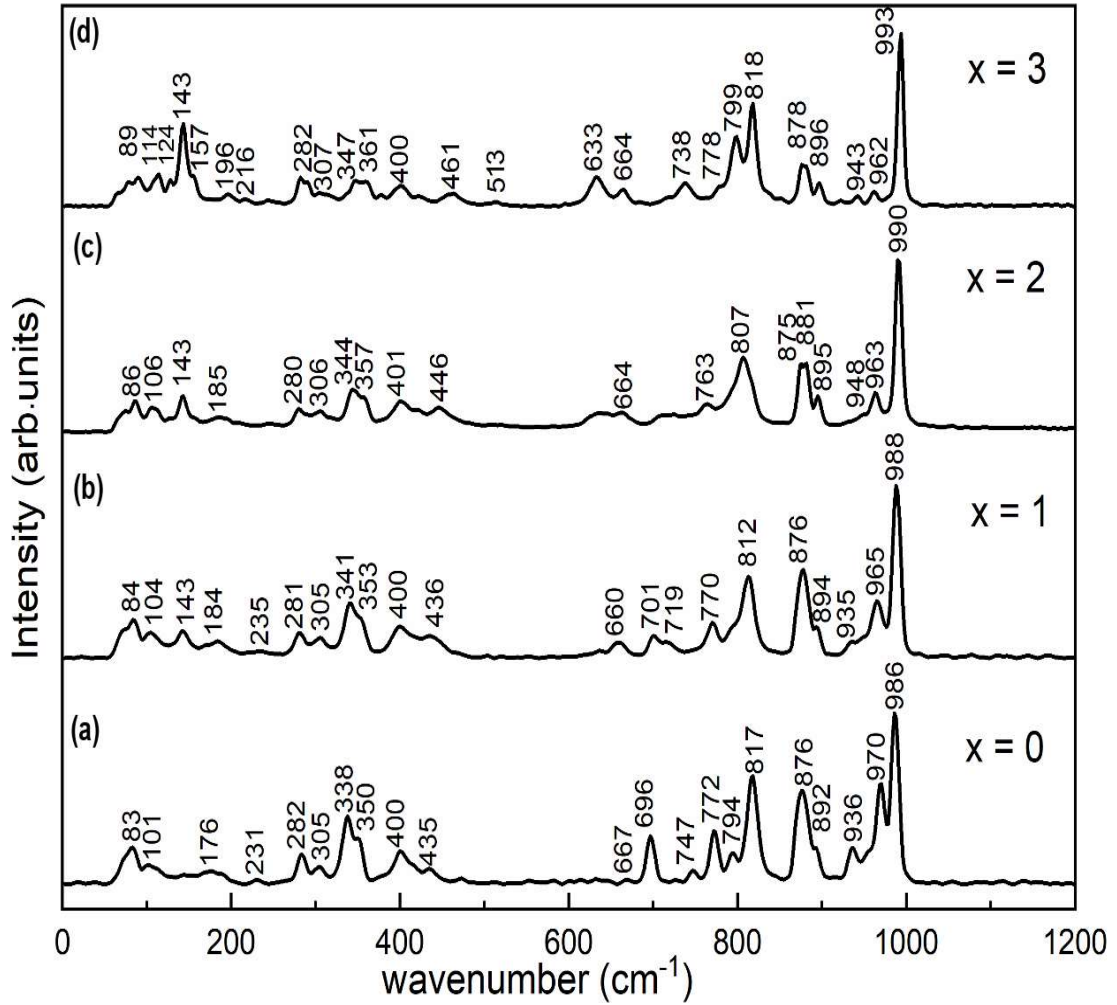
Figure 7.3 Laser Raman spectra of $Pr_2Zr_{(3-x)}Ti_x(MoO_4)_9$ (x= 0,1,2,3) sintered ceramics

Table 7.2 Raman mode assignments of $Pr_2Zr_{(3-x)}Ti_x(MoO_4)_9$ (x= 0,1,2,3) ceramics

$Pr_2Zr_3(MoO_4)_9$ (cm⁻¹)	$Pr_2Zr_2Ti(MoO_4)_9$ (cm⁻¹)	$Pr_2ZrTi_2(MoO_4)_9$ (cm⁻¹)	$Pr_2Ti_3(MoO_4)_9$ (cm⁻¹)	Assignments [*1,2]
986 vs	988 vs	990 vs	993 vs	
970 s	965 m	963 w	962 w	
		948 vw	943 vw	
936 w	935 vw			
892 wsh	894 wsh	895 w	896 m	
		881 m		
876 s	876 s	875 m	878 m	$\nu_s\,(MoO_4)^{2-}$
817 s	812 s	807 s	818 s	$\nu_{as}(MoO_4)^{2-}$
794 wsh			799 m	
772 m	770 m	763 w	778 vw	
747 vw			738 w	
	719 w			
696 m	701 w			
667 vw	660 w	664 w	664 w	
			633 m	$\nu_1\,(TiO_6)$
			513 vw	$\nu_2\,(TiO_6)$
			461 w	
435 w	436 w	446 w		$\nu_s\,(ZrO_6)$
400 m	400 mbr	401 w	400 vw	$\delta_{as}(MoO_4)^{2-}$
350 mbr	353 m	357 m	361 mbr	$\delta_s(MoO_4)^{2-}$
338 m	341 mbr	344 mbr	347 m	
305 vw	305 w	306 vw	307 vw	
282 w	281 w	280 w	282 m	
231 vw	235 vw		216 vw	
			196 w	$\nu_5(TiO_6)$
176 vw	184 vw	185 vw	157 w	
	143 w	143 m	143 m	$\nu_6(TiO_6)$
			124 w	
			114 w	& Lattice-mode vibrations
101 w	104 w	106 w		
83 w	84 w	86 w	89 w	

[*1] ν_s – symmetric stretching ν_{as} – asymmetric stretching δ_{as} – asymmetric bending
δ_s – symmetric bending
[*2] vs very strong; s strong; m medium; w weak; br broad; vw very weak; sh shoulder

7.3.3 Morphological studies

The SEM micrographs of $Pr_2Zr_3(MoO_4)_9$ and $Pr_2Ti_3(MoO_4)_9$ ceramics are shown in Figure 7.4 (a) and (b) respectively.
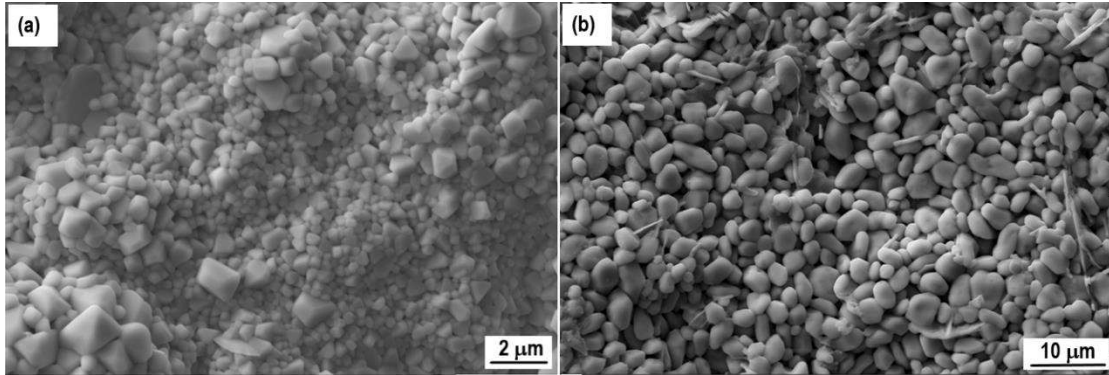
Figure 7.4 SEM micrographs of (a) $Pr_2Zr_3(MoO_4)_9$ ceramic sintered at $790^{\circ}C/1h$ and (b) $Pr_2Ti_3(MoO_4)_9$ ceramic sintered at $630^{\circ}C/1h$

The $Pr_2Zr_3(MoO_4)_9$ ceramic exhibits densely packed microstructure with polygonal grains together with phase homogeneity. Whereas $Pr_2Ti_3(MoO_4)_9$ ceramic exhibits polygonal grains with less close packing along with needle like structures indicating multiphase nature. The backscattered SEM micrograph of the cross-section of $Pr_2Ti_3(MoO_4)_9$ ceramic is given in Figure 7.5, which reveals the presence of three distinct phases. The EDS point analysis at spot 1 reveals the presence of Mo and O and confirms the formation of plate like structures of α-MoO_3 which was earlier detected in the XRD pattern of the sample. The EDS point analysis at spot 2 and spot 3 shows the presence of Pr, Mo, Ti and O but with varying proportions. The chemical composition of the phases formed in $Pr_2Ti_3(MoO_4)_9$ ceramic can be determined accurately only after detailed structural investigations using neutron diffraction or synchrotron X-ray diffraction followed by Rietveld refinement.
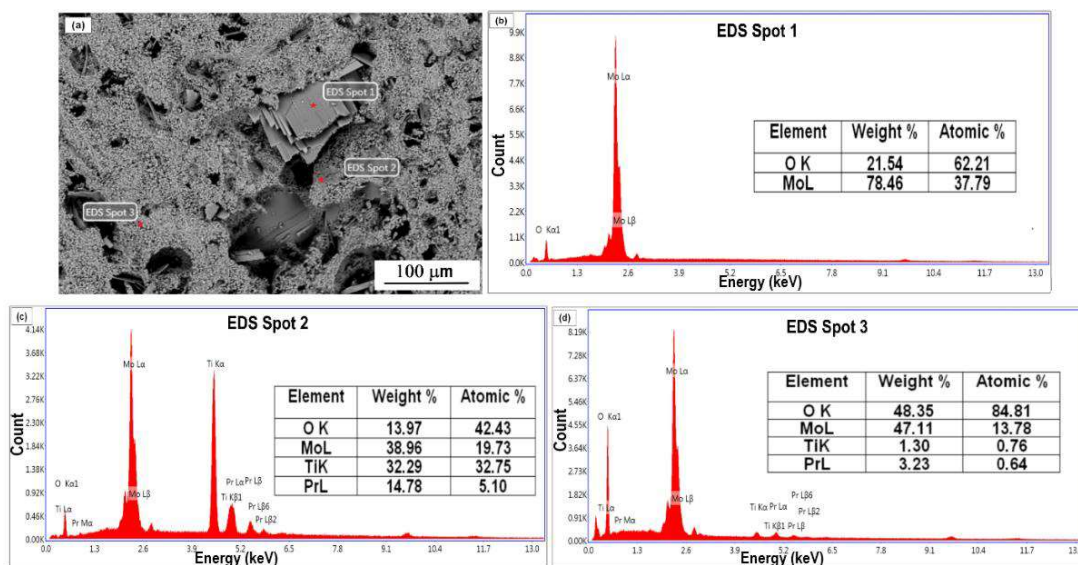
Figure 7.5 (a) Backscattered SEM micrograph; EDS point analysis spectra (b) spot 1, (c) spot 2 and (d) spot 3 of $Pr_2Ti_3(MoO_4)_9$ ceramic sintered at $630^{\circ}C/1h$

7.3.4 Microwave dielectric studies

The optimum sintering temperature, maximum density of the sintered samples and the microwave dielectric properties including dielectric constant ε_r, quality factor $Q_u \times f$ (GHz) and the temperature coefficient of resonant frequency τ_f are given in Table 7.3. The $Pr_2Ti_3(MoO_4)_9$ sample exhibits maximum dielectric constant of 12.7 and $Pr_2Zr_3(MoO_4)_9$ has the lowest dielectric constant of 9.6. The variation of density, dielectric constant and quality factor of the $Pr_2Zr_3(MoO_4)_9$ ceramic as a function of sintering temperature is shown in Figure 7.6 and the variation of resonant frequency with temperature of the $Pr_2Zr_3(MoO_4)_9$ ceramic sintered at optimum temperature is given in Figure 7.7.

The quality factor $Q_u \times f$ decreases with increasing Ti^{4+} substitution from 42,900 GHz for $Pr_2Zr_3(MoO_4)_9$ ceramics to 27,400 GHz for $Pr_2Ti_3(MoO_4)_9$ ceramics. Evidently this is caused due to the porosity and multiphase nature of the titanium rich compositions. Interestingly, the τ_f value decreases from -30 ppm/$^{\circ}$C for $Pr_2Zr_3(MoO_4)_9$ ceramic to 0 ppm/$^{\circ}$C for $Pr_2Ti_3(MoO_4)_9$ ceramic. The variation of τ_f and c/a ratio with x value 0, 1, 2 and 3 is shown in Figure 7.8. The τ_f variation with Ti^{4+} substitution follows the variation of c/a ratio calculated for the unit cell of the compounds under study.

Table 7.3 Sintering temperature, maximum sintered density and dielectric properties of $Pr_2Zr_{(3-x)}Ti_x(MoO_4)_9$ (x = 0,1,2,3) ceramics

Compositions	Sintering temperature (°C)/1h	Density (g/cm³)	ε_r @ GHz	Q_u x f (GHz)	τ_f (ppm/°C)
$Pr_2Zr_3(MoO_4)_9$	790	3.63	9.6	42,900	-30
$Pr_2Zr_2Ti(MoO_4)_9$	760	3.25	9.7	35,600	-16
$Pr_2ZrTi_2(MoO_4)_9$	700	3.32	11.8	34,900	-11
$Pr_2Ti_3(MoO_4)_9$	630	3.18	12.7	27,400	0
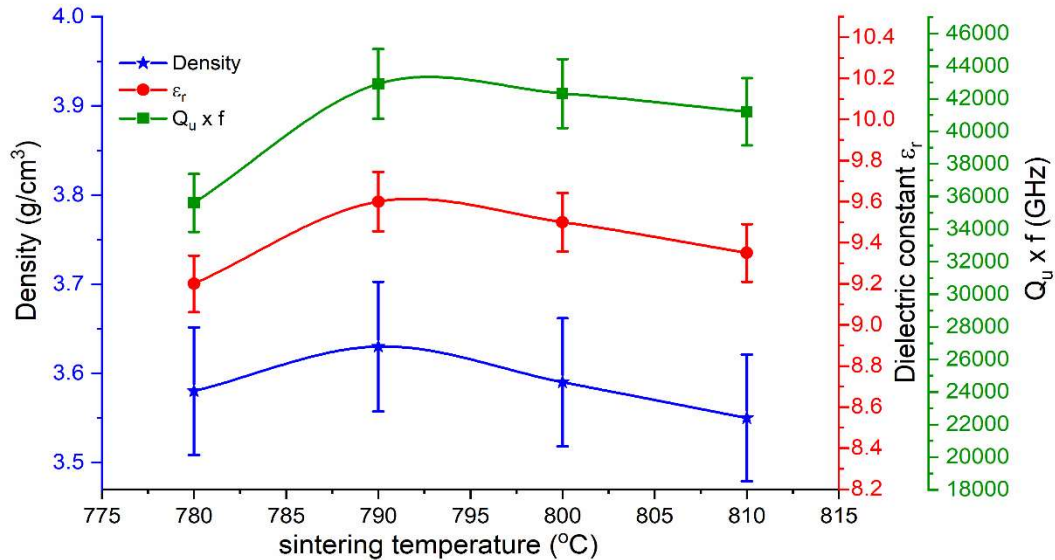
Figure 7.6 Variation of sintered density, dielectric constant and quality factor of $Pr_2Zr_3(MoO_4)_9$ ceramic with sintering temperature
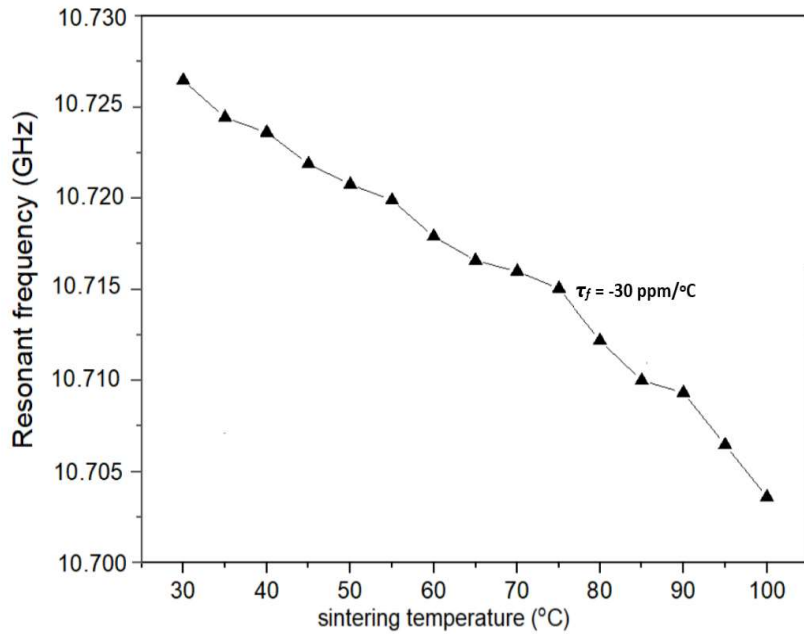
Figure 7.7 Variation of resonant frequency with temperature of $Pr_2Zr_3(MoO_4)_9$ ceramic sintered at optimum temperature
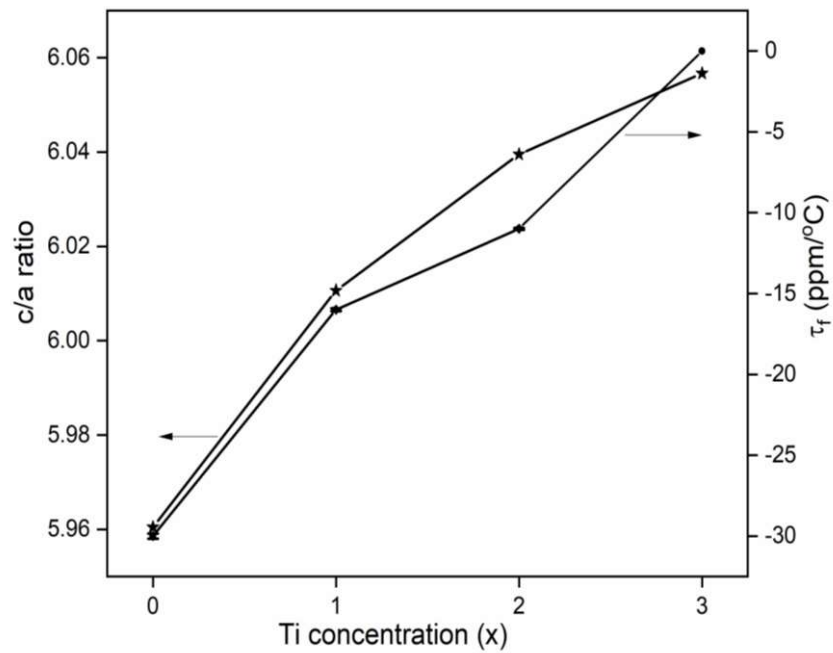
Figure 7.8 Variation of c/a ratio and τ_f with Ti concentration for $Pr_2Zr_{(3-x)}Ti_x(MoO_4)_9$ (x= 0,1,2,3) ceramics

7.3.5 Compatibility studies

The $Pr_2Zr_3(MoO_4)_9$, $Pr_2Zr_2Ti(MoO_4)_9$ and $Pr_2ZrTi_2(MoO_4)_9$ ceramics are sintered above 660°C, and hence they are co-fired with 20 wt% Ag to determine their suitability for LTCC applications. The $Pr_2Ti_3(MoO_4)_9$ ceramic with optimum sintering temperature of 630°C is co-fired with 20 wt% Al. The powder X-ray diffraction patterns of the 20 wt% Ag co-fired samples of $Pr_2Zr_3(MoO_4)_9$ are given in Figure 7.9.
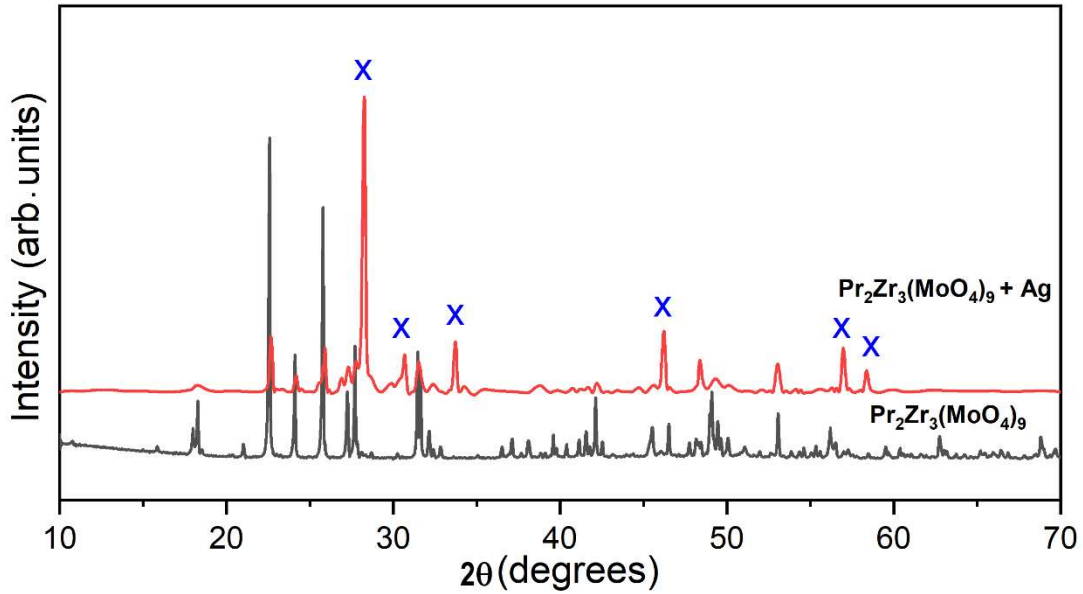
Figure 7.9 XRD patterns of $Pr_2Zr_3(MoO_4)_9$ ceramic and $Pr_2Zr_3(MoO_4)_9$ ceramic co-fired with 20 wt% Ag at 790°C/1h

The XRD pattern of the $Pr_2Zr_3(MoO_4)_9$ ceramic co-fired with silver confirms the chemical reaction between the ceramic and silver. The peaks of silver are absent in the XRD pattern and secondary phase formation is marked with 'x'. The co-firability is further investigated using EDS analysis. The backscattered SEM micrograph of the $Pr_2Zr_3(MoO_4)_9$ ceramic co-fired with 20 wt% Ag at 790°C/1h along with the point analysis results and the EDS phase map are given in Figure 7.10 a-c.
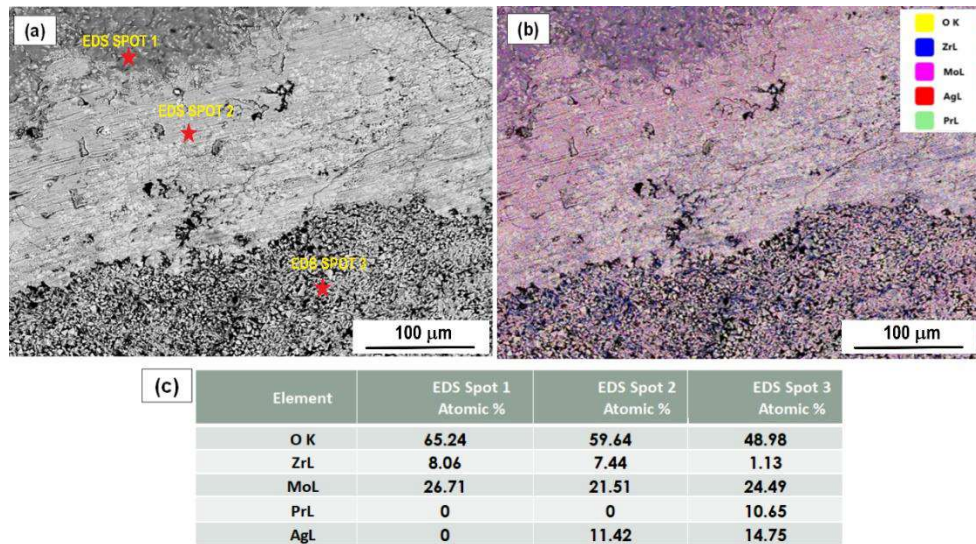
Figure 7.10 (a) Backscattered SEM image; (b) EDS phase map and (c) EDS point analysis results of $Pr_2Zr_3(MoO_4)_9$ ceramic co-fired with 20 wt% Ag at 790ºC/1h

The EDS investigation revealed three distinct regions marked as EDS spot 1, spot 2 and spot 3 in Figure 7.10 (a) and the atomic percentage of each element is compiled in Figure 7.10 (c). The EDS elemental mapping image is given in Figure 7.10 (b). The EDS analysis of the co-fired sample reveals multiphase formation.

The powder X-ray diffraction patterns of the 20 wt% Ag co-fired samples of $Pr_2Zr_2Ti(MoO_4)_9$ is given in Figure 7.11. The XRD pattern of the $Pr_2Zr_2Ti(MoO_4)_9$ ceramic co-fired with silver confirms that chemical reaction occurred between the ceramic and silver. The peaks of silver are absent in the XRD pattern and secondary phase formation is marked with 'x'.
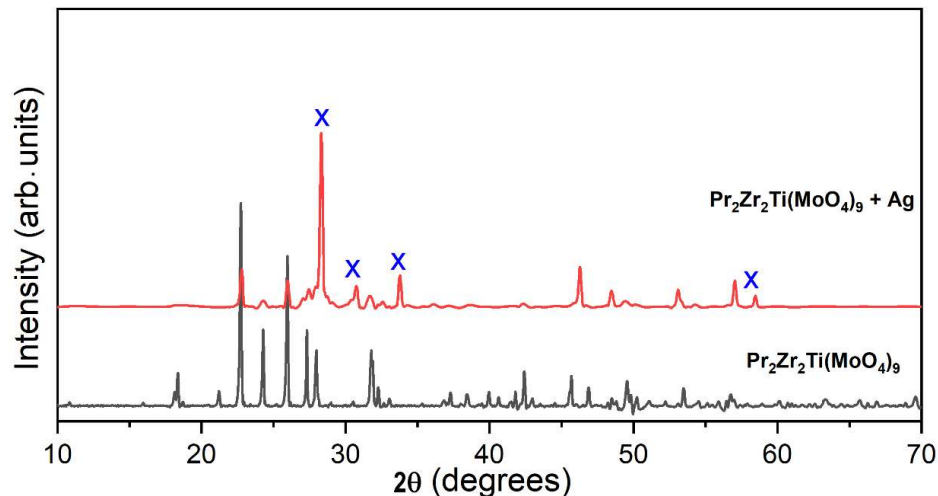
Figure 7.11 XRD patterns of $Pr_2Zr_2Ti(MoO_4)_9$ ceramic and $Pr_2Zr_2Ti(MoO_4)_9$ ceramic co-fired with 20 wt% Ag at 760ºC/1h

The co-firability is further investigated using EDS analysis. The backscattered SEM micrograph of the $Pr_2Zr_2Ti(MoO_4)_9$ ceramic co-fired with 20 wt% Ag at 760 °C/1h along with the point analysis results and the EDS phase map are given in Figure 7.12 a-c.

(c) Element	EDS Spot 1 Atomic %	EDS Spot 2 Atomic %	EDS Spot 3 Atomic %
O K	64.49	52.77	70.21
ZrL	7.32	1.28	8.44
MoL	22.37	22.65	12.33
TiK	0.56	0.17	2.68
PrL	5.27	12.53	0
AgL	0	10.61	6.35
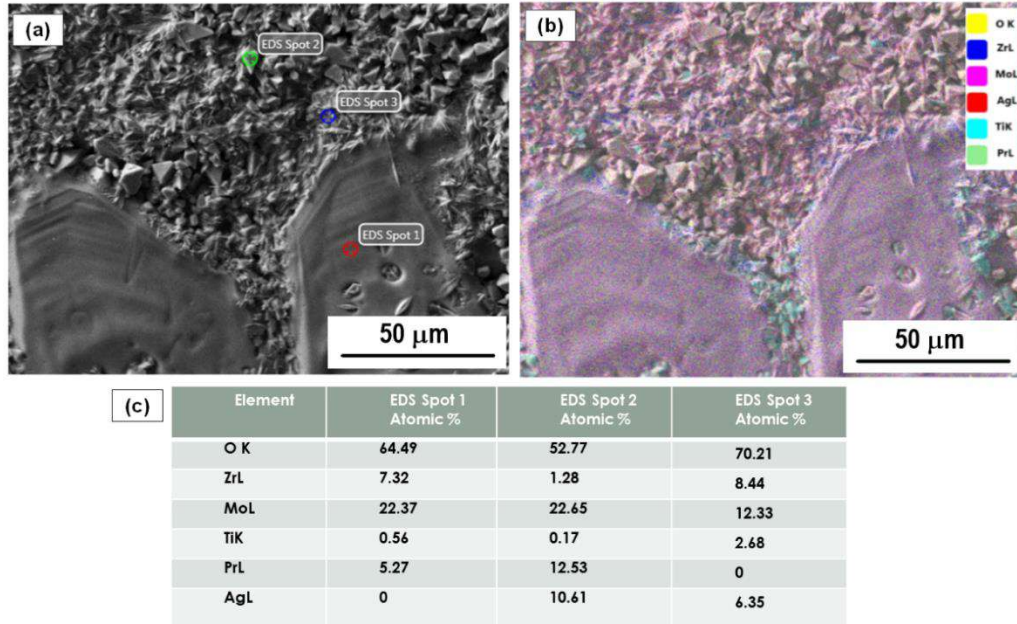
Figure 7.12 (a) Backscattered SEM image; (b) EDS phase map and (c) EDS point analysis results of $Pr_2Zr_2Ti(MoO_4)_9$ ceramic co-fired with 20 wt% Ag at 760°C/1h

The EDS investigation revealed three distinct regions marked as EDS spot 1, spot 2 and spot 3 in Figure 7.12 (a) and the atomic percentage of each element is compiled in Figure 7.12 (c). The EDS elemental mapping image is given in Figure 7.12 (b). The secondary phase formation as a result of silver co-firing follows a similar pattern as that of $Pr_2Zr_3(MoO_4)_9$, however the substitution of Zr with Ti have resulted in the formation of ceramic regions containing Pr, Ti, Zr, Mo and O without the presence of Ag.

The powder X-ray diffraction patterns of the 20 wt% Ag co-fired samples of $Pr_2ZrTi_2(MoO_4)_9$ is given in Figure 7.13. The XRD pattern of the $Pr_2ZrTi_2(MoO_4)_9$ ceramic co-fired with silver confirms that chemical reaction has taken place between the ceramic and silver. The peaks of silver are absent in the XRD pattern and secondary phase formation is marked with 'x'. The co-firability is further investigated by EDS analysis. The backscattered SEM micrographs of the $Pr_2ZrTi_2(MoO_4)_9$ ceramic co-fired with 20 wt% Ag at 700 °C/1h along with the point analysis results and the EDS phase map are given in Figure 7.14 a-c.
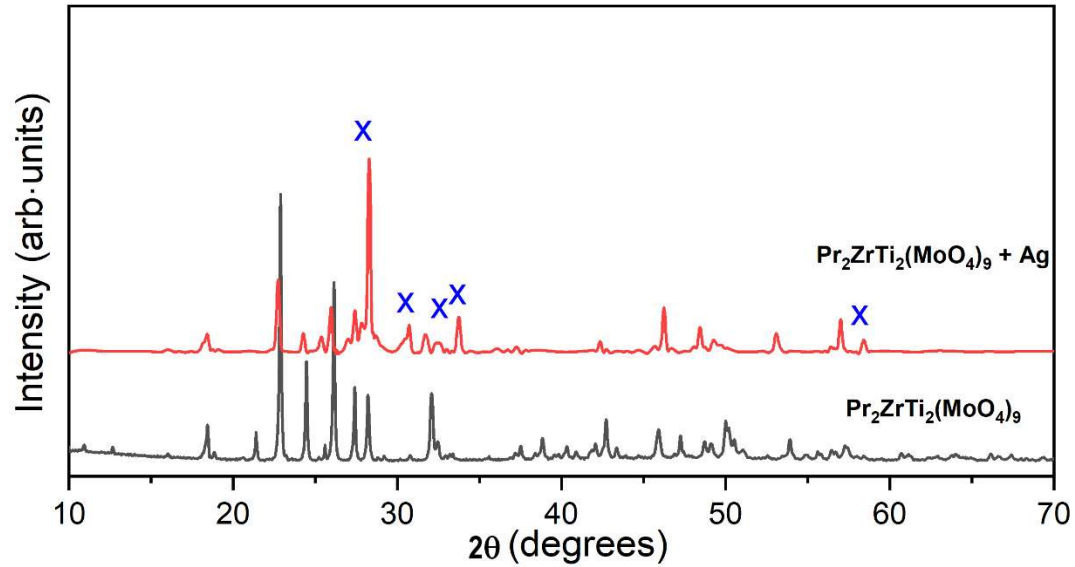
Figure 7.13 XRD patterns of $Pr_2ZrTi_2(MoO_4)_9$ ceramic and $Pr_2ZrTi_2(MoO_4)_9$ ceramic co-fired with 20 wt% Ag at 700°C/1h

(c) Element	EDS Spot 1 Atomic %	EDS Spot 2 Atomic %	EDS Spot 3 Atomic %
O K	60.74	62.66	53.92
ZrL	8.31	1.56	1.51
MoL	24.49	17.99	14.15
TiK	0.59	0.51	23.77
PrL	5.87	8.41	0
AgL	0	8.88	6.65
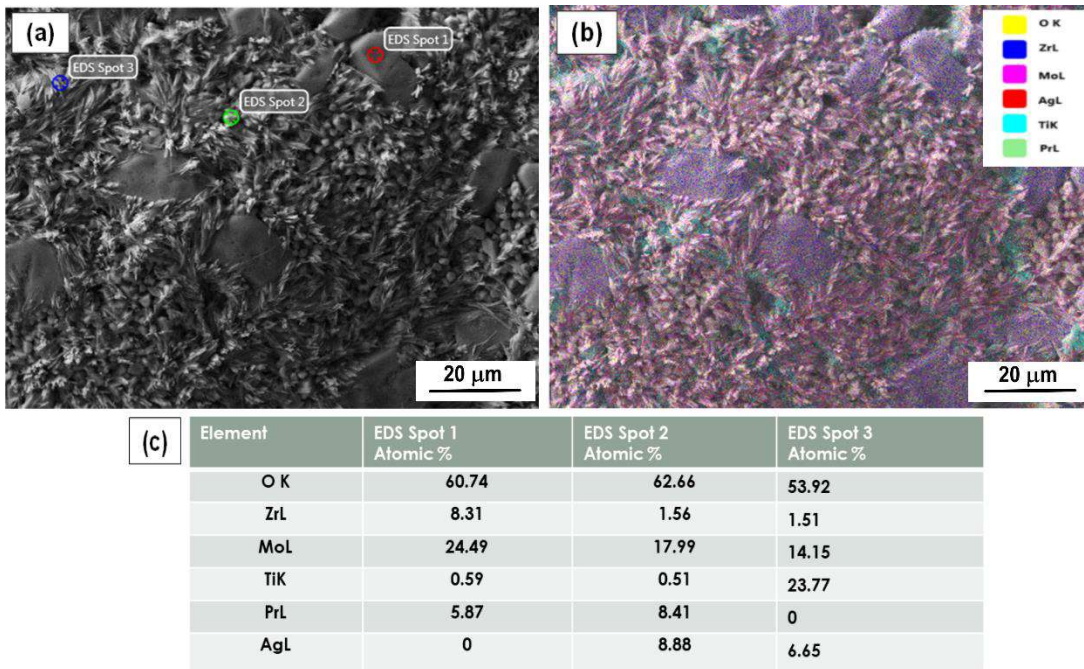
Figure 7.14 (a) Backscattered SEM image; (b) EDS phase map and (c) EDS point analysis results of $Pr_2ZrTi_2(MoO_4)_9$ ceramic co-fired with 20 wt% Ag at 700°C/1h

The EDS investigation revealed three distinct regions marked as EDS spot 1, spot 2 and spot 3 in Figure 7.14 (a) and the atomic percentage of each element is compiled in Figure 7.14 (c). The EDS elemental mapping image is given in Figure 7.14 (b). The EDS analysis shows islands of ceramic without the presence of Ag.

The EDS phase map of the 20 wt% Ag co-fired samples of $Pr_2Zr_3(MoO_4)_9$, $Pr_2Zr_2Ti(MoO_4)_9$ and $Pr_2ZrTi_2(MoO_4)_9$ ceramics showing the distribution of Ag is given in Figure 7.15 a-c. The co-firability of the ceramic improves with Ti substitution for Zr in the $Pr_2Zr_3(MoO_4)_9$ ceramics.
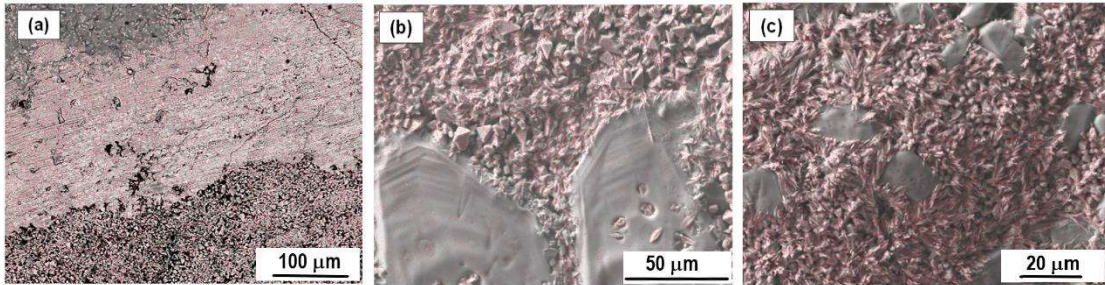
Figure 7.15 EDS phase map of Ag for 20 wt% Ag co-fired samples of
(a) $Pr_2Zr_3(MoO_4)_9$, (b) $Pr_2Zr_2Ti(MoO_4)_9$ and (c) $Pr_2ZrTi_2(MoO_4)_9$ ceramics
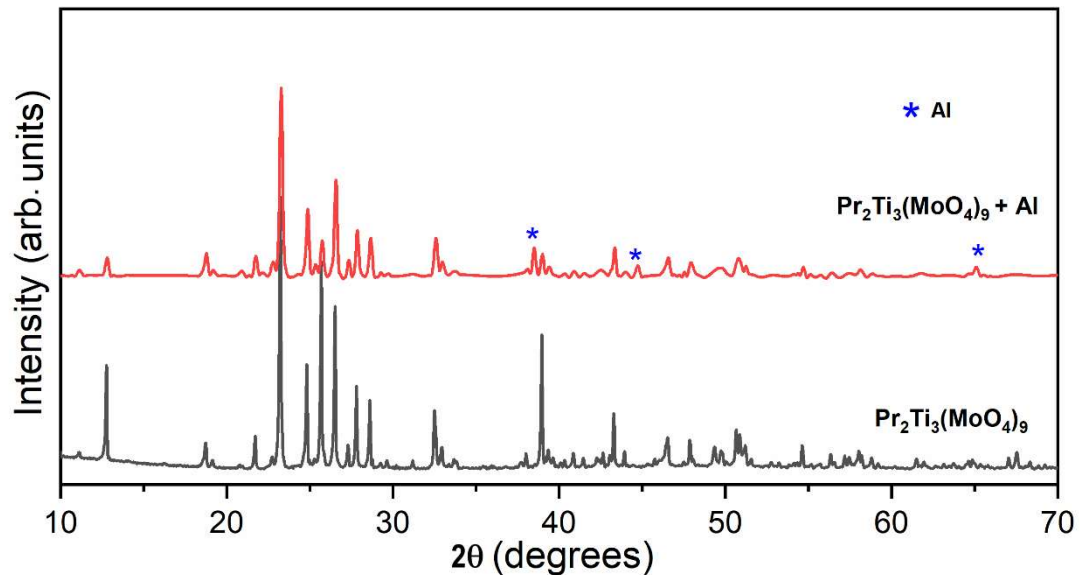
Figure 7.16 XRD patterns of $Pr_2Ti_3(MoO_4)_9$ ceramic and $Pr_2Ti_3(MoO_4)_9$ ceramic co-fired with 20 wt% Al at 630°C/1h
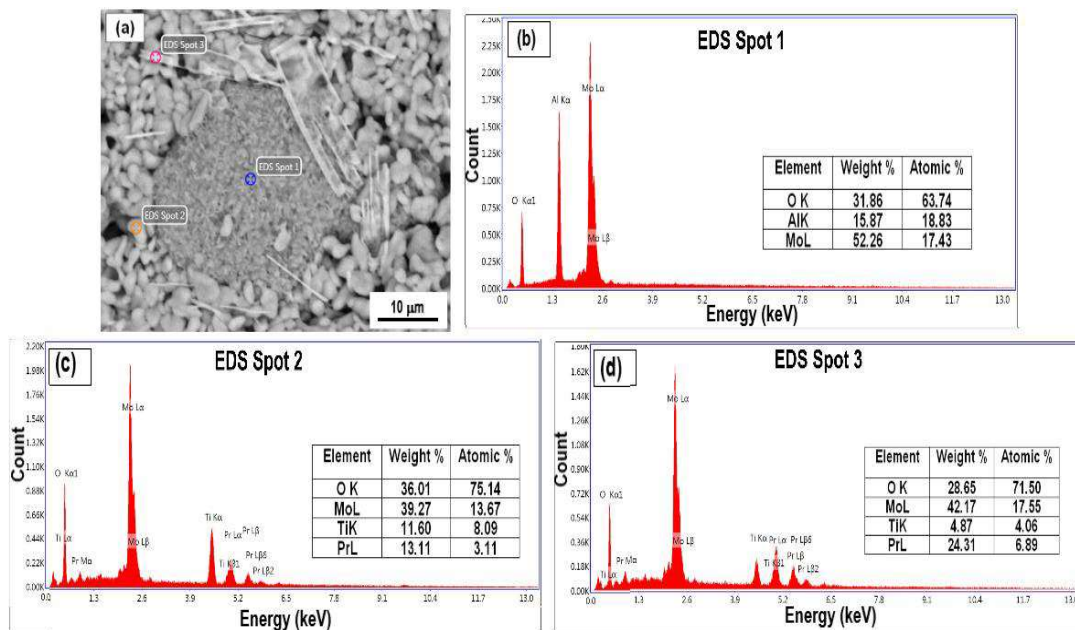
Figure 7.17 (a) Backscattered SEM image; EDS point analysis spectra at (b) spot 1, (c) spot 2 and (d) spot 3 of $Pr_2Ti_3(MoO_4)_9$ ceramic co-fired with 20 wt% Al at $630^{\circ}C/1h$
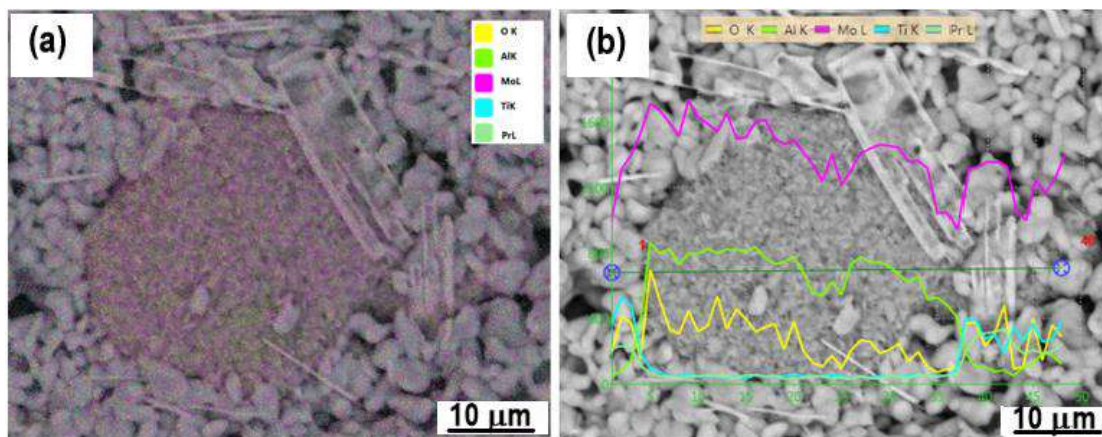
Figure 7.18 (a) EDS phase map and (b) EDS line scan of $Pr_2Ti_3(MoO_4)_9$ ceramic co-fired with 20 wt% Al at $630^{\circ}C/1h$

The XRD pattern of $Pr_2Ti_3(MoO_4)_9$ ceramic co-fired with aluminium is given in Figure 7.16 and is compared with the XRD pattern of $Pr_2Ti_3(MoO_4)_9$ ceramic. The XRD pattern exhibits the characteristic peaks of aluminium, as per ICDD file no. 89-2769 at 2θ values 38.5°, 44.7° and 65.1° marked with '*'. The backscattered SEM micrographs of the $Pr_2Ti_3(MoO_4)_9$ ceramic co-fired with aluminium and the EDS point analysis results are shown in Figure 7.17 a-d. The EDS elemental mapping image and the EDS line scan are given in Figure 7.18 (a) and (b) respectively. The EDS point analysis at spot 1 reveals the presence of Mo and O along with Al, however at spot 2

181

and spot 3 Al is absent. The EDS line scan clearly exhibits the presence of Mo and O in the aluminium region, indicating the formation of aluminium molybdate. However, Al is absent in the ceramic region.

7.4 Conclusions

$Pr_2Zr_{(3-x)}Ti_x(MoO_4)_9$ (x = 0,1,2,3) ceramics are prepared by solid-state ceramic route. The Zr^{4+} ion was systematically substituted with Ti^{4+} ion and associated changes in the crystal structure have been studied using XRD and laser Raman spectroscopy. The effect of Ti^{4+} substitution on the microstructure and microwave dielectric properties are also investigated. The samples show excellent microwave dielectric properties. Raman spectroscopic studies confirm the presence of $(MoO_4)^{2-}$ tetrahedra in the crystal structure. The presence of α-MoO_3 is detected in the XRD patterns of $Pr_2ZrTi_2(MoO_4)_9$ and $Pr_2Ti_3(MoO_4)_9$ ceramics. $Pr_2Zr_3(MoO_4)_9$ ceramic has a dielectric constant of 9.6, Q_u x f of 42,900 GHz and τ_f of -30 ppm/ºC at optimum sintering temperature of 790 ºC for 1h. As the Ti^{4+} substitution increases, the dielectric constant increases, quality factor decreases, and τ_f decreases to 0 ppm/ºC. The EDS analysis of Ag co-fired $Pr_2Zr_3(MoO_4)_9$, $Pr_2Zr_2Ti(MoO_4)_9$ and $Pr_2ZrTi_2(MoO_4)_9$ ceramics shows that the ceramics react with Ag and secondary phases are formed. The EDS analysis of Al co-fired $Pr_2Ti_3(MoO_4)_9$ ceramic confirmed that the ceramic react with Al with the formation of aluminium molybdate. Although the materials are not co-firable with Ag/Al, they are ideally suitable for microwave circuit applications as substrates owing to their excellent microwave dielectric properties. In addition, phase pure $Pr_2Zr_3(MoO_4)_9$ ceramics can be used as particulate filler in polymer matrix for planar composites fabrication. They can also be used for substrate integrated waveguide (SIW) applications.

References

[1] W. Liu, R. Zuo, Low temperature fired $Ln_2Zr_3(MoO_4)_9$ (Ln=Sm, Nd) microwave dielectric ceramics, Ceram. Int., 43 [18] (2017) 17229-17232.

[2] W. Liu, R. Zuo, A novel low-temperature firable $La_2Zr_3(MoO_4)_9$ microwave dielectric ceramic, J. Eur. Ceram. Soc., 38 [1] (2018) 339-342.

[3] J. G. Bazarova, Y. L. Tushinova, B. G. Bazarov, S. G. Dorzhieva, Double molybdates of rare earth elements and zirconium, Russ. Chem. Bull., 66 [4] (2017) 587-592.

[4] B. G. Bazarov, V. G. Grossman, R. F. Klevtsova, A. G. Anshits, T. A. Vereshchagina, L. A. Glinskaya, Y. L. Tushinova, K. N. Fedorov, Z. G. Bazarova, Crystal structure of binary molybdate $Pr_2Hf_3(MoO_4)_9$, J. Struct. Chem., 50 [3] (2009) 566-569.

[5] R. F. Klevtsova, S. F. Solodovnikov, Y. L. Tushinova, B. G. Bazarov, L. A. Glinskaya, Z. G. Bazarova, A new type of mixed framework in the crystal structure of binary molybdate $Nd_2Zr_3(MoO_4)_9$, J. Struct. Chem., 41 [2] (2000) 280-284.

[6] Z. G. Bazarova, Y. L. Tushinova, B. G. Bazarov, E. Y. Badmaeva, S. F. Solodvnikov, E. S. Zolotova, Phase formation in the $Ln_2(MoO_4)_3$-$Hf(MoO_4)_2$ (Ln= La-Lu, Y, Sc) systems, Zh. Neorg. Khim., 49 [2] (2004) 324-328.

[7] Z. G. Bazarova, Y. L. Tushinova, B. G. Bazarov, K. N. Fedorov, R. F. Klentsova, S. F. Solodovnikov, N. A. Pyl'neva, A. M. Yurkin, Phase formation in the Ln_2O_3-ZrO_2-MoO_3 (Ln = La-Lu, Y, Sc) systems, Zh. Neorg. Khim., 46 [1] (2001) 146-148.

[8] S. F. Solodovnikov, B. G. Bazarov, E. Y. Badmaeva, Y. L. Tushinova, E. S. Zolotova, Z. G. Bazarova, Phase formation in the Dy_2O_3-HfO_2-MoO_3 system. Crystal structure of the new binary molybdate $Dy_2Hf_2(MoO_4)_7$, J. Struct. Chem., 45 [4] (2004) 657-662.

[9] V. G. Grossman, B. G. Bazarov, T. T. Bazarova, L. A. Glinskaya, J. G. Bazarova, J. Temuujin, Phase equilibria in the Tl_2MoO_4-$Ho_2(MoO_4)_3$-$Zr(MoO_4)_2$ system and the crystal structure of $Ho_2Zr_2(MoO_4)_7$ and $TlHoZr_{0.5}(MoO_4)_3$, J. Ceram. Process. Res., 18 [12] (2017) 875-881.

[10] M. E. Brownfield, E. E. Foord, S. J. Sutley, T. Botinelly, Kosnarite, $KZr_2(PO_4)_3$, a new mineral from Mount Mica and Black Mountain, Oxford County, Maine, Am. Mineral., 78 [5-6] (1993) 653-656.

[11] K. V. Martynov, G. M. Akhmedzhanova, A. R. Kotel'nikov, I. G. Tananaev, B. F. Myasoedov, Synthesis and study of structural analogs of kosnarite mineral under hydrothermal conditions, Radiochemistry, 57 [4] (2015) 356-365.

[12] T. A. Vereshchagina, E. V. Fomenko, N. G. Vasilieva, L. A. Solovyov, S. N. Vereshchagin, Z. G. Bazarova, A. G. Anshits, A novel layered zirconium molybdate as a precursor to a ceramic zirconomolybdate host for lanthanide bearing radioactive waste, J. Mater. Chem., 21 [32] (2011) 12001-12007.

[13] S. G. Dorzhieva, Y. L. Tushinova, B. G. Bazarov, A. I. Nepomniashchikh, R. Y. Shendrik, Z. G. Bazarova, Luminescence of Ln-Zr molybdates, Bull. Russ. Acad. Sci. Phys., 79 [2] (2015) 276-279.

[14] B. W. Hakki, P. D. Coleman, A dielectric resonator method of measuring inductive capacities in the millimeter range, IRE Trans. Microwave Theory Tech., 8 [4] (1960) 402-410.

[15] J. Krupka, K. Derzakowski, B. Riddle, J. B. Jarvis, A dielectric resonator for measurements of complex permittivity of low loss dielectric materials as a function of temperature, Meas. Sci. Technol., 9 [10] 1751-1756.

[16]   R. D. Shannon, Revised effective ionic radii and systematic studies of interatomic distances in halides and chalcogenides, Acta crystallogr. A, 32 [5] (1976) 751-767.

[17]   N. K. James, R. Ratheesh, Microwave dielectric properties of low-temperature sinterable $BaCe_2(MoO_4)_4$ ceramics, J. Am. Ceram. Soc., 93 [4] (2010) 931-933.

[18]   F. D. Hardcastle, I. E. Wachs, Molecular structure of molybdenum oxide in bismuth molybdates by Raman spectroscopy, J. Phys. Chem., 95 [26] 10763-10772.

[19]   F. D. Hardcastle, I. E. Wachs, Determination of molybdenum–oxygen bond distances and bond orders by Raman spectroscopy, J. Raman Spectrosc., 21 [10] (1990) 683-691.

[20]   A. Surjith, R. Ratheesh, High Q ceramics in the $ACe_2(MoO_4)_4$ (A= Ba, Sr and Ca) system for LTCC applications, J. Alloys Compd., 550 (2013) 169-172.

[21]   M. J. Bushiri, C. J. Antony, A. Aatiq, Raman and FTIR studies of the structural aspects of Nasicon-type crystals; $AFeTi(PO_4)_3$ [A= Ca, Cd], J. Phys. Chem. Solids, 69 [8] (2008) 1985-1989.

[22]   C. S. Tu, A. R. Guo, R. Tao, R. S. Katiyar, R. Guo, A. S. Bhalla, Temperature dependent Raman scattering in $KTiOPO_4$ and $KTiOAsO_4$ single crystals, J. Appl. Phys., 79 [6] (1996) 3235-3240.

[23]   P. McMillan, N. Ross, The Raman spectra of several orthorhombic calcium oxide perovskites, Phys. Chem. Miner., 16 [1] (1988) 21-28.

[24]   U. L. C. Hemamala, F. El-Ghussein, D. V. S. Muthu, A. K. Andersen, S. Carlson, L. Ouyang, M. B. Kruger, High-pressure Raman and infrared study of ZrV_2O_7, Solid State Commun., 141 [12] (2007) 680-684.

[25]   J. Shu, M. Shui, D. Xu, S. Gao, T. Yi, D. Wang, X. Li, Y. Ren, Design and comparison of ex situ and in situ devices for Raman characterization of lithium titanate anode material, Ionics, 17 [6] (2011) 503-509.

Chapter 8

Preparation and characterization of $Pr_2Zr_3(MoO_4)_9$ filled HDPE composites, microstrip patch antenna fabrication and evaluation for ISM band applications

8.1 Introduction

8.2 Materials and methods

8.3 Results and discussion

8. 4 Conclusions

8.1 Introduction

Polymer-ceramic composites consist of a phase pure ceramic particulate filler uniformly dispersed in a polymer matrix which possess tailor-made dielectric, thermal and mechanical properties for microwave circuit and electronic packaging applications. The polymer-ceramic composites prepared by intimate mixing and compression moulding involves the melting of polymer phase and thereby encapsulates the ceramic filler phase. Thermoplastic polymers like polytetrafluoroethylene (PTFE), High-density polyethylene (HDPE), Polyether ether ketone (PEEK), polystyrene etc. are used for the fabrication of flexible microwave substrates [1-3]. These substrates can be used for the fabrication of patch antennas for variety of communication applications.

The ceramic particulate filler in a composite must have phase purity on calcination together with excellent microwave dielectric properties, such as stable dielectric constant, low dielectric loss and good temperature stability of dielectric properties. In the present study, $Pr_2Zr_3(MoO_4)_9$ ceramic reported in chapter 7 is used as the particular filler material for the preparation of HDPE composites. HDPE is selected as the polymer matrix as it is easily processable and at the same time possesses excellent dielectric properties of $\varepsilon_r = 2.3$, tan $\delta = 6$ x 10^{-4} and CTE $=250$ ppm/^{o}C [4-6]. HDPE is a non-polar, semicrystalline polymer with -CH_2-CH_2- monomeric units and exhibits good thermal and mechanical properties [6]. $Ca_4La_6(SiO_4)_4(PO_4)_2O_2$ filled HDPE composites with 0.4 volume fraction as optimum loading is reported to have $\varepsilon_r = 5.1$, tan $\delta = 2.3$ x 10^{-3} at 5 GHz [5]. $ZrSiO_4$ reinforced HDPE composites are reported to have $\varepsilon_r = 5.6$, tan $\delta = 0.003$ at 5 GHz at optimum loading [6]. HDPE/$Ba(Zn_{1/3}Ta_{2/3})O_3$ composites have $\varepsilon_r = 8.2$, tan $\delta = 0.0016$ at 10 GHz, CTE $= 92$ ppm/^{o}C and tensile strength $=18$ MPa at optimum filler loading [7]. HDPE/$Sr_2Ce_2Ti_5O_{15}$ composites with 0.4 volume fraction as optimum loading are reported to have $\varepsilon_r = 11$ and tan $\delta = 0.006$ at 8 GHz [8]. HDPE/CeO_2 composites with 0.4 volume fraction as optimum loading have $\varepsilon_r = 5.7$, tan $\delta = 0.0068$ at 7 GHz [9].

As the volume fraction of filler loading in a polymer matrix increases, the density and dielectric constant of the composite also increase and reach an optimum value, beyond which the properties of the composite deteriorates. This percolation threshold in a composite is the maximum filler loading possible in a polymer matrix beyond which the ceramic to ceramic connectivity increases and the composites loses 0-3 connectivity. The effective dielectric constant of a composite is determined by the

individual dielectric constant of the filler and the matrix, volume fraction of filler loading, shape and size of the particulate filler, porosity, homogeneity of filler distribution and the matrix filler interphase [10]. The effective dielectric constant of a polymer-ceramic composite is theoretically modelled using volume fraction and dielectric constant of the ceramic filler and the polymer.

8.2 Materials and methods

8.2.1 Preparation of HDPE/Pr$_2$Zr$_3$(MoO$_4$)$_9$ composites

Pr$_2$Zr$_3$(MoO$_4$)$_9$ ceramic filler was prepared by conventional solid-state ceramic route using high purity oxides Pr$_6$O$_{11}$ (99.9%, Aldrich), ZrO$_2$ (99.9%, Aldrich) and MoO$_3$ (99%, Himedia). Stoichiometric amounts of these oxides were weighed accurately and transferred to an agate mortar and wet mixed in distilled water for an hour. The resultant slurry was dried at 100ºC in a hot air oven, ground well and calcined at 700ºC for three hours. Commercial grade HDPE granules (Reliance Industries Limited, India) were dissolved in Xylene (Merck, 95%) at 130ºC along with continuous stirring using a magnetic stirrer. HDPE powder was prepared by drying and grinding of these dissolved samples. High-density polyethylene (HDPE) powder and phase pure Pr$_2$Zr$_3$(MoO$_4$)$_9$ ceramic filler were taken in correct proportion and dry mixed inside a polypropylene bottle for an hour. The HDPE/Pr$_2$Zr$_3$(MoO$_4$)$_9$ composites were fabricated through compression moulding method using a hydraulic laminating press.

8.2.2 Characterization techniques

The phase purity of the calcined filler was determined by powder X-ray diffraction (XRD) technique using CuKα radiation (Bruker 5005, Germany) and the morphology by using scanning electron microscopy (Carl Zeiss, Model No: EVO18 Research, Germany). The X-band waveguide cavity perturbation technique using a vector network analyzer (Agilent PNA E8362B, Bayan Lepas, Malaysia) was used for the microwave dielectric characterization of HDPE/ Pr$_2$Zr$_3$(MoO$_4$)$_9$ composites. The low frequency dielectric characterization of the composites including the dielectric constant and temperature coefficient of dielectric constant were done using an impedance analyzer (Agilent, 4294A, Malaysia). EXSTAR 6000 model thermo mechanical analyzer (SII Nano technology INC., Japan) was used to determine the coefficient of thermal expansion (CTE) of the samples in the temperature range 30-100ºC. A Universal Testing Machine (Shimadzu, AGS-1000G, Japan) was used to

measure the ultimate tensile strength of the polymer/ceramic composites at different filler loadings.

8.2.3 Microstrip patch antenna fabrication and evaluation

The microstrip patch antenna consists of a conducting patch of any planar or nonplanar geometry on one side of a PCB or dielectric substrate with a ground plane on the other side [11]. Rectangular and circular patch antennas are widely used. Microstrip patch antennas find applications in mobile phones, radars, feed elements in complex antennas, command guidance and telemetry in missiles, satellite communication etc. For a substrate with thickness h and dielectric constant ε_r, the width W and L_{eff} the effective length of the patch of the antenna are given by equations 8.1 and 8.2 respectively, for a given operating frequency f_0. L is the geometric length of the antenna and ΔL the change in length of the patch due to the fringing of the electric field given by equation 8.3. ε_{reff} the effective dielectric constant is given by the equation 8.4 and w the width of the 50 Ω microstrip feed line is calculated by the equation 8.5 [11,12].

$$W = \frac{c}{2f_o} \sqrt{\frac{2}{\varepsilon_r + 1}} \tag{8.1}$$

$$L_{eff} = \frac{c}{2f_o\sqrt{\varepsilon_{reff}}} = L + 2\Delta L \tag{8.2}$$

$$\Delta L = 0.412h \; \frac{\varepsilon_{reff} + 0.300}{\varepsilon_{reff} - 0.258} \; \frac{W/h + 0.264}{W/h + 0.813} \tag{8.3}$$

$$\varepsilon_{reff} = \frac{\varepsilon_r + 1}{2} + \frac{\varepsilon_r - 1}{2\sqrt{1 + 12\frac{h}{W}}} \tag{8.4}$$

$$Z_o = \frac{120\pi}{\sqrt{\varepsilon_{reff}} \left(1.393 + \frac{w}{h} + \frac{2}{3} \ln\left(\frac{w}{h} + 1.444\right)\right)} \tag{8.5}$$

The HDPE/Pr$_2$Zr$_3$(MoO$_4$)$_9$ composite with optimum filler loading is copper claded on both sides using 35 µm oxygen free copper foil through vacuum lamination process at a temperature of 123°C for 1h. The microstrip patch antenna design for 5.8 GHz operating frequency was done using ANSYS HFSS (High Frequency Structure Simulator) software optimized for the typical dielectric constant and loss tangent values of the optimum filler loaded composite sample for a given thickness. The operating frequency, radiation efficiency and return loss of the microstrip patch antenna depend on the dielectric constant, loss tangent and dimension of the substrate material.

The microstrip patch antenna was fabricated on the copper cladded substrate by photolithographic technique as follows. The copper cladded substrate was cut in to suitable dimension and coated with a photoresist material. The negative mask of the antenna design shown in Figure 8.1 (a) was placed on the coated substrate and exposed to UV light. Later, the UV exposed substrate is dipped in a developer solution followed by FeCl$_3$ solution to etch the copper in the region outside the desired antenna geometry. The antenna fabricated on the composite substrate is given in Figure 8.1 (b). The fabricated antenna is connected to a SMA connector for testing in a vector network analyzer.
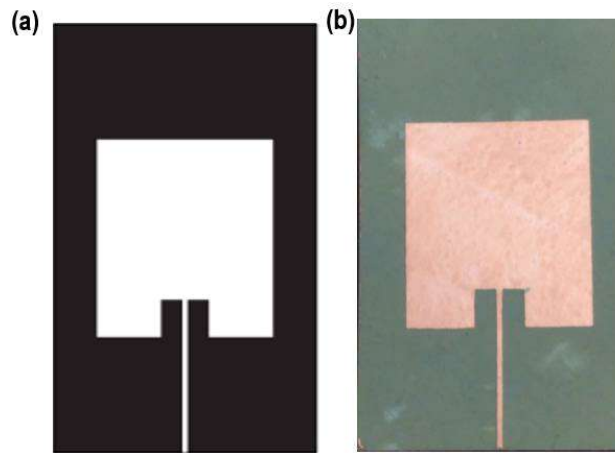
Figure 8.1 (a) Negative antenna mask; (b) Fabricated microstrip patch antenna on copper cladded substrate

8.3 Results and discussion

8.3.1 Density of the composites and the optimum filler loading

The Pr$_2$Zr$_3$(MoO$_4$)$_9$ filled HDPE composites were prepared by intimate mixing and compression moulding technique with filler loading varying from 10 vol% to 50 vol% at intervals of 10 vol%. The variation of experimental density and calculated density of the composite samples as a function of vol% of filler loading are given in Figure 8.2. The density of Pr$_2$Zr$_3$(MoO$_4$)$_9$ filler is 3.62 g/cm^3 and HDPE has density of 0.92 g/cm^3. The density of the composite sample increases with increase in filler loading due to the higher density of the filler compared to the polymer and the effective

density is calculated using rule of mixtures [2]. The 40 vol% filler loaded composite sample has a density of 1.89 g/cm^3 and 50 vol% loaded composite sample has density of 2.15 g/cm^3. However, on further increasing the filler loading to 52 vol%, the composite sample becomes brittle and as a result measurements were not possible. Hence, it can be inferred that the optimum filler loading has to be in between 40 and 50 vol% and accordingly composite samples with 42, 44, 46 and 48 vol% were prepared to fine tune the density. The variation of experimental density as a function of vol% of filler loading in the range 40 to 50 is given in Figure 8.3. The maximum density of 2.18 g/cm^3 was obtained for 48 vol% loaded sample at a processing temperature of 168ºC/1h, which is higher than the density of 2.15 g/cm^3 for 50 vol% loaded sample. Beyond 48 vol%, the sample becomes porous and non-homogeneous with agglomeration of the filler in the composite, which in turn deteriorates the density, dielectric and mechanical properties.
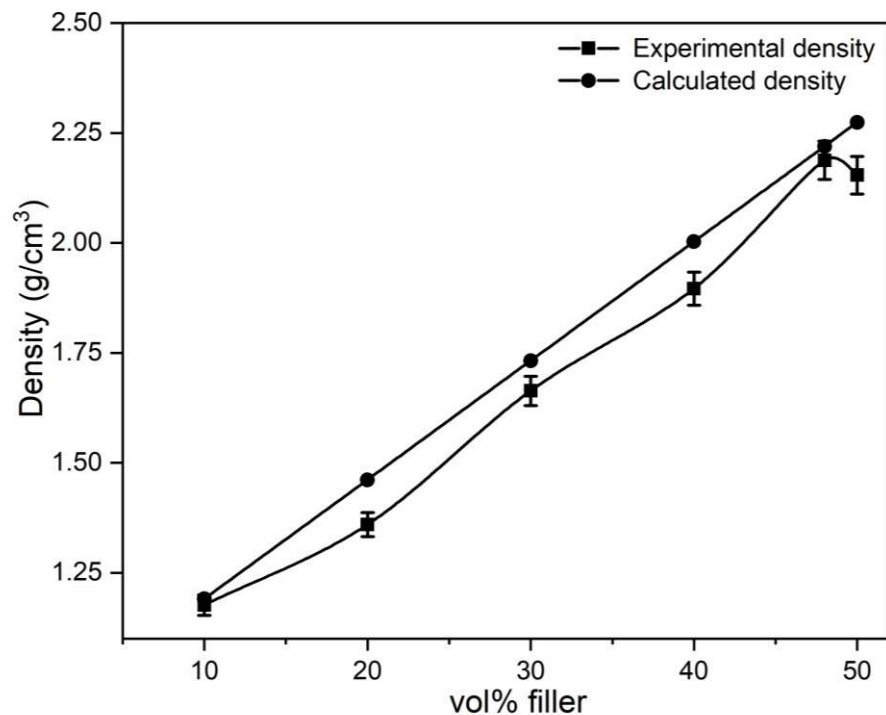
Figure 8.2 Vol% of the filler vs experimental and calculated density of the composites
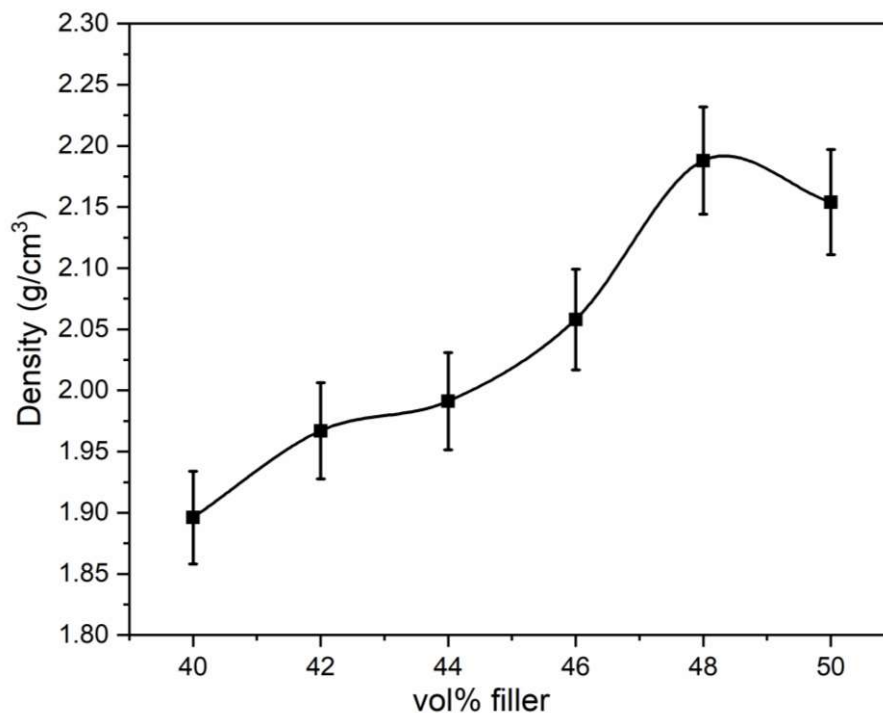
Figure 8.3 Vol% of the filler vs experimental density of the composites

8.3.2 X-ray diffraction studies

The powder X-ray diffraction patterns of $Pr_2Zr_3(MoO_4)_9$ filled HDPE composite at optimum filler loading of 48 vol%, $Pr_2Zr_3(MoO_4)_9$ ceramic filler calcined at 700ºC for 3hrs and that of the pure HDPE are given in Figure 8.4. The XRD pattern of the calcined filler matches with the standard ICDD file no. 51-1851 of the $Pr_2Zr_3(MoO_4)_9$ ceramic and is indexed accordingly. $Pr_2Zr_3(MoO_4)_9$ is reported to have rhombohedral crystal structure with space group $R\bar{3}c$ and lattice parameters of $a = 9.820$ Å and $c = 58.666$ Å respectively. The strong crystalline peaks of HDPE are observed at 2θ values 21º and 24º [8,9]. The XRD pattern of the composite consists of diffraction peaks of the $Pr_2Zr_3(MoO_4)_9$ filler and HDPE separately and hence it can be inferred that there is no chemical interaction between $Pr_2Zr_3(MoO_4)_9$ filler and HDPE polymer matrix.
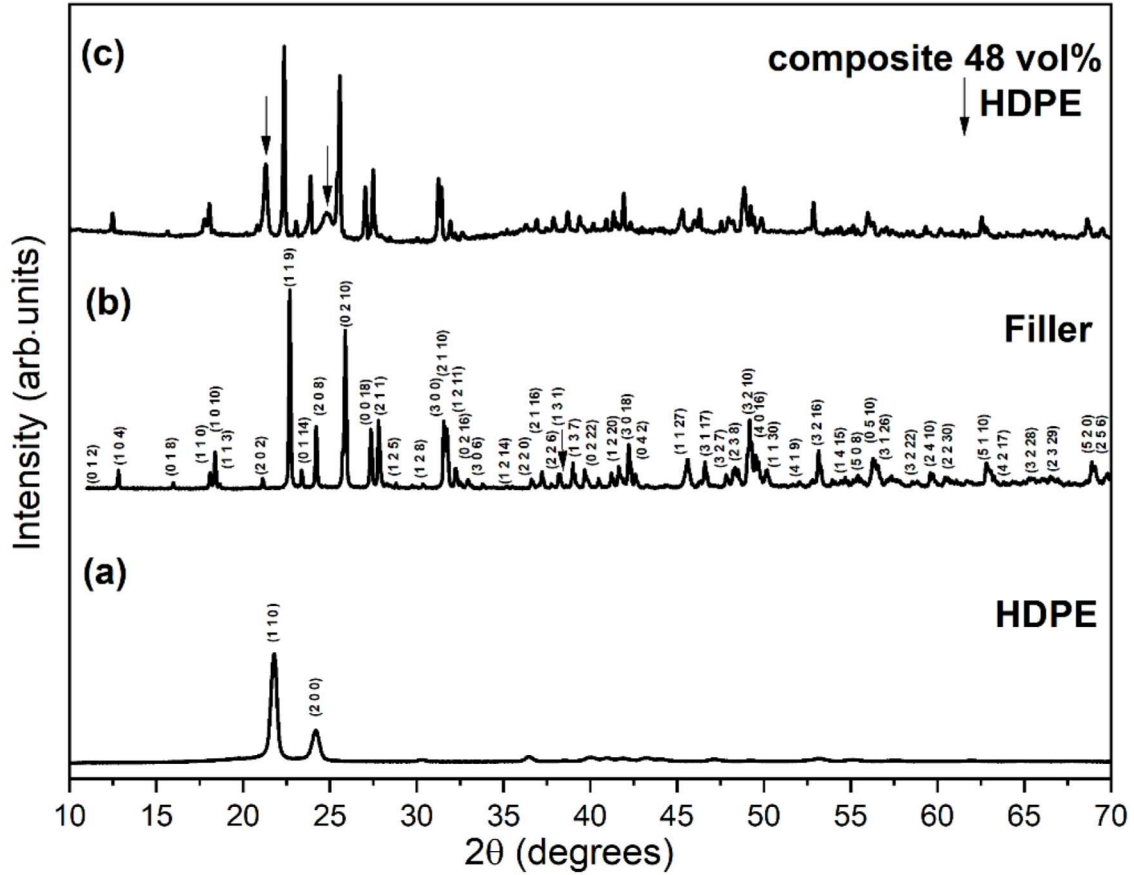
Figure 8.4 X-ray diffraction patterns of (a) Pure HDPE (b) $Pr_2Zr_3(MoO_4)_9$ filler and (c) HDPE+48 vol% $Pr_2Zr_3(MoO_4)_9$ composite

8.3.3 Morphology of the composites

The morphology of the $Pr_2Zr_3(MoO_4)_9$ filler and $Pr_2Zr_3(MoO_4)_9$/HDPE composites were investigated by scanning electron microscopy. The SEM image of the $Pr_2Zr_3(MoO_4)_9$ filler is given in Figure 8.5 (a) which shows nearly polygonal morphology. The cross-sectional SEM micrograph of the 48 vol% $Pr_2Zr_3(MoO_4)_9$ filled HDPE composite is shown in Figure 8.5 (b). The SEM micrographs of the planar surfaces of the 46, 48 and 50 vol% $Pr_2Zr_3(MoO_4)_9$ filled HDPE composites are given in Figure 8.5 c-e. The surface morphology of the composite samples shows homogeneous distribution of filler in the HDPE matrix without pores for 46 and 48 vol% filler loaded samples. The maximum filler loading achieved without agglomeration is 48 vol%. The SEM micrograph of 50 vol% sample clearly shows that the composite has reached its percolation threshold and has uneven distribution of filler in the HDPE matrix. The 50 vol% filler loaded sample manifests increased ceramic to ceramic connectivity and losses 0-3 connectivity of the composite. At optimum filler

192

loading, the ceramic particles are evenly distributed whereas for higher filler loading the interparticle distance decreases and filler particles agglomerate. The SEM image of the cross-section clearly shows the presence of ceramic and filler as well differentiated entities, which further affirm the non-reactivity of the filler and the matrix as inferred from the XRD results.
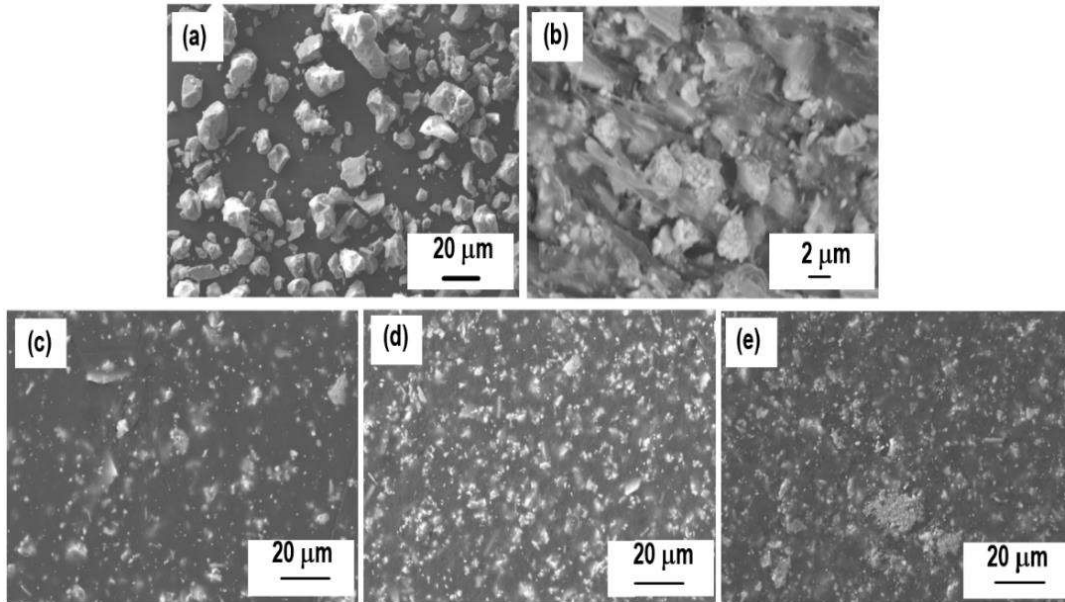
Figure 8.5 SEM micrographs of (a) $Pr_2Zr_3(MoO_4)_9$ filler (b) cross section of 48 vol% $Pr_2Zr_3(MoO_4)_9$ filled HDPE composite (c) 46 vol% (d) 48 vol% and (e) 50 vol% $Pr_2Zr_3(MoO_4)_9$ filled HDPE composites

8.3.4 Dielectric characterization of composites

$Pr_2Zr_3(MoO_4)_9$ and HDPE have dielectric constant values of 9.6 and 2.3 respectively in the X-band region. The variation of experimental density and dielectric constant at X-band of $Pr_2Zr_3(MoO_4)_9$ filled HDPE composites as a function of filler loading with an interval of 10 vol% is shown in Figure 8.6. The dielectric constant of the composite increases with filler loading due to the relatively high dielectric constant of the filler. At higher filler loading the particles come closer and as a result of this the contribution from interface region increases, which inturn increases the effective dielectric constant of the composite system [13].
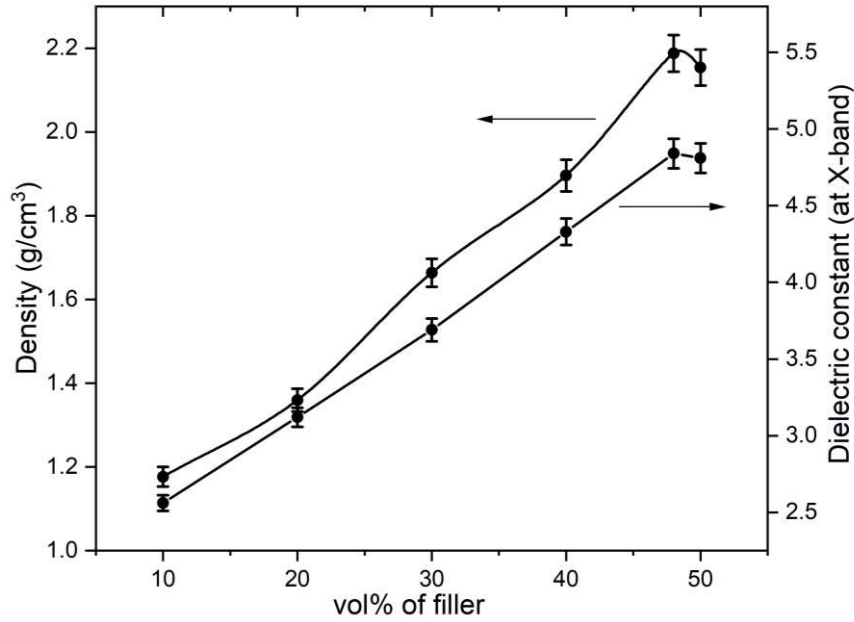
Figure 8.6 Vol% of filler vs experimental density and dielectric constant at X-band

The dielectric constant of the composite samples for the filler loading in the range 40 to 50 vol% is fine tuned and the variation of density and the dielectric constant at X-band with the vol% of filler loading is shown in Figure 8.7. It is clear from the Figure 8.7 that the dielectric constant and density of the composite increases up to 48 vol% filler loading and beyond which both the properties decreases. Beyond optimum filler loading (48 vol%), the dielectric constant of the composite sample decreases due to ceramic to ceramic connectivity and associated porosity in the samples. The variation of loss tangent with vol% of filler loading at X-band is given in Figure 8.8. The loss tangent also increases with filler loading. The loss tangent of a composite as a whole is largely caused by the heterogeneity, porosity, agglomeration and matrix-filler interphase region [13-15]. The 48 vol% loaded composite sample has $\varepsilon_r = 4.84$, tan δ = 0.003 at X-band and $\varepsilon_r = 5.24$, tan δ = 0.019 at 1MHz. The variation of dielectric constant at 1 MHz with volume fraction of filler loading is compared with that of the X-band dielectric constant and the results are shown in Figure 8.9. The dielectric constant of the composite at microwave frequency is lower than that at 1 MHz due to the absence of polarization mechanisms especially dipolar polarization prevalent at low frequencies [3]. The filler $Pr_2Zr_3(MoO_4)_9$ has a τ_{ε_r} of +464 ppm/^{o}C and the composite samples exhibit negative τ_{ε_r} values with decrease in dielectric constant as a function of

temperature in the range 30°C to 100°C. The variation of temperature coefficient of dielectric constant τ_{ε_r} with volume fraction of filler loading is given in Figure 8.10.
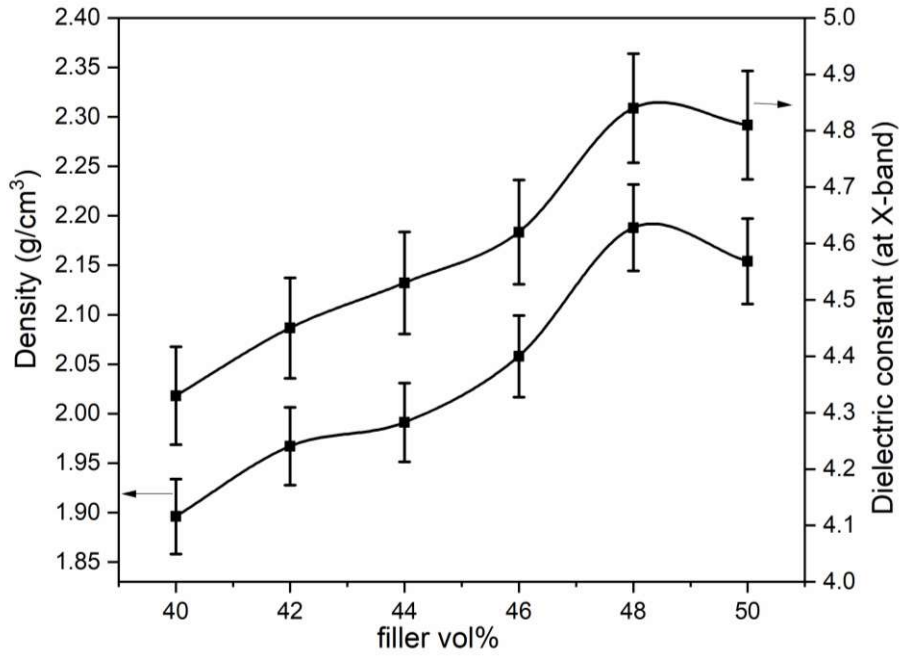
Figure 8.7 Fine tuning of density and dielectric constant at X-band with vol% of filler
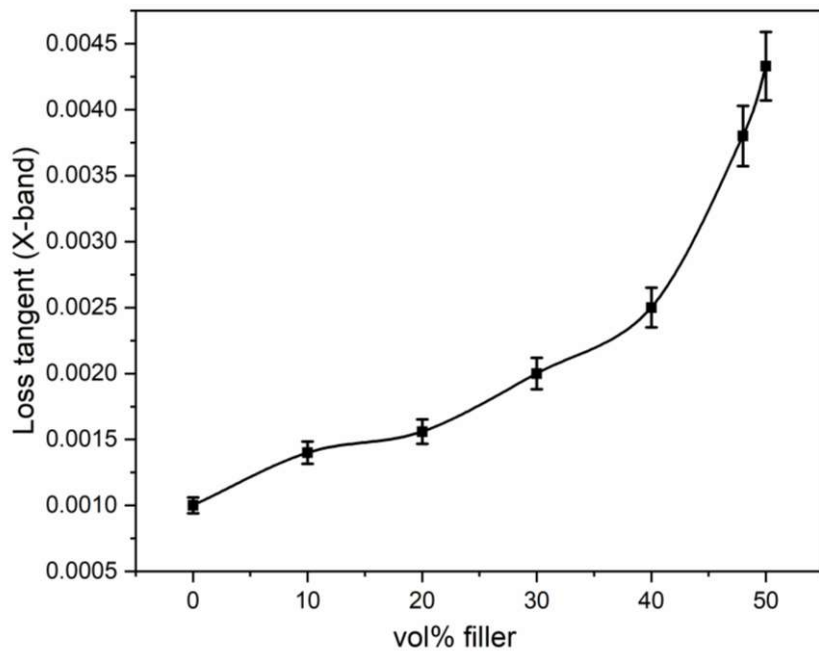
Figure 8.8   Variation of loss tangent of HDPE/Pr$_2$Zr$_3$(MoO$_4$)$_9$ composites with filler loading at X-band
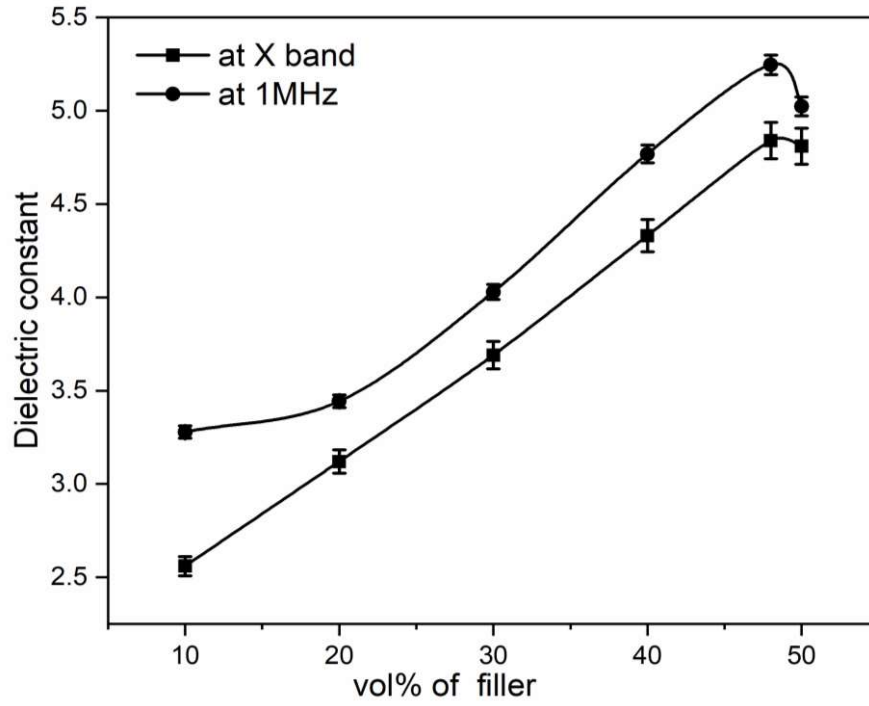
Figure 8.9 Vol% of filler vs dielectric constant at X-band and 1 MHz
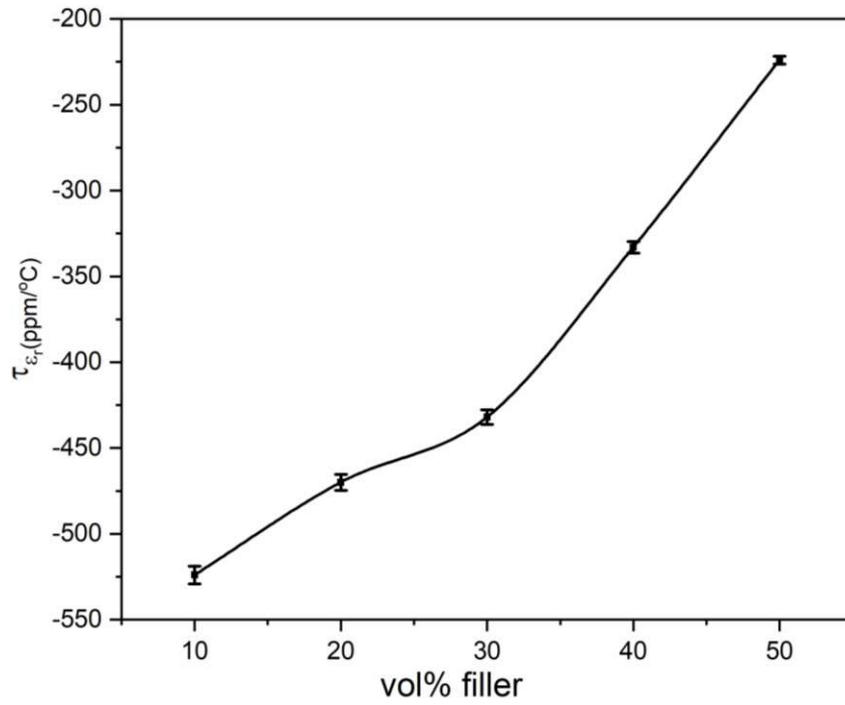
Figure 8.10 Vol% of filler loading vs temperature coefficient of dielectric constant

8.3.5 Theoretical modelling of dielectric constant

The effective dielectric constant and density of a biphasic composite are determined from the dielectric constant and density of constituent filler and matrix phases using equations 8.6 and 8.7 wherein ε_f, ε_m are the dielectric constant and v_f, v_m are the volume fractions of the ceramic filler and polymer matrix, respectively [2].

$$\varepsilon_{eff} = \varepsilon_f v_f + \varepsilon_m v_m \tag{8.6}$$

$$\rho_{eff} = \rho_f v_f + \rho_m v_m \tag{8.7}$$

Lichtenecker model is a logarithmic mixing rule in which the composite system is made up of randomly oriented spheroids in a continuous matrix without taking into account the filler matrix interaction and the equation is given in 8.8. This model gives better fitting near low volume fractions, however deviates more from the experimental values as the filler content increases due to porosity and inhomogeneous distribution of filler in the matrix [2,10]. Modified Lichtenecker model takes into account the filler matrix interaction as well by a fitting factor k=0.3 determined by filler shape, size of the filler particles and the interphase between the ceramic and polymer [2].

$$\log \varepsilon_{eff} = v_f \log \varepsilon_f + v_m \log \varepsilon_m \tag{8.8}$$

$$\log \varepsilon_{eff} = \log \varepsilon_f + v_m (1\text{-}k)\log \left(\frac{\varepsilon_m}{\varepsilon_f}\right) \tag{8.9}$$

Jayasundere-Smith model [2,16], Maxwell-Garnet model [2,17], Effective Medium Theory (EMT) model [2,18] and Maxwell-Wagner-Sillars (MWS) model [1,19] are given in equations 8.10, 8.11, 8.12 and 8.13 respectively.

$$\varepsilon_{eff} = \frac{\varepsilon_m(1-v_f) + \varepsilon_f v_f \left[\frac{3\varepsilon_m}{\varepsilon_f + 2\varepsilon_m}\right]\left[\frac{1+3v_f(\varepsilon_f-\varepsilon_m)}{\varepsilon_f + 2\varepsilon_m}\right]}{1-v_f + v_f \left[\frac{3\varepsilon_m}{\varepsilon_f + 2\varepsilon_m}\right]\left[\frac{1+3v_f(\varepsilon_f-\varepsilon_m)}{\varepsilon_f + 2\varepsilon_m}\right]} \tag{8.10}$$

$$\frac{\varepsilon_{eff}-\varepsilon_m}{\varepsilon_{eff}+2\varepsilon_m} = v_f \frac{\varepsilon_f-\varepsilon_m}{\varepsilon_f+2\varepsilon_m} \tag{8.11}$$

$$\varepsilon_{eff} = \varepsilon_m\left[1 + \frac{v_{fei}(\varepsilon_f-\varepsilon_m)}{\varepsilon_m + n(1-V_{fei})(\varepsilon_f-\varepsilon_m)}\right] \tag{8.12}$$

$$\varepsilon_{eff} = \varepsilon_m \frac{2\varepsilon_m + \varepsilon_f + 2v_f(\varepsilon_f-\varepsilon_m)}{2\varepsilon_m + \varepsilon_f - v_f(\varepsilon_f-\varepsilon_m)} \tag{8.13}$$

Jayasundere-Smith model considers the composite as a biphase system with dielectric spheres dispered in continous matrix taking into account the interactions between neighbouring particles only and is valid for low volume fraction of filler.

Maxwell-Garnet model assumes that the particles are embedded in the host polymer matrix and matches with the experimental results in the lower filler loading. The EMT model assumes that each filler is surrounded by a concentric matrix layer and the ceramic particle morphology fitting factor 'n' is incorporated which is determined empirically. Maxwell-Wagner-Sillars (MWS) model shows better fitting with experimental results if the properties of the filler and the matrix are similar [2]. The theoretical modelling of the dielectric constant of $Pr_2Zr_3(MoO_4)_9$ filled HDPE composites are done using Lichtnecker, modified Lichtnecker, Maxwell Garnet, Maxwell Wagner-Sillars (MWS), Effective Medium Theory (EMT) and Jayasundere Smith models and the results are given in Figure 8.11. The results are compared with the experimental dielectric constant and the porosity corrected dielectric constant values. Present study shows that the EMT model better matches with the experimental results.
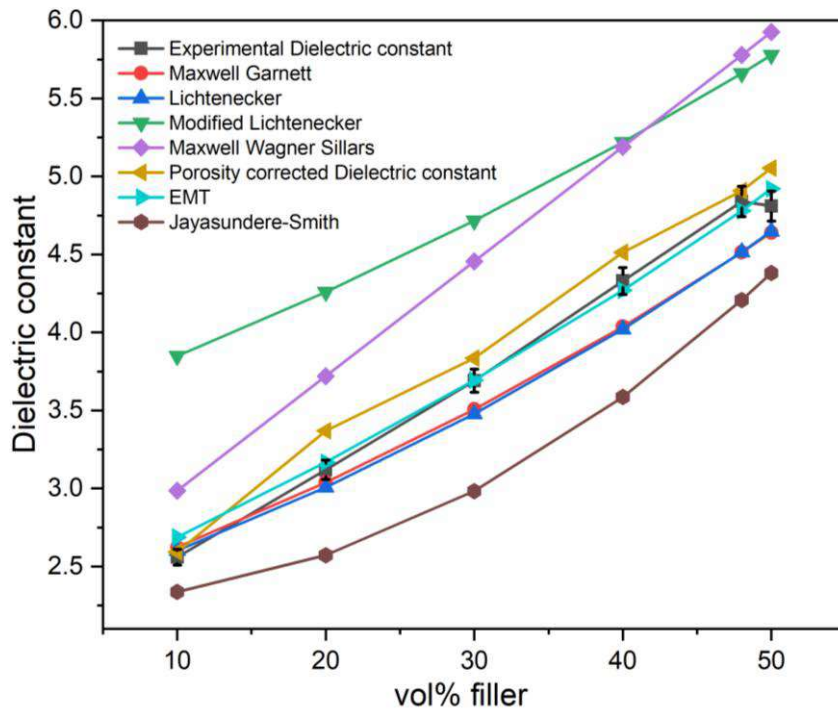
Figure 8.11 Comparison of experimental dielectric constant with different theoretical models

8.3.6 Coefficient of linear thermal expansion (CTE)

The coefficient of linear thermal expansion (CTE) of $Pr_2Zr_3(MoO_4)_9$ filled HDPE composites is determined as a function of vol% of filler loading and the results

are given in Figure 8.12. The pure HDPE is reported to have a CTE of 250 ppm/°C [4,5]. In the present study, the CTE of the HDPE/ $Pr_2Zr_3(MoO_4)_9$ composite is found to decrease with filler loading. The HDPE/$Pr_2Zr_3(MoO_4)_9$ composite with optimum filler loading of 48 vol% has a CTE of 57 ppm/°C. The CTE of the composite samples is found to decrease with increase in filler loading. The polymer shows higher expansion, which is limited by the higher amounts of particulate filler loaded in the polymer, which in turn arrests the movement of polymer chains [20,21]. The matrix-filler interphases are able to transmit the thermal stresses developed and result in the decrease of CTE for higher filler loading.
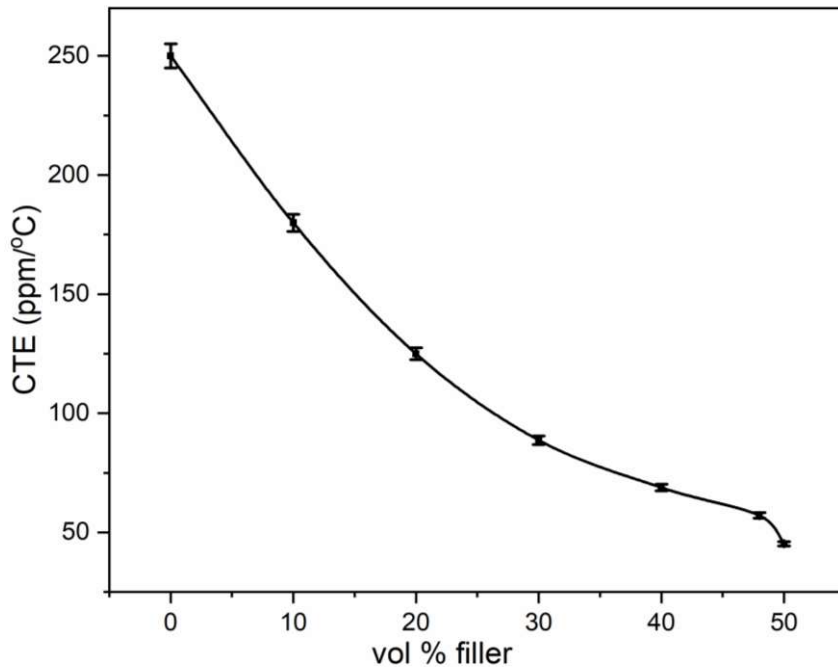
Figure 8.12   Variation of CTE as a function of filler loading in HDPE/$Pr_2Zr_3(MoO_4)_9$ composites

8.3.7 Ultimate tensile strength (UTS)

The variation of mechanical strength of HDPE/$Pr_2Zr_3(MoO_4)_9$ composites as a function of vol% of filler loading is shown in Figure 8.13. Pure HDPE is reported to have a maximum ultimate tensile strength of 20.04 MPa [22]. In the present study, the ultimate tensile strength of the HDPE/ $Pr_2Zr_3(MoO_4)_9$ composite is found to decrease with filler loading. The HDPE/$Pr_2Zr_3(MoO_4)_9$ composite with optimum filler loading

of 48 vol% has an ultimate tensile strength of 7.8 MPa. This reduction in the tensile strength is attributed to the increased ceramic content in the composite, which increase the filler-filler connectivity and in turn weaken the filler-matrix interaction. The presence of porosity decreases the tensile strength since it weakens the filler-matrix interphase. As the filler loading increases, the deformation area of polymer decreases and hence the ultimate tensile strength decreases [16,23]
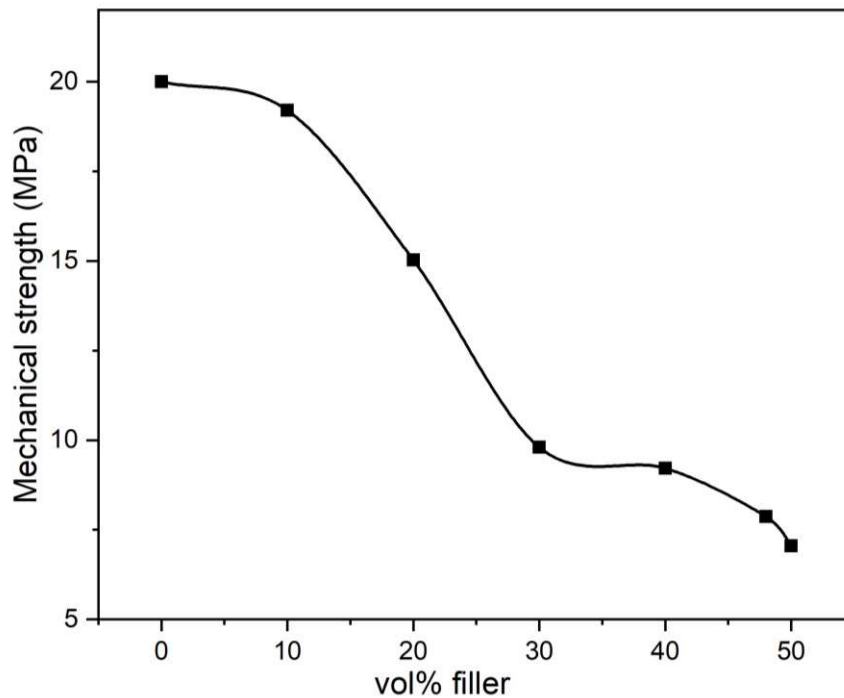
Figure 8.13   Variation of ultimate tensile strength of HDPE/ $Pr_2Zr_3(MoO_4)_9$ composites as a function of filler loading

8.3.8 Microstrip patch antenna measurements

The microstrip patch antenna with an operating frequency of 5.8 GHz is designed using ANSYS HFSS software. 5.8 GHz frequency is selected since it falls under the industrial, scientific and medical (ISM) radio band frequency range which is from 5.180 – 5.825 GHz. Lumped ports are assigned to excite the antennas. The frequency sweep is set over the desired range of frequencies before the simulations are commenced. The return loss is plotted as a function of frequency from the simulated results. The microstrip patch antenna is fabricated using 48 vol% filler loaded

composite substrate having ε_r = 4.84, tan δ = 0.003 and thickness = 0.8 mm through photolithography. The fabricated antenna with 50 Ω SMA connector attached is shown in Figure 8.14 (a) and the antenna measurement set up using vector network analyzer is shown in Figure 8.14 (b).
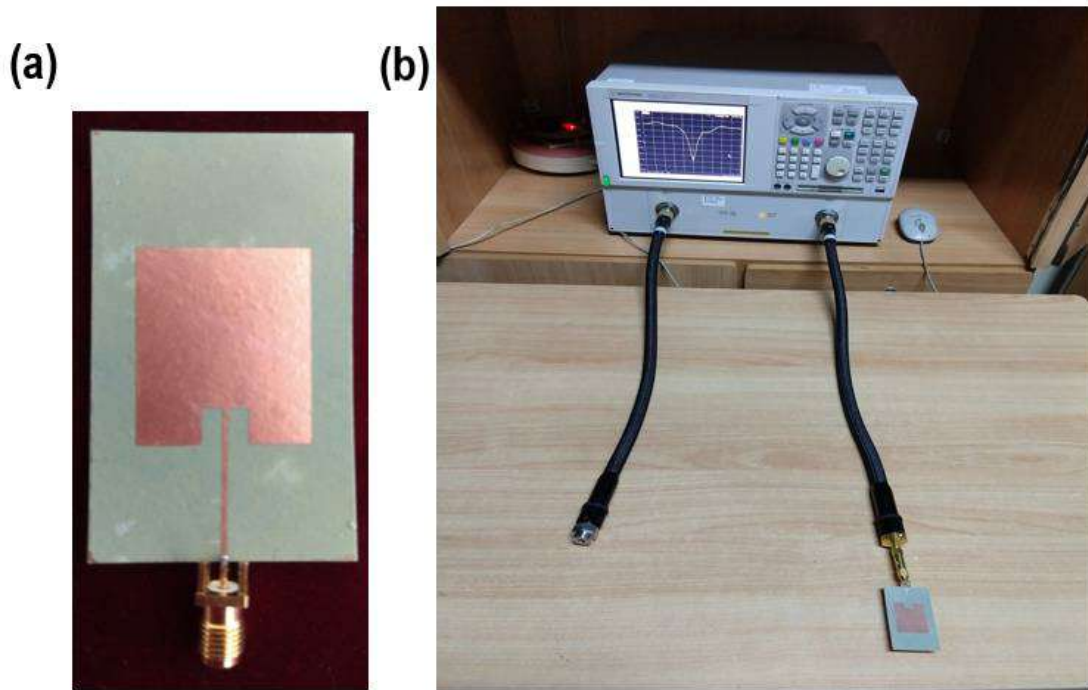
Figure 8.14   (a) Microstrip patch antenna fabricated for 5.8 GHz with SMA connector ready for measurement (b) Measurement setup for microstrip patch antenna using vector network analyzer

The simulated and measured reflection coefficients of the microstrip patch antenna are given in Figures 8.15 (a) and 8.15 (b) respectively. The microstrip patch antenna fabricated using HDPE/ $Pr_2Zr_3(MoO_4)_9$ substrate with 0.8 mm thickness exhibited an operating frequency of 5.63 GHz, bandwidth of 22.69 MHz and an insertion loss of -12.5 dB. The radiation pattern of the antenna is given in Figure 8.16. The experimental frequency is very near to the design frequency and hence it can be concluded that the HDPE/ $Pr_2Zr_3(MoO_4)_9$ composites are ideal for antenna substrate applications.

(a)

(b)
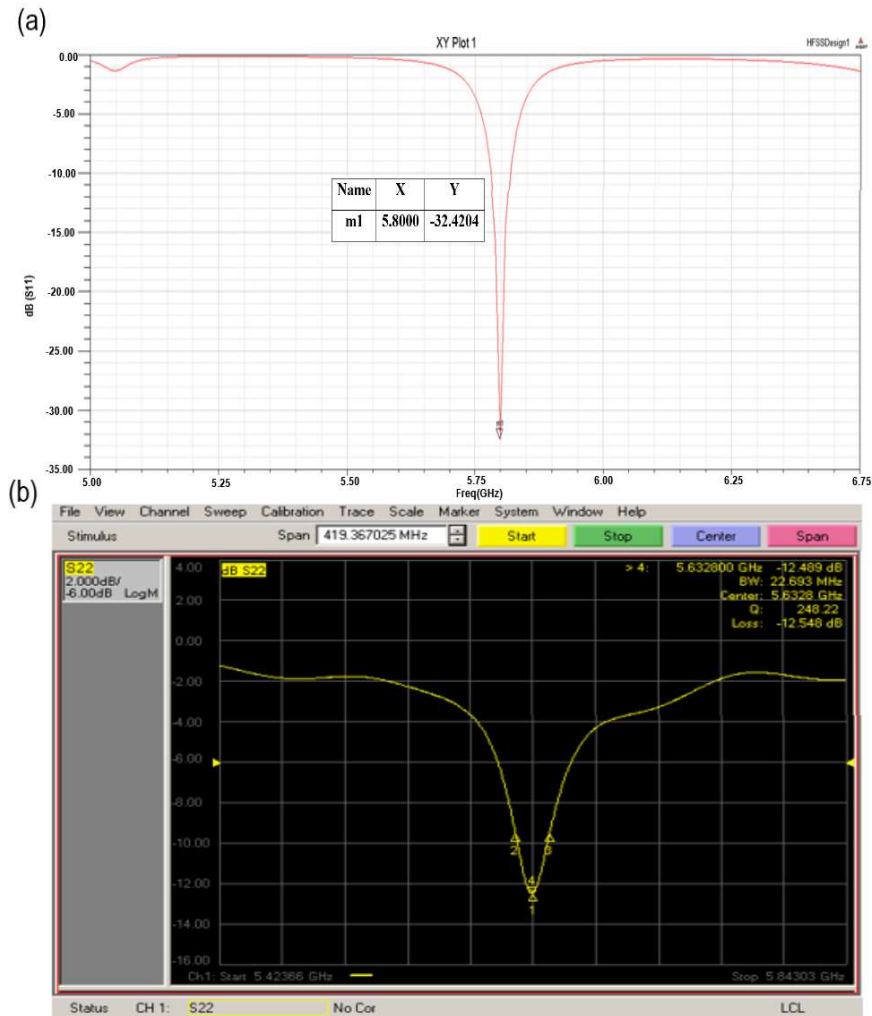
Figure 8.15   (a) Simulated and (b) measured return loss characteristics of the
patch antenna using substrate having $\varepsilon_r = 4.84$ and tan $\delta = 0.003$
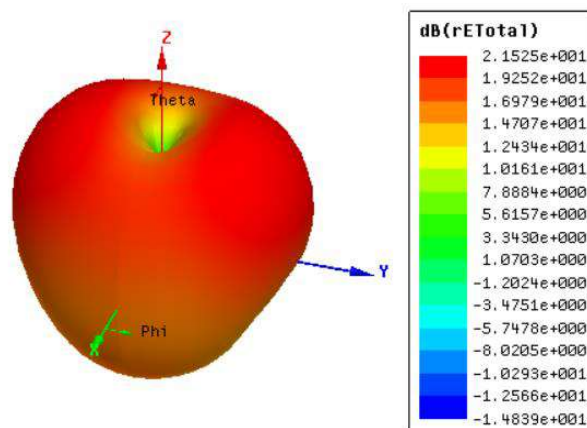
Figure 8.16 Simulated radiation pattern of the microstrip patch antenna

8. 4 Conclusions

Cost effective ceramic filled HDPE composites have been prepared using $Pr_2Zr_3(MoO_4)_9$ ceramic filler by intimate mixing and compression moulding techniques. The density and dielectric properties of the composites have been determined for different filler loadings and the optimum filler loading in the HDPE matrix is found out as 48 vol% through fine tuning. HDPE/$Pr_2Zr_3(MoO_4)_9$ composite at 48 vol% filler loading exhibits a dielectric constant of 4.84 and loss tangent of 0.003 in the X-band frequency region. The composite shows an ultimate tensile strength of 7.8 MPa and CTE of 57 ppm/ºC at the optimum filler loading of 48 vol%. XRD and SEM analyses confirm the non-reactivity between the ceramic filler and HDPE matrix. Theoretical modelling of dielectric constant of the composite system has been done and compared with experimental results. The temperature coefficient of dielectric constant, coefficient of thermal expansion (CTE) and ultimate tensile strength of the HDPE/$Pr_2Zr_3(MoO_4)_9$ composites decrease with respect to filler loading. The optimum filler loaded composite sample is Cu cladded through vacuum lamination process and designed microstrip patch antenna using ANSYS HFSS with an operating frequency of 5.8 GHz. The microstrip patch antenna is fabricated on 48 vol% Cu cladded HDPE/$Pr_2Zr_3(MoO_4)_9$ substrate through photolithographic technique. The fabricated antenna is tested using vector network analyzer and it operates at 5.63 GHz, with a bandwidth of 22.69 MHz, return loss of -12.5 dB, which can be used for ISM band applications. Present study shows that HDPE/$Pr_2Zr_3(MoO_4)_9$ composites are ideal substrates for microstrip patch antenna fabrication.

References

[1] M. T. Sebastian, *Dielectric materials for wireless communication*, Elsevier (2008).

[2] M. T. Sebastian, H. Jantunen, High Temperature Cofired Ceramic (HTCC), Low Temperature Cofired Ceramic (LTCC), and Ultralow Temperature Cofired Ceramic (ULTCC) Materials, *Microwave Materials and Applications*, 2V Set, (2017) 355-425.

[3] M. T. Sebastian, H. Jantunen, Polymer–ceramic composites of 0–3 connectivity for circuits in electronics: a review, Int. J. Appl. Ceram. Technol., 7 [4] (2010) 415-434.

[4] S. Thomas, V. Deepu, S. Uma, P. Mohanan, J. Philip, M. T. Sebastian, Preparation, characterization and properties of $Sm_2Si_2O_7$ loaded polymer composites for microelectronic applications, Mater. Sci. Eng. B, 163 [2] (2009) 67-75.

[5] D. Thomas, M. T. Sebastian, HDPE matrix composites filled with $Ca_4La_6(SiO_4)_4(PO_4)_2O_2$ for microwave substrate applications, J. Electron. Packag., 136 [3] (2014) 031002.

[6] J. Varghese, D. R. Nair, P. Mohanan, M. T. Sebastian, Dielectric, thermal and mechanical properties of zirconium silicate reinforced high density polyethylene composites for antenna applications, Phys. Chem. Chem. Phys., 17 [22] (2015) 14943-14950.

[7] K. M. Manu, S. Soni, V. R. Murthy, M. T. Sebastian, $Ba(Zn_{1/3}Ta_{2/3})O_3$ ceramics reinforced high density polyethylene for microwave applications, J. Mater. Sci.: Mater. Electron., 24 [6] (2013) 2098-2105.

[8] G. Subodh, V. Deepu, P. Mohanan, M. T. Sebastian, Dielectric response of $Sr_2Ce_2Ti_5O_{15}$ ceramics reinforced high density polyethylene, J. Phys. D: Appl. Phys., 42 [22] (2009) 225501.

[9] P. S. Anjana, V. Deepu, S. Uma, P. Mohanan, J. Philip, M. T. Sebastian, Dielectric, thermal, and mechanical properties of CeO_2-filled HDPE composites for microwave substrate applications, J. Polym. Sci. B: Polym. Phys., 48 [9] (2010) 998-1008.

[10] K. Lichtenecker, Dielectric constant of natural and synthetic mixtures, Phys. Z, 27 (1926) 115-158.

[11] R. Garg, P. Bhartia, I. J. Bahl, A. Ittipiboon, *Microstrip antenna design handbook*, Artech house (2001).

[12] K. F. Lee, K. M. Luk, H. W. Lai, *Microstrip patch antennas*, World Scientific (2017).

[13] D. H. Kuo, C. C. Chang, T. Y. Su, W. K. Wang, B. Y. Lin, Dielectric properties of three ceramic/epoxy composites, Mater. Chem. Phys., 85 [1] (2004) 201-206.

[14] A. Gemant, The Role of Solid Friction in Synthetic Dielectrics, J. Appl. Phys., 9 [11] (1938) 730-734.

[15] M. G. Todd, F. G. Shi, Molecular basis of the interphase dielectric properties of microelectronic and optoelectronic packaging materials, IEEE Trans. Compon. Packag. Technol., 26 [3] (2003) 667-672.

[16] N. Jayasundere, B. V. Smith, B.V., Dielectric constant for binary piezoelectric 0-3 composites, J. Appl. Phys., 73 [5] (1993) 2462-2466.

[17] A. H. Sihvola, *Electromagnetic mixing formulas and applications* (No. 47), Iet (1999).

[18]   Y. Rao, J. Qu, T. Marinis, C. P. Wong, A precise numerical prediction of effective dielectric constant for polymer-ceramic composite based on effective-medium theory, IEEE Trans. Compon. Packag. Technol., 23 [4] (2000) 680-683.

[19]   K. P. Murali, S. Rajesh, O. Prakash, A. R. Kulkarni, R. Ratheesh, Preparation and properties of silica filled PTFE flexible laminates for microwave circuit applications, Composites, Part A, 40 [8] (2009) 1179-1185.

[20]   L. Holliday, J. Robinson, The thermal expansion of composites based on polymers, J. Mater. Sci., 8 [3] (1973) 301-311.

[21]   R. S. Raghava, Thermal expansion of organic and inorganic matrix composites: A review of theoretical and experimental studies, Polym. Compos., 9 [1] (1988) 1-11.

[22]   S. Faiz, A. Anis, M. Luqman, S. M. Al Zahrani, Studies on thermal, mechanical, morphological, and viscoelastic properties of polybenzimidazole fiber reinforced high density polyethylene composites, Polym. Compos., 37 [1] (2016) 5-13.

[23]   T. Joseph, S. Uma, J. Philip, M. T. Sebastian, Dielectric, thermal and mechanical properties of $Sr_2ZnSi_2O_7$ based polymer/ceramic composites, J. Mater. Sci.: Mater. Electron., 23 [6] (2012) 1243-1254.

Chapter 9

Summary and scope of future work

9.1 Summary

9.2 Scope for future work

9.1 Summary

Microwaves are the carrier waves in the modern telecommunication devices. World over is heading towards 5G regime using high speed data connectivity enabling device to device communication. Design of microwave and millimeter wave circuits are oriented towards miniaturization of the communication devices. The medium for unattenuated propagation of electromagnetic energy in high frequency devices utilize microwave ceramics having low dielectric loss, stable dielectric constant together with temperature independent dielectric properties. Multilayer co-firing technology is employed for the fabrication of microwave circuits, which can be broadly classified into HTCC (High Temperature Co-fired Ceramics), LTCC (Low Temperature Co-fired Ceramics) and ULTCC (Ultra Low Temperature Co-fired Ceramics).

Multilayer stacking technique consists of tape casting the ceramic powder, followed by screen printing of the required microwave circuits, stacking the different layers and co-firing them into a single monolithic package. The screen printing has to be done using a conductive ink formulation which is based on a high conductive metal, but at the same time compatible with the ceramic. LTCC materials are those ceramics which can be co-fired with silver metal electrode and are having sintering temperatures below 961°C, which is the melting point of silver. Whereas ULTCC materials are ceramics having sintering temperatures below 660°C, the melting point of aluminium.

Low melting glass phases or sintering aids can be added for lowering the sintering temperature of ceramics. But this method detrimentally affects the dielectric properties of the ceramics. Phase pure ceramics with low sintering temperature are the much sought after materials for LTCC and ULTCC substrate fabrication. Lowering of sintering temperature as well as the use of cheap metal electrodes make LTCC and ULTCC technology cost effective. These substrates exhibit excellent signal propagation characteristics compared to conventional PCBs and can be used for the fabrication of a host of microwave devices like implantable antennas, 5G MIMO antennas, substrate integrated waveguides, diplexers, RF front end etc.

The thesis investigates the structure and microwave dielectric properties of a wide range of molybdate ceramics and studied their suitability for LTCC and ULTCC applications. The compounds selected for the study are binary molybdates in the alkaline earth molybdate - rare earth molybdate $AMoO_4$-$R_2(MoO_4)_3$, sodium molybdate

- alkaline earth molybdate Na_2MoO_4-$AMoO_4$ and sodium molybdate - rare earth molybdate Na_2MoO_4-$R_2(MoO_4)_3$ systems, which are having crystal structures related to the scheelite crystal structure. The scheelite structured compounds are selected for the study based on the phase purity of these compositional type, their low loss tangent and compatibility with Ag and Al metal electrodes, which are ideally suited for LTCC and ULTCC applications.

$Na_5R(MoO_4)_4$ type phase pure compositions in the Na_2MoO_4-$R_2(MoO_4)_3$ (R = La, Pr, Nd, Sm, Y and Yb) systems were prepared by solid-state ceramic route and the crystal structure, microstructure, microwave dielectric properties and chemical compatibility with metal electrodes have been investigated. The phase purity of the compositions were confirmed through powder X-ray diffraction studies and uniform microstructure manifested using SEM investigation. These compositions were reported to have modulated scheelite-like structure with Na^+ and R^{3+} ions replacing the Ca^{2+} ions in the scheelite structure. All the compositions had ultra low sintering temperatures. $Na_5Y(MoO_4)_4$ ceramic exhibited ε_r of 7.8, Q_u x f of 56,800 GHz and τ_f of -83 ppm/°C at a sintering temperature of 600°C for 1h, whereas $Na_5Yb(MoO_4)_4$ ceramic exhibited ε_r of 6.9, Q_u x f of 43,400 GHz and τ_f of -68 ppm/°C at a sintering temperature of 570°C for 1h. On the other hand, $Na_5R(MoO_4)_4$ (R = La, Pr, Nd and Sm) ceramics exhibited weak mode in the microwave region and hence the accurate measurement of τ_f was not possible. In addition to this, the compositions reacted with Al during co-firing, which limits their utility for ULTCC applications. Among the compositions studied, $Na_5Yb(MoO_4)_4$ ceramic showed good quality factor together with excellent compatibility with Al electrode and can be utilized as ideal candidate material for ULTCC applications.

$NaR_5(MoO_4)_8$ (R = La, Pr, Nd, Sm) ceramics with incommensurately modulated scheelite structure have been prepared and correlated their structure-property relationship to identify their suitability for LTCC/ULTCC applications. Present study shows that the compositions are phase pure in nature which is manifested from XRD, laser Raman and back scattered SEM studies. The dielectric constant of these compositions ranges from 10.6 to 11.5, quality factor from 56,200 to 78,600 GHz and τ_f from -42 to -72 ppm/°C. The FWHM of the symmetric stretching Raman modes of these ceramics were correlated with the quality factor. $NaR_5(MoO_4)_8$ (R = La, Pr, Nd, Sm) ceramics were co-fired with silver and their compatibility have been evaluated by

XRD and EDS analyses. The XRD patterns of the co-fired samples showed characteristic peaks of the ceramics, together with weak Ag peaks. The EDS analysis revealed the diffusion of silver into the ceramic during co-firing, which limits their application in LTCC devices. $NaR_5(MoO_4)_8$ (R = La, Pr, Nd, Sm) ceramics with incommensurately modulated scheelite structure consisted of less number of modes in the stretching region compared to that of $Na_5R(MoO_4)_4$ (R = La, Pr, Nd, Sm, Y and Yb) ceramics with scheelite-like structure and hence possess higher $Q_u \times f$ values and better temperature stability of dielectric properties due to less distortion of the MoO_4 tetrahedra. However, unlike $Na_5R(MoO_4)_4$ with scheelite-like structure which exhibited excellent Al compatibility, $NaR_5(MoO_4)_8$ ceramics with incommensurately modulated scheelite structure possess less compatibility with Ag electrodes. The plausible reason for this could be due to the more number of cation vacancies present in the crystal structure which in turn enhance the migration of co-fired metal atoms into the ceramic.

The $Na_2A_5(MoO_4)_6$ (A = Zn, Mg, Ca, Ba, Sr) compositions in the Na_2MoO_4-$AMoO_4$ binary systems were prepared by solid-state ceramic route. Among the ceramics studied, $Na_2Zn_5(MoO_4)_6$ and $Na_2Mg_5(MoO_4)_6$ were reported as phase pure compositions with triclinic structure. $Na_2Zn_5(MoO_4)_6$ ceramic exhibited a dielectric constant of 8.1, quality factor $Q_u \times f$ of 35,800 GHz, temperature coefficient of resonant frequency τ_f of -95 ppm/^oC at 590^oC along with excellent compatibility with Al electrode, which was confirmed by XRD and EDS analyses of the co-fired sample. $Na_2Mg_5(MoO_4)_6$ ceramic also possesses good microwave dielectric properties, although the application is limited because of its hygroscopic nature. In the present work, Ba, Sr and Ca analogues of these compositions were also prepared and characterized. The XRD and Raman analyses affirm that the Ba, Sr and Ca compositions exist as a solid solution consisting of corresponding alkaline earth molybdate and sodium molybdate, which can be represented as Na_2MoO_4-5($AMoO_4$) (A = Ba, Sr and Ca). Among the ceramics studied, $Na_2Zn_5(MoO_4)_6$, $Na_2Mg_5(MoO_4)_6$, Na_2MoO_4-5($BaMoO_4$) and Na_2MoO_4-5($SrMoO_4$) showed Al compatibility, whereas Na_2MoO_4 -5($CaMoO_4$) reacted with Al.

Other than the sodium molybdate based systems, alkaline earth - rare earth molybdate based systems in the $AMoO_4$-$R_2(MoO_4)_3$ (A = Ba, Sr, Ca; R = La, Pr, Nd, Sm) phase diagram with scheelite derived structure type $AR_4(MoO_4)_7$ were investigated. Among the compositions studied, $BaLa_4(MoO_4)_7$ and $AR_4(MoO_4)_7$ (A =

Sr, Ca; R = La, Pr, Nd and Sm) are single phase whereas $BaR_4(MoO_4)_7$ (R = Pr, Nd, Sm) existed as multiphase comprising of $BaR_2(MoO_4)_4$ and $R_2(MoO_4)_3$ phases. The dielectric constant of the phase pure compositions range from 9 to 11.8, quality factor Q_u x f from 30,200 to 91,000 GHz and τ_f from -39 to -90 ppm/°C. The highest Q_u x f was obtained for $CaPr_4(MoO_4)_7$ ceramic. The co-firability of these compositions with silver has been investigated, however as in the case of $NaR_5(MoO_4)_8$ ceramics, the XRD patterns of the co-fired samples contain all the ceramic peaks together with weak Ag peaks. The EDS analysis revealed the presence of Ag in the ceramic, which limits the suitability of these compositions for LTCC applications.

The compositions investigated so far exhibited reasonably good dielectric constant, high quality factor and good compatibility with Al electrodes. However, temperature coefficient of resonant frequency is one of the decisive factors for utilizing these materials for outdoor wireless applications. In a view to bring down the τ_f value binary molybdate composition in $Pr_2(MoO_4)_3$-$Zr(MoO_4)_2$ phase diagram, $Pr_2Zr_3(MoO_4)_9$ composition has been selected and appropriate substitution for Zr^{4+} with Ti^{4+} was attempted. The dielectric constant of $Pr_2Zr_{(3-x)}Ti_x(MoO_4)_9$ (x = 0,1,2,3) ceramics ranges from 9.6 to 12.7, quality factor Q_u x f from 42,900 to 27,400 GHz and τ_f from -30 to 0 ppm/°C. Present study shows that this material system is phase pure up to $Pr_2Zr_2Ti(MoO_4)_9$ ceramic and exhibit excellent microwave dielectric properties with a τ_f value of -16 ppm/°C, beyond which the compositions show multiphase nature. However, these ceramics were found to react with Ag/Al electrodes during co-firing. Although these materials are not suitable for LTCC or ULTCC applications, $Pr_2Zr_3(MoO_4)_9$ can be used as a particulate ceramic filler material in a low loss polymer system owing to its excellent quality factor and relatively low τ_f. In order to accomplish this, High-density polyethylene (HDPE) is selected as the polymer matrix because of its low loss tangent and relatively good service temperature. The optimum filler loading of $Pr_2Zr_3(MoO_4)_9$ in the HDPE matrix was found as 48 vol% through intimate mixing and compression moulding techniques. The dielectric, thermal and mechanical properties of the composite sample at optimum loading of 48 vol% has ε_r of 4.84, tan δ of 0.003, CTE of 57 ppm/°C (coefficient of thermal expansion) and ultimate tensile strength of 7.8 MPa. The planar HDPE/$Pr_2Zr_3(MoO_4)_9$ composite was copper cladded on both sides through vacuum lamination process for circuit fabrication. ANSYS HFSS was used to design microstrip patch antenna on copper cladded substrates for operations

at ISM band (5.8 GHz). The microstrip patch antenna is fabricated using photolithographic technique and antenna parameters were measured using a vector network analyzer.

The phase pure compositions studied in this thesis, their crystal structure, sintering temperature, microwave dielectric properties and their suitability for co-firing as well as substrate applications are compiled in the Table 9.1.

Compositions in the present study possess dielectric constant ranging from 6 to 12, Q_u x f from 20,000 GHz to as high as 90,000 GHz and τ_f values from -16 to -95 ppm/°C. It can be concluded that the molybdate ceramics show better co-firability with Al electrodes than Ag and are ideal materials for ULTCC applications. Among the ultra low sinterable materials, molybdate compositions show better compatibility with Al compared to vanadate and tellurate compositions together with improved quality factor. These materials can also be used as filler materials for polymer-composite applications.

Table 9.1 Sintering temperature, microwave dielectric properties and co-firability of microwave ceramics

Compound	Crystal structure and spacegroup	Sintering temperature (°C)	ε_r @ GHZ	Q_u x f (GHz)	τ_f (ppm/ °C)	Co-firability
$Na_5La(MoO_4)_4$	Tetragonal $I4_{1/a}$	530/1h	6.2	18,800	#	Reacts with Al
$Na_5Pr(MoO_4)_4$	Tetragonal $I4_{1/a}$	540/1h	6.4	19,900	#	Reacts with Al
$Na_5Nd(MoO_4)_4$	Tetragonal $I4_{1/a}$	550/1h	7.1	21,250	#	Reacts with Al
$Na_5Sm(MoO_4)_4$	Tetragonal $I4_{1/a}$	560/1h	6.3	26,800	#	Reacts with Al
$Na_5Y(MoO_4)_4$	Tetragonal $I4_{1/a}$	600/1h	7.8	56,800	-83	Reacts with Al
$Na_5Yb(MoO_4)_4$	Tetragonal $I4_{1/a}$	570/1h	6.9	43,400	-68	Al compatible
$Na_2Zn_5(MoO_4)_6$	Triclinic $P\bar{1}$	590/1h	8.1	35,800	-95	Al compatible
$Na_2Mg_5(MoO_4)_6$	Triclinic $P\bar{1}$	540/1h	7.8	37,600	-87	Al compatible
Na_2MoO_4 + $5(CaMoO_4)$	Multiphase	640/1h	8.1	28,500	-67	Reacts with Al
Na_2MoO_4 + $5(SrMoO_4)$	Multiphase	620/1h	7.6	20,500	-44	Al compatible

| Compound	Crystal structure and spacegroup	Sintering temperature (°C)	ε_r @ GHZ	$Q_u \times f$ (GHz)	τ_f (ppm/°C)	Co-firability
Na_2MoO_4 + $5(BaMoO_4)$	Multiphase	610/1h	6.1	43,000	-74	Al compatible
$NaLa_5(MoO_4)_8$	Monoclinic I2/b($\alpha\beta0$)00	780/1h	11.5	56,200	-72	Ag *
$NaPr_5(MoO_4)_8$	Monoclinic I2/b($\alpha\beta0$)00	780/1h	11.4	71,900	-52	Ag*
$NaNd_5(MoO_4)_8$	Monoclinic I2/b($\alpha\beta0$)00	770/1h	11.1	78,600	-42	Ag*
$NaSm_5(MoO_4)_8$	Monoclinic I2/b($\alpha\beta0$)00	760/1h	10.6	59,400	-51	Ag*
$BaLa_4(MoO_4)_7$	Monoclinic	710/1h	11.8	39,300	-68	Ag*
$SrLa_4(MoO_4)_7$	Monoclinic	740/1h	11.7	44,200	-83	Ag*
$SrPr_4(MoO_4)_7$	Monoclinic	740/1h	9.6	78,600	-73	Ag*
$SrNd_4(MoO_4)_7$	Monoclinic	740/1h	9	39,400	-90	Reacts with Ag
$SrSm_4(MoO_4)_7$	Monoclinic	730/1h	9.5	30,500	-79	Reacts with Ag
$CaLa_4(MoO_4)_7$	Monoclinic	750/1h	11.4	30,200	-90	Ag*
$CaPr_4(MoO_4)_7$	Monoclinic	750/1h	10.6	91,000	-39	Reacts with Ag
$CaNd_4(MoO_4)_7$	Monoclinic	750/1h	10.4	68,400	-44	Ag*
$CaSm_4(MoO_4)_7$	Monoclinic	740/1h	9.7	34,000	-48	Ag*
$Pr_2Zr_3(MoO_4)_9$	Rhombohedral $R\bar{3}c$	790/1h	9.6	42,900	-30	Reacts with Ag
$Pr_2Zr_2Ti(MoO)_9$	Rhombohedral	760/1h	9.7	35,600	-16	Reacts with Ag
$Pr_2ZrTi_2(MoO)_9$	Multiphase	700/1h	11.8	34,900	-11	Reacts with Ag
$Pr_2Ti_3(MoO_4)_9$	Multiphase	630/1h	12.7	27,400	0	Reacts with Al

* Presence of Ag detected in ceramic

\# τ_f could not be measured due to weak resonance

9.2 Scope for future work

In conclusion, the thesis presents an extensive study of molybdate based ULTCC and LTCC materials with excellent microwave dielectric properties, compatibility with metal electrodes, HDPE/ceramic composite preparation, microstrip patch antenna fabrication and system level testing for ISM band applications. The ceramics with low and ultra low sintering temperature with good microwave dielectric properties and co-firability can be utilized for LTCC/ULTCC applications. The ceramics presented in this work are ideal materials for substrate integrated waveguide (SIW) applications due to their superior microwave dielectric properties and good machinability of the molybdate ceramics. The design and fabrication of a SIW system is proposed as the future work. A typical substrate integrated waveguide structure is shown in Figure 9.1, which is fabricated on a dielectric substrate by arraying via-holes which connect the upper and lower metal plates of the substrate [1-3].
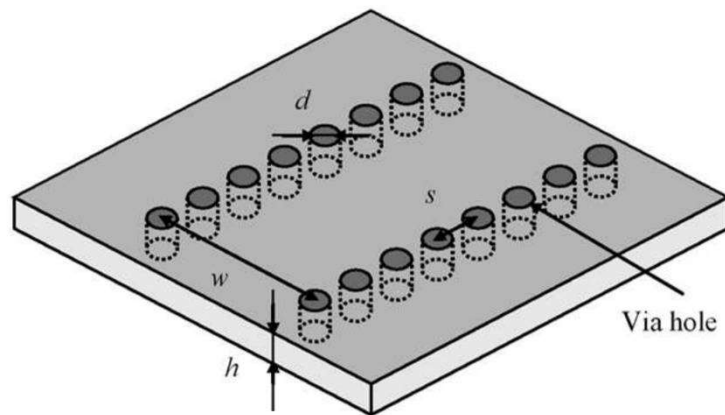
Figure 9.1 Substrate integrated waveguide [Ref. 1]

The compositions identified in this study can be tape casted and the desired LTCC/ULTCC circuits can be fabricated. The silver electrode diffusion into the ceramic on co-firing can be circumvented by suitably identifying dielectric nano ink formulations which can be co-fired with the ceramic. In addition to this, these ceramics can be used as fillers in polymer/ceramic composites for planar antenna substrate applications.

References

[1] F. Xu, K. Wu, Guided-wave and leakage characteristics of substrate integrated waveguide, IEEE Trans. Microw. Theory Tech., 53 [1] (2005) 66-73.

[2] Y. J. Cheng, *Substratre Integrated antennas and arrays*, CRC Press (2015).

[3] M. Bozzi, A. Georgiadis, K. Wu, Review of substrate-integrated waveguide circuits and antennas, IET Microw. Antennas Propag., 5 [8] (2011) 909-920.